# Wave and modal approach for multi-scale analysis of periodic structures

Changwei Zhou

**Numéro d'ordre : 2014-40** **Année 2014**

**ÉCOLE CENTRALE DE LYON**

École Doctorale Mécanique, Énergétique, Génie Civil et Acoustique

# THÈSE

---

# Wave and modal coupled approach for multi-scale analysis of periodic structures

-

# Approche couplée propagative et modale pour l'analyse multi-échelle des structures périodiques

---

Soutenue le 10 Dec 2014

par

**Changwei ZHOU**

en vue d'obtenir le titre de

**DOCTEUR DE L'ÉCOLE CENTRALE DE LYON**

spécialité

**MÉCANIQUE**

Devant le jury composé de :

| | | |
|---|---|---|
| M. COLLET | Directeur de recherche, LTDS, ECL | *Président* |
| M. OUISSE | Professeur, ENSMM | *Rapporteur* |
| H. RIOU | Professeur agrégé HDR, ENS, Cachan | *Rapporteur* |
| L. LI | Professeur, Université Beihang, Chine | *Examinateur* |
| M. N. ICHCHOU | Professeur, LTDS, ECL | *Directeur* |
| J. -P. LAINÉ | Maitre de conférence, LTDS, ECL | *Co-encadrant* |
| A. -M. ZINE | Maitre de conférence, ICJ, ECL | *Co-directeur* |

# Remerciement

Peut-être que toutes les thèses réussies se ressemblent, chaque thèse échouée l'est à sa façon. Mais il n'y a pas de thèse sans émotion. La joie, la tristesse et la colère se combinent, se mélangent pour former un souvenir inoubliable. Quant à moi, je suis surtout reconnaissante pour ces 3 années.

Tout d'abord, je voudrais remercier les membres de jury, surtout les deux rapporteurs pour leurs conseils précieux sur la correction de ce mémoire. Merci à mon directeur de thèse, Mohammed Ichchou. Il a créé un environnement de travail formidable pour moi, il m'a fait confiance et encouragé même lorsque je doutais de moi même. Je remercie aussi mon co-directeur de thèse, Abdel-Malek Zine, pour ses réponses sur les problèmes mathématiques et aussi pour sa gentillesse. Mes remerciement s'adressent encore plus particulièrement à toi, Jean-Pierre. Je pense que j'ai probablement du sauver le monde dans une vie précédente pour mériter un tuteur aussi exceptionnel. Ton remarquable professionnalisme, ta curiosité incessante, ton enthousiasme pur et désintéressé pour la recherche, me touche, m'influence et m'apprends. Ton aide interrompue durant ces 3 années: pendant la première année, tu ne manquais jamais de patience pour moi, moi à qui il manquait tant de connaissances. En deuxième année, tes nouvelles idées brillantes alimentaient mes recherches. En troisième enfin, tu me poussais à aller toujours plus loin. Pendant les quinzaine de jours avant la soutenance, lorsque je paniquais en voyant mon agenda rempli, tu ne comptais plus ton temps pour m'aider, à préparer les cours, me monter les TP, jouer les pompiers quand je n'arrives pas à répondre à des questions d'élèves, corriger un à un les transparents de soutenance en allant jusqu'à examiner chaque phrase. On ne peut pas imaginer de meilleur tuteur que toi.

Je voudrais exprimer mes gratitudes à Olivier Bareille, même s'il n'est pas mon encadrant officiel, mais il m'a beaucoup aidé. Il a pris soin de moi lorsque j'étais en 3A, et j'ai pu découvrir son efficacité et sa méthodologie quand je travaillais avec lui en tant ATER. J'ai appris tant de choses... Merci à Stéphane Lemahieu pour son aide pour l'installation de mon expérience. Merci à Olivier Dessombz pour son soutien technique. Merci à Jean-Jacques Sinou pour son accueil chaleureux dans le département MSGMGC. Merci à Isabelle Tixier pour ses aides diverses, elle a

pratiquement fait de moi une écologiste convaincue. Merci à Cheng Sun pour sa confiance, elle m'a confié les cours de Chinois pendant 2 ans, me permettant ainsi d'acquérir une première expérience d'enseignement supérieur.

Je remercie sincèrement mes collègues des départements de mécanique des fluides et mécanique des solides. Merci à Zhou Wenjin pour ses excellents résultats d'expérience sur plaque raidie. Merci à Huang Tianli qui m'a introduit dans le monde de la WFEM. Merci à Zhang Kai pour ses conseils pour la rédaction d'un article scientifique. Merci à "post-master" Fan Yu pour nos nombreuses discussions philosophiques sur la dualité onde-mode. Merci à Li Zhe pour ses encouragements aux moments difficiles de ma thèse. Merci à Gao Feng pour son soutien informatique sur LATEX. Merci à Dimitrios Chronopoulos pour son aide sur le calcul du facteur de perte. Merci à Christophe Droz et Jean-Loup Christen, c'était un plaisir de travailler avec eux, ils m'ont aidé dans mes recherches, à améliorer mon français, ma guitare ainsi que mes talents de conductrice... J'oublie pas les copines et les copains: Diane Huang Xingrong, Sun Xiangkun, Zhang Lu, Chen Xu, Wang Yonghua, Liu Huanhuan, Yu Hang, Wang Liuqing, Qu Bo, Liu Xiaoxiang, Yi Kaijun, Sun Jinjing... Leurs présences à mes cotés m'a fait chaud au coeur.

Finalement, je veux simplement dire un grand merci à mes chers parents, et à mon copain Huang Gang. Merci de m'avoir donné la vie et d'en avoir enrichi le sens. Vous m'avez accompagné, et aviez continué à me soutenir dans mes pires moments. Vous avez fait de moi une meilleure personne. Je vous aime.

Merci à China Scholarship Council (CSC) pour le financement de la thèse.

# 致谢

成功的博士经历可能大致相同,失败的博士经历则各有各的不幸.但所有的博士都肯定有一个共同点,就是这段经历一定会伴随着非常强烈的情绪起伏以及感情波动.而我的五味杂陈的感情中,有一条最为强烈不容忽略的就是"感恩".着实的庆幸自己在博士期间碰见这么一群可爱的人啊.

首先要感谢答辩委员会的老师们,尤其是两位审稿人,感谢他们对此论文宝贵的修改意见.感谢我的导师Mohammed Ichchou, 感谢他为我创造了一个这么好的工作环境.感谢他对我博士工作的认可,以及当我对自己都不认可时给予我的信任以及鼓励.还要感谢我的副导师Abdel-Malek Zine,感谢他对我数学方面的指导以及热忱的关怀.最要感谢的导师就是你了,Jean-Pierre.我可能是前世拯救了地球,今世才得以有你做我的导师.你对工作严谨认真的态度,永不熄灭的好奇心,以及对科研巨大的纯粹的热情都深深触动着,影响着,教育着我.你对我博士三年始终如一的帮助让我感恩终生.一年级刚接触博士工作时,你对缺乏基础知识的我从来都不缺乏耐心;二年级工作起步时,你不断的好点子给我的科研不断添加动力;三年级做出一定工作后,你还不愿止步,帮助我实验验证让我把工作做到尽善尽美.答辩前半个月我看着我那满满的日程本慌得不行,你就开足马达,帮我备课,给我讲完理论之后实验示范;在我教课的时候做我的后援;帮我修改每页答辩ppt,帮我字斟句酌ppt的讲解词.感谢你三年多以来的亦师亦父亦友的陪伴.

感谢Olivier Bareille,他虽然名义上不是我的导师,但是我觉得他就跟导师一样,我从3A的时候就承蒙他师长的关怀.在我担任ATER期间得以见到他对教学工作的认真,效率以及井井有条.他给了我很大的帮助同时让我学到了很多.感谢Stéphane Lemahieu对我实验台的搭建以及实验顺利展开的帮助.感谢Olivier Dessombz对我的技术支持,感谢MSGMGC系主任Jean-Jacques Sinou对我热情的接待.感谢Isabelle Tixier对我的帮助,她对我节约环保意识的培养也有着巨大的功劳.感谢白澄老师对我的信任,让我负责汉语口语课的教学任务.我在两年的教学经历中受益匪浅.

感谢我们流固耦合两小组的师兄弟姐们工作上的帮助:周文晋博士做的加筋板的对比实验;黄天力博士把我带入波有限元的世界;张凯博士帮我改文章和指导我如何写科技论文;范雨硕士后同我数次上升到哲学层面的波模态二象性的讨论;李哲(音同)博士在我科研受挫时对我珍贵的劝导;高锋博士对我写论文期间Latex的技术支持;Dimitrios Chronopoulos博士对我算加筋板的声辐射工作的帮助.还有同Christophe Droz和Jean-Loup Christian的合作以及各种学术及非学术的讨论. 还有一起玩耍的小伙伴们:黄行蓉,孙祥坤,张陆,陈旭,王永华博士,刘焕焕博士,于航博士,王柳青博士,曲波,刘晓湘,易凯军,孙瑾静等.我们聚是一团火,彼此温暖;散为满天星,互相闪烁,惜缘,感恩.

我要对我的父母和我的男朋友黄刚说一句谢谢，你们赐予我生命并赋予其意义.你们陪伴我,理解我,支持我,让我成为更好的我.我爱你们.

最后，我要感谢国家留学基金委博士期间的全额资助。

# Acknowledgements

Perhaps all successful thesis are all alike and every unsuccessful thesis fails in its own way. But there is no thesis without strong emotions. Happiness can be joined by the sadness, maybe even anger, creates the symphony of the unforgettable Ph.D experience. As for me, I am particularly grateful for these 3 years.

First, I would like to thank all the members of the jury, especially the two reviewers, for their precious advice on the correction of this dissertation. I'd like to thank my thesis supervisor, Mohammed Ichchou. He provided an enjoyable working environment for me, he trusted me and encouraged me even when I have doubt on myself. I want to thank my co-supervisor, Abdel-Malek Zine, for his guidance in mathematics and for his kindness. I really don't know how to thank you, Jean-Pierre. I think I've probably saved the world in my previous life to have you as my tutor. Your outstanding professionalism, your permanent curiosity, your pure and selfless enthusiasm for research affect me, touch me. Your help is always with me during these three years: In the first year, you were so patient to me, while I lacked knowledge and experience. In the second year, your bright new ideas boosted my research. In the final year, you pushed me to go even further. 15 days before my Ph.D defense, I've panicked with my filled agenda, you passed the whole day with me: help me prepare my lessons, show me how to do the experiences, help me out when I failed to answer the questions of the students in the class. You corrected slide by slide of my defence power-point, checked phrase by phrase my speech for the presentation. I can not expect and ask more from you.

I would like to express my gratitude to Olivier Bareille, even he is not my official supervisor, but he helped a lot. He took care of me when I was in 3A, and I recently discovered his effectiveness and methodology when I worked with him as ATER. I learned so much from him... I'd like to thanks Stéphane Lemahieu for his help in installing my experiment platform, Olivier Dessombz for technical support, Jean-Jacques Sinou for his warm welcome in the department MSGMGC. My sincere thanks also goes to Isabelle Tixier for her various helps, she made me a more environmental friendly person. Thank Cheng Sun for her trust, she gave me the opportunity to teach Chinese to engineer students. It became my first experience in higher education.

My sincere thanks goes also to colleagues in fluid mechanics and solids mechanics: Zhou Wenjin for the excellent experimental results on the stiffened plate; Huang Tianli for introducing me to the world of WFEM; Zhang Kai for his advice in writing scientific article; "Post-master" Fan Yu for our numerous philosophical discussions on the wave-modes duality; Li Zhe for his encouragement in difficult time

in my thesis; Gao Feng for his IT support in LATEX; Dimitrios Chronopoulos for his help on the calculation of transmission loss; Christophe Droz and Jean-Loup Christian for their help on my research, my french, guitar and driving skills... Also we must not forget to thank my friends in Lyon: Diane Huang Xingrong, Sun Xiangkun, Zhang Lu, Chen Xu, Wang Yonghua, Liu Huanhuan, Yu Hang, Wang Liuqing, Qu Bo, Liu Xiaoxiang, Yi Kaijun, Sun Jinjing... Your company kept me warm when it was cold outside.

Finally, I want to give a huge thanks to my dear parents and my boyfriend Huang Gang. Thank you for giving me my life and making it meaningful. You stayed with me, continued to love me and support me in my worst days and nights. You made me a better me. I love you.

I gratefully acknowledge Chinese Scholarship Council (CSC). It provides the funding source to support my Ph.D work.

# Abstract

Structural dynamics can be described in terms of structural modes as well as elastic wave motions. The mode-based methods are widely applied in mechanical engineering and numerous model order reduction (MOR) techniques have been developed. When it comes to the study of periodic structures, wave description is mostly adopted where periodicity is fully exploited based on the Bloch theory. For complex periodic structures, several MOR techniques conducted on wave basis have been proposed in the literature.

In this work, a wave and modal coupled approach is developed to study the wave propagation in periodic structures. The approach begins with the modal description of a unit cell (mesoscopic scale) using Component Mode Synthesis (CMS). Subsequently, the wave-based method - Wave Finite Element Method (WFEM) is applied to the structure (macroscopic scale). The method is referred as "CWFEM" for Condensed Wave Finite Element Method. It combines the advantages of CMS and WFEM. CMS enables to analyse the local behaviour of the unit cell using a reduced modal basis. On the other hand, WFEM exploits fully the periodic propriety of the structure and extracts directly the propagation parameters. Thus the analysis of the wave propagation in the macroscopic scale waveguides can be carried out considering the mesoscopic scale behaviour. The effectiveness of CWFEM is illustrated via several one-dimensional (1D) periodic structures and two-dimensional (2D) periodic structures. The criterion of the optimal reduction to ensure the convergence is discussed. Typical wave propagation characteristics in periodic structures are identified, such as pass bands, stop bands, wave beaming effects, dispersion relation, band structure and slowness surfaces...Their proprieties can be applied as vibroacoustics barriers, wave filters.

CWFEM is subsequently applied to study wave propagation characteristics in perforated plates and stiffened plate. A homogenization method to find the equivalent model of perforated plate is proposed. The high frequency behaviours such as wave beaming effect are also predicted by CWFEM. Three plate models with different perforations are studied. Experimental validation is conducted on two plates. For the stiffened plate, the influence of internal modes on propagation is discussed. The modal density in the mid- and high- frequency range is estimated for a finite stiffened plate, where good correlation is obtained compared to the mode count from modal analysis.

**Keywords:** Periodic structures, Wave propagation, Wave finite element method, Component mode synthesis, Multi-scale analysis, Wave-mode duality

# Résumé

La dynamique d'une structure peut être vue aussi bien en termes de modes (ondes stationnaires) qu'en termes d'ondes élastiques libres. Les approches modales sont largement utilisées en mécanique et de nombreuses techniques de réduction de modèles (Model Order Reduction - MOR) ont été développées dans ce cadre. Quant à la dynamique des structures périodiques, les approches propagatives sont majoritairement utilisées, où la périodicité est exploitée en utilisant la théorie de Bloch. Pour les structures périodiques complexes, plusieurs techniques MOR sur la base d'onde ont été proposées dans la littérature.

Dans ce travail, une approche couplée propagative et modale a été développée pour étudier la propagation des ondes dans les structures périodiques. Cette approche commence par la description modale d'une cellule unitaire (échelle mésoscopique) en utilisant la synthèse modale (Component Mode Synthesis - CMS). Par la suite, la méthode propagative - Wave Finite Element Method (WFEM) est appliquée sur la structure (échelle macroscopique). Cette méthode est nommée "CWFEM" pour Condensed Wave Finite Element Method. Elle combine les avantages de la CMS et WFEM. La CMS permet d'analyser le comportement local d'en extraire une base réduite. La WFEM exploite la périodicité de la structure d'en extraire les paramètres de propagation. Ainsi, l'analyse de la propagation des ondes dans la structure à l'échelle macroscopique peut être réalisée en prenant en compte l'échelle mésoscopique. L'efficacité de la CWFEM est illustrée par de nombreuse applications aux structures périodiques monodimensionnelle (1D) et bidimensionnelle (2D). Le critère de réduction optimale assurant la convergence est discuté. Les caractéristiques de propagation dans les structures périodiques sont identifiées: bande passante, bande interdite, la directivité marquée (wave beaming effects), courbe de dispersion, band structure, surface des lenteurs... Ces propriétés peuvent répondre au besoin de conception des barrières vibroacoustiques, pièges à ondes.

La CWFEM est ensuite appliquée pour étudier la propagation des ondes dans des plaques perforées et plaques raidies. Une méthode d'homogénéisation pour déterminer le modèle equivalent de la plaque perforée est proposée. Les comportements à haute fréquence tels que la directivité marquée sont également prédits par CWFEM. Trois modèles de plaques avec perforations différentes sont étudiées dans ce travail. Une validation expérimentale est effectuée sur deux plaques. Pour la plaque raidie, l'influence des modes internes sur la propagation globale est discutée. La densité modale est estimée, en moyenne et haute frequences, pour une plaque raidie finie, où une bonne corrélation est obtenue en comparant les résultats à l'issue des analyses modales.

**Mots-clés** : Structure périodiques, Propagation des ondes, Wave finite element method, Component mode synthesis, Analyse multi-échelle, Dualité approche modale/propagative

# Contents

# List of abbreviations

- 1D: One Dimensional
- 2D: Two Dimensional
- CMS: Component Mode Synthesis
- CWFEM: Condensed Wave Finite Element Method
- DFT: Discrete Fourier Transform
- DMM: Diffusion Matrix Method
- DOF: Degree of freedom
- FFT: Fast Fourier transformation
- IBZ: Irreducible Brillouin Zone
- $k$-space: Wavenumber space
- MAC: Modal Assurance Criterion
- MOR: Model Order Reduction
- PCs: Phononic Crystals
- SAFE: Semi-Analytical Finite Element
- SEA: Statistical Energy Analysis
- TMM: Transfer Matrix Method
- WFEM: Wave Finite Element Method

# Introduction

A material or structural system which can be obtained by repeating a single unit cell is called periodic medium. Their periodicity can be in the constituent material phases, the internal geometry or the boundary conditions. Mechanical periodic medium can be divided into two categories: engineering periodic structures and phononic materials, the latter includes also Phononic Crystals (PCs) and acoustic meta-materials.

Periodic engineering structures, referred as periodic structures in this work, has been widely investigated for decades. Typical examples include multi-storey buildings, multi-span bridges, multi-blade turbines, chemical pipelines, stiffened plates and layered composite structures in aerospace and ship structures. In the design of these structures, the vibration levels caused by the time dependent forces, pressures or motions should be taken into consideration. The nature of the forcing function may be different depending on the applications. In the building, the excitation may come from an earthquake or periodic forces given by a rotting machinery. The multi-span bridges are exposed to the moving weight of vehicles. The aeroplane structures are subjected to random convected pressure fields from jet noise at low speed and turbulent boundary layers at high speed. Whatever the nature of the forcing function, elastic wave motion is generated within the structure. The vibration and shock response of these structures should be of great concern to minimize the probability of catastrophic damage or malfunction in service.

Over the past two decades, the study of elastic waves in phononic materials has proved to be of great interest. Phononic materials consist of a periodic array of acoustic scatterers embedded in a host medium. Initially, the photonic crystal was proposed to describe the propagation of optical waves in refraction index-modulated periodic structures analogous to the propagation of electrons in real crystals. Inspired by the photonic crystals, the concept of PCs was proposed with elastic waves propagating in periodic structures modulated with periodic elastic moduli and mass densities [Kushwaha *et al.*, 1993]. Band structures in PCs have been investigated a lot in physics, and then compared with other kinds of waves: while the electrons in a semiconductor can only occupy certain energy bands, a PC allows acoustic waves in pass bands to travel through; other frequencies are forbidden by stop bands. The wave filter proprieties promise applications such as vibroacoustic and mechanical wave filters, acoustic barriers, vibration isolators and so on. Compared with PCs, the key feature of the acoustic meta-materials

is the presence of local resonance, which may form stop bands at low frequency. The particular characteristics may well reduce the size of these meta-materials and enhance their integration into devices, overcoming the deficiencies of PCs.

## The duality between wave approach and modal approach

The response of vibrating periodic structures can be studied by the wave approach as well as the modal approach. In the wave approach, the vibration of the structures is viewed in terms of elastic wave motion, while in the modal approach, it is considered in terms of structural modes. The equivalence between the two types of approach is known as wave-mode duality.

Numerous wave-based methods have been developed during the studies or designs of homogeneous or periodic structures. In the Semi-Analytical Finite Element (SAFE) approach, the displacement field is formulated following a decomposition into plane waves (sinusoidal interpolation functions) in the direction of propagation, and using finite elements in the directions perpendicular to propagation one. The numerical method - Wave Finite Element Method (WFEM) has been proposed to overcome the limitations of analytical model in SAFE by combining the periodic structures theory introduced by Mead [1973] to the FEM. The method is based on periodic structures theory [Bloch, 1929], converting the study of the whole periodic structure into a single unit cell. Free harmonic wave motion can be deduced from the dynamic stiffness matrix of the unit cell. The obtained wave motion corresponds to the wave basis. All waves propagating (free or forced) in this structure can be decomposed into this wave basis. The wave basis is associated to the propagation constants $\mu = \exp(kL)$, with $k$ the wavenumber and $L$ the length of the unit cell in the propagation direction. The propagation constants can provide useful information about how the waves propagate through the macroscopic structures. However, the analysis on mesoscopic unit cell still needs to be carried out. This is particularly important in the mid-frequency range where both the local behaviour of the unit cell and the global behaviour of the structure play important roles. The influence of local dynamics on the global propagation needs to be revealed as well. In addition, the waveguides with complex cross-section, computation based on wave basis may be time-consuming. Several reduction formulations of WFEM have been proposed, most of them are very advantageous when studying waveguides with complex cross-section with a large number of coupling coordinates. But few reduction method is developed to deal with the periodic structures with numerous internal DOFs in the unit cell, which may also lead to excessive computational time.

On the other hand, Component Mode Synthesis (CMS) is an efficient mode-based method to study complex structures [Thorby, 2008]. CMS enables structures to be analysed as a set of components, which form the whole structure when joined together. It has many advantages, such as allowing analysis to proceed independently on each component, and making each anal-

ysis smaller. However, few mode-based method has been applied on periodic structures. Their main disadvantage is that they don't exploit the periodicity of the structures. The matrices of all the unit cells, although identical, still need to be assembled together to form the overall matrices. Moreover, the periodic structures may contain numerous unit cells, which may lead to a large computation time.

## The proposed wave/modal coupled method

In this work, the mode-based method - Craig-Bampton method (fixed boundary CMS method) [Thorby, 2008] is coupled with the wave-based method - WFEM to study the periodic structures. The proposed method combines advantage of CMS and WFEM. CMS is applied on the mesoscopic unit cell level. The numerous physical internal coordinates of the unit cell are represented by a reduced set of modal coordinates, while the physical coupling coordinates are conserved. The reduction is robust and easy to implement to WFEM formulation. The reduced model is valid in all the frequency range of interest, while the other wave-based reduction techniques depend on the band of frequency studied. In addition, the selection of the modal basis allows us to study the influence of local dynamics on the global behaviours. Once the dynamics of the unit cell are captured, the wave-based method - WFEM is employed to study the wave propagation in the whole structure. WFEM models only a unit cell and the global behaviours of the structure are deduced from the transfer matrix between the unit cells. Different scales related to multi-scale modelling of periodic structure in this thesis is defined as follows:

**Macroscopic scale:** The whole periodic structure which possesses periodicity in one direction (1D periodic structure) or in two directions (2D periodic structure). It can be infinite or finite with sufficient number of unit cells.

**Mesoscopic scale:** The unit cell of the periodic structure. By repeating this unit cell in one direction (1D periodic structure) or two directions (2D periodic structure), one can obtain the whole periodic structure.

The proposed method employs the modal description of vibration on the mesoscopic scale of unit cell, and the wave description is used on the macroscopic scale of periodic structure. The combination of the two approaches is ensured by the wave-mode duality. It allows, when passing from a unit cell to the whole structure, to alternate from the modal description to wave description. The wave-mode duality can also be interpreted by the fact that the displacements of the vibration are just projected on two different basis. The proposed wave and modal coupled approach is referred as CWFEM for "Condensed wave finite element method". More details about the advantages of CWFEM can be found in 1.5, where the involved wave-mode duality is discussed as well.

# Thesis contributions

The main contributions of the work in this thesis are:

1. Develop an wave and modal coupled approach (CWFEM) which
   - is able to predict wave propagation characteristics in 1D/2D periodic structures
   - can analyse the local behaviour of the mesoscopic scale of the unit cell and reveal its influence on the propagation of the whole structure.
   - is more efficient in computation compared to existing methods.
2. Illustrate the validity of the CWFEM on binary periodic beams and beam grid. Study the forced response as well as the dispersion relation in binary beam. Investigate the stop band phenomena in binary periodic beams and wave beaming effects in beam grid and perforated plates.
3. In the 2D beam grid example, the boundary conditions under which the cell modes are equivalent with the waves at bounding frequencies of stop band are found; the wave is proved to be stationary at these frequencies.
4. Apply CWFEM to predict wave propagation characteristics in perforated plates. Based on the obtained dispersion relation, propose homogenization methods for the perforated plates at low frequency.
5. Validate CWFEM by experimental investigation on perforated plates.
6. Predict wave propagation feature in the orthogonally rib-stiffened plate, investigate influence of the internal modes on wave propagation. Deduce the modal density in mid- and high- frequency range based on the slowness surfaces of the wave propagation.

Part of the work in this thesis are presented in relevant communications, some journal papers are under review.

- The peer-reviewed international journal publications: [Zhou *et al.*, 2015c], [Zhou *et al.*, 2015a], [Zhou *et al.*, 2015b], [Droz *et al.*, 2015].

- The international conference/workshop communications: [Zhou *et al.*, 2013b], [Zhou *et al.*, 2014a], [Zhou *et al.*, 2014b], [Droz *et al.*, 2014b]

- The national conference/workshop communications: [Zhou *et al.*, 2013a], [Zhou *et al.*, 2014c]

# Thesis outline

Chapter 1 presents the results of the conducted literature survey. The survey concerns the review of previous researches on periodic medium, of existing methods on the studying of periodic structures and the MOR techniques. The terminology of wave description and wave/mode duality involved in the proposed method are discussed at the end of this chapter.

Chapter 2 employs CWFEM on 1D periodic structures, to study the free and forced wave propagation. The criterion for the selection of reduced modal basis is given, the effectiveness of the proposed method is illustrated by several numerical examples.

Chapter 3 extends CWFEM to 2D periodic structures, a numerical example of a beam grid is given to validate the proposed method. The wave beaming effects phenomenon in this case is studied, the equivalence of cells modes and stationary waves at bounding frequencies of stop bands is discussed.

In chapter 4, the CWFEM is applied to study the wave propagation in perforated plates. Experiments are carried out to illustrate the accuracy of the CWFEM. Homogenized methods at low frequency are proposed based on dispersion relation computed by CWFEM. The validation of the homogenized model is carried out by comparing the natural modes of the two models using FEM.

Application of the proposed method on periodically stiffened plate is given in chapter 5. Attention is paid to study the mid- and high- frequency behaviour such as the modal density. The wave shapes are given at several points on the band structures to illustrate the wave propagation characteristics in the structure.

Finally, the conclusions and perspectives are drawn in chapter 6.

# Chapter 1

# Literature survey

## 1.1 Introduction

The study of periodic medium can traced back to 17th century with Newton's attempt to describe the propagation of sound in air, where a system of lumped masses joined by massless springs was considered. Afterwards, researchers in the mechanics community, have conducted a fair amount of work on key theoretical foundations, concepts and analysis techniques that are relevant to periodic systems in other nonmechanics disciplines.

The chapter begins with a review about the studies on periodic medium, which is then followed by a literature survey of existing methods to study periodic structures and model order reduction techniques. Throughout the survey, attention is paid on separating wave-based methods apart from mode-based methods. Last but not least, the proposed wave and modal coupled approach is briefly explained, while its combined advantages are examined in detail. The terminology in the wave description is given, the wave/mode duality involved in the proposed method is discussed as well.

## 1.2 Periodic medium

Mechanical periodic medium consists of engineering periodic structures and phononic materials, the latter includes also Phononic Crystals (PCs) and acoustic meta-materials.

(a) Train rail

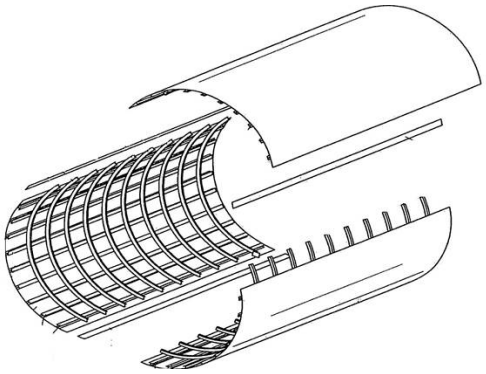

(b) Fuselage of an aircraft

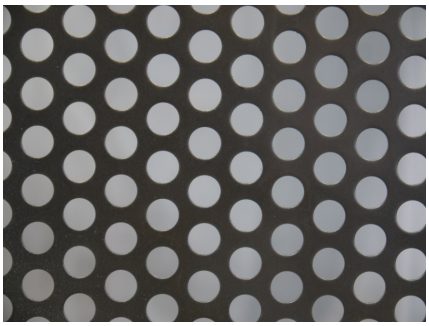

(c) Perforated plate

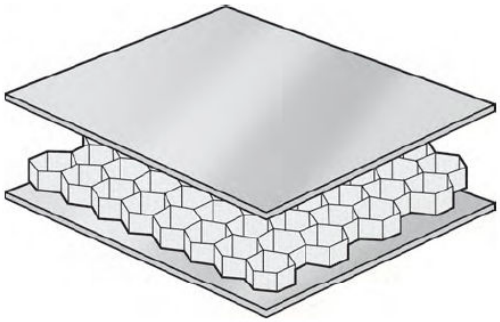

(d) Honeycomb sandwich

Figure 1.1: Examples of engineering periodic structures

### 1.2.1 Engineering periodic structures

Lots of structures employed in various engineering domains can be considered as periodic. For example: composite sandwich panels, stiffened plates, truss beams used in aircraft and marine structure; perforated plate used in the tube sheet heat exchangers in nuclear power plants; periodic foundation for buildings, multi-story building and multi-span bridges in civil engineering. Some examples are given in Fig. 1.1. Due to its wide applications in engineering domain, the study of wave propagation characteristic and their dynamic behaviours is of big concern in mechanics community.

Rayleigh [1887] made the first study of a continuous periodic structure, considering a stretched string with a periodic and continuous variation of density along its length and undergoing transverse harmonic vibration. Cremer & Leilich [1953] were among the first to investigate harmonic flexural wave motion along a one-dimensional periodic beam either with simple supports. It constitutes a "mono-coupled" periodic system, as its unit cell is coupled to each other through just one displacement co-ordinate. Its wave characteristics at any frequency are therefore described by a wave basis with only one wave shape and by a single pair of equal and opposite propagation constants. Heckl [1964] investigated a two-dimensional periodic structure consisting of a rectangular grillage of interconnected uniform beams which had both flexural

and torsional stiffness.

From the 1960s, Mead and his coworkers at the University of Southampton have widely contributed in this area. A review of their work has been given by Mead [1996] himself. In early age of their research, they developed the receptance method [Mead & Wilby, 1966], which was mainly used to calculate propagation constant in periodically simply supported beam and plate stiffened periodically in one direction. Lin & McDaniel [1969] were pioneering the proposition of Transfer Matrix Method (TMM) to the analysis of stiffened plate vibration and periodic structures. In the method, the generalized displacement and forces at the left-hand end and right-hand end of one periodic element are combined into state vectors. The state vectors at two ends are related through the "periodic transfer matrix". Transfer matrices are all symplectic, and therefore have a number of very useful properties which have been exploited in modern control theory and periodic structure analyses. The propagation constants can be found from the eigenvalues of the transfer matrix. However, much effort was required to overcome numerical ill-conditioning of the problem. Zhong & Williams [1995] proposed a formulation of eigen problem to conquer the ill-conditioning using the symplectic property of period transfer matrices. Orris & Petyt [1974] introduced finite element method in transfer matrix method to calculate the propagation constants in the one-dimensional periodic skin-rib structure. The method is named "Wave Finite Element method" (WFEM). Recently, WFEM has been extended to homogeneous structures in a lot of studies. Mace and his co-workers proposed the forced WFEM [Duhamel *et al.*, 2006] and discussed the numerical issues in free and forced WFEM [Waki *et al.*, 2009]. Ichchou and his co-workers at Ecole Centrale de Lyon extended WFEM to study the coupled structure with damage or with shunted piezoelectric patches. Through the Diffusion Matrix Model (DMM), WFEM was employed to quantify the reflections and transmissions of waves inside structures. Hence it constitutes an attractive tool for structural health monitoring [Ichchou *et al.*, 2009] or investigating the performance of shunted piezoelectric patches on the control of wave propagation [Huang *et al.*, 2013]. They also proposed several reduction techniques of WFEM to study complex systems such as multi-layered systems [Mencik & Ichchou, 2008] or composite structure [Droz *et al.*, 2014a].

Acoustic characteristic is another important aspect of the study in periodic structures. Interests mainly lie in the calculation of sound transmission and sound radiation of structures. Two methods are mainly developed, space-harmonics method and Fourier transform method. Space-harmonics method is firstly proposed by Mead & Pujara [1971], to study the response and sound radiation of the periodically supported beams. The method is then applied to study the sound transmission [Lee & Kim, 2002] and sound radiation [Mead, 1990] in periodically stiffened plates. Based on the same concept as space-harmonics method, the Fourier transform method is proposed and improved by Mace [1980a,b,c] Recently, the methods are applied to study the double panel with periodic stiffeners [Legault & Atalla, 2009, 2010].

### 1.2.2 Phononic materials

While research in engineering periodic structures has evolved among mechanicians, the notion of artifical periodicity has also been appealing to the electromagnetic and photonics communities [Hussein *et al.*, 2014]. A few years after the concept of photonic crystal was invented, the same concept emerged for acoustic or elastic waves, which was subsequently called Phononic Crystals (PC). A PC is a composite or nonuniform material consisting of one, two or more material phases arranged periodically in space. Sigalas & Economou [1992] considered in-plane elastic wave propagation in a 2D PC, albeit composed of fictitious materials. An analysis of in-plane wave propagation in a 2D PC consisting of carbon cylinders as inclusions and an epoxy resin as a matrix material was conducted around the same time by Vasseur *et al.* [1994]. A lot of works have been carried out in the design of PCs. Attentions have been paid to maximize stop bands or to localize stop bands in certain frequency regions [Halkjaer *et al.*, 2006; Li *et al.*, 2013; Yu *et al.*, 2006]. Two distinct features were identified as critical for the design of PCs: the unit-cell topology and the lattice symmetry [Hussein *et al.*, 2014]. It was shown that for elastic waves a "cermet topology," in which a stiff/dense material form the matrix and a compliant/light materials is used as inclusions, generally produces the largest stop bands [Economou & Sigalas, 1993]. As for lattice symmetry, it was revealed that PCs patterned over a hexagonal lattice typically display larger stop bands compared to those based on square lattices [Kushwaha & Halevi, 1994].

Same as PCs, acoustic meta-materials were also broadly considered as phononic materials. The added feature of acoustic meta-materials is the presence of local resonance. Introduced by Liu [2000], the conceptual realization of an acoustic meta-materials has opened up a new major thrust in phononic materials research. In his paper, a 3D array of lead spheres coated with a 2.5-mm layer of silicone rubber was stacked in a simple cubic arrangement with an epoxy matrix. The period length was 1.55 cm. Under excitation of acoustic waves, the medium exhibited a stop band at a wave-length well below period length. The localized resonant structure was shown to cause the material to behave as if its effective elastic constants were negative at certain frequency ranges. Subsequently, numerous other configurations for locally resonant phononic materials have been proposed. These include the use of three-phase composite material, binary materials, hollow cylinders or spheres, split rings or spheres and so on [Hussein *et al.*, 2014].

### 1.2.3 Wave propagation characteristics in periodic medium

The Bloch wave theory is largely employed in quantum mechanics and photonics crystal, and has been progressively applied in phononic physics and engineering periodic structures [Bloch, 1929]. In the description of wave propagation characteristics, wave vectors can be expressed in terms of the reciprocal lattice basis. Since the reciprocal lattice is also peri-

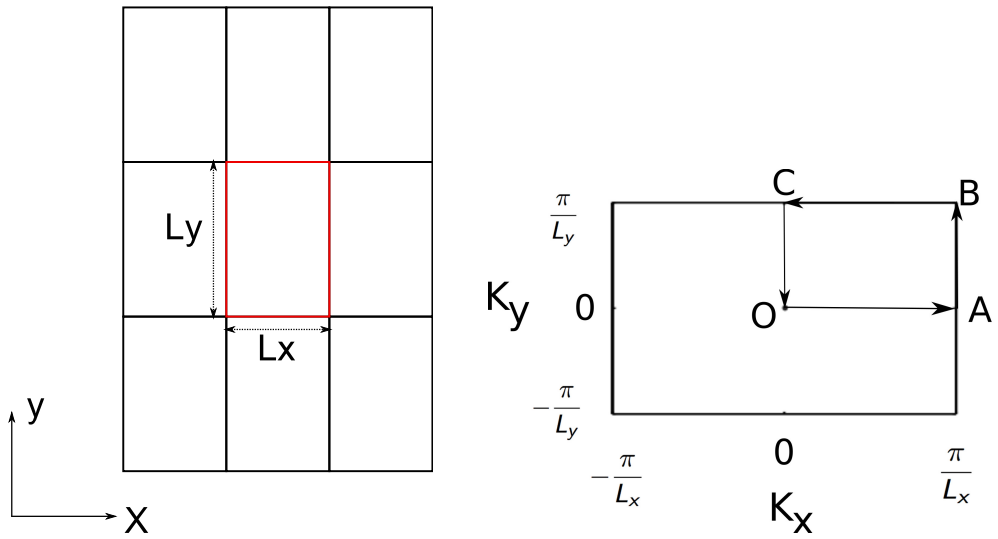


(a) 2D periodic structure with unit cell of size $L_x \times L_y$

(b) First Brillouin zone and IBZ (OABC)

Figure 1.2: 2D Periodic structures with rectangular unit cell and its Brillouin zone

odic, one can restrict the wave vectors to certain regions in the reciprocal lattice called first Brillouin zone [Brillouin, 1953]. Fig. 1.2(a) illustrates a 2D periodic structure with a unit cell of size $L_x \times L_y$. the first Brillouin zone corresponds to the wavenumber space within $[-\frac{\pi}{L_x}, \frac{\pi}{L_x}]$ $\times$ $[-\frac{\pi}{L_y}, \frac{\pi}{L_y}]$. Due to the symmetric properties in the reciprocal lattice, the wave vectors may be restricted to the Irreducible Brillouin Zone (IBZ) where the wavenumbers are positive (see zone OABC in Fig. 1.2(b)). In some descriptions of the wave propagation characteristics, only the contour of the IBZ (O-A-B-C-O) is considered, where the band extrema almost always occur [Kittel, 2004].

The wave number with respect to frequency along the contour of IBZ forms the band structure (called also band diagram). In physics, this diagram represents the backbone of electronic structure theory, credited for forming a basis for the classification of all crystals into metals, semiconductors and insulators [Hussein *et al.*, 2014]. In mechanics, a band structure is precisely a representation of dispersion relation describing the nature of free wave propagation in an elastic (or acoustic) medium. For 1D periodic structures, the term "dispersion relation" is employed, and for 2D periodic structures, "band structure" is used.

The stop bands of the propagation can be identified from the band structure/dispersion relation, as shown in Fig. 1.3. It is well known that wave filtering property exists in periodic structures and phononic materials. Elastic/acoustic waves cannot propagate freely within some frequency ranges, which are called stop bands (or band gaps). For 2D periodic structures, the stop band can be complete or partial, a partial stop band is a frequency range where waves can not propagate in certain directions, the phenomenon is known also as wave beaming effect [Ruzzene *et al.*, 2003]. There are two types of stop bands mechanisms in the periodic

medium: Bragg Scattering and Local Resonance. Bragg scattering stop band is due to the spatial periodicity of the impedance mismatch. It appears when wavelengths are on the same order as the period length. In contrary, local resonance stop band depend on the properties of the local resonator and not on the period length, the geometric arrangement within the unit cell or even the presence of periodicity. It can lie in the sub-wavelength regime whereby waves with wavelengths larger than that of the unit cell will be prohibited from propagation. Furthermore, it has been observed that unlike Bragg scattering which produces symmetric frequency-dependent transmission functions, local resonances exhibit Fano-like transmission characteristics [Goffaux *et al.*, 2002]. The distinction between the two mechanisms has also been addressed from the point of view of differences in wave shapes at stop band edges [Liu *et al.*, 2002] and the nature of the spatial attenuation profile downstream to the periodic media [Achaoui *et al.*, 2011].

## 1.3 Existing methods to study periodic structures

Lots of methods have been developed during the studies of the engineering periodic structures, or in the design of phononic materials. These methods include plane-wave expansion method, finite difference time domain method, time-domain spectral element method, multiple scattering method, TMM, WFEM. An excellent review and comparison between these methods are given in article of Hussein *et al.* [2014].

Some of these methods are mainly used in phononic materials to handle multiple media states, such as multiple scattering method [Kafesaki & Economou, 1999] which assures good convergence when other methods fail. Here the methods mostly applied on engineering periodic structures are presented, since the attentions of this works lie on the studies of engineering periodic structures, called periodic structures thereafter.

### 1.3.1 Plane-wave expansion

The general approach used in the plane-wave expansion method for continuous systems is to expand the solution field and the material properties in a Fourier series, and then invoke orthogonality of the basis functions to solve individually each of the introduced solution coefficients [Hussein *et al.*, 2014]. The basic idea is illustrated on a one-dimensional, continuous system, which is governed by the periodic wave equation:

$$\rho \frac{\partial^2 u}{\partial t^2} = \frac{\partial}{\partial x}(\rho c^2 \frac{\partial u}{\partial x}) \tag{1.1}$$

where $u(x,t)$ denotes the displacement field, $\rho(x)$ the density, and $c(x)$ the speed of sound through the media. The material properties $\rho(x)$ and $c(x)$ are assumed to vary periodically with

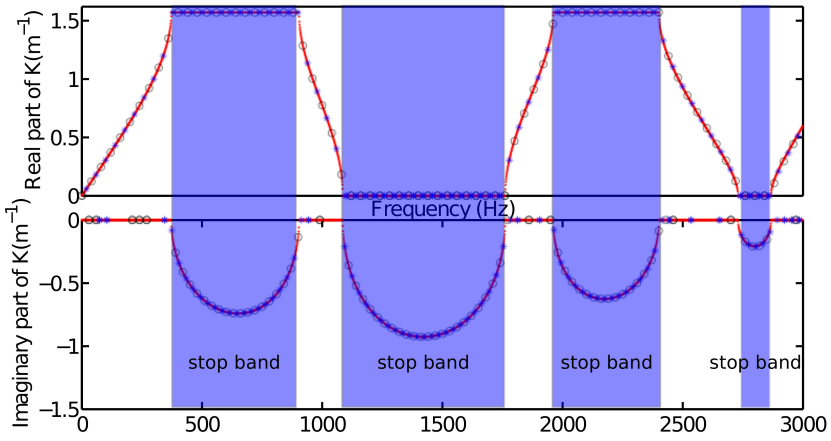


(a) Dispersion relation of a 1D periodic structure

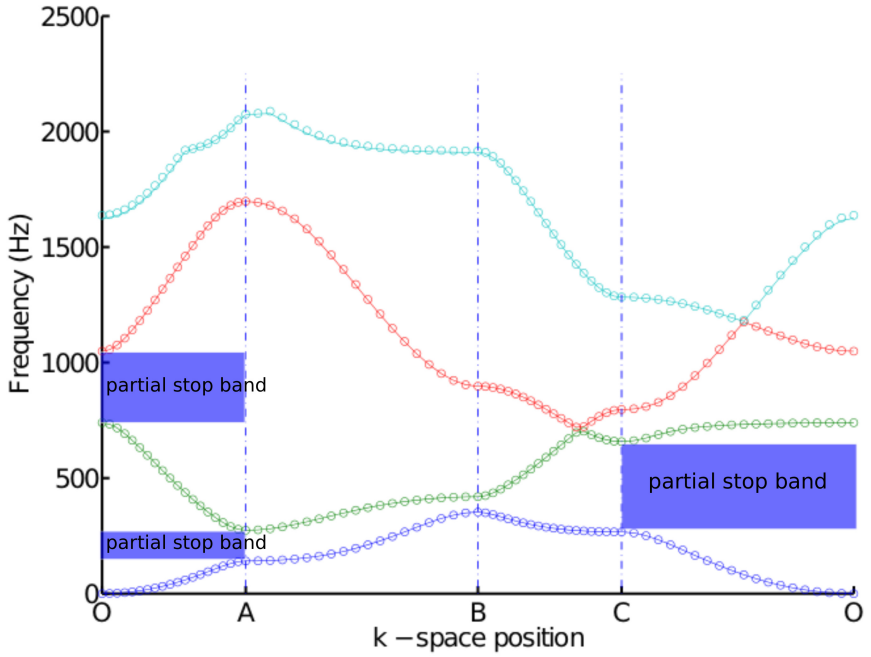


(b) Band structure of a 2D periodic structure

Figure 1.3: An example of band structure/dispersion relation and stop bands (Bragg scattering)

period length $L$. A reciprocal lattice vector can be written as $\mathbf{G}_m = \frac{m}{L}\hat{\mathbf{x}}$, where $\hat{\mathbf{x}}$ denotes a unit vector and $m$ denotes an integer. The method introduces following expansions:

$$u(x,t) = e^{i(\mathbf{k}\cdot\mathbf{r}-\omega\mathbf{t})}\sum_{\mathbf{G}_l} u_k(\mathbf{G}_l)e^{i\mathbf{G}_l\cdot\mathbf{r}} \tag{1.2a}$$

$$\rho(x) = \sum_{\mathbf{G}_m} \rho(\mathbf{G}_m)e^{i\mathbf{G}_m\cdot\mathbf{r}} \tag{1.2b}$$

$$\rho(x)c^2(x) = \sum_{\mathbf{G}_m} \tau(\mathbf{G}_m)e^{i\mathbf{G}_m\cdot\mathbf{r}} \tag{1.2c}$$

where $\mathbf{r} = x\hat{\mathbf{x}}$ denotes position, $\mathbf{k} = k\hat{\mathbf{x}}$ denotes the wavevector and $\sum_{G_m}, \sum_{G_l}$ denote sums over all reciprocal lattice vectors (over all $m, l$). The transformed density and stiffness are denoted by $\rho(\mathbf{G}_m)$ and $\tau(\mathbf{G}_m)$, respectively. The transformed displacement for wavenumber $k$ is $u_k(\mathbf{G}_l)$. Substituting the expansions into Eq. (1.1) and forming the complex inner product with $e^{i\mathbf{G}_n\cdot\mathbf{r}}$ leads to

$$\sum_{G_l}[-\omega^2\rho(\mathbf{G}_n-\mathbf{G}_l) + (k+\mathbf{G}_l)\cdot(k+\mathbf{G}_n)\tau(\mathbf{G}_n-\mathbf{G}_l)]u_k(\mathbf{G}_l) = 0 \tag{1.3}$$

For each $\mathbf{G}_n$, the nonzero terms in the inner product satisfies $\mathbf{G}_l + \mathbf{G}_m - \mathbf{G}_n = 0$. By truncating the expansion for $\mathbf{G}_l$, and evaluating Eq. (1.3) for a truncated set of $\mathbf{G}_n$, the eigenvalue problems leads to eigenfrequencies $\omega(k)$ and eigen vector $[u_k(\mathbf{G}_{-N})u_k(\mathbf{G}_{-N+1})...u_k(\mathbf{G}_N)]^T$, while $(2N+1)$ represents the number of retained terms. By solving the problems for all the wavenumbers $k$ in IRZ, the eigenfrequencies are obtained and they can be used to represent the band structures. As in any approximation technique, a convergence criterion should be used to determine an appropriate value for $N$.

### 1.3.2 Transfer matrix method

TMM is employed to provide reference results for flexural waves in periodic binary beam in 2.3.2. The binary beam consists of an infinite repetition of alternating sections A with length $l_1$ and section B with length $l_2$. The unit cell of the beam consists of 3 parts with first part formed by section B of length $a_1 = l_2/2$, second part formed by section A of length $a_2 = l_1$, third part formed by section B of length $a_3 = l_2/2$. As shown in Fig. 1.4.

Euler-Bernoulli model is adopted here, then for each part of the beam, the equation of equilibrium is given as follows :

$$E_n I_n \frac{d^4 W_{(n)}(x)}{dX^4} = w^2\rho_n S_n W_n(x), \quad x \in [0, a_n], n = 1,2,3 \tag{1.4}$$

where $E$ is the Young's modulus of the beam, $S$ the cross-section area, $\rho$ the beam density, $I$ the

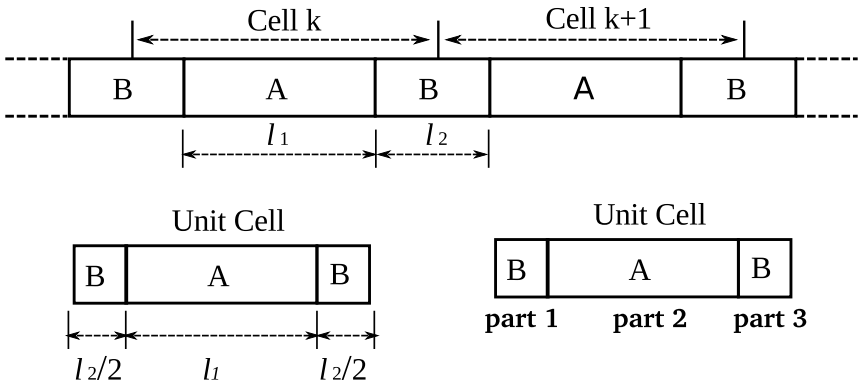


Figure 1.4: Periodic binary beam and its symmetric unit cell

second area moment of inertia about the neutral axis, and $\omega$ the circular frequency. $W$ represents the transverse deflection, and $x$ denotes the local coordinates. The subscript $(n)$ stands for the part $n$. The solution of the equation can be written in the following form [Thorby, 2008]:

$$W_n(x) = A_n cos(b_n x) + B_n sin(b_n x) + C_n cosh(b_n x) + D_n sinh(b_n x) \tag{1.5}$$

with $b_n^4 = w^2 \rho S_n / E_n I_n$. Then for each element, the state vector consisting of the deflection, slope, moment and shear force can be obtained using the following formulation:

$$\begin{bmatrix} W_n(x) \\ W_n'(x) \\ -EIW_n''(x) \\ EIW_n'''(x) \end{bmatrix} = \mathbf{T}_n(x) \begin{bmatrix} A_n \\ B_n \\ C_n \\ D_n \end{bmatrix} \tag{1.6}$$

with

$$\mathbf{T}_n(x) = \begin{pmatrix} \cos(b_n x) & \sin(b_n x) & \cosh(b_n x) & \sinh(b_n x) \\ -b_n \sin(b_n x) & b_n \cos(b_n x) & b_n \sinh(b_n x) & b_n \cosh(b_n x) \\ E_n I_n b^2 \cos(b_n x) & E_n I_n b_n^2 \sin(b_n x) & -E_n I_n b_n^2 \cosh(b_n x) & -E_n I_n b_n^2 \sinh(b_n x) \\ E_n I_n b_n^3 \sin(b_n x) & -E_n I_n b_n^3 \cos(b_n x) & E_n I_n b_n^3 \sinh(b_n x) & E_n I_n b_n^3 \cosh(b_n x) \end{pmatrix} \tag{1.7}$$

considering element $n$ of the cell,

$$\begin{bmatrix} W_n(a_n) \\ W_n'(a_n) \\ -E_n I_n W_n''(a_n) \\ E_n I_n W_n'''(ln) \end{bmatrix} = \mathbf{T}_n(a_n)(\mathbf{T}_n(0))^{-1} \begin{bmatrix} W_n(0) \\ W_n'(0) \\ -E_n I_n W_n''(0) \\ E_n I_n W_n'''(0) \end{bmatrix} \tag{1.8}$$

$[\mathbf{R}_n] = \mathbf{T}_n(a_n)(\mathbf{T}_n(0))^{-1}$ is the transfer matrix between the state vectors of the two extremities of element $n$. At the junction, the continuity of deflection, slope, moment and shear force has to be preserved, for element $m$ and element $(m+1)$, where $m \in \{1, 2\}$, leading to the following

relations:

$$W_m(a_m) = W_{m+1}(0), \tag{1.9}$$

$$W_m^{'}(a_m) = W_{m+1}^{'}(0) \tag{1.10}$$

$$-E_m I_m W_m^{''}(a_m) = -E_{m+1} I_{m+1} W_{m+1}^{''}(0)$$

$$E_m I_m W_m^{'''}(a_m) = E_{m+1} I_{m+1} W_{m+1}^{'''}(0) \tag{1.11}$$

The relationship between the left and right section state vectors can be expressed in the following manner:

$$\begin{bmatrix} W_3(a_3) \\ W_3'(a_3) \\ -E_3 I_3 W_3^{''}(a_3) \\ E_3 I_3 W_3^{'''}(l3) \end{bmatrix} = \mathbf{R} \begin{bmatrix} W_1(0) \\ W_1'(0) \\ -E_1 I_1 W_1^{''}(0) \\ E_1 I_1 W_1^{'''}(0) \end{bmatrix} \tag{1.12}$$

with $\mathbf{R} = [\mathbf{R}_3][\mathbf{R}_2][\mathbf{R}_1]$ the transfer matrix between the state vectors at the left boundary and the right boundary of the unit cell. When a free wave travels along the periodic system with the propagation constant $\mu$, the state vectors of the two boundaries are related by $\lambda = \exp(\mu)$ [Floquet, 1883]. Hence $\lambda$ is the eigenvalue of transfer matrix $\mathbf{R}$. The dispersion characteristic of the structure can be deduced from solving the eigen problem of the transfer matrix at the interested frequency range.

### 1.3.3 Wave finite element method

Initially developed for periodic structures, WFEM was then widely used to study free and forced vibration in homogeneous structures. The applications go from thin-walled structures [Houillon *et al.*, 2005], fluid-filled pipes [Mencik & Ichchou, 2007] to curved members [Zhou & Ichchou, 2010]. The method is based on periodic structures theory [Bloch, 1929; Floquet, 1883], converting the study of the whole periodic structure into a single unit cell or a small segment of the structure. Conventional FE software packages can be used for modelling. The dynamic stiffness and mass matrix of the unit cell is built explicitly. This means that structures with complex geometries or material distributions can be analysed with relative ease.

For free wave propagation, no external forces act on the structures apart from those on its boundaries from ajacent unit cells. So the equation of motion of the unit cell, assuming time-harmonic behaviour and neglecting damping, becomes:

$$[\tilde{\mathbf{K}} - \omega^2 \tilde{\mathbf{M}}] \begin{pmatrix} \mathbf{q}_{\mathtt{bd}} \\ \mathbf{q}_{\mathtt{I}} \end{pmatrix} = \begin{pmatrix} \mathbf{f}_{\mathtt{bd}} \\ \mathbf{0} \end{pmatrix} \tag{1.13}$$

The displacement and the force of the boundary nodes are denoted $\mathbf{q}_{\mathtt{bd}}$ and $\mathbf{f}_{\mathtt{bd}}$, while $\mathbf{q}_{\mathtt{I}}$ represents the internal nodes. Eq. (1.13) can take different forms which depend on the type of

solution being sought. There are mainly two forms: first one is direct form, which computes the wavenumber for an assigned value of frequency; second one is inverse form, which derives the dispersion properties for an assigned value of the wavenumber.

In the direct form, the equation of motion can be rewritten with the dynamic stiffness matrix since the frequency is known:

$$\begin{bmatrix} \tilde{\mathbf{D}}_{\mathtt{bdbd}} & \tilde{\mathbf{D}}_{\mathtt{bdI}} \\ \tilde{\mathbf{D}}_{\mathtt{Ibd}} & \tilde{\mathbf{D}}_{\mathtt{II}} \end{bmatrix} \begin{pmatrix} \mathbf{q}_{\mathtt{bd}} \\ \mathbf{q}_{\mathtt{I}} \end{pmatrix} = \begin{pmatrix} \mathbf{f}_{\mathtt{bd}} \\ \mathbf{0} \end{pmatrix} \tag{1.14}$$

After dynamic condensation, it becomes

$$\mathbf{D}_{\mathtt{bd}}\mathbf{q}_{\mathtt{bd}} = \mathbf{f}_{\mathtt{bd}} \tag{1.15}$$

with

$$\mathbf{D}_{\mathtt{bd}} = \tilde{\mathbf{D}}_{\mathtt{bdbd}} - \tilde{\mathbf{D}}_{\mathtt{bdI}}\tilde{\mathbf{D}}_{\mathtt{II}}^{-1}\tilde{\mathbf{D}}_{\mathtt{Ibd}} \tag{1.16}$$

For complex periodic structure, there maybe numerous internal nodes in the unit cell, which leads the inversion of $\tilde{\mathbf{D}}_{\mathtt{II}}$ time-consuming. So in the presented work, a reduction technique is coupled with WFEM to increase computation efficiency and to avoid the eventual ill-conditioning problem due to the inversion of $\tilde{\mathbf{D}}_{\mathtt{II}}$.

#### 1.3.3.1 One-dimensional wave finite element method

The unit cell of a periodic structure can be various, such as the two choices of cell in Fig. 1.5. It is advantageous to use the element with the minimum number of coupling coordinates to decrease the computational size [Mead, 1975b]. So it is more convenient to choose Fig. 1.5(b1) as the unit cell which contains less boundary DOFs. The length of the unit cell is denoted by $L$.

**Direct form of WFEM1D** Eq. (1.15) can be reformed into the following form:

$$\mathbf{u}_{\mathtt{R}} = \mathbf{S}\mathbf{u}_{\mathtt{L}}, \tag{1.17}$$

Where $\mathbf{u}_{\mathtt{L}} = ((\mathbf{q}_{\mathtt{L}})^{\mathtt{T}}(-\mathbf{F}_{\mathtt{L}})^{\mathtt{T}})^{\mathtt{T}}$ and $\mathbf{u}_{\mathtt{R}} = ((\mathbf{q}_{\mathtt{R}})^{\mathtt{T}}(\mathbf{F}_{\mathtt{R}})^{\mathtt{T}})^{\mathtt{T}}$ represent the left and right state vectors for the unit cell $k$. $\mathbf{S}$ is a symplectic matrix [Zhong & Williams, 1995] with following expression:

$$\mathbf{S} = \begin{bmatrix} -\mathbf{D}_{\mathtt{LR}}^{-1}\mathbf{D}_{\mathtt{LL}} & -\mathbf{D}_{\mathtt{LR}}^{-1} \\ -\mathbf{D}_{\mathtt{RL}} + \mathbf{D}_{\mathtt{RR}}\mathbf{D}_{\mathtt{LR}}^{-1}\mathbf{D}_{\mathtt{LL}} & -\mathbf{D}_{\mathtt{RR}}\mathbf{D}_{\mathtt{LR}}^{-1} \end{bmatrix} \tag{1.18}$$

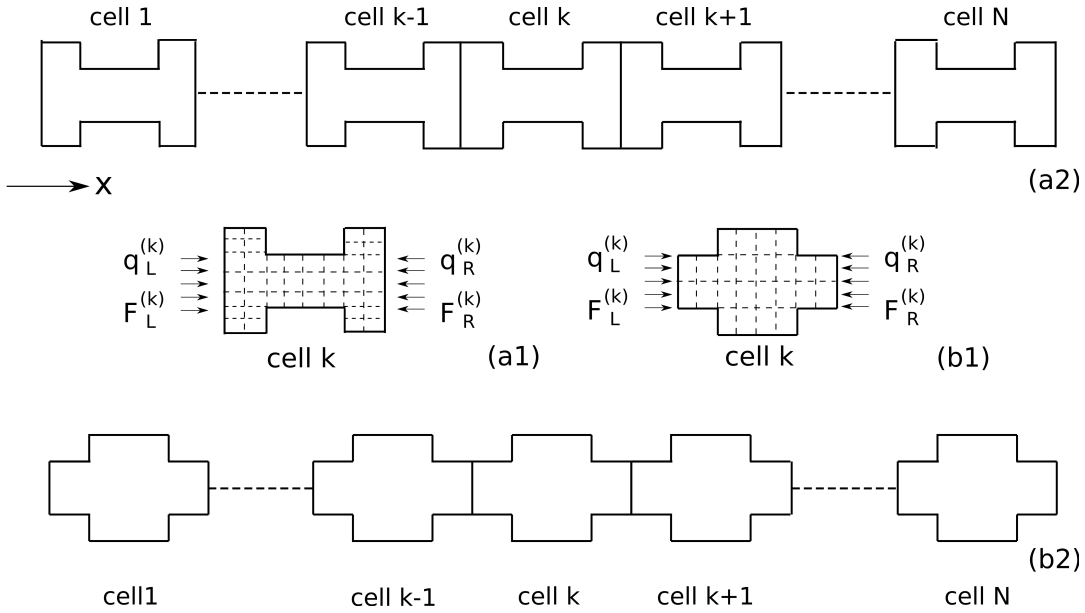


Figure 1.5: (a1) 1st choice of unit cell (a2) Periodic structure considering a1 as unit cell. (b1) 2nd choice of unit cell (b2) Same periodic structure as a2 considering b1 as unit cell

Free wave propagation characteristic are represented by wavenumbers and wave basis, which are associated to the eigen values and eigen vectors of the following eigen-problem

$$\mathbf{S}\mathbf{\Phi}_i = \lambda_i \mathbf{\Phi}_i \quad , \quad |\mathbf{S} - \lambda_i \mathbf{I_{2}}_n| = \mathbf{0}. \tag{1.19}$$

The eigen values are related to wavenumbers by $\lambda = \exp(-jkL)$. It is valid in all the formulations of WFEM. For complex cross-sections, $\mathbf{S}$ may be poor conditioned [Mace *et al.*, 2005]. An alternative formulation of eigen problem can be found in 2.2.2. Other propositions to avoid numerical issue can be found in reference [Waki *et al.*, 2009]. The direct form of WFEM1D is the most applied among the forms of WFEM. It can determine not only the propagating wave shapes, but also the decaying wave shapes. Thus it can be used to study the damped structure and the forced response of the structure [Duhamel *et al.*, 2006]. A model reduction technique is combined with direct form of WFEM1D in chapter 2, where formulation related to forced response is given as well.

**Inverse form of WFEM1D** Suppose a real value of wavenumber is assigned as first. The value of $\lambda$ can then be derived since $\lambda = \exp(-jkL)$. According to periodic structures theory, for free wave propagation, we have:

$$\mathbf{q}_{\mathrm{R}} = \lambda \mathbf{q}_{\mathrm{L}}, \mathbf{f}_{\mathrm{R}} = -\lambda \mathbf{f}_{\mathrm{L}} \tag{1.20}$$

the relations can be written using matrix $\mathbf{\Lambda_L}, \mathbf{\Lambda_R}$ as follows:

$$\begin{pmatrix} \mathbf{q}_{\mathrm{L}} \\ \mathbf{q}_{\mathrm{R}} \\ \mathbf{q}_{\mathrm{I}} \end{pmatrix} = \begin{bmatrix} \mathbf{I} & \mathbf{0} \\ \lambda\mathbf{I} & \mathbf{0} \\ \mathbf{0} & \mathbf{I} \end{bmatrix} \begin{pmatrix} \mathbf{q}_{\mathrm{L}} \\ \mathbf{q}_{\mathrm{I}} \end{pmatrix} = \mathbf{\Lambda_R} \begin{pmatrix} \mathbf{q}_{\mathrm{L}} \\ \mathbf{q}_{\mathrm{I}} \end{pmatrix} \tag{1.21}$$

and for nodal forces:

$$\begin{bmatrix} \mathbf{I} & -\lambda\mathbf{I} & \mathbf{0} \\ \mathbf{0} & \mathbf{0} & \mathbf{I} \end{bmatrix} \begin{pmatrix} \mathbf{f}_{\mathrm{L}} \\ \mathbf{f}_{\mathrm{R}} \\ \mathbf{0} \end{pmatrix} = \mathbf{\Lambda_L} \begin{pmatrix} \mathbf{f}_{\mathrm{L}} \\ \mathbf{f}_{\mathrm{R}} \\ \mathbf{0} \end{pmatrix} = \mathbf{0} \tag{1.22}$$

So Eq. (1.13) can be rewritten

$$[\mathbf{\Lambda_L}\tilde{\mathbf{K}}\mathbf{\Lambda_R} - \omega^2\mathbf{\Lambda_L}\tilde{\mathbf{M}}\mathbf{\Lambda_R}] \begin{pmatrix} \mathbf{q}_{\mathrm{L}} \\ \mathbf{q}_{\mathrm{I}} \end{pmatrix} = \mathbf{0} \tag{1.23}$$

Since $k$ is supposed to be real, the matrix $\mathbf{\Lambda_L}$ is the conjugate transpose of matrix $\mathbf{\Lambda_R}$. The equation becomes a standard and linear eigen problem of $\omega^2$. The size of problem is the sum of the size of $\mathbf{q}_{\mathrm{L}}$ and $\mathbf{q}_{\mathrm{I}}$. No numerical issue will appear in this case, however the attenuation of the waves can not be predicted.

#### 1.3.3.2 Two-dimensional wave finite element method

A scheme for 2D periodic structure and its unit cell is given in Fig. 1.6. The nodes in the unit cell are divided into: four corners, left, bottom, right, top and internal DOFs. They are classified as $[\mathbf{q}_{\mathrm{bd}} \quad \mathbf{q}_{\mathrm{I}}] = [\mathbf{q}_1 \quad \mathbf{q}_2 \quad \mathbf{q}_3 \quad \mathbf{q}_4 \quad \mathbf{q}_{\mathrm{L}} \quad \mathbf{q}_{\mathrm{B}} \quad \mathbf{q}_{\mathrm{R}} \quad \mathbf{q}_{\mathrm{T}} \quad \mathbf{q}_{\mathrm{I}}]$. $\mathbf{q}_{\mathrm{bd}}$ includes all the DOFs at the boundary of the unit cell, $\mathbf{q}_1$, $\mathbf{q}_2$, $\mathbf{q}_3$ and $\mathbf{q}_4$ are of $s$ DOFs, $\mathbf{q}_{\mathrm{L}}$ and $\mathbf{q}_{\mathrm{R}}$ are of $ms$ DOFs, $\mathbf{q}_{\mathrm{B}}$ and $\mathbf{q}_{\mathrm{T}}$ are of $ns$ DOFs, $\mathbf{q}_{\mathrm{I}}$ are of $i$ DOFs. The nodal forces are classified in the same way. According to the periodic structures theory, the nodal DOFs are related through:

$$\mathbf{q}_2 = \lambda_x\mathbf{q}_1, \mathbf{q}_3 = \lambda_y\mathbf{q}_1, \mathbf{q}_4 = \lambda_x\lambda_y\mathbf{q}_1, \mathbf{q}_{\mathrm{R}} = \lambda_x\mathbf{q}_{\mathrm{L}}, \mathbf{q}_{\mathrm{T}} = \lambda_y\mathbf{q}_{\mathrm{B}} \tag{1.24}$$

In addition to the periodic structures theory, for free wave propagation, the sum of nodal forces of all the elements connected to nodes 1, L, B is zero, which leads to:

$$\mathbf{f}_1 + \lambda_x^{-1}\mathbf{f}_2 + \lambda_{\mathbf{y}}^{-1}\mathbf{f}_3 + \lambda_{\mathbf{x}}^{-1}\lambda_{\mathbf{y}}^{-1}\mathbf{f}_4 = \mathbf{0} \tag{1.25a}$$

$$\mathbf{f}_{\mathrm{L}} + \lambda_x^{-1}\mathbf{f}_{\mathrm{R}} = \mathbf{0} \tag{1.25b}$$

$$\mathbf{f}_{\mathrm{B}} + \lambda_y^{-1}\mathbf{f}_{\mathrm{T}} = \mathbf{0} \tag{1.25c}$$

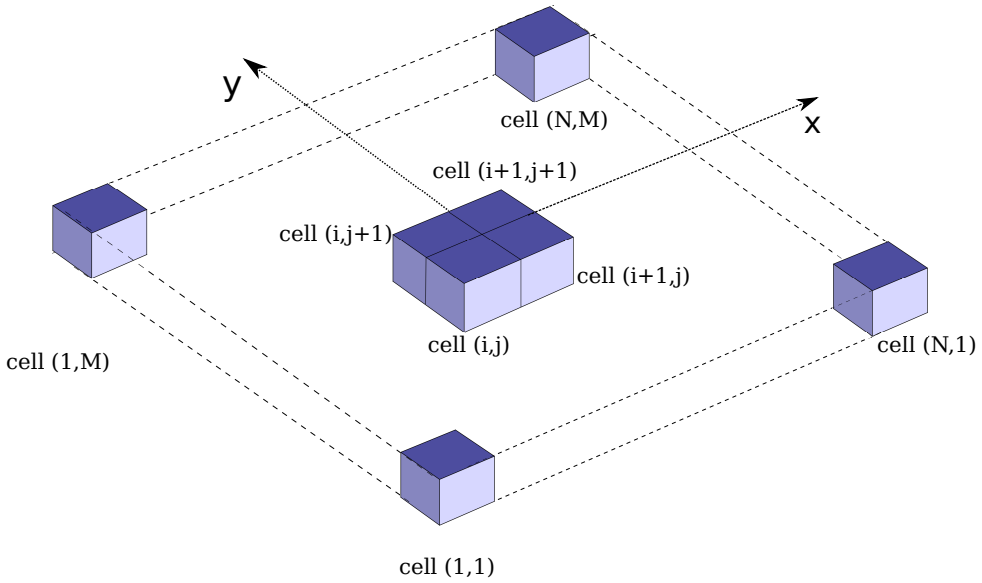


(a) 2D periodic structure

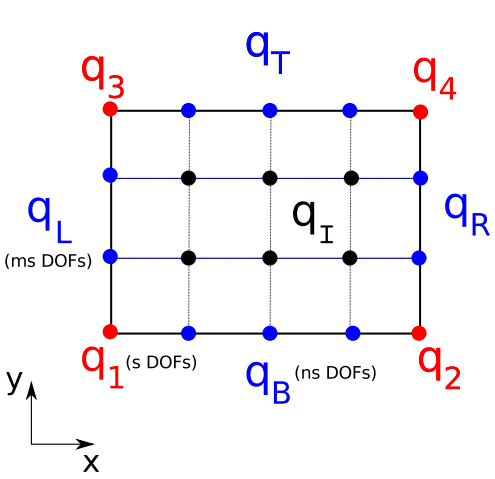


(b) View 2D

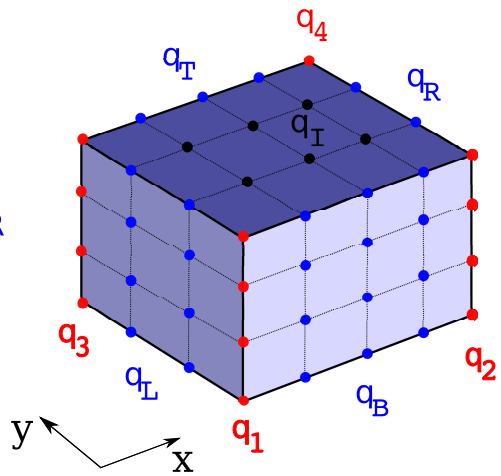


(c) View 3D

Figure 1.6: Nodes definition of unit cell in WFEM2D

**Direct form of WFEM2D** The internal nodes of the unit cell are condensed. For the boundary nodes:

$$\mathbf{q}_{\mathtt{bd}} = \tilde{\mathbf{\Lambda}}_{\mathbf{R}} \begin{pmatrix} \mathbf{q}_{\mathtt{1}} \\ \mathbf{q}_{\mathtt{L}} \\ \mathbf{q}_{\mathtt{B}} \end{pmatrix} \tag{1.26}$$

with

$$\tilde{\mathbf{\Lambda}}_{\mathbf{R}} = \begin{bmatrix} \mathbf{I}_{\mathtt{s}} & \mathbf{0} & \mathbf{0} \\ \lambda_x \mathbf{I}_{\mathtt{s}} & \mathbf{0} & \mathbf{0} \\ \lambda_y \mathbf{I}_{\mathtt{s}} & \mathbf{0} & \mathbf{0} \\ \lambda_x \lambda_y \mathbf{I}_{\mathtt{s}} & \mathbf{0} & \mathbf{0} \\ \mathbf{0} & \mathbf{I}_{\mathtt{sm}} & \mathbf{0} \\ \mathbf{0} & \mathbf{0} & \mathbf{I}_{\mathtt{sn}} \\ \mathbf{0} & \lambda_x \mathbf{I}_{\mathtt{sm}} & \mathbf{0} \\ \mathbf{0} & \mathbf{0} & \lambda_y \mathbf{I}_{\mathtt{sn}} \end{bmatrix} \tag{1.27}$$

$\mathbf{I}_{\mathtt{s}}, \mathbf{I}_{\mathtt{sn}}, \mathbf{I}_{\mathtt{sm}}$ represent the identity matrix of size $s$, $sn$, $sm$ respectively. The vector $((\mathbf{q}_{\mathtt{1}})^{\mathtt{T}}(\mathbf{q}_{\mathtt{L}})^{\mathtt{T}}(\mathbf{q}_{\mathtt{B}})^{\mathtt{T}})^{\mathtt{T}}$ is of $(s + ns + ms)$ lines, and $\mathbf{\Lambda}_R$ is of $(4s + 2ns + 2ms)$ lines and $(s + ns + ms)$ columns. Similar for the nodal forces

$$\tilde{\mathbf{\Lambda}}_{\mathbf{L}} \mathbf{f}_{\mathbf{bd}} = \mathbf{0} \tag{1.28}$$

while

$$\tilde{\mathbf{\Lambda}}_{\mathbf{L}} = \begin{bmatrix} \mathbf{I}_{\mathtt{s}} & \lambda_x^{-1}\mathbf{I}_{\mathtt{s}} & \lambda_y^{-1}\mathbf{I}_{\mathtt{s}} & \lambda_x^{-1}\lambda_y^{-1}\mathbf{I}_{\mathtt{s}} & \mathbf{0} & \mathbf{0} & \mathbf{0} & \mathbf{0} \\ \mathbf{0} & \mathbf{0} & \mathbf{0} & \mathbf{0} & \mathbf{I}_{\mathtt{sm}} & \mathbf{0} & \lambda_x^{-1}\mathbf{I}_{\mathtt{sm}} & \mathbf{0} \\ \mathbf{0} & \mathbf{0} & \mathbf{0} & \mathbf{0} & \mathbf{0} & \mathbf{I}_{\mathtt{sn}} & \mathbf{0} & \lambda_y^{-1}\mathbf{I}_{\mathtt{sn}} \end{bmatrix} \tag{1.29}$$

so the equation of motion Eq. (1.15) becomes:

$$\tilde{\mathbf{\Lambda}}_{\mathbf{L}}(\lambda_{\mathbf{x}}, \lambda_{\mathbf{y}}) * \mathbf{D} * \tilde{\mathbf{\Lambda}}_{\mathbf{R}}(\lambda_{\mathbf{x}}, \lambda_{\mathbf{y}}) \begin{pmatrix} \mathbf{q}_{\mathtt{1}} \\ \mathbf{q}_{\mathtt{L}} \\ \mathbf{q}_{\mathtt{B}} \end{pmatrix} = \mathbf{0} \tag{1.30}$$

Suppose one of $(\lambda_x, \lambda_y)$ is given, for example $\lambda_y$. Eq. (1.30) then becomes a quadratic eigenvalue problem in $\lambda_x$ as follows:

$$\frac{1}{\lambda_x}(\lambda_x^2 \begin{bmatrix} \mathbf{A}_{\mathtt{11}} & \mathbf{A}_{\mathtt{1L}} & \mathbf{A}_{\mathtt{1B}} \\ \mathbf{A}_{\mathtt{L1}} & \mathbf{A}_{\mathtt{LL}} & \mathbf{A}_{\mathtt{LB}} \\ \mathbf{A}_{\mathtt{B1}} & \mathbf{A}_{\mathtt{BL}} & \mathbf{A}_{\mathtt{BB}} \end{bmatrix} + \lambda_x \begin{bmatrix} \mathbf{B}_{\mathtt{11}} & \mathbf{B}_{\mathtt{1L}} & \mathbf{B}_{\mathtt{1B}} \\ \mathbf{B}_{\mathtt{L1}} & \mathbf{B}_{\mathtt{LL}} & \mathbf{B}_{\mathtt{LB}} \\ \mathbf{B}_{\mathtt{B1}} & \mathbf{B}_{\mathtt{BL}} & \mathbf{B}_{\mathtt{BB}} \end{bmatrix} + \begin{bmatrix} \mathbf{C}_{\mathtt{11}} & \mathbf{C}_{\mathtt{1L}} & \mathbf{C}_{\mathtt{1B}} \\ \mathbf{C}_{\mathtt{L1}} & \mathbf{C}_{\mathtt{LL}} & \mathbf{C}_{\mathtt{LB}} \\ \mathbf{C}_{\mathtt{B1}} & \mathbf{C}_{\mathtt{BL}} & \mathbf{C}_{\mathtt{BB}} \end{bmatrix}) \begin{pmatrix} \mathbf{q}_{\mathtt{1}} \\ \mathbf{q}_{\mathtt{L}} \\ \mathbf{q}_{\mathtt{B}} \end{pmatrix} = \mathbf{0} \tag{1.31}$$

Once the coefficients in the matrices $\mathbf{A}$, $\mathbf{B}$ and $\mathbf{C}$ are known, the quadratic eigenvalue problem can be solved using the *polyeig* function in Matlab, of which there are $2(s + ns + ms)$ solutions. The formulations for matrices $\mathbf{A}, \mathbf{B}, \mathbf{C}$ can be found in Appendix A.

**Inverse form of WFEM2D** In inverse form, the internal nodes are conserved since the dynamic condensation can not be performed, so we have:

$$\begin{pmatrix} \mathbf{q}_{\mathtt{bd}} \\ \mathbf{q}_{\mathtt{I}} \end{pmatrix} = \mathbf{\Lambda}'_{\mathbf{R}} \begin{pmatrix} \mathbf{q}_{\mathtt{1}} \\ \mathbf{q}_{\mathtt{L}} \\ \mathbf{q}_{\mathtt{B}} \\ \mathbf{q}_{\mathtt{I}} \end{pmatrix} \tag{1.32}$$

$\mathbf{\Lambda}'_{\mathbf{R}}$ contains an identity matrix $\mathbf{I}_{\mathtt{i}}$ of size $i$

$$\mathbf{\Lambda}'_{\mathbf{R}} = \begin{pmatrix} \tilde{\mathbf{\Lambda}}_{\mathbf{R}} & \mathbf{0} \\ \mathbf{0} & \mathbf{I}_{\mathtt{i}} \end{pmatrix} \tag{1.33}$$

Similarly for the nodal forces

$$\mathbf{\Lambda}'_{\mathbf{L}} \begin{pmatrix} \mathbf{f}_{\mathbf{bd}} \\ \mathbf{0} \end{pmatrix} = \mathbf{0} \tag{1.34}$$

with

$$\mathbf{\Lambda}'_{\mathbf{L}} = \begin{pmatrix} \tilde{\mathbf{\Lambda}}_{\mathbf{L}} & \mathbf{0} \\ \mathbf{0} & \mathbf{I}_{\mathbf{i}} \end{pmatrix} \tag{1.35}$$

The formulation of $\tilde{\mathbf{\Lambda}}_{\mathbf{R}}$ and $\tilde{\mathbf{\Lambda}}_{\mathbf{L}}$ are the same as in 1.27 and 1.29. The Eq. (1.13) becomes

$$\mathbf{\Lambda}'_{\mathbf{L}} * (\mathbf{K} - \omega^{\mathbf{2}}\mathbf{M}) * \mathbf{\Lambda}'_{\mathbf{R}} \begin{pmatrix} \mathbf{q}_{\mathtt{1}} \\ \mathbf{q}_{\mathtt{L}} \\ \mathbf{q}_{\mathtt{B}} \\ \mathbf{q}_{\mathtt{I}} \end{pmatrix} = \mathbf{0} \tag{1.36}$$

which becomes the following standard, linear eigenvalue problem in $\omega^2$,

$$[\mathbf{K}'(\lambda_{\mathbf{x}}, \lambda_{\mathbf{y}}) - \omega^{\mathbf{2}}\mathbf{M}'(\lambda_{\mathbf{x}}, \lambda_{\mathbf{y}})] \begin{pmatrix} \mathbf{q}_{\mathtt{1}} \\ \mathbf{q}_{\mathtt{L}} \\ \mathbf{q}_{\mathtt{B}} \\ \mathbf{q}_{\mathtt{I}} \end{pmatrix} = \mathbf{0} \tag{1.37}$$

For the undamped structure, $\mathbf{K}$ and $\mathbf{M}$ are positive definite Hermitian matrices, so as the matrices $\mathbf{K}'$ and $\mathbf{M}'$ with $|\lambda_x| = 1$ and $|\lambda_y| = 1$. The eigvalues $\omega^2$ for which free wave propagation is possible are real and positive. Since the size of the eigen problem is the same as $((\mathbf{q}_{\mathtt{1}})^{\mathtt{T}}(\mathbf{q}_{\mathtt{L}})^{\mathtt{T}}(\mathbf{q}_{\mathtt{B}})^{\mathtt{T}}(\mathbf{q}_{\mathtt{I}})^{\mathtt{T}})^{\mathtt{T}}$. In chapter 3, a reduction technique is included in WFEM2D, which decreases the size of the eigen problem.

### 1.3.4 Homogenization methods

Numerous homogenization methods have been developed to study the heterogeneous materials or periodic structures. The equivalent strain energy method is initially proposed by Nemat-Nasser *et al.* [1982] for periodically distributed inclusions of spherical and cylindrical geometries. Then it is applied to study periodic masonry structure [Wang *et al.*, 2007] or in the topology optimal design of material [Zhang *et al.*, 2007]. The two-scale asymptotic homogenization method is also widely used to find equivalent model of composite structures [Challagulla *et al.*, 2010; Kalamkarov *et al.*, 2009] or masonry panel [Cecchi & Rizzi, 2001]. Based on two-scale approach, high frequency homogenization is then proposed by Craster *et al.* [2012] which can accurately capture the behaviour of a periodic structure at high frequencies.

During the study of perforated plate in chapter 4, wave-based homogenization methods are proposed to find their homogenized models with different patterns of penetration.

#### 1.3.4.1 Asymptotic homogenization method

Here the classical asymptotic homogenization method is revised. Consider a periodic structure occupying domain $\Omega$ with boundary $\partial\Omega$. The first step is to define the fast or microscopic variables $y_i$ in the domain of the unit cell Y.

$$y_i = x_i/\varepsilon \tag{1.38}$$

the derivatives must be transformed according to

$$\frac{\partial}{\partial x_i} \to \frac{\partial}{\partial x_i} + \frac{1}{\varepsilon}\frac{\partial}{\partial y_i} \tag{1.39}$$

so the boundary-value problem which describes the elastic deformation of the periodic structure can be written as:

$$\frac{\partial \sigma_{ij}^{\varepsilon}}{\partial x_j} + \frac{1}{\varepsilon}\frac{\partial \sigma_{ij}^{\varepsilon}}{\partial y_j} = f_i \quad \text{in} \quad \Omega, \quad u_i^{\varepsilon} = 0 \quad \text{on} \quad \partial\Omega \tag{1.40}$$

$$\sigma_{ij}^{\varepsilon}(\mathbf{x},\mathbf{y}) = C_{ijkl}(\mathbf{y})\frac{\partial u_k}{\partial x_l}(\mathbf{x},\mathbf{y}) \tag{1.41}$$

The next step is to consider the asymptotic expansions in terms of the small parameter $\varepsilon$. Asymptotic expansion for the displacement field:

$$\mathbf{u}^{\varepsilon}(\mathbf{x},\mathbf{y}) = \mathbf{u}^{(0)}(\mathbf{x},\mathbf{y}) + \varepsilon\mathbf{u}^{(1)}(\mathbf{x},\mathbf{y}) + \varepsilon^2\mathbf{u}^{(2)}(\mathbf{x},\mathbf{y}) + ... \tag{1.42}$$

Asymptotic expansion for the stress field:

$$\sigma_{ij}^{\varepsilon}(\mathbf{x},\mathbf{y}) = \sigma_{ij}^{(0)}(\mathbf{x},\mathbf{y}) + \varepsilon\sigma_{ij}^{(1)}(\mathbf{x},\mathbf{y}) + \varepsilon^2\sigma_{ij}^{(2)}(\mathbf{x},\mathbf{y}) + ... \tag{1.43}$$

It is understood that all functions in $\mathbf{y}$ are all periodic with the unit cell Y. Considering terms with like powers of $\varepsilon$, one obtains a series of differential equations. The next step is the model development is the homogeniztion procedure. The resulting expression is eventually integrated over the domain Y of the unit cell. This yields

$$\frac{1}{|Y|}\int_Y \frac{\partial \sigma_{ij}^{(1)}(\mathbf{x},\mathbf{y})}{\partial y_j}dv + \tilde{C}_{ijkl}\frac{\partial^2 u_k^{(0)}(\mathbf{x})}{\partial x_j \partial x_i} = f_i \tag{1.44}$$

where the homogenized elastic coefficients $\tilde{C}_{ijkl}$ can be expressed as follows:

$$\tilde{C}_{ijkl} = \frac{1}{|Y|}\int_Y \left( C_{ijkl}(\mathbf{y}) + C_{ijmn}(\mathbf{y})\frac{\partial N_m^{kl}}{\partial y_n} \right) dv \tag{1.45}$$

then the effective coefficients can be used to study a wide variety of boundary value problems associated with a given composite structure. One can refer [Kalamkarov *et al.*, 2009] for the formulation of $N_m^{kl}$ and more details.

#### 1.3.4.2 Equivalent strain energy method

Based on equivalent strain energy method, one can replace the periodic structure by an equivalent homogenized model with the same volume. It satisfies the following conditions: the stress and the strain tensors of the homogeneous medium are equivalent to the average stress and strain of the unit cell with $\frac{1}{V}\int \boldsymbol{\sigma} dV = \bar{\boldsymbol{\sigma}}$ and $\frac{1}{V}\int \boldsymbol{\varepsilon} dV = \bar{\boldsymbol{\varepsilon}}$. $V$ denotes the volume of the unit cell. The average stress and strain of the homogenized model follow the Hooke's law

$$\bar{\boldsymbol{\sigma}} = \mathbf{D}^{\mathrm{H}}\bar{\boldsymbol{\varepsilon}} \tag{1.46}$$

where $\mathbf{D}^{\mathrm{H}}$ is the effective elastic tensor of the material. The effective elastic tensor of 2D orthotropic material under plane-stress can be written in matrix form as

$$\mathbf{D}^{\mathrm{H}} = \begin{bmatrix} D_{1111}^{\mathrm{H}} & D_{1122}^{\mathrm{H}} & 0 \\ D_{1122}^{\mathrm{H}} & D_{2222}^{\mathrm{H}} & 0 \\ 0 & 0 & D_{1212}^{\mathrm{H}} \end{bmatrix} \tag{1.47}$$

Besides, the strain energies stored in the periodic structure and the homogenized model have to be equal

$$E(\boldsymbol{\varepsilon}) = \frac{1}{2V}\int_\Omega (\sigma_{11}\varepsilon_{11} + \sigma_{22}\varepsilon_{22} + \sigma_{12}\varepsilon_{12})d\Omega = \frac{1}{2}(\bar{\sigma}_{11}\bar{\varepsilon}_{11} + \bar{\sigma}_{22}\bar{\varepsilon}_{22} + \bar{\sigma}_{12}\bar{\varepsilon}_{12}) = E(\bar{\boldsymbol{\varepsilon}}) \tag{1.48}$$

Based on Eqs. (1.47) - (1.48), the effective elastic tensor can be identified from the strain energies of unit cell under the specific boundary conditions. For example, for the 1st boundary condition, suppose the average strain of the unit cell is $\bar{\boldsymbol{\varepsilon}}^{(1)} = (1 \quad 0 \quad 0)^T$, the average stress

tensor is $\bar{\boldsymbol{\sigma}}^{(1)} = (D^H_{1111} \quad D^H_{1122} \quad 0)^T$ correspondingly, Then, the component $D_{1111}$ can be obtained as $D^H_{1111} = 2E^{(1)}$. In order to calculate all the effective elastic tensor components, four different boundary conditions should be considered.

#### 1.3.4.3 Mode-based method to determine equivalent model of perforated plate

Jhung & JO [2006] proposed to find equivalent Young's Modulus of solid plate in order to match the natural frequencies of the perforated plate. His method consists of the following 4 steps.

1. Develop a finite element model for solid plates and perforated plates.
2. Perform the modal analysis for the perforated and solid plates with original properties.
3. Compare the frequencies and determine the ratio of frequencies for the perforated plate to those of solid plate.
4. Find the multipliers of the Young's modulus of solid plate in order to match the frequencies of the perforated plate with the original properties using the relationship between the frequency and Young's modulus.

Similar to Jhung & JO [2006], Wang & Lai [2003] proposed also a method based on the natural modes of the structure to find homogenized model of perforated plate. He combined experimental and numerical methods and used Modal Assurance Criterion (MAC) [Ewins, 1984] to judge the degree of similarity between experimental and numerical models. However, there are several drawbacks of the mode-based approach to determine the equivalent parameters. First, one may find different equivalent parameters if the modal analysis is carried out under different boundary conditions. Second, the perforated structure may contain numerous holes, making the modal analysis of the full model time-consuming. Third, it can not predict the frequency range where the homogenized model is valid.

#### 1.3.4.4 Wave-based method to find equivalent flexural and shear stiffness

Chronopoulos *et al.* [2013] has proposed a wave-based method to find equivalent flexural and shear stiffness of composite panels. Following classic or modern plate theories, the propagating flexural $(k_{fx}, k_{fy})$ and shear $k_{s,xy}$ wavenumbers can be expressed as a function of the mechanical characteristics of the structure. He used WFEM to numerically calculate the values of propagating wavenumbers for a wide frequency range and then derived the expressions for the equivalent dynamic mechanical characteristics. The classical laminated plate theory was

used to give following expressions:

$$D_{eq,i} = \frac{\omega^2 \rho_s}{k_{f,i}^4} \tag{1.49a}$$

$$B_{eq,i} = \frac{\omega^2 \rho_s}{k_{s,i}^2} \tag{1.49b}$$

with $\rho_s$ the mass per unit of area, $D_{eq,i}$ the equivalent flexural stiffness of the structure towards direction $i$, and $B_{eq,i}$ its equivalent shear stiffness in the plane of the plate. The obtained equivalent single layer model of the composite panel is proved to be time efficient and accurate to predict the dynamic responses for a wide frequency range.

## 1.4 Model order reduction technique

To predict propagation characteristics in periodic structures, the computational effort is usually high because it involves solving a complex eigenvalue problem and doing as many times as the value of wavenumber $k$ or frequency $f$ is varied. Therefore, several techniques have been developed to speed up band structure calculation [Chern *et al.*, 2003; Dobson, 1999]. Here the techniques related to Model Order Reduction (MOR) are presented. MOR techniques have been widely treated in the literature within the frameworks of component mode method, SVD-based and Krylov-based methods [Antoulas & Sorensen, 2001] to study large-scale dynamical systems. However, few application of these techniques has been applied to the WFEM matrix formulations. In this thesis, a mode-base MOR technique - fixed interface component mode synthesis method [Craig & Bampton, 1968] is combined to the WFEM. Here the free boundary component mode synthesis method and branch mode method [Gladwell, 1964] are briefly reviewed as alternative mode-based MOR technique.

The WFEM formulation, as derived before, consists of projecting the kinematic variables of unit cell on a wave basis. Reducing these wave basis efficiently appears crucial in many applications. However, attention should be paid when proposing a reduced wave basis. Since most of the matrices involved by the WFEM formulations depend on the frequency, as opposed to classic FE approaches where conventional mass/stiffness matrices are rather of concern.

### 1.4.1 Model order reduction technique based on modal basis

MOR based on component mode methods are now described. The first of these, known as Component Mode Synthesis (CMS), contains two variants (1) the fixed interface method and (2) the free interface method. Another method, less well documented, but very useful in practical work, is the branch mode method.

In our proposed method, the fixed interface method (Craig-Bampton method) is combined with WFEM. In Craig-Bampton method, the physical DOFs of the boundary nodes are conserved. It is easy to implement to WFEM formulation, since wavenumbers are deduced from relation between physical DOFs at different boundaries of unit cell. The free interface component mode synthesis and brand mode method are revised here, and the Craig-Bampton method is explained in chapter 2 and chapter 3.

#### 1.4.1.1 Free interface component mode synthesis

Suppose a structure with 2 substructures, "a" and "b". In free interface method, the initial modal analysis of each substructure is carried out with the interface coordinates free to move. Assume harmonic vibration, the equation of motion for an undamped, unforced equation of motion for subsystem "a" in global coordinates, is

$$\mathbf{K}^{\mathrm{a}}\mathbf{q}^{\mathrm{a}} - \omega^2\mathbf{M}^{\mathrm{a}}\mathbf{q}^{\mathrm{a}} = \mathbf{0} \tag{1.50}$$

The physical coordinates are then transformed into modal coordinates,

$$\mathbf{q}^{\mathrm{a}} = \mathbf{\Psi}^{\mathrm{a}}\mathbf{p}^{\mathrm{a}} \tag{1.51}$$

similarly as substructure "a", the substructure "b" is also transformed into modal coordinates, then equations of motion of the two substructures without connection, can be written as

$$\omega^2 \begin{bmatrix} \bar{\mathbf{M}}^{\mathrm{a}} & \mathbf{0} \\ \mathbf{0} & \bar{\mathbf{M}}^{\mathrm{b}} \end{bmatrix} \begin{pmatrix} \mathbf{p}^{\mathrm{a}} \\ \mathbf{p}^{\mathrm{b}} \end{pmatrix} - \begin{bmatrix} \bar{\mathbf{K}}^{\mathrm{a}} & \mathbf{0} \\ \mathbf{0} & \bar{\mathbf{K}}^{\mathrm{b}} \end{bmatrix} \begin{pmatrix} \mathbf{p}^{\mathrm{a}} \\ \mathbf{p}^{\mathrm{b}} \end{pmatrix} = \begin{pmatrix} \mathbf{0} \\ \mathbf{0} \end{pmatrix} \tag{1.52}$$

with

$$\bar{\mathbf{M}}^{\mathrm{a}} = [\mathbf{\Psi}^{\mathrm{a}}]^{\mathrm{T}}\mathbf{M}^{\mathrm{a}}\mathbf{\Psi}^{\mathrm{a}}, \bar{\mathbf{K}}^{\mathrm{a}} = [\mathbf{\Psi}^{\mathrm{a}}]^{\mathrm{T}}\mathbf{K}^{\mathrm{a}}\mathbf{\Psi}^{\mathrm{a}} \tag{1.53}$$

If the global coordinates at junctions are separated out, and designated $\mathbf{q}^{\mathrm{a}}_{\mathrm{B}}$ and $\mathbf{q}^{\mathrm{b}}_{\mathrm{B}}$ for substructures "a" and "b", respectively, then they must be equal when the substructures are joined.

$$\mathbf{q}^{\mathrm{a}}_{\mathrm{B}} = \mathbf{\Psi}^{\mathrm{a}}_{\mathrm{B}}\mathbf{p}^{\mathrm{a}} = \mathbf{q}^{\mathrm{b}}_{\mathrm{B}} = \mathbf{\Psi}^{\mathrm{b}}_{\mathrm{B}}\mathbf{p}^{\mathrm{b}} \tag{1.54}$$

$\mathbf{\Psi}_{\mathrm{B}}$ contains $n_{\mathrm{B}}$ rows which correspond to global coordinate displacements at junction nodes. The generalized coordinates, to be used in Lagrange's equations, must be independent. Then the dependent or superfluous coordinates can be eliminated as follows:

$$\begin{bmatrix} \mathbf{\Psi}^{\mathrm{a}}_{\mathrm{B}} & -\mathbf{\Psi}^{\mathrm{b}}_{\mathrm{B}} \end{bmatrix} \begin{pmatrix} \mathbf{p}^{\mathrm{a}} \\ \mathbf{p}^{\mathrm{b}} \end{pmatrix} = \mathbf{0} \tag{1.55}$$

or

$$\begin{bmatrix} \mathbf{A}_1 & -\mathbf{A}_2 \end{bmatrix} \begin{pmatrix} \mathbf{p}_\mathtt{d} \\ \mathbf{p}_\mathtt{f} \end{pmatrix} = \mathbf{0} \tag{1.56}$$

The matrix $\mathbf{A}_1$, which must not be singular, is a square matrix, formed from the columns associated with the dependent coordinates $\mathbf{p}_\mathtt{d}$ of size $n_\mathtt{B}$. The matrix $\mathbf{A}_2$ is associated with the independent coordinates $\mathbf{p}_\mathtt{f}$. In theory, it does not matter which $n_\mathtt{B}$ coordinates are chosen to be dependent, but some choices may be more convenient than others in practical cases [Thorby, 2008].

$$\begin{pmatrix} \mathbf{p}_\mathtt{d} \\ \mathbf{p}_\mathtt{f} \end{pmatrix} = \begin{bmatrix} -\mathbf{A}_1^{-1}\mathbf{A}_2 \\ \mathbf{I} \end{bmatrix} \mathbf{p}_\mathtt{f} \tag{1.57}$$

the elements in the vector $(\mathbf{p}_\mathtt{d} \quad \mathbf{p}_\mathtt{f})^\mathtt{T}$ must be changed back to the original order $(\mathbf{p}^\mathtt{a} \quad \mathbf{p}^\mathtt{b})^\mathtt{T}$ with corresponding changes to the matrix, which becomes $\boldsymbol{\beta}$.

$$\begin{pmatrix} \mathbf{p}^\mathtt{a} \\ \mathbf{p}^\mathtt{b} \end{pmatrix} = \boldsymbol{\beta}\mathbf{p}_\mathtt{f} \tag{1.58}$$

So the equation of motion of the complete, joined system is as follows:

$$\omega^2 \boldsymbol{\beta}^\mathtt{T} \begin{bmatrix} \bar{\mathbf{M}}^\mathtt{a} & \mathbf{0} \\ \mathbf{0} & \bar{\mathbf{M}}^\mathtt{b} \end{bmatrix} \boldsymbol{\beta}\mathbf{p}_\mathtt{f} - \boldsymbol{\beta}^\mathtt{T} \begin{bmatrix} \bar{\mathbf{K}}^\mathtt{a} & \mathbf{0} \\ \mathbf{0} & \bar{\mathbf{K}}^\mathtt{b} \end{bmatrix} \boldsymbol{\beta}\mathbf{p}_\mathtt{f} = \mathbf{0} \tag{1.59}$$

The equation will then be solved for natural frequencies and normal modes in the usual way.

#### 1.4.1.2 The branch mode method

Another variant of the component mode method is known as branch mode method. The method exhibits some of the same feature as CMS, although differences exist. The system considered can be chain-like configuration, in which every component is connected to two other components, or can be extended to cases in which several component are connected at one point. The components are grouped into subsets called branches. The motion of each branch is represented by branch modes, which are generally modes of vibration of the separate branch. The method uses a special way of defining the shapes of the assumed modes, avoiding the use of constraint modes or constraint equations, as required in CMS methods. The branch modes may be defined by letting only one of the components in the branch be flexible while the other are either fixed or free, where in the latter case the component can vibrate as a rigid body.

The method is most easily explained by a simple example. Consider the L-shaped lumped-mass structure shown in Fig. 1.7. It consists of two branches “AB”, and “BC”. Assume that the whole structure contains $n$ DOF. Four examples of the many possible branch modes are sketched in Fig. 1.7(b). Branch mode 1 consists of the first bending normal mode of beam

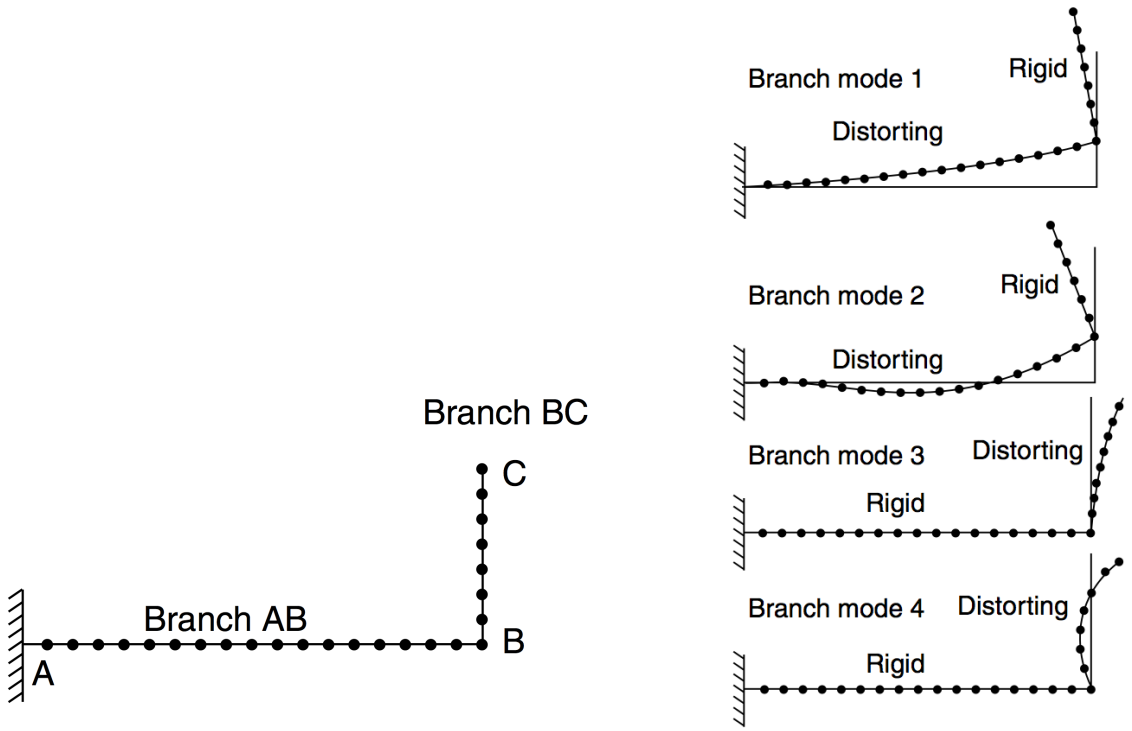


(a) A branched structure (b) Branch modes

Figure 1.7: The branch mode method [Thorby, 2008]

AB, with beam BC attached to it, but the part BC is constrained to be rigid, although free to move with AB. The branch modes, say the four shown in Fig. 1.7(b), are now used in a straightforward "Rayleigh–Ritz", assumed modes analysis, which is carried out by applying Lagrange's equations. Then number of DOFs will be reduced from $n$ to only 4. The way to derive the mass and stiffness matrices is given in the reference [Thorby, 2008], where the normal modes of each branch are used.

### 1.4.2 Model order reduction technique based on wave basis

Several works can be found which proposed wave-based MOR technique in WFEM. Droz *et al.* [2014a] have proposed a reduction formulation to determine the propagating wave in 1D refined model of a laminated composite beam. The main idea is to use the wave basis at cut-on frequencies to describe the wave basis in the whole frequency range. Then the spectral problem on the dynamic stiffness matrix of unit cell is expressed by reduced wave coordinates. Similarly, a reduced wave basis expansion method has been proposed by Hussein [2009] for fast calculation of band structure in 2D periodic structures. However, instead of forming the reduced wave basis using the waves basis at cut-on frequencies, the eigenvectors corresponding to a selected wavenumbers are employed. Mencik [2012] has proposed a reduction technique by selecting the wave modes that are relevant for computing the forced response of elastic

waveguides. However, the numerical costs for computation of the wave basis are not reduced. Mead [2009] has presented a reduced method by identifying, in a preliminary investigation, the characteristic waves which contribute to the motion of the structure. Then the computation time to calculate the wave basis as well as the forced response of the structure is reduced.

#### 1.4.2.1 Interpolation of reduced wave basis

Droz *et al.* [2014a] proposed a reduction technique to study the free wave propagation in 1D laminated composite beam. The main feature is to reduce the matrix $\mathbf{S}(\lambda, \omega)$ using a subset of eigensolutions. The main assumption is that a waveguide cross-sectional deformed shape at frequency $\omega_i$ can be used to describe the motion of the periodic cell for the same wave in a large frequency range around $\omega_i$.

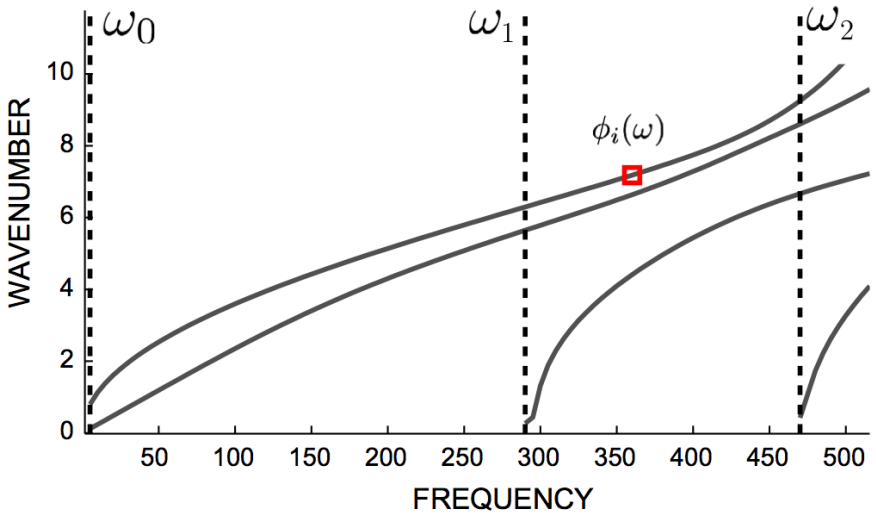


Figure 1.8: Frequency interpolation of reduced wave basis [Droz *et al.*, 2014a]

An illustration is given for the wave frequency interpolation in Fig. 1.8. The dispersion curves of propagating waves are represented by the grey curves, dashed vertical lines are called cut-on frequencies at $\omega_0$, $\omega_1$ and $\omega_2$, where the waves shapes are supposed known. They are denoted $\left\{\vec{\phi}_i^{(0)}\right\}_{1\leq i\leq r_0}$, $\left\{\vec{\phi}_i^{(1)}\right\}_{1\leq i\leq r_1}$ and $\left\{\vec{\phi}_i^{(2)}\right\}_{1\leq i\leq r_2}$. The solution $\vec{\phi}(\omega)$ marked by a red square is of our interest. This solution is approximated using the aforementioned eigenvectors as :

$$\vec{\phi}(\omega) \simeq \sum_{i=1}^{r_0} \vec{\phi}_i^{(0)} \nu_i^{(0)}(\omega) + \sum_{i=1}^{r_1} \vec{\phi}_i^{(1)} \nu_i^{(1)}(\omega) + \sum_{i=1}^{r_2} \vec{\phi}_i^{(2)} \nu_i^{(2)}(\omega) \tag{1.60}$$

where $\nu_i^{(0)}$, $\nu_i^{(1)}$, $\nu_i^{(2)}$ are reduced wave amplitudes.

Denoting $\omega_{A(k)}$ with $1 \leq k \leq n_A$ the cut-on frequency of the k-th wave, the exact eigensolutions can be computed for each new propagating wave from the system of $n_A$ independent

quadratic eigenproblems:

$$\begin{cases} \mathbf{S}(\lambda, \tilde{\omega}_1)\mathbf{\Phi} = \mathbf{0} \\ \vdots \\ \mathbf{S}(\lambda, \tilde{\omega}_k)\mathbf{\Phi} = \mathbf{0} \qquad ; \quad \tilde{\omega}_k \in \tilde{\Omega} \\ \vdots \\ \mathbf{S}(\lambda, \tilde{\omega}_{n_A})\mathbf{\Phi} = \mathbf{0} \end{cases} \tag{1.61}$$

Eigenvectors $\mathbf{\Phi}_i(\tilde{\omega}_k)$ stands for the deformed shape on the left side of a cell, associated with i-th wave at k-th wave cut-on frequency. The wave shape basis $\mathbf{\Phi}$ is improved to ensure that they are purely real, normalized and well-conditioned. The obtained basis denotes $\mathbf{\Gamma} = [\Gamma_1, \cdots, \Gamma_r]$. Then the state vector can be written in terms of wave participations :

$$\begin{pmatrix} \mathbf{q}_{\mathrm{L}} \\ \mathbf{q}_{\mathrm{R}} \end{pmatrix} = \begin{bmatrix} \mathbf{\Gamma} & \mathbf{0} \\ \mathbf{0} & \mathbf{\Gamma} \end{bmatrix} \begin{pmatrix} \mathbf{p}_{\mathrm{L}} \\ \mathbf{p}_{\mathrm{R}} \end{pmatrix} \tag{1.62}$$

where $\mathbf{\Gamma}$ is associated to the displacements of the left boundary of the periodic cell, while $\mathbf{p}_{\mathrm{L}}$ is a vector of size $r$, containing the reduced wave participations. The spectral problem then becomes

$$\mathbf{\Gamma}^T\mathbf{S}(\lambda, \omega)\mathbf{\Gamma}\mathbf{p}_{\mathrm{L}} = \tilde{\mathbf{S}}(\lambda, \omega)\mathbf{p}_{\mathrm{L}} = \mathbf{0} \tag{1.63}$$

Therefore, the dispersion characteristics can be computed on the frequency range $\Omega$ with minor CPU cost by solving for example the following $2r \times 2r$ reduced eigenproblem.

#### 1.4.2.2 Expansion of reduced wave basis in 2D periodic structures

Similarly, a reduced wave basis expansion method is proposed by Hussein [2009] for fast calculation of band structure in 2D periodic structures. However, instead of selecting propagating waves at cut-on frequencies to form the reduced wave basis, the eigenvectors corresponding to a selected wavenumbers are used to form the wave basis.

The formulation of the inverse form of WFEM2D will be applied to demonstrate the model reduction technique. The eigenvalue problem of Eq. (1.37) is first solved at a reduced set of selected wavevector points. This provides the eigenvectors from which a reduced wave basis, denoted $\mathbf{\Phi}$, is formed. Several schemes are available for the selection, the simplest of which is the set of eigenvectors corresponding to the first few branches at the high-symmetry points, for example the O, A, B, C points in fig. 1.2(b). At each of these high symmetry points, a number of eigenvectors are selected up to the frequency range of interest for the band structure calculations. The matrix $\mathbf{\Phi}$ is then used to expand the eigenvectors $\mathbf{q} = \begin{bmatrix} \mathbf{q}_{\mathrm{I}} & \mathbf{q}_{\mathrm{L}} & \mathbf{q}_{\mathrm{B}} & \mathbf{q}_{\mathrm{I}} \end{bmatrix}^{\mathrm{T}}$ ,

i.e.,

$$\mathbf{q}_{(n\times 1)} = \mathbf{\Phi}_{(n\times m)}\mathbf{V}_{(m\times 1)} \tag{1.64}$$

where $\mathbf{V}$ is a vector of wave amplitude of the wave shape. In Eq. (1.64), $n$ and $m$ refer to the number of rows and number of columns for the matrix equation. Usually, $m \ll n$ which enables a significant model reduction. Substituting Eq. (1.64) into Eq. (1.37), and premultiplying by the complex transpose of $\mathbf{\Phi}$, yields a reduced eigenvalue problem of size $m \times m$

$$\mathbf{\Phi}^*\mathbf{K}'(\lambda_\mathbf{x}, \lambda_\mathbf{y})\mathbf{\Phi}\mathbf{V} - \omega^2\mathbf{\Phi}^*\mathbf{M}'(\lambda_\mathbf{x}, \lambda_\mathbf{y})\mathbf{\Phi}\mathbf{V} = \mathbf{0} \tag{1.65}$$

The eigenvalue problem can be solved for the entire region of interest at a significantly lower cost compared to the full model given in Eq. (1.37).

## 1.5 The proposed wave and modal coupled method and wave-mode duality discussion

It is well known that the response of a vibrating system can be viewed either in terms of modes or in terms of elastic wave motion, known as "wave-mode duality". Plenty of discussions regarding the relationship between the wave and the modal descriptions can be found [Langley, 1997; Lyon & DeJong, 1995]. For 1D waveguide, the wave-mode duality is demonstrated in a mathematical sense. The vibration can be written both as a sum of right- and left-going components and a sum of participation of all the modes under the same boundary conditions. However for 2D structure, the duality has not been proved precisely due to ill-conditioning problem in numerical computation [Langley, 1997].

Both the wave-based and mode-based approaches can be applied to study periodic structures. In this thesis, a combined wave/mode-based approach is proposed. Modal description is employed on the mesoscopic unit cell level, then the macroscopic structure is considered as a waveguide and the vibration is described with elastic waves. The terminology on wave description is clarified to avoid ambiguity, since the term "mode" employed here implies only the structural mode, not the "wave mode" as used in a lot of work related to WFEM. The equivalence of structural modes and stationary waves are also discussed in this section. The formulations to derive the structural modal density from the wave propagation characteristics are given at the end of this section.

### 1.5.1 Analysis of periodic structures using modal approach - Component Mode Synthesis

One of the most common CMS methods is the Craig-Bampton method. To build the component (unit cell) model, we use a reduced basis of fixed boundary modes $\mathbf{\Psi}_{\mathtt{c}}$. Constraint modes of the component interfaces $\mathbf{\Psi}_{\mathtt{bd}}$ are also introduced. The modal basis $\mathbf{\Psi}^{\mathtt{s}}$ of the structure can be deduced by assembling all the components, after expanding the reduced modal coordinates to the physical coordinates. Subsequently, the physical displacement $\mathbf{q}$ is related to the modal displacement $\eta$ using the following equation:

$$\mathbf{q}(\vec{r},\omega) = \sum_{i=1}^{n} \eta_i(\omega,\omega_{0i})\psi_{\mathtt{i}}^{\mathtt{s}}(\vec{r},\omega_{0i}) \tag{1.66}$$

where $\vec{r}$ represents the physical coordinates. "Modes shapes" $\psi_{\mathtt{i}}^{\mathtt{s}}$ are associated with natural frequency $\omega_{0i}$, which form a "structural modal basis" $\mathbf{\Psi}^{\mathtt{s}} = [\psi_{\mathtt{1}}^{\mathtt{s}}, \psi_{\mathtt{2}}^{\mathtt{s}}..., \psi_{\mathtt{n}}^{\mathtt{s}}]$. In this thesis, the modes (cell modes and structural modes) shapes are represented by $\psi_{\mathtt{i}}$, whereas wave shapes are represented by $\phi_{\mathtt{i}}$ in wave description.

### 1.5.2 Analysis of periodic structures using wave approach - Wave Finite Element Method

In wave description, the displacement field (free or forced) of structure is regarded as a sum of harmonic waves:

$$\mathbf{q}(\vec{r},\omega) = \sum_{i=1}^{n} a_i(\omega,\vec{x_1},k_i)\phi_i(\omega,\vec{x_2},k_i) \tag{1.67}$$

where $\omega$ is the frequency of the propagating wave. Physical coordinates $\vec{r}$ are divided into $(\vec{x_1},\vec{x_2})$, with $\vec{x_1}$ representing coordinates in the propagation direction and $\vec{x_2}$ representing the local coordinates in the unit cell. Instead of the standard FEM where the whole waveguide is meshed (coordinate $(\vec{x_1}\vec{x_2})$), WFEM meshes only a unit cell (coordinate $\vec{x_2}$). Then the wave propagation characteristic in coordinate $\vec{x_1}$ of the whole structure can be derived using the transfer matrix between the unit cells.

**Terminology concerning the wave description of vibration** In wave description, $k$ represents the "wavenumber" of the harmonic wave at frequency $\omega$. It is related to the "propagation constant" $\mu$ using $\mu = -ikL$, giving $L$ the length of the unit cell in the propagating direction. Wavenumber $k$ can be complex with its real part $\Re(k)$ determining the phase constant and its imaginary part $\Im(k)$ determining the attenuation constant. The "wave shape" $\phi_i$ which is associated with wavenumber $k_i$, gives the distribution of displacements in the unit cell. All the wave

shapes at a fixed frequency form a frequency-dependent "wave basis" $\mathbf{\Phi}(\omega) = [\phi_1, \phi_2 ..., \phi_n]$ on which the displacement is projected. The coefficients $a_i$ in Eq. (1.67) are called "wave amplitudes". In 1D waveguide, the characteristics of a wave propagation can be represented by $(\omega, k, \phi)$. The curves $k = f(\omega)$ are called "dispersion curves". The frequency range in which no propagating wave exists is called "stop band".

In 2D waveguide, the wave description is formed by $(\omega, k_x, k_y, \phi)$. The plane wave which propagates in angle $\theta$ with wavenumber $k_\theta$, is related by $k_x = k_\theta \cos\theta$ and $k_y = k_\theta \sin\theta$ as shown in Fig. 1.2(a). Wavenumber $(k_x, k_y)$ varying within first Brillouin zone $[-\frac{\pi}{L_x}, \frac{\pi}{L_x}] \times [-\frac{\pi}{L_y}, \frac{\pi}{L_y}]$ is studied. The surfaces formed by $\omega_i = f(k_x, k_y)$ are called "slowness surfaces". A section of the surface with fixed frequency $\omega_0 = f(k_x, k_y)$ is called "Iso-frequency contour of the slowness surface" or "$k$-space". The directivity of the propagation in the structure is called "wave beaming effect". In fact, it is a "partial stop band" for certain directions. The "absolute stop band" of the waveguide (if exists) consists of frequency range where no slowness surface exists. A simplified 2D plot of the slowness surfaces is the "band structure". It is obtained by plotting the wavenumber of the slowness surfaces along the contour of IBZ (O-A-B-C-O), as displayed in Fig. 1.2(b). The point O,A,B,C are called "bounding points of stop band", as explained in detail in subsection 1.5.4.

### 1.5.3 Combination of modal description on mesoscopic scale and wave description on macroscopic scale, Wave-mode duality

When CMS is employed to study periodic structures, the method has two advantages when analysing the mesoscopic unit cell. First, it speeds up the calculation since only a small modal basis is retained, which is very interesting when the unit cell becomes complex. Second, the selection of the local modes can show the influences of the local dynamics of the unit cell on the global behaviours of the whole structures. However, when analysing the whole structure, the identical matrices of unit cells are assembled together. It may become time-consuming when the unit cells are numerous. On the other side, WFEM makes full use of the periodicity of the structures since only one unit cell needs to be modelled, and the displacement of the other cells are obtained by transfer relations. The wave amplitudes between the unit cells are related using simply the wavenumber $k$. However, the size of the transfer matrices can be large when all the internal DOFs of the unit cell are conserved. Moreover, matrices ill-conditioning problems may occur in case of internal DOFs dynamic condensation.

The proposed method in this thesis combines the advantages of CMS and WFEM. Component mode technique is used to model the mesoscopic scale of the unit cell. Once the dynamics of the unit cell is captured, the WFEM is used to study the global behaviours of the macroscopic structures. The proposed method is referred henceforth as "CWFEM" for "Condensed

Wave Finite Element Method". The combination of two methods is assured by wave-mode duality. It allows, when passing from a unit cell to the whole structure, to alternate from the modal description to wave description. The wave-mode duality can also be interpreted by the fact that the two expressions in Eq. (1.66) and Eq. (1.67) describe both the vibrations of the system. It is just two different basis on which displacements are projected.

### 1.5.4 At bounding frequency of stop band: stationary wave / cell mode

It is well known that modes correspond to stationary waves under certain boundary conditions. In Mead [1975a,b], he has studied the relationship between the bounding frequencies of stop band of one-dimensional periodic structures and the nature frequencies of its symmetric unit cell. He concluded that in mono-coupled structures [Mead, 1975b], the bounding frequencies of stop bands are identical with the natural frequencies of a symmetric unit cell with its ends either free or fixed. For multi-coupled structures [Mead, 1975a], the bounding frequencies of stop bands are identical with the natural frequencies of a symmetric unit cell with the two different types of coupling DOFs appropriately locked or free. When the element vibrates in a symmetric mode, type I coupling DOFs have the same sign and magnitude, whereas the type II coupling DOFs have opposite signs and equal magnitudes. In antisymmetric modes, the type I DOFs have opposite signs, whereas the type II DOFs have the same signs. In this thesis, we use the following ways to distinguish type I coupling DOFs from type II DOFs: Type I DOFs consist of orthogonal projection of displacement vectors onto the symmetric plane, and orthogonal projection of rotation vectors onto the normal of the symmetric plane. Type II DOFs consist of orthogonal projection of rotation vectors onto the symmetric plane, and orthogonal projection of displacement vectors onto the normal of the symmetric plan.

In chapter 3, the equivalence found by Mead is extended to 2D periodic beam grid. The boundary conditions of a double symmetrical unit cell are found, under which the natural frequencies of the unit cell is equivalent with the bounding frequencies of stop band. For periodic structures where a symmetrical unit cell cannot be found, the Von Karman boundary condition [Brillouin, 1953] of two unit cells (1D) or four unit cells (2D) should be applied.

### 1.5.5 Calculation of modal density based on propagation characteristics

The modal parameters of 1D periodic structures can be related to certain properties of the dispersion curves. While in 2D periodic structures, the parameters are related to slowness surfaces. For a finite 2D periodic structure with sufficient large number of unit cells, its modal density can be derived easily once the slowness surfaces are known. Langley [1994] demonstrated that one needs only to compute the area of the slowness surfaces lying below the frequency $\omega$

so that

$$n(\omega) = \frac{\partial N}{\partial \omega}, \text{where} \quad N(\omega) = \frac{N_x N_y L_x L_y}{4\pi^2} \sum_n \int_{-\pi}^{\pi} H(\omega - \Omega_n(k_x, k_y)) dk_x dk_y \tag{1.68}$$

where $N_x$ and $N_y$ is the number of unit cells in the $x$- and $y$- directions. $H$ is the Heaviside step function with $H(x < 0) = 0, H(x > 0) = 1$. The summation $n$ in Eq. (1.68) runs over the slowness surfaces.

Cremer & Heckl [2005] have shown that a number of results concerning the response of a general system to harmonic point loading may be expressed very simply in terms of the modal density. Many of the qualitative aspects of the response, such as amplitude of the response or the input power may be deduced from a knowledge of the modal density.

## 1.6 Conclusion

The literature survey presented in this chapter was guided on two aspects: the investigations on periodic structures and MOR techniques. A historical review of the studies on periodic structures and phononic materials was given at the beginning of this chapter. Numerous methods have been developed during these studies. Among them, the plane-wave expansion method, transfer matrix method, wave finite element method and several homogenization methods were explained. As for MOR techniques, two mode-based MOR methods and two wave-based MOR methods were developed in detail.

The second part of this chapter described the proposed wave and modal coupled method, referred as CWFEM in this thesis. The unique feature of the proposed CWFEM is the combination of the advantages of the modal approach and wave approach. The modal description is applied on mesoscopic scale of the unit cell while the wave description is employed on macroscopic scale of the structures. The equivalence between the two descriptions, known as wave-mode duality as well as the terminology concerning the wave description is clarified. The formulation to compute modal density from the slowness surfaces is given at the end of this chapter.

# Chapter 2

# Wave finite element method based on reduced model for complex one-dimensional periodic structures

## 2.1 Introduction

In this chapter, the proposed method CWFEM (Condensed Wave Finite Element Method) is developed to study complex one-dimensional (1D) periodic structures. The formulation of the method is given to calculate the dispersion relation for free wave propagation as well as the forced responses. The effectiveness of the proposed method is illustrated via both a binary circular beam and a binary thin-walled beam including warping effect using finely meshed solid elements.

## 2.2 The formulation of proposed "CWFEM" on 1D periodic structures

The method begins with establishing the equation of motion of the unit cell for free vibration. The mass and stiffness matrices $\mathbf{M}$ and $\mathbf{K}$ can be extracted from conventional FE packages.

$$\begin{bmatrix} \tilde{\mathbf{M}}_{\mathtt{LL}} & \tilde{\mathbf{M}}_{\mathtt{LR}} & \tilde{\mathbf{M}}_{\mathtt{LI}} \\ \tilde{\mathbf{M}}_{\mathtt{RL}} & \tilde{\mathbf{M}}_{\mathtt{RR}} & \tilde{\mathbf{M}}_{\mathtt{RI}} \\ \tilde{\mathbf{M}}_{\mathtt{IL}} & \tilde{\mathbf{M}}_{\mathtt{IR}} & \tilde{\mathbf{M}}_{\mathtt{II}} \end{bmatrix} \begin{pmatrix} \ddot{\mathbf{q}}_{\mathtt{L}} \\ \ddot{\mathbf{q}}_{\mathtt{R}} \\ \ddot{\mathbf{q}}_{\mathtt{I}} \end{pmatrix} + \begin{bmatrix} \tilde{\mathbf{K}}_{\mathtt{LL}} & \tilde{\mathbf{K}}_{\mathtt{LR}} & \tilde{\mathbf{K}}_{\mathtt{LI}} \\ \tilde{\mathbf{K}}_{\mathtt{RL}} & \tilde{\mathbf{K}}_{\mathtt{RR}} & \tilde{\mathbf{K}}_{\mathtt{RI}} \\ \tilde{\mathbf{K}}_{\mathtt{IL}} & \tilde{\mathbf{K}}_{\mathtt{IR}} & \tilde{\mathbf{K}}_{\mathtt{II}} \end{bmatrix} \begin{pmatrix} \mathbf{q}_{\mathtt{L}} \\ \mathbf{q}_{\mathtt{R}} \\ \mathbf{q}_{\mathtt{I}} \end{pmatrix} = \begin{pmatrix} \tilde{\mathbf{F}}_{\mathtt{L}} \\ \tilde{\mathbf{F}}_{\mathtt{R}} \\ \mathbf{0} \end{pmatrix} \tag{2.1}$$

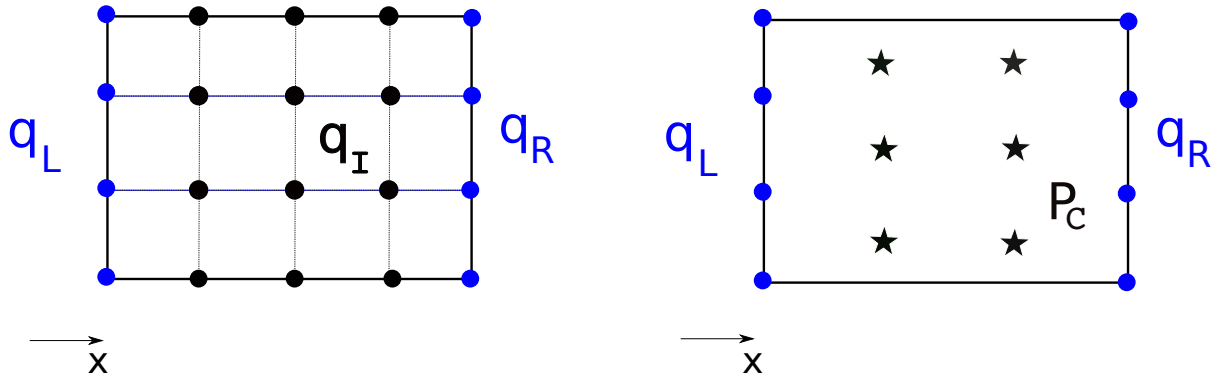


(a) Full model with physical internal DOFs $\mathbf{q}_{\mathtt{I}}$ (b) Reduced model with modal internal DOFs $\mathbf{P}_{\mathtt{C}}$

Figure 2.1: MOR on the unit cell of 1D periodic structure (propagation in the $x$- direction)

where "$\sim$" represents the matrix of the full model before reduction. Coordinates $\mathbf{q}_{\mathtt{R}}$, $\mathbf{q}_{\mathtt{L}}$, $\mathbf{q}_{\mathtt{I}}$ represent the physical DOFs of the left boundary, right boundary and internal nodes, as shown in Fig 2.1(a). The size of the $\mathbf{q}_{\mathtt{L}}$ and $\mathbf{q}_{\mathtt{R}}$ are both $n$, while the one of $\mathbf{q}_{\mathtt{I}}$ is of $n_{\mathtt{I}}$.

### 2.2.1 Model order reduction on the unit cell

The fixed interface component mode synthesis, known as the Craig-Bampton method, is applied to carry out the MOR on the unit cell. Compared to other reduction methods, such as the free interface method or the branch mode method, Craig-Bampton method is employed because it is more straightforward with the boundary DOFs expressed using physical coordinates.

The physical DOFs $\mathbf{q}_{\mathtt{I}}$ are then reformulated to a reduced modal basis of modal DOFs, with generalized coordinate $\mathbf{P}_{\mathtt{C}}$, the size of which is $n_{\mathtt{c}}$. The MOR on the unit cell is illustrated in Fig. 2.1. Then the Craig-Bampton hybrid coordinates are related to the physical coordinates using matrix $\mathbf{B}$:

$$((\mathbf{q}_{\mathtt{L}})^{\mathtt{T}}(\mathbf{q}_{\mathtt{R}})^{\mathtt{T}}(\mathbf{q}_{\mathtt{I}})^{\mathtt{T}})^{\mathtt{T}} = \mathbf{B}((\mathbf{q}_{\mathtt{L}})^{\mathtt{T}}(\mathbf{q}_{\mathtt{R}})^{\mathtt{T}}(\mathbf{P}_{\mathtt{C}})^{\mathtt{T}})^{\mathtt{T}} \tag{2.2}$$

with

$$\mathbf{B} = \begin{bmatrix} \mathbf{I_n} & \mathbf{0} & \mathbf{0} \\ \mathbf{0} & \mathbf{I_n} & \mathbf{0} \\ \mathbf{\Psi}_{\mathtt{L}} & \mathbf{\Psi}_{\mathtt{R}} & \mathbf{\Psi}_{\mathtt{C}} \end{bmatrix} \tag{2.3}$$

$[\mathbf{\Psi}_{\mathtt{L}} \quad \mathbf{\Psi}_{\mathtt{R}}]$ represents the constraint modes with

$$\mathbf{\Psi}_{\mathtt{L}} = -\tilde{\mathbf{K}}_{\mathtt{II}}^{-1}\tilde{\mathbf{K}}_{\mathtt{IL}} \quad , \quad \mathbf{\Psi}_{\mathtt{R}} = -\tilde{\mathbf{K}}_{\mathtt{II}}^{-1}\tilde{\mathbf{K}}_{\mathtt{IR}} \tag{2.4}$$

Fixed interface modes $\mathbf{\Psi}_{\mathtt{I}}$ are calculated with $\mathbf{q}_{\mathtt{L}} = \mathbf{q}_{\mathtt{R}} = \mathbf{0}$

$$[\tilde{\mathbf{K}}_{\mathtt{II}} - \omega_0^2\tilde{\mathbf{M}}_{\mathtt{II}}]\mathbf{\Psi}_{\mathtt{I}} = 0 \tag{2.5}$$

Matrix $\mathbf{\Psi}_{\mathtt{C}}$ is a reduced basis in $\mathbf{\Psi}_{\mathtt{I}}$ with $n_{\mathtt{I}}$ rows and $n_{\mathtt{c}}$ columns. The selection of $\mathbf{\Psi}_{\mathtt{C}}$ will be discussed via a converge study in the numerical example later. Then the equation of motion of the reduced model can be written into the following form:

$$\begin{bmatrix} \mathbf{M}^*_{\mathtt{LL}} & \mathbf{M}^*_{\mathtt{LR}} & \mathbf{M}^*_{\mathtt{LC}} \\ \mathbf{M}^*_{\mathtt{RL}} & \mathbf{M}_{\mathtt{RR}} & \mathbf{M}^*_{\mathtt{RR}} \\ \mathbf{M}^*_{\mathtt{CL}} & \mathbf{M}^*_{\mathtt{CR}} & \mathbf{M}^*_{\mathtt{CC}} \end{bmatrix} \begin{pmatrix} \ddot{\mathbf{q}}_{\mathtt{L}} \\ \ddot{\mathbf{q}}_{\mathtt{R}} \\ \ddot{\mathbf{P}}_{\mathtt{C}} \end{pmatrix} + \begin{bmatrix} \mathbf{K}^*_{\mathtt{LL}} & \mathbf{K}^*_{\mathtt{LR}} & \mathbf{K}^*_{\mathtt{LC}} \\ \mathbf{K}^*_{\mathtt{RL}} & \mathbf{K}^*_{\mathtt{RR}} & \mathbf{K}^*_{\mathtt{RR}} \\ \mathbf{K}^*_{\mathtt{CL}} & \mathbf{K}^*_{\mathtt{CR}} & \mathbf{K}^*_{\mathtt{CC}} \end{bmatrix} \begin{pmatrix} \mathbf{q}_{\mathtt{L}} \\ \mathbf{q}_{\mathtt{R}} \\ \mathbf{P}_{\mathtt{C}} \end{pmatrix} = \begin{pmatrix} \mathbf{F}_{\mathtt{L}} \\ \mathbf{F}_{\mathtt{R}} \\ \mathbf{0} \end{pmatrix} \tag{2.6}$$

The viscous or structural damping is not included. When applying WFEM on homogeous waveguides, it is typical to use complex dynamic stiffness matrix to include damping [Mace & Manconi, 2008]. In this chapter, damping is not considered in the model of periodic waveguides. Damping may precipitate the wave attenuations. Since in the first place attention is focused on the attenuation related to the periodicity of the waveguides. The presence of damping makes it difficult to define the stop band of propagation and make the wave attenuation phenomena more complicated.

The new mass matrix as well as the stiffness matrix can then be written in the following manner:

$$\begin{bmatrix} \mathbf{M}^*_{\mathtt{LL}} & \mathbf{M}^*_{\mathtt{LR}} & \mathbf{M}^*_{\mathtt{LC}} \\ \mathbf{M}^*_{\mathtt{RL}} & \mathbf{M}^*_{\mathtt{RR}} & \mathbf{M}^*_{\mathtt{RR}} \\ \mathbf{M}^*_{\mathtt{CL}} & \mathbf{M}^*_{\mathtt{CR}} & \mathbf{M}^*_{\mathtt{CC}} \end{bmatrix} = \mathbf{B}^{\mathtt{T}} \begin{bmatrix} \tilde{\mathbf{M}}_{\mathtt{LL}} & \tilde{\mathbf{M}}_{\mathtt{LR}} & \tilde{\mathbf{M}}_{\mathtt{LI}} \\ \tilde{\mathbf{M}}_{\mathtt{RL}} & \tilde{\mathbf{M}}_{\mathtt{RR}} & \tilde{\mathbf{M}}_{\mathtt{RI}} \\ \tilde{\mathbf{M}}_{\mathtt{IL}} & \tilde{\mathbf{M}}_{\mathtt{IR}} & \tilde{\mathbf{M}}_{\mathtt{II}} \end{bmatrix} \mathbf{B} \tag{2.7}$$

The generalized force remains the same value as before:

$$\begin{pmatrix} \mathbf{F}_{\mathtt{L}} \\ \mathbf{F}_{\mathtt{R}} \\ \mathbf{0} \end{pmatrix} = \mathbf{B}^{\mathtt{T}} \begin{pmatrix} \tilde{\mathbf{F}}_{\mathtt{L}} \\ \tilde{\mathbf{F}}_{\mathtt{R}} \\ \mathbf{0} \end{pmatrix} = \begin{pmatrix} \tilde{\mathbf{F}}_{\mathtt{L}} \\ \tilde{\mathbf{F}}_{\mathtt{R}} \\ \mathbf{0} \end{pmatrix} \tag{2.8}$$

Assuming harmonic response, the equation can be written with the dynamic stiffness matrix $\mathbf{D}^* = \mathbf{K}^* - \omega^2 \mathbf{M}^*$.

$$\begin{bmatrix} \mathbf{D}^*_{\mathtt{LL}} & \mathbf{D}^*_{\mathtt{LR}} & \mathbf{D}^*_{\mathtt{LC}} \\ \mathbf{D}^*_{\mathtt{RL}} & \mathbf{D}^*_{\mathtt{RR}} & \mathbf{D}^*_{\mathtt{RC}} \\ \mathbf{D}^*_{\mathtt{CL}} & \mathbf{D}^*_{\mathtt{CR}} & \mathbf{D}^*_{\mathtt{CC}} \end{bmatrix} \begin{pmatrix} \mathbf{q}_{\mathtt{L}} \\ \mathbf{q}_{\mathtt{R}} \\ \mathbf{P}_{\mathtt{C}} \end{pmatrix} = \begin{pmatrix} \mathbf{F}_{\mathtt{L}} \\ \mathbf{F}_{\mathtt{R}} \\ \mathbf{0} \end{pmatrix} \tag{2.9}$$

From the third line of Eq. (2.9), internal DOFs can be removed using dynamic condensation. The Eq. (2.9) becomes

$$\begin{bmatrix} \mathbf{D}_{\mathtt{LL}} & \mathbf{D}_{\mathtt{LR}} \\ \mathbf{D}_{\mathtt{RL}} & \mathbf{D}_{\mathtt{RR}} \end{bmatrix} \begin{pmatrix} \mathbf{q}_{\mathtt{L}} \\ \mathbf{q}_{\mathtt{R}} \end{pmatrix} = \begin{pmatrix} \mathbf{F}_{\mathtt{L}} \\ \mathbf{F}_{\mathtt{R}} \end{pmatrix} \tag{2.10}$$

where

$$\begin{aligned} \mathbf{D}_{\mathtt{LL}} &= \mathbf{D}^*_{\mathtt{LL}} - \mathbf{D}^*_{\mathtt{LC}} (\mathbf{D}^*_{\mathtt{CC}})^{-1} \mathbf{D}^*_{\mathtt{CL}}, \\ \mathbf{D}_{\mathtt{LR}} &= \mathbf{D}^*_{\mathtt{LR}} - \mathbf{D}^*_{\mathtt{LC}} (\mathbf{D}^*_{\mathtt{CC}})^{-1} \mathbf{D}^*_{\mathtt{CR}}, \\ \mathbf{D}_{\mathtt{RL}} &= \mathbf{D}^*_{\mathtt{RL}} - \mathbf{D}^*_{\mathtt{RC}} (\mathbf{D}^*_{\mathtt{CC}})^{-1} \mathbf{D}^*_{\mathtt{CL}}, \\ \mathbf{D}_{\mathtt{RR}} &= \mathbf{D}^*_{\mathtt{RR}} - \mathbf{D}^*_{\mathtt{RC}} (\mathbf{D}^*_{\mathtt{CC}})^{-1} \mathbf{D}^*_{\mathtt{CR}} \end{aligned} \tag{2.11}$$

Vectors in $\mathbf{\Psi}_{\mathtt{C}}$ are normalized with respect to the modal mass matrix, i.e., $[\mathbf{\Psi}_{\mathtt{C}}]^{\mathtt{T}}[\tilde{\mathbf{M}}_{\mathtt{II}}][\mathbf{\Psi}_{\mathtt{C}}] = \mathbf{I}_{\mathtt{n_c}}$. The modal stiffness matrix is $[\mathbf{\Psi}_{\mathtt{C}}]^{\mathtt{T}}[\tilde{\mathbf{K}}_{\mathtt{II}}][\mathbf{\Psi}_{\mathtt{C}}] = [\mathbf{\Omega}^2]$. So we have $\mathbf{D}^*_{\mathtt{CC}} = \mathbf{K}^*_{\mathtt{CC}} - \omega^2\mathbf{M}^*_{\mathtt{CC}} = \mathbf{\Omega}^2 - \omega^2\mathbf{I}_{\mathtt{n_c}}$, which is a diagonal matrix and of smaller size than $\mathbf{D}^*_{\mathtt{II}} = \mathbf{K}^*_{\mathtt{II}} - \omega^2\mathbf{M}^*_{\mathtt{II}}$. $\mathbf{D}^*_{\mathtt{CC}}$ is much easier to be inverted. The poor conditioned due to the inversion of $\mathbf{D}^*_{\mathtt{II}}$ can be avoided.

### 2.2.2 Application of WFEM on reduced model of the unit cell-CWFEM

After dynamic condensation of the internal modal DOFs, the equation of motion of the unit cell becomes the same as the classical WFEM in direct form. For the unit cell $\mathtt{k}$, we have

$$\mathbf{u}^{(\mathtt{k})}_{\mathtt{R}} = \mathbf{S}\mathbf{u}^{(\mathtt{k})}_{\mathtt{L}}, \tag{2.12}$$

remind that $\mathbf{u}^{(\mathtt{k})}_{\mathtt{L}} = ((\mathbf{q}^{(\mathtt{k})}_{\mathtt{L}})^{\mathtt{T}}(-\mathbf{F}^{(\mathtt{k})}_{\mathtt{L}})^{\mathtt{T}})^{\mathtt{T}}$ and $\mathbf{u}^{(\mathtt{k})}_{\mathtt{R}} = ((\mathbf{q}^{(\mathtt{k})}_{\mathtt{R}})^{\mathtt{T}}(\mathbf{F}^{(\mathtt{k})}_{\mathtt{R}})^{\mathtt{T}})^{\mathtt{T}}$ represent the left and right state vectors for the unit cell $\mathtt{k}$. The expression of $\mathbf{S}$ can be found in Eq. 1.18. The wave basis and wavenumbers are associated to the eigen solution of the following problem:

$$\mathbf{S}\mathbf{\Phi}_i = \lambda_i\mathbf{\Phi}_i \quad , \quad |\mathbf{S} - \lambda_i\mathbf{I_{2}}_n| = \mathbf{0}. \tag{2.13}$$

where $\mathbf{I_{2n}}$ represents the identity matrix of size $2n$. However, for large numbers of DOFs, typically for 2D cross-sections, direct application of numerical solvers can lead to difficulties because $\mathbf{S}$ may be poor conditioned [Mace *et al.*, 2005]. So the eigenvalue problem can be reformulated as follows [Inquiete, 2008]:

$$[\mathbf{N}]\mathbf{\Phi}' = \lambda[\mathbf{L}]\mathbf{\Phi}', \tag{2.14}$$

where

$$\mathbf{\Phi}' = \begin{pmatrix} \mathbf{q}_{\mathtt{L}} \\ \mathbf{q}_{\mathtt{R}} \end{pmatrix} \tag{2.15}$$

and

$$[\mathbf{N}] = \begin{bmatrix} \mathbf{0} & \mathbf{I_n} \\ \mathbf{D}_{\mathtt{RL}} & \mathbf{D}_{\mathtt{RR}} \end{bmatrix} \quad , [\mathbf{L}] = \begin{bmatrix} \mathbf{I_n} & \mathbf{0} \\ -\mathbf{D}_{\mathtt{LL}} & -\mathbf{D}_{\mathtt{LR}} \end{bmatrix} \tag{2.16}$$

For the state vector $\mathbf{\Phi}$, it is related using matrix $\mathbf{L}$.

$$\mathbf{\Phi} = \begin{pmatrix} \mathbf{q}_{\mathtt{L}} \\ -\mathbf{F}_{\mathtt{L}} \end{pmatrix} = \mathbf{L}\begin{pmatrix} \mathbf{q}_{\mathtt{L}} \\ \mathbf{q}_{\mathtt{R}} \end{pmatrix} = \mathbf{L}\mathbf{\Phi}' \tag{2.17}$$

Other formulations were also suggested, such as the eigenvalue problem in terms of $(\lambda + 1/\lambda)$ proposed by Zhong [Zhong & Williams, 1995].

The eigenvalues $\lambda_i$ and wavenumbers $k_i$ are linked through the relation $\lambda_i = e^{-jk_i d_x}$, while $d_x$ denotes the length of the unit cell in propagation direction $x$-axis and $j^2 = -1$. The direction

of the phase velocity of the corresponding waves can be distinguished in the following manner: If $|\lambda_i| < 1$, then the phase propagates in the positive direction. If $|\lambda_i| > 1$, the phase propagates in the negative direction. For the propagative waves in the passing band with $|\lambda_i| = 1$, the propagation direction can be identified using the sign of the $\Re(k_i)$, where $\Re(k_i)$ represents the real part of the complex wavenumber $k_i$. $\Re(k_i) > 0$ indicates that the phase propagates in the positive $x$ direction, $\Re(k_i) < 0$ the phase propagates in the negative $x$ direction. The matrix $\mathbf{\Phi}$ of the eigenvectors can be written as follows:

$$\mathbf{\Phi} = \begin{bmatrix} \mathbf{\Phi}_{\mathbf{q}}^{+} & \mathbf{\Phi}_{\mathbf{q}}^{-} \\ \mathbf{\Phi}_{\mathbf{F}}^{+} & \mathbf{\Phi}_{\mathbf{F}}^{-} \end{bmatrix}, \tag{2.18}$$

where the subscripts $\mathbf{q}$ and $\mathbf{F}$ refer to the components which corresponds to the displacements and the forces, respectively; $((\mathbf{\Phi}_{\mathbf{q}}^{+})^{\mathtt{T}}(\mathbf{\Phi}_{\mathbf{F}}^{+})^{\mathtt{T}})^{\mathtt{T}}$ stands for the wave basis vectors which propagate in the positive direction, while $((\mathbf{\Phi}_{\mathbf{q}}^{-})^{\mathtt{T}}(\mathbf{\Phi}_{\mathbf{F}}^{-})^{\mathtt{T}})^{\mathtt{T}}$ stands for the wave basis vectors which propagate in the negative direction. Finally, state vector $\mathbf{u}_{\mathtt{L}}^{(\mathtt{k})}$ and $\mathbf{u}_{\mathtt{R}}^{(\mathtt{k})}$ of any cell $\mathtt{k}$ can be expressed using eigenvectors $\{\mathbf{\Phi}_i\}_{i=1,\ldots,2n}$ [Zhong & Williams, 1995]:

$$\mathbf{u}_{\mathtt{L}}^{(\mathtt{k})} = \mathbf{\Phi}\mathbf{Q}^{(\mathtt{k})} \quad , \quad \mathbf{u}_{\mathtt{R}}^{(\mathtt{k})} = \mathbf{\Phi}\mathbf{Q}^{(\mathtt{k}+1)} \quad \forall \mathtt{k} \in \{1, \ldots, \mathtt{N}\}. \tag{2.19}$$

The analysis of the dynamic response consists of evaluating a set of amplitudes associated with positive and negative going modes.

$$\mathbf{Q}^{(\mathtt{k})} = \begin{pmatrix} \mathbf{Q}^{+(\mathtt{k})} \\ \mathbf{Q}^{-(\mathtt{k})} \end{pmatrix}. \tag{2.20}$$

### 2.2.3 The forced response of the structure by CWFEM

The forced-WFEM formulation are widely employed to study the stationary response of continuous structures [Mencik & Ichchou, 2007; Renno & Mace, 2010; Waki *et al.*, 2009]. The formulations of forced-CWFEM can be deduced in a similar way.

According to the coupling relations between two consecutive cells $\mathtt{k}$ and $\mathtt{k}-1$ ($\mathtt{k} \in \{2, \ldots, \mathtt{N}\}$), $\mathbf{q}_L^{(\mathtt{k})} = \mathbf{q}_R^{(\mathtt{k}-1)}$ and $-\mathbf{F}_L^{(\mathtt{k})} = \mathbf{F}_R^{(\mathtt{k}-1)}$, the following relation can be found:

$$\mathbf{u}_L^{(\mathtt{k})} = \mathbf{u}_R^{(\mathtt{k}-1)} \quad \forall \mathtt{k} \in \{2, \ldots, N\} \tag{2.21}$$

which conducts to

$$\mathbf{u}_L^{(\mathtt{k})} = \mathbf{S}\mathbf{u}_L^{(\mathtt{k}-1)} \quad \forall \mathtt{k} \in \{2, \ldots, N\} \tag{2.22}$$

Eq. (2.22) leads to:

$$\mathbf{u}_L^{(\mathtt{k})} = \mathbf{S}^{k-1}\mathbf{u}_L^{(1)} \quad \forall \mathtt{k} \in \{1, \ldots, N\} \tag{2.23}$$

In addition to the relation in cell N:

$$\mathbf{u}_R^{(N)} = \mathbf{S}\mathbf{u}_L^{(N)} \tag{2.24}$$

we have

$$\mathbf{u}_R^{(N)} = \mathbf{S}^N\mathbf{u}_L^{(1)} \tag{2.25}$$

where $\mathbf{S}^0 = \mathbf{I}_{2n}$. Eqs. (2.23) and (2.25) are projected on the wave basis $\{\mathbf{\Phi}_i\}_i$ considering Eq. (2.19). Since it has been assumed that matrix eigenvectors $\{\mathbf{\Phi_i}\}_\mathbf{i}$ are linearly independent, so $\mathbf{\Phi}$ is invertible, which leads to:

$$\mathbf{Q}^{(\mathtt{k})} = \mathbf{\Phi}^{-1}\mathbf{S}^{\mathtt{k}-1}\mathbf{\Phi}\mathbf{Q}^{(1)} \quad \forall \mathtt{k} \in \{1, \ldots, N+1\} \tag{2.26}$$

that is (cf. Eq. (2.13))

$$\mathbf{Q}^{(\mathtt{k})} = \begin{bmatrix} \mathbf{\Lambda} & \mathbf{0} \\ \mathbf{0} & \mathbf{\Lambda^{-1}} \end{bmatrix}^{\mathtt{k}-1} \mathbf{Q}^{(1)} \quad \forall \mathtt{k} \in \{1, \ldots, N+1\} \tag{2.27}$$

where $\mathbf{\Lambda}$ stands for the $(n \times n)$ diagonal eigenvalue matrix for wave modes propagating in $x$ positive direction, expressed by Eq. (2.28).

$$\mathbf{\Lambda} = \begin{bmatrix} \lambda_1 & 0 & \ldots & 0 \\ 0 & \lambda_2 & \ldots & 0 \\ \vdots & \vdots & \ddots & \vdots \\ 0 & 0 & \ldots & \lambda_n \end{bmatrix} \tag{2.28}$$

For the classical Neumann and Dirichlet boundary conditions can be expressed as follows:

$$[\mathbf{0} \mid \mathbf{I}]\,\mathbf{u} = \mathbf{F} \qquad \text{(Neumann)} \tag{2.29a}$$

$$[\mathbf{I} \mid \mathbf{0}]\,\mathbf{u} = \mathbf{q} \qquad \text{(Dirichlet)} \tag{2.29b}$$

The left side of cell 1 satisfies Neumann boundary condition while the right side of cell N satisfies Dirichlet boundary condition. Then the two boundary conditions can be rewritten via the projection of the state vector $\mathbf{u}$ onto the wave basis:

$$\mathbf{\Phi}_\mathbf{F}^+\mathbf{Q}^{+(1)} + \mathbf{\Phi}_\mathbf{F}^-\mathbf{Q}^{-(1)} = \mathbf{F}_0 \tag{2.30a}$$

$$\mathbf{\Phi}_\mathbf{q}^+\mathbf{Q}^{+(\mathtt{N}+1)} + \mathbf{\Phi}_\mathbf{q}^-\mathbf{Q}^{-(\mathtt{N}+1)} = \mathbf{q}_{\mathtt{N}+1} \tag{2.30b}$$

Using Eq. (2.27), the above equations can be simplified as:

$$\mathbf{\Phi}_\mathbf{F}^+\mathbf{Q}^{+(1)} + \mathbf{\Phi}_\mathbf{F}^-\mathbf{Q}^{-(1)} = \mathbf{F}_0 \tag{2.31a}$$

$$\mathbf{\Phi}_\mathbf{q}^+\mathbf{\Lambda}^\mathbf{N}\mathbf{Q}^{+(1)} + \mathbf{\Phi}_\mathbf{q}^-\mathbf{\Lambda}^{-\mathbf{N}}\mathbf{Q}^{-(1)} = \mathbf{q}_{\mathtt{N}+1} \tag{2.31b}$$

then the amplitude of the positive going wave modes of the first cell can be deduced in the

following manner:

$$\begin{pmatrix} \mathbf{Q}^{+(1)} \\ \mathbf{Q}^{-(1)} \end{pmatrix} = \begin{bmatrix} \mathbf{\Phi}_{\mathbf{F}}^{+} & \mathbf{\Phi}_{\mathbf{F}}^{-} \\ \mathbf{\Phi}_{\mathbf{q}}^{+}\mathbf{\Lambda}^{\mathbf{N}} & \mathbf{\Phi}_{\mathbf{q}}^{-}\mathbf{\Lambda}^{-\mathbf{N}} \end{bmatrix}^{-1} \begin{pmatrix} \mathbf{F}_{0} \\ \mathbf{q}_{\mathtt{N}+1} \end{pmatrix} \tag{2.32}$$

Once the amplitude of the wave modes $\mathbf{Q}^{(1)}$ is obtained, the wave amplitude as well as physical response at the boundaries of all unit cells can be obtained using Eqs. (2.27) and (2.19). As for the internal nodes of unit cell $k$, the displacement can be deduced based on Eq. (3.2) and Eq. (2.3):

$$\mathbf{q}_{\mathtt{I}}^{(\mathtt{k})} = \mathbf{\Psi}_{\mathtt{L}}\mathbf{q}_{\mathtt{L}}^{(\mathtt{k})} + \mathbf{\Psi}_{\mathtt{R}}\mathbf{q}_{\mathtt{R}}^{(\mathtt{k})} + \mathbf{\Psi}_{\mathtt{C}}\mathbf{P}_{\mathtt{C}}^{(\mathtt{k})} \tag{2.33}$$

The constraint modes of the unit cell $[\mathbf{\Psi_L} \quad \mathbf{\Psi_R}]$ and truncated fixed boundary mode $\mathbf{\Psi_C}$ are shown in Eq. (2.4) and Eq. (2.5). As for modal coordinates $\mathbf{P}_{\mathtt{C}}$, it can be deduced from Eq. (2.9) that

$$\mathbf{P}_{\mathtt{C}} = -(\mathbf{D}_{\mathtt{CC}}^{*})^{-1}(\mathbf{D}_{\mathtt{CL}}^{*}\mathbf{q}_{\mathtt{L}} + \mathbf{D}_{\mathtt{CR}}^{*}\mathbf{q}_{\mathtt{R}}) \tag{2.34}$$

In this manner, the forced response of the all the nodes (internal and boundary) in finite waveguide can be determined. However, attention should be paid when inverting the matrix in Eq. (2.32) since it may be ill-conditioned. Alternative formulations to avoid numerical issue can be found in the reference [Waki *et al.*, 2009].

### 2.2.4 Stop band of periodic structures

The waves which occur in periodic media, known as Bloch waves [Kittel, 2004], have very unusual dispersion and attenuation characteristics compared to those in continuum media. The periodic waveguide, even a non-dissipative one, strongly attenuates waves on bands of the frequency spectrum known as stop bands [Bradley, 1991]. Noise control and vibration absorption techniques can be developed based on the stop bands of the periodic structures. As a result, the optimum design and parameter study of the stop band width have attracted a lot of interest among researchers [Olhoff *et al.*, 2012; Xiang & Shi, 2009; Xiao *et al.*, 2013; Yu *et al.*, 2009].

According to Mead, wave propagation can occur when $k_i$ is a real number [Mead, 1975a], since $\lambda_i + 1/\lambda_i = e^{-jk_i d_x} + e^{jk_i d_x} = 2\cos(k_i d_x)$, so in the pass bands we have:

$$-2 \leq \lambda_i + 1/\lambda_i \leq 2 \tag{2.35}$$

Therefore the pass bands are bounded by the frequencies at which $\lambda_i + 1/\lambda_i = \pm 2$, $\lambda_i = \pm 1$. So the stop bands can be calculated easily using the dynamic stiffness matrix. Since the left

state vector and the right state vector are related by $\lambda$, we have

$$\begin{pmatrix} \mathbf{q}_{\mathrm{R}}^{(\mathrm{k})} \\ \mathbf{F}_{\mathrm{R}}^{(\mathrm{k})} \end{pmatrix} = \lambda \begin{pmatrix} \mathbf{q}_{\mathrm{L}}^{(\mathrm{k})} \\ -\mathbf{F}_{\mathrm{L}}^{(\mathrm{k})} \end{pmatrix} \tag{2.36}$$

the Eq. (2.6) becomes:

$$\begin{bmatrix} \mathbf{D}_{\mathrm{LL}}^{*} & \mathbf{D}_{\mathrm{LR}}^{*} & \mathbf{D}_{\mathrm{LC}}^{*} \\ \mathbf{D}_{\mathrm{RL}}^{*} & \mathbf{D}_{\mathrm{RR}}^{*} & \mathbf{D}_{\mathrm{RC}}^{*} \\ \mathbf{D}_{\mathrm{CL}}^{*} & \mathbf{D}_{\mathrm{CR}}^{*} & \mathbf{D}_{\mathrm{CC}}^{*} \end{bmatrix} \begin{pmatrix} \mathbf{q}_{\mathrm{L}} \\ \lambda \mathbf{q}_{\mathrm{L}} \\ \mathbf{P}_{\mathrm{C}} \end{pmatrix} = \begin{pmatrix} \mathbf{F}_{\mathrm{L}} \\ -\lambda \mathbf{F}_{\mathrm{L}} \\ \mathbf{0} \end{pmatrix} \tag{2.37}$$

With $\lambda = 1$, the equation is reformulated to:

$$\begin{bmatrix} \mathbf{D}_{\mathrm{LL}}^{*} + \mathbf{D}_{\mathrm{LR}}^{*} + \mathbf{D}_{\mathrm{RL}}^{*} + \mathbf{D}_{\mathrm{RR}}^{*} & \mathbf{D}_{\mathrm{LC}}^{*} + \mathbf{D}_{\mathrm{RC}}^{*} \\ \mathbf{D}_{\mathrm{CR}}^{*} + \mathbf{D}_{\mathrm{CL}}^{*} & \mathbf{D}_{\mathrm{CC}}^{*} \end{bmatrix} \begin{pmatrix} \mathbf{q}_{\mathrm{L}} \\ \mathbf{P}_{\mathrm{C}} \end{pmatrix} = \begin{pmatrix} 0 \\ 0 \end{pmatrix} \tag{2.38}$$

To obtain the non-trivial solution, the determinant of the matrix should be zero. Note that $\mathbf{D}_{\mathrm{ij}}^{*} = \mathbf{K}_{\mathrm{ij}}^{*} - \omega^2 \mathbf{M}_{\mathrm{ij}}^{*}$, so the linear eigen problem can be solved and the eigenvalues $\omega^2$ can be calculated, which correspond to the bounding frequencies of the stop bands. Along with the bounding frequencies calculated by $\lambda = -1$, all the stop bands of the structure can be found using only the dynamic stiffness matrix of the reduced model.

## 2.3 Numerical examples and discussions

The proposed CWFEM is applied on three kinds of binary periodic beam in this section. The binary beam consists of a repetition of section A of length $l_1$ and section B of length $l_2$, as shown in Fig. 2.2. A symmetric unit cell is used in CWFEM. Section A and section B are

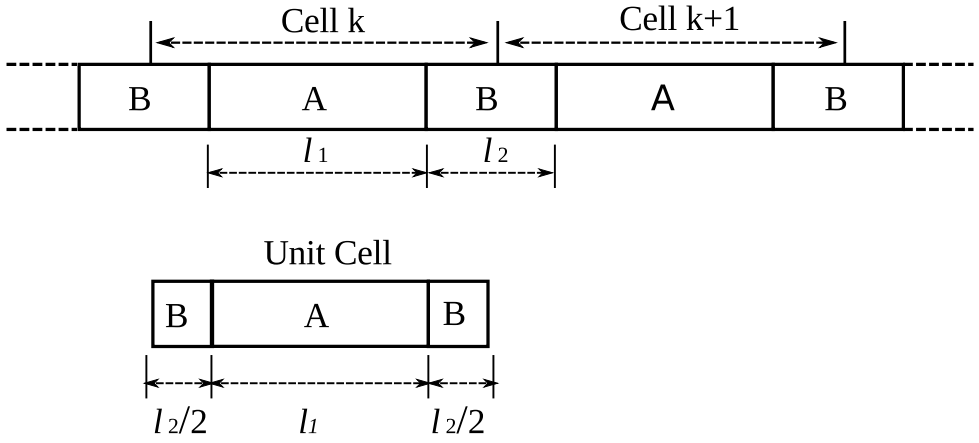


Figure 2.2: Binary periodic beam and its symmetric unit cell

of different materials, the materials used in this section can be found in Tab. 2.1. Firstly, the

| Materials | Young's Modulus E (Gpa) | Shear modulus G (Gpa) | Density $\rho\,(kg/m^3)$ |
|---|---|---|---|
| Epoxy | 4.35 | 1.59 | 1180 |
| Aluminium | 77.56 | 28.87 | 2730 |
| Steel | 210.6 | 81.0 | 7780 |

Table 2.1: Material proprieties

longitudinal waves and flexural waves in a circular beam are studied in 2.3.1 and 2.3.2. Subsequently, flexural-torsional coupled waves in a nonsymmetrical thin-walled beam is analysed in 2.3.3, where the beam is modelled using solid elements which take warping effect in consideration.

### 2.3.1 Longitudinal waves in binary periodic beam

First, CWFEM is used to study longitudinal waves in binary periodic beam with epoxy in section A and aluminium in section B. Both sections are circular with a radius of 6.44 cm, and the lengths $l_1$ and $l_2$ are both 1 m, then the period length $a = l_1 + l_2$ equals to 2 m. The unit cell is divided into 100 elements, so that each wavelength contains at least 10 elements in the frequency range up to 3 kHz. The results obtained by CWFEM is compared with the analytical solution of the wavenumber $k$ given by Tian *et al.* [2011]:

$$\cos(ak) = \cos(\omega t_1)\cos(\omega t_2) - (\frac{Z_1}{2Z_2} + \frac{Z_2}{2Z_1})\sin(\omega t_1)\sin(\omega t_2) \tag{2.39}$$

where $Z = \rho c$ is the characteristic acoustic impedance of a section, $c = \sqrt{E/\rho}$ is the wave velocity in the section, and $t_i = l_i/c$ is the time for the wave to pass through the section.

#### 2.3.1.1 The selection of the modes and the convergence

The convergence study of the reduced modal basis is carried out here. The frequency ranges of the stop bands are obtained with different reduced basis, using the formulation in 2.2.4.

$f_c$, the frequencies of the stop bands calculated by CWFEM, are compared with $f_0$, the frequencies obtained by classical WFEM. The relative errors listed in Tab. 2.2 equal to $\frac{|f_c - f_0|}{f_0}$. The analytical result $f_a$ is given as well, with the sum of the relative errors between the $f_0$ and $f_a$ equals to 0.5%. It can be seen from Tab. 2.2 that the frequencies $f_c$ converge rapidly with $n = f_{mode}/f_{max}$. Using a reduced basis with $n$=3 , a total relative error around 1% is obtained.

Table 2.2: The first four stop bands: relative error is compared with $f_0$

| Frequency of bounds stop bands | $f_c$ (Hz) by CWFEM With $n = f_{mode}/f_{max}$ | | | | | $f_0$ (Hz) by Classical WFEM | $f_a$ (Hz) Analytical result |
|---|---|---|---|---|---|---|---|
| | n=1 | n=1.5 | n=2 | n=2.5 | n=3 | | |
| First(L) | 372.4 | 372.4 | 372.4 | 372.4 | 372.4 | 372.4 | 372.4 |
| First(R) | 906.9 | 904.9 | 904.4 | 904.3 | 904.3 | 904.2 | 903.8 |
| Second(L) | 1087.6 | 1087.1 | 1086.7 | 1086.4 | 1086.3 | 1086.2 | 1085.7 |
| Second(R) | 1762.9 | 1762.9 | 1762.9 | 1762.9 | 1762.9 | 1762.9 | 1761.6 |
| Third(L) | 1963.1 | 1963.1 | 1963.1 | 1963.1 | 1963.1 | 1963.1 | 1961.2 |
| Third(R) | 2439.4 | 2410.9 | 2405.9 | 2404.7 | 2404.2 | 2403.1 | 2401.4 |
| Forth(L) | 2732.2 | 2732.2 | 2732.2 | 2732.2 | 2732.2 | 2732.2 | 2730.3 |
| Forth(R) | 2909.3 | 2895.5 | 2882.3 | 2877.0 | 2875.1 | 2872.6 | 2868.4 |
| Sum relative error | 2.9% | 1.2% | 0.5% | 0.24% | 0.1% | | |

#### 2.3.1.2 Dispersion relation of the longitudinal waves

The real part of wavenumber $k$, $\Re(k)$ represents the phase shift per unit length. While the imaginary part of $k$, $\Im(k)$ represents the attenuation per unit length. The dispersion relation is illustrated in Fig. 2.3, only the positive-going waves with $\Re(k) > 0$ are presented because the wavenumbers of the positive and negative-going waves are symmetric with respect to the $x$-axis. Several noteworthy characteristics of dispersion relation can be observed:

- At pass band frequencies, the wavenumber is real with $\Im(k) = 0$.
- At stop band frequencies, $\Im(k) \neq 0$, which is associated with the exponential attenuation of the wave.
- At stop band frequencies, $\Re(k)$ remains constant in the whole band, either $\Re(k) = 0$ or $\Re(k) = \pm\pi/d_x$. For $\Re(k) = \pm\pi/d_x$, the stop band are bounded with $\lambda = -1$, and associated with a single wavelength. As to $\Re(k) = 0$, the stop band frequencies are bounded with $\lambda = 1$ and are associated with non-oscillating and exponential attenuated waves.
- $\Re(k)$ is limited in the first Brillouin zone [Brillouin, 1953], which is between $[-\pi/d_x, \pi/d_x]$.

As shown in Fig. 2.3, there exists four stop bands between 0 Hz and 3 kHz, the same as those given in Tab. 2.2. The dispersion relation issued from CWFEM is compared to those calculated with the classical WFEM and analytical method. With a reduced modal basis with $f_{mode} \geq 3f_{max}$, CWFEM is able to predict the dispersion relation with high precision.

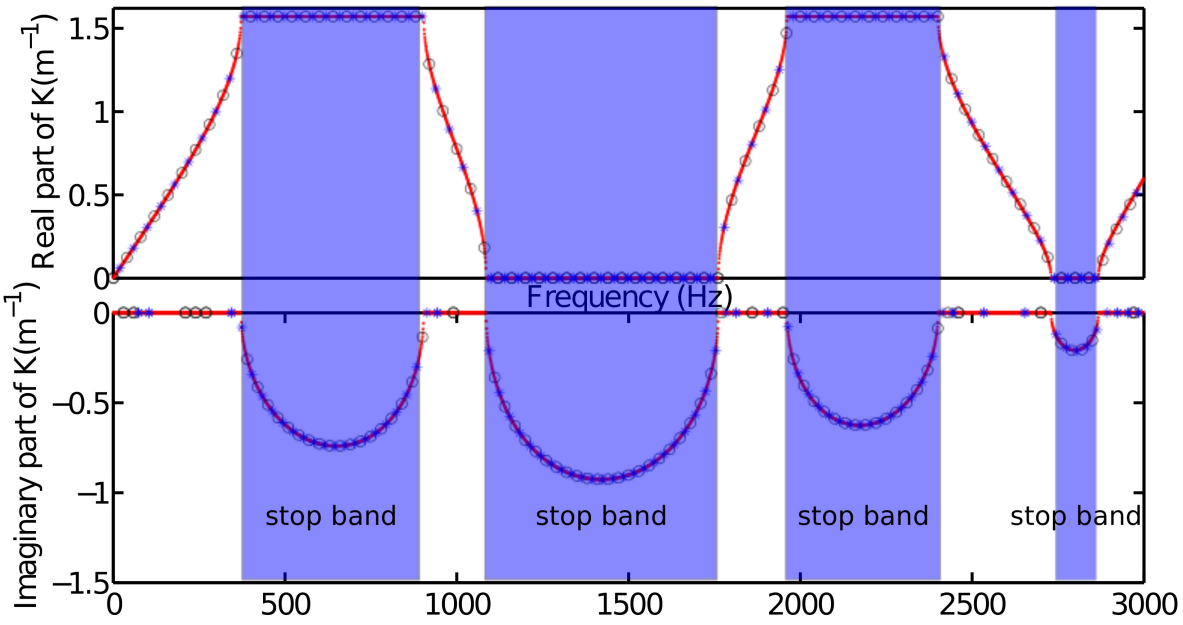


Figure 2.3: Dispersion relation for the longitudinal waves by different methods: Analytical (-), WFEM (o), CWFEM with $f_{mode} = 3f_{max}$(∗)

#### 2.3.1.3 Forced response of the beam

In the given formulation of forced-CWFEM in 2.2.3, the length of the waveguide is no longer infinite and should be specified as well as the boundary conditions. The beam consisting of 10 identical unit cells is clamped at one end and is subjected to harmonic axial loading on the other end.

The frequency response at the point of excitation is shown in Fig. 2.4 and a zoom between 2200 Hz and 3000 Hz is given in Fig. 2.5. It can be seen that the response via the forced-CWFEM corresponds quite well with the results by FEM. The size of the FE model is 1010, while the size of the model in CWFEM is 12, which leads to a significant decrease of computation time.

The peaks in the forced response correspond to the resonances at natural frequencies. The frequency ranges where no resonance occurs are identical with the stop bands determined in the dispersion relation. Here if boundary condition is changed from clamped to free, same frequency ranges without resonance are identified. The stop bands identified from the forced response function of a finite waveguides should be independent of the unit cells number and boundary condition.

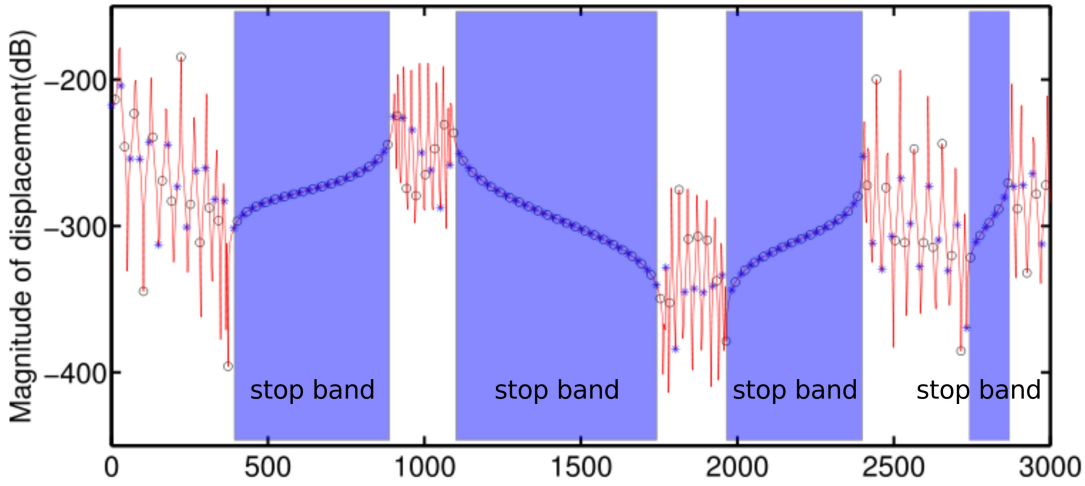


Figure 2.4: The response at excitation point by FEM (-), forced-WFEM (o), forced-CWFEM with $f_{mode} = 3f_{max}$ ($*$)

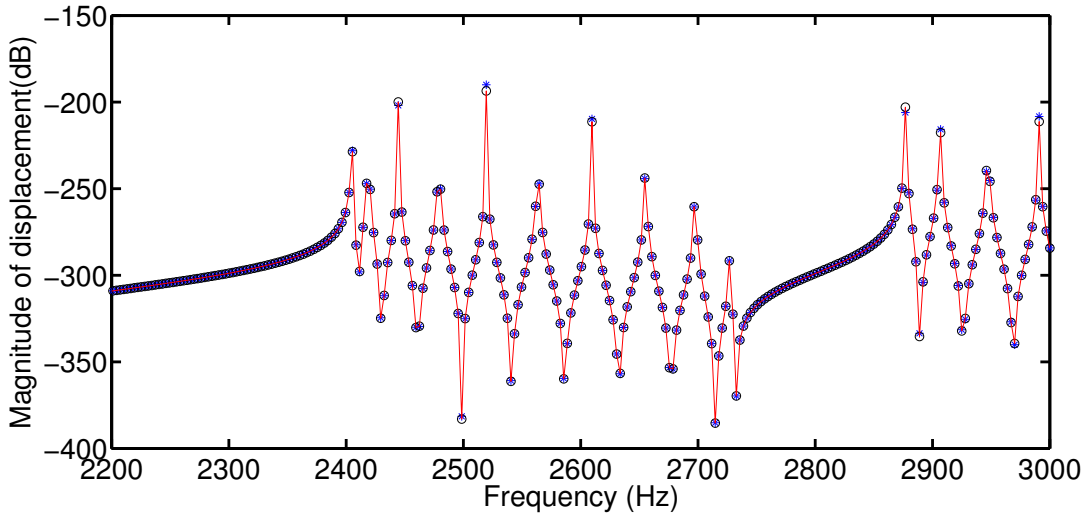


Figure 2.5: A magnified view of the response at excitation point by FEM (-), forced-WFEM (o), forced-CWFEM with $f_{mode} = 3f_{max}$ ($*$)

### 2.3.2 Flexural waves in binary periodic beam

The study of bending waves in binary periodic beam is carried out in this subsection. The materials and the geometry parameters remain the same as in the longitudinal case except that the radius of the two beams is set to 2.5 cm. The model of Euler-Bernoulli beam is used since the length of each beam section is much smaller than the height of each section and that the effects of shear and rotational inertia can be ignored.

#### 2.3.2.1 Dispersion relation of the bending waves

The dispersion relation of the positive-going bending waves calculated with different methods are given in Fig. 2.6. The characteristics of dispersion relation mentioned in the longitudinal waves are also observed in the bending ones. In addition, an evanescent wave at all frequency range with $\Im(k) \neq 0$ and $\Re(k) = 0$ is noted in Fig. 2.6, named "rapidly attenuated wave". The CWFEM with $f_{mode} = 3f_{max}$ and $f_{mode} = 80f_{max}$ are applied to calculate the dispersion relation. The results are compared to the ones obtained by Transfer Matrix Method (TMM) [Lin & McDaniel, 1969] and WFEM. The CWFEM with $f_{mode} = 3f_{max}$ is able to predict all the wavenumbers except the one of rapidly attenuated wave. More internal modes until $f_{mode} = 80f_{max}$ are needed to determine the rapidly attenuated waves.

In the frequency domain studied, the unit cell is divided into 80 elements of 160 DOFs. In the reduced model by CWFEM with $f_{mode} = 3f_{max}$, the number of DOFs is decreased from 160 to 16. For reduced model with $f_{mode} = 80f_{max}$, the number of DOFs is less than 50. The size of the reduced model is not more than one third of the full model.

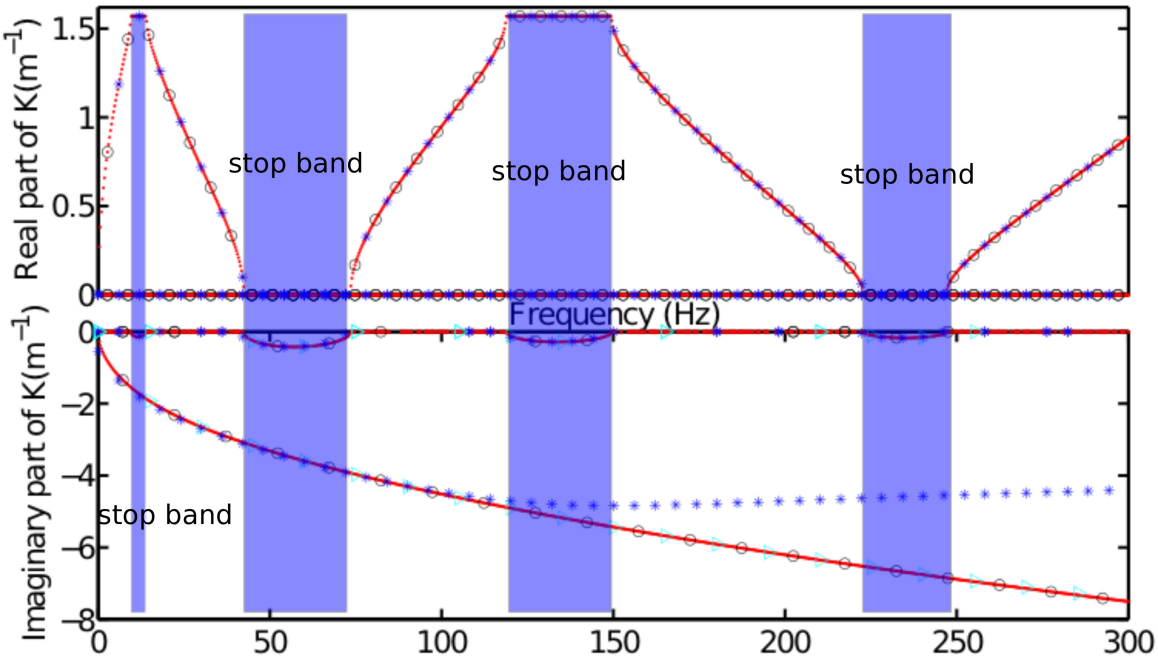


Figure 2.6: Dispersion relation for the bending waves by different methods: TMM (-), Classical WFEM (o), CWFEM with $f_{mode} = 3f_{max}$(∗), CWFEM with $f_{mode} = 80f_{max}$(▷)

#### 2.3.2.2 Forced response of the beam

The bending motion of a 10-period binary periodic beam is studied by the forced-CWFEM. A harmonic force perpendicular to the beam with an amplitude of 100 N is applied at the left

extremity of the 1st cell, and the beam is clamped at the right extremity of the last cell. The response at the excitation point is illustrated in Fig. 2.7. The result by forced-CWFEM is compared with the results from FEM and forced-WFEM. A relative big error is obtained when approaching the resonance or antiresonance frequencies. Since the damping is not included in the model, it is absurd to discuss the magnitude of the response when approaching these frequencies. The response level is supposed to be infinite. A global good estimation of the forced response is given by forced-CWFEM except at frequencies close to resonance or antiresonance.

In addition, compared to the forced response of longitudinal motion, two characteristics should be noted:

- The result by CWFEM in Fig. 2.7 is applied with $f_{mode} = 3f_{max}$. The reduced model in CWFEM which fails to determine the wavenumbers of the rapidly attenuated waves is able to obtain the forced response of the beam. An explanation is proposed: Since the attenuated waves decay rapidly with distance, they have negligible contribution to the forced response of the structure.

- Contrary to the longitudinal case, a peak of resonance is observed in the second stop band around 61 Hz. It indicates that the evanescent waves in stop band can generate resonance phenomenon. The phenomenon is studied in the next subsection.

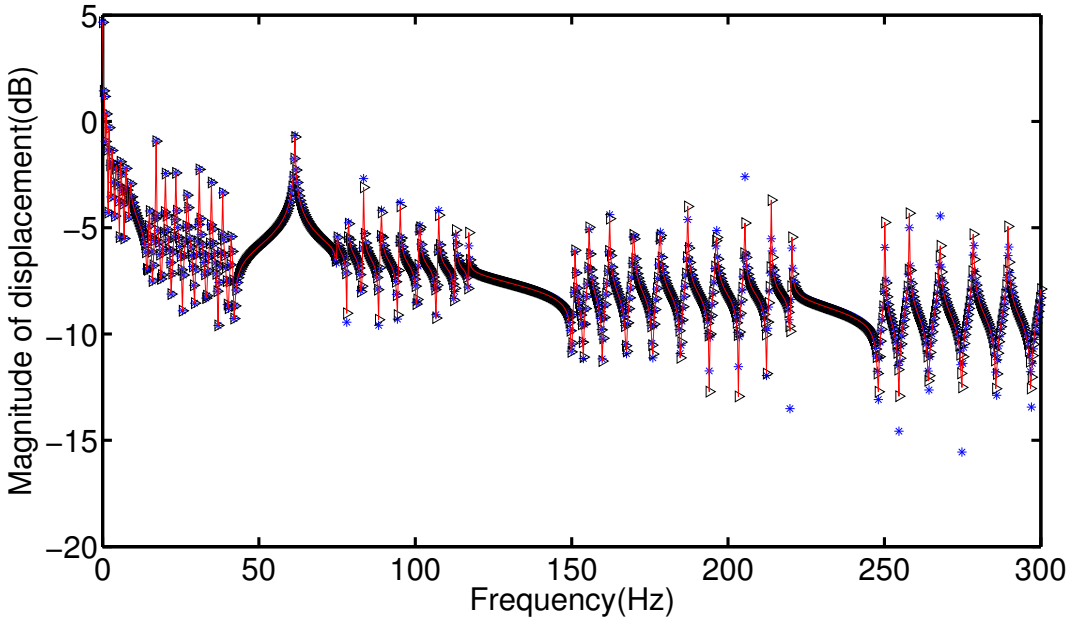


Figure 2.7: The response at excitation point by FEM (-), forced-WFEM (▷), forced-CWFEM with $f_{mode} = 3f_{max}$ (∗)

#### 2.3.2.3 Resonance in stop band

The forced response corresponding to the resonance in the stop band is given in Fig. 2.8, which coincides with the natural mode shape at 61 Hz under the same boundary condition.

For free wave propagation to x positive direction at 61 Hz, two evanescent waves were identified in the dispersion curve in Fig. 2.6: a rapidly attenuated wave (referred as wave I) with purely imaginary wavenumber equalling to -3.6i, a slowly attenuated wave (wave II) with purely imaginary wavenumber equalling to -0.4i. For wave I, the wave amplitude drops to $exp(-(-3.6i) * i * 2) = 0.0007$ when the wave goes through a unit cell. 2m is the unit cell length. For wave II, the wave amplitude decrease $exp(-(-0.4i) * i * 2) = 0.45$ when the wave goes through a unit cell. The forced response amplitudes under excitation of 61 Hz at the unit cell boundaries are indicated in Fig. 2.8. It can be seen that the amplitude drops (1-0.26)=74% from the 1st unit cell to the 2nd unit cell. Starting from the 2nd unit cell, the ratio between the displacements at left boundary of two adjacent unit cells is always 0.45. It indicates that the contribution of the wave I (rapidly attenuated wave) is only limited in the first unit cell.

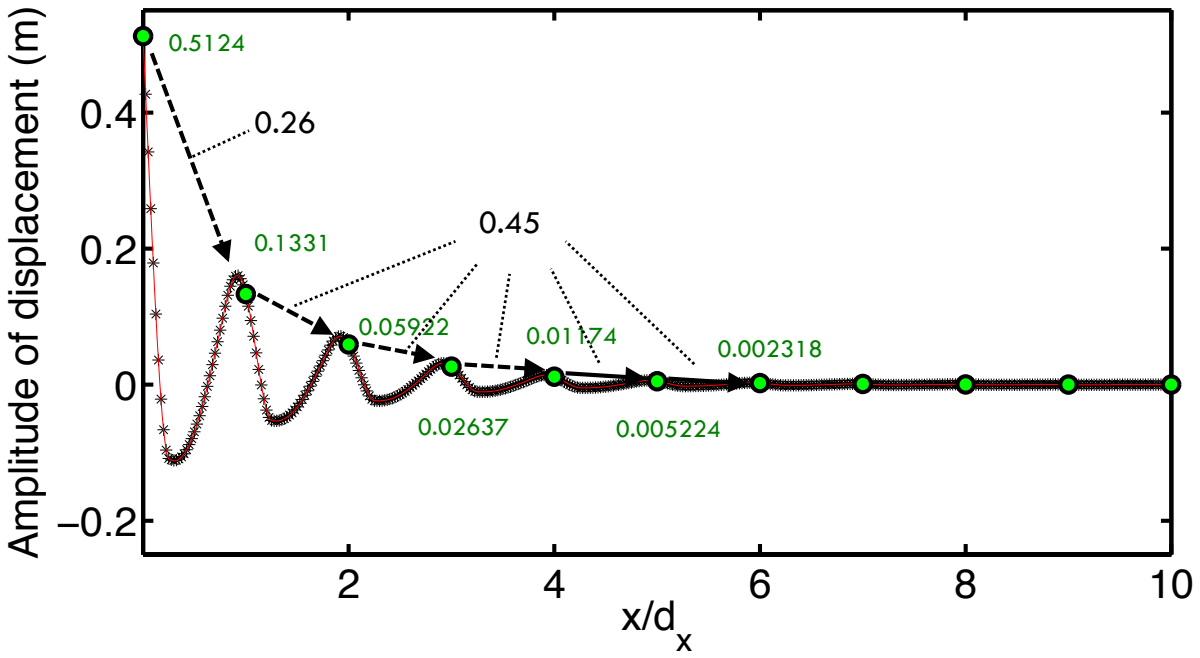


Figure 2.8: The mode shape with natural frequency at 61 Hz by FEM (-). The response of the beam under harmonic excitation at 61 Hz by forced-CWFEM (∗). The response of the unit cell boundaries by forced-WFEM (•)

It can be seen that the displacement of the beam is located near the excitation point at the left extremity of the beam. The resonance at 61 Hz can be interpreted as follows: The incident waves due to the excitation at left extremity are reflected at the interface of material A and material B. The resonance then occur since the reflected waves are in phase with the incident ones. The incident waves are totally reflected at discontinuities of the materials, so they cannot

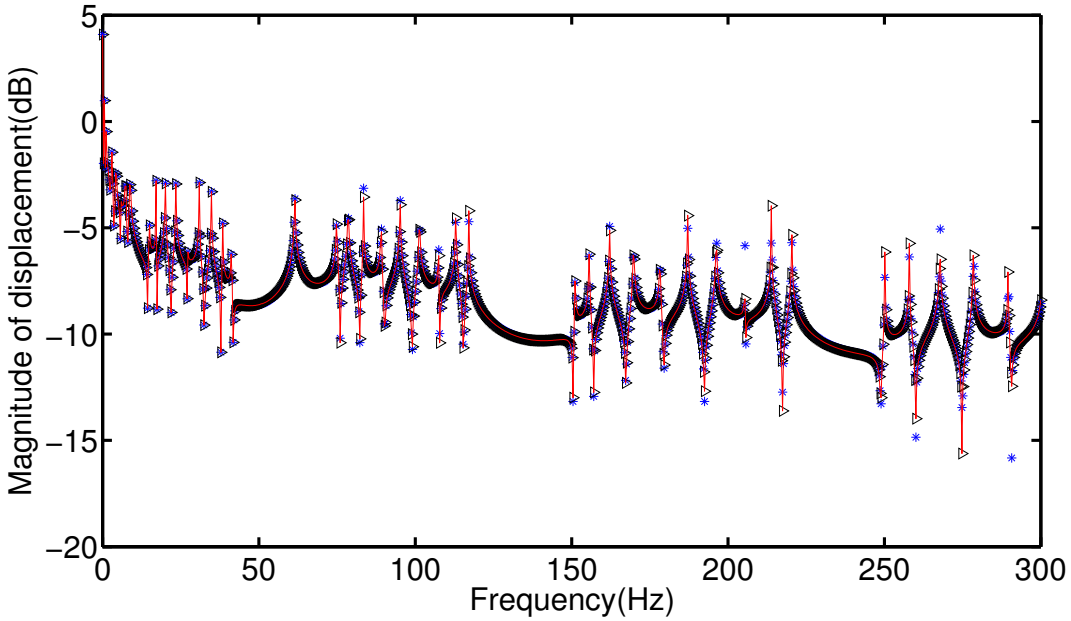


Figure 2.9: The response at right end of the 3rd unit cell by FEM (-), forced-WFEM (▷), forced-CWFEM with $f_{mode} = 3f_{max}$ ($*$)

reach the right extremity of the 10-period beam. If the boundary conditions at right extremity are changed from clamped to simply supported, the same mode shape is obtained. Or for a longer beam with more unit cells, the response remains the same for the first 10 unit cells.

Many ongoing researches focus only on the stop band of free propagation in the design of periodic structure as vibration isolator. However, the existence of the resonance in stop band indicates that stop band might not always equivalent to low response level. So attention needs to be paid to these resonances. Especially when the excitation is limited to a small band of frequency. If the excitation is distributed in a large band of frequency, the resonance peaks at few frequencies in stop band should not increase significantly the response level.

### 2.3.3 Binary periodic and nonsymmetrical thin-walled beam including warping effect

Thin-walled beams, such as angles and channel beams are basic structural elements in mechanical, aeronautical and civil engineering. It is demonstrated that the warping effect should be included when it comes to modelling the open section beams. Yu *et al.* have studied a binary periodic and asymmetrical thin-walled beam, the model of Bernoulli-Euler beam including warping effect is used with TMM [Yu *et al.*, 2009]. Their results are used as reference in this paper. The same structure is modelled using finely meshed solid elements. The element Solid185 in ANSYS is used in this study to obtain the dynamic matrix of the unit cell.

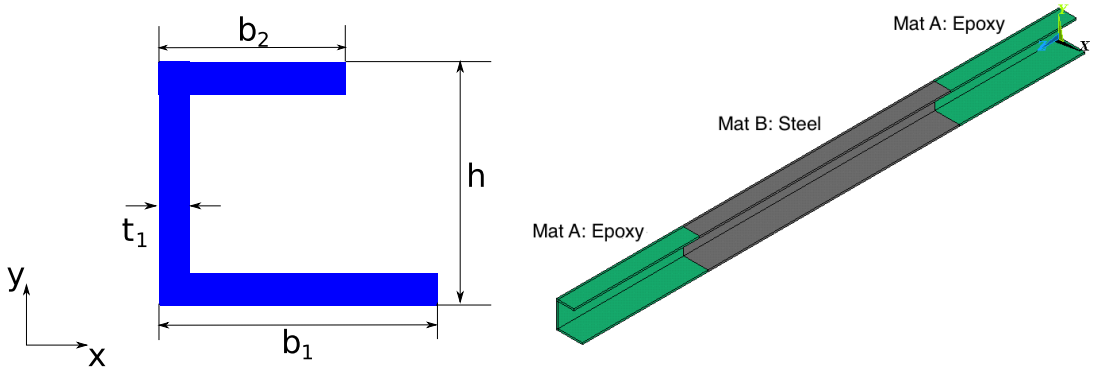


(a) Schema of the cross-section (b) The unit cell used in CWFEM

Figure 2.10: The thin-walled beam modelled with Solid element

The beam is binary periodic as shown in Fig. 2.2 with $l_1 = l_2 = 150$ mm, material A is epoxy and material B is steel. The cross-section of the beam is as shown in Fig. 2.10(a), with geometrical parameters: $b_1 = 15.5$ mm, $b_2 = 9.5$ mm, $t_1 = 1$ mm, $h = 16$ mm.

The unit cell used in CWFEM is shown in Fig. 2.10(b). The cross-section is in $x - y$ plan, and waves propagate in the $z$-direction. The cross-section is divided into 15 elements which contains 96 DOFs. The unit cell is divided into 90 elements in the $z$-direction. The size of the whole unit cell is of 8736 DOFs. This mesh assures the convergence of the natural frequencies below 1 kHz.

#### 2.3.3.1 Dispersion relation and gain of computation time

To study the wave propagation characteristics, the fixed boundary modes under 3 kHz are retained in CWFEM. The result of which is compared with the one obtained by WFEM, it can be seen that CWFEM predicted the same wavenumbers as WFEM.

The internal modes with fixed boundary under 3 kHz consist the first 15 modes. So the size of the model is reduced from 8736 DOFs to 207 DOFs, with 15 internal DOFs and 192 boundary DOFs. And computation time decreases from more than 15 hours to less than 7 minutes, as shown in Tab. 3.2. For each frequency, to apply the dynamic condensation, instead of inverting matrix $\mathbf{D}^*_{\mathtt{II}}$, which is not diagonal with size $8544 \times 8544$, a diagonal matrix $\mathbf{D}^*_{\mathtt{cc}}$ of size $15 \times 15$ is inverted. CWFEM allows gaining computation time and avoiding the numerical issue due to inverting $\mathbf{D}^*_{\mathtt{II}}$. Four kinds of wave are identified at low frequencies. The one with the smallest wavenumber corresponds to the longitudinal waves since it is the fastest wave propagating in the structure. Another three waves are all the flexural-torsional coupled waves. The two kinds of wave shapes are given in Fig. 2.12.

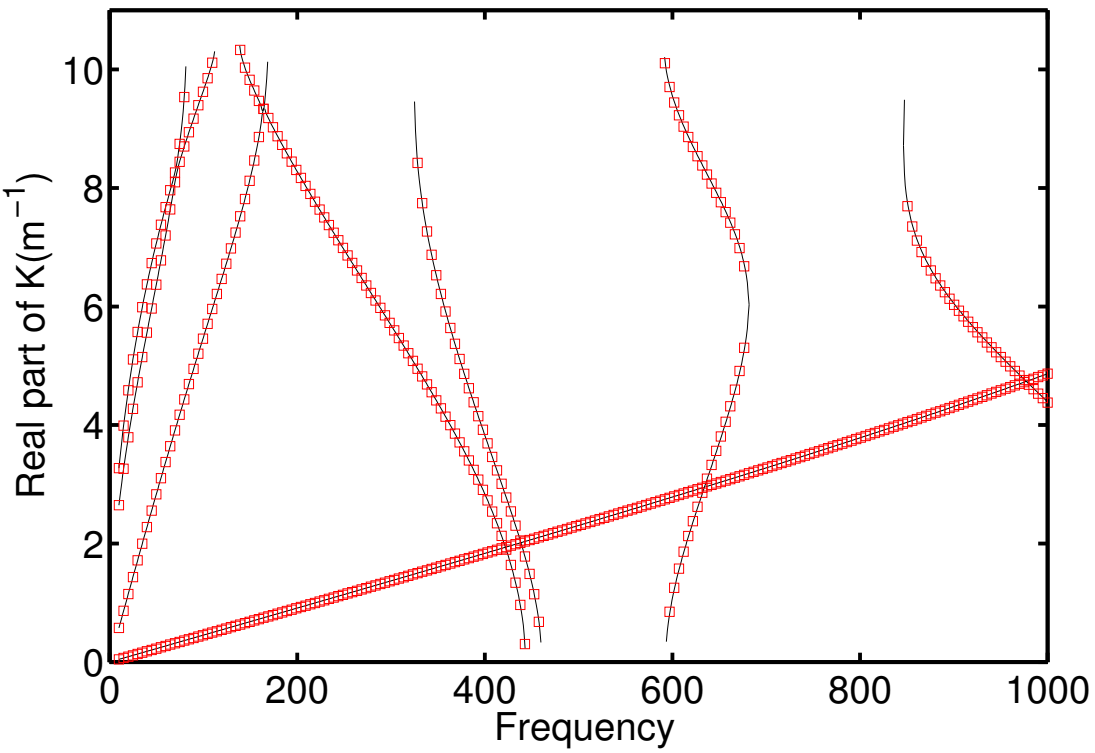


Figure 2.11: Dispersion relation by different methods: CWFEM with $f_{mode} = 3f_{max}$ (-), WFEM on the full model (□)

#### 2.3.3.2 The stop bands of the binary thin-walled beam

The dispersion relation predicted by CWFEM is compared with the work of Yu *et al.* [2009], where only flexural-torsion coupled waves are studied. It can be seen that a good correlation is observed between the two results. However, a considerable discrepancy is observed around 500 Hz, which changes the frequency range of a stop band.

The forced response function of a 8-period beam is calculated by FEM in reference [Yu *et al.*, 2009]. It predicts also the frequency range of stop bands where a sharp drop in frequency response occurs.

It can be seen from Tab. 2.4 that almost the same stop bands are identified by FEM and CWFEM, while TMM has a discrepancy around 500 Hz with the two other methods. The error in the analytical model may arise because higher order inertia terms are ignored in Euler-Bernoulli beam model [Yu *et al.*, 2009].

| | Computation time | Model size |
|---|---|---|
| Classical WFEM | Dynamic condensation: 15 hrs<br>Linear eigen problem: 55 secs<br>Total: $>$ 15 hours | 8736 DOFs |
| Proposed CWFEM | Modal analysis: 356 secs<br>Dynamic condensation: 1 sec<br>Linear eigen problem: 55 secs<br>Total: $<$ 7 minutes | 207 DOFs |
| Gain | 99 % | 97.6 % |

Table 2.3: Comparsion of computation time and model size by CWFEM and WFEM

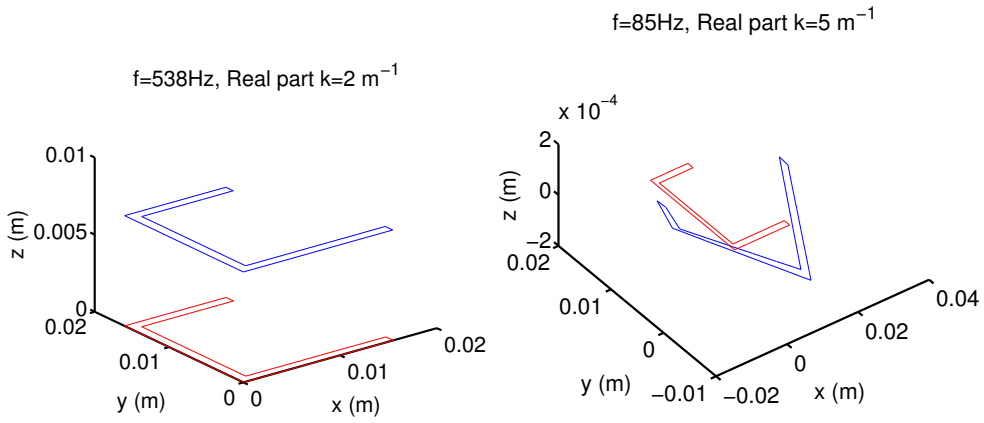


(a) Longitudinal wave (b) Flexural-torsional coupled wave

Figure 2.12: Wave shapes (Blue), the undeformed cross-section (Red)

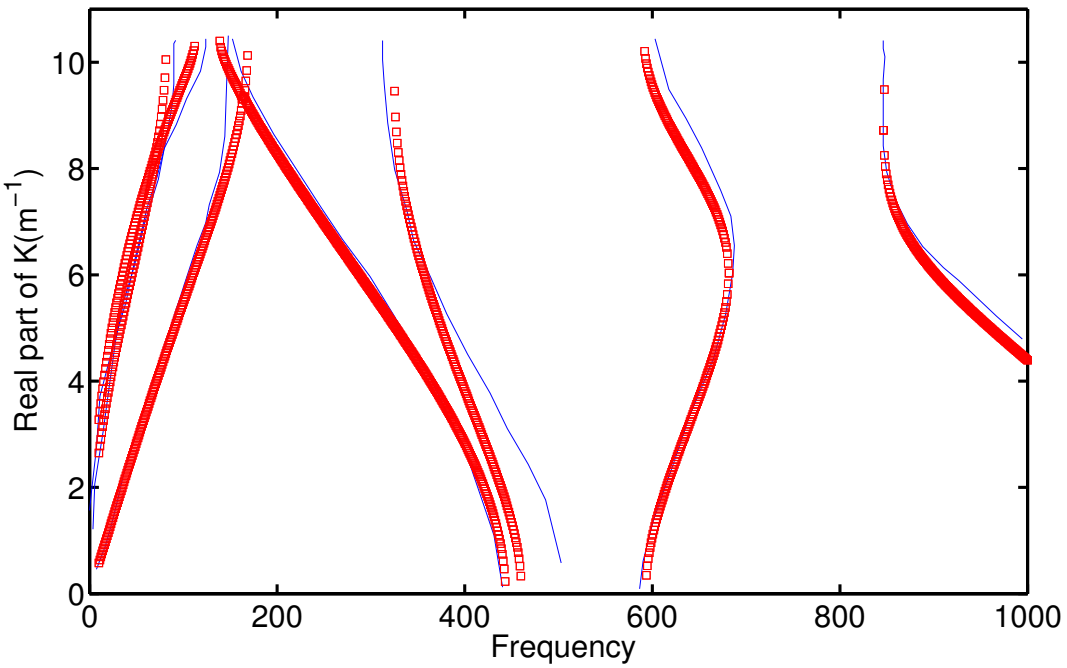


Figure 2.13: Dispersion relation by different methods: Reference (-), CWFEM with $f_{mode} = 3f_{max}$ (□)

| Stop bands | Analytical [Yu *et al.*, 2009] | FEM [Yu *et al.*, 2009] | CWFEM |
|---|---|---|---|
| 1 | (156, 163) | - | - |
| 2 | (501, 598) | (460, 590) | (460, 592) |
| 3 | (694, 853) | (660, 860) | (680, 846) |

Table 2.4: The frequency (Hz) range of stop bands for binary periodic thin-walled beam

## 2.4 Conclusions

In this chapter, an efficient numerical approach - CWFEM was proposed to study the free and forced vibration of complex 1D periodic structures. The method proved that with a reduced modal basis, precise wave propagation characteristics can be obtained. The effectiveness of the method was illustrated using 3 numerical examples. Main conclusions of this chapter can be drawn as follows:

- The formulation of the proposed CWFEM was developed and applied in numerical examples. CWFEM is able to predict precisely the dispersion relation and forced response compared to WFEM and analytical methods.

- To ensure the convergence of CWFEM, the internal modes with natural frequency lower than three times of the maximum investigated frequency should be retained in the modal basis. In this case, CWFEM is able to predict correctly the propagating waves and some

of the evanescent waves. Even significant differences may exist for the rapidly attenuated waves, they have a negligible contribution to the forced response of the structure except at the excitation point.

- CWFEM can speed up the computation of unit cell dynamics (from 15 hours to 7 minutes in the 3rd example). It can also avoid the poor conditioned issues which may occur due to the dynamic condensation.

- The frequency ranges without resonance in forced response function of finite waveguides are independent of boundary conditions and the number of unit cells. And they correspond to the stop bands of a infinite waveguides with the same unit cell. However, resonance can exist in the stop bands, while the displacements of the waveguides are located near near the boundaries of the systems.

The decrease of the computation time due to the MOR would be very desirable for the optimisation of complex waveguides.

# Chapter 3

# Multi-scale modelling for two-dimensional periodic structures using condensed wave finite element method

## 3.1 Introduction

The proposed CWFEM is extended to two-dimensional (2D) periodic structures in this chapter. Firstly, the method is developed in detail, then it is applied on a numerical example of a beam grid to illustrate its validity. A convergence study is carried out to study the selection of the internal modes. The results are compared with those given by WFEM on the full model and harmonic displacement field of FE model. The wave beaming effects phenomenon is studied, and equivalence of the cell modes and stationary waves at bounding frequencies of stop bands is discussed.

## 3.2 The formulation and result representation of proposed "CWFEM" on 2D periodic structures

For free wave propagation, the equation of motion of the unit cell can be written as follows:

$$\left(\begin{bmatrix} \tilde{\mathbf{K}}_{\mathtt{bdbd}} & \tilde{\mathbf{K}}_{\mathtt{bdI}} \\ \tilde{\mathbf{K}}_{\mathtt{Ibd}} & \tilde{\mathbf{K}}_{\mathtt{II}} \end{bmatrix} - \omega^2 \begin{bmatrix} \tilde{\mathbf{M}}_{\mathtt{bdbd}} & \tilde{\mathbf{M}}_{\mathtt{bdI}} \\ \tilde{\mathbf{M}}_{\mathtt{Ibd}} & \tilde{\mathbf{M}}_{\mathtt{II}} \end{bmatrix}\right) \begin{pmatrix} \mathbf{q}_{\mathtt{bd}} \\ \mathbf{q}_{\mathtt{I}} \end{pmatrix} = [\tilde{\mathbf{K}} - \omega^{\mathbf{2}}\tilde{\mathbf{M}}] \begin{pmatrix} \mathbf{q}_{\mathtt{bd}} \\ \mathbf{q}_{\mathtt{I}} \end{pmatrix} = \begin{pmatrix} \mathbf{f}_{\mathtt{bd}} \\ \mathbf{0} \end{pmatrix} \tag{3.1}$$

$\mathbf{q}_{\mathtt{bd}}$ represents the boundary DOFs, which are classified as $[\mathbf{q}_1 \quad \mathbf{q}_2 \quad \mathbf{q}_3 \quad \mathbf{q}_4 \quad \mathbf{q}_{\mathtt{L}} \quad \mathbf{q}_{\mathtt{B}} \quad \mathbf{q}_{\mathtt{R}} \quad \mathbf{q}_{\mathtt{T}}]$. The notation of the nodes can be found in Fig 3.1(a). To model the dynamic behaviours in high

frequency, the unit cell is finely meshed, which may lead to a large size of $\mathbf{q}_{\mathtt{I}}$.

### 3.2.1 Model reduction on the unit cell

Based on Craig-Bampton method, the physical coordinates $[\mathbf{q}_{\mathtt{bd}} \quad \mathbf{q}_{\mathtt{I}}]$ are reduced to $[\mathbf{q}_{\mathtt{bd}} \quad \mathbf{P}_{\mathtt{C}}]$

$$\begin{pmatrix} \mathbf{q}_{\mathtt{bd}} \\ \mathbf{q}_{\mathtt{I}} \end{pmatrix} = \begin{bmatrix} \mathbf{I_n} & \mathbf{0} \\ \mathbf{\Psi}_{\mathtt{bd}} & \mathbf{\Psi}_{\mathtt{C}} \end{bmatrix} \begin{pmatrix} \mathbf{q}_{\mathtt{bd}} \\ \mathbf{P}_{\mathtt{C}} \end{pmatrix} = \mathbf{B} \begin{pmatrix} \mathbf{q}_{\mathtt{bd}} \\ \mathbf{P}_{\mathtt{C}} \end{pmatrix} \tag{3.2}$$

where $[\mathbf{\Psi}_{\mathtt{bd}}]$ represents the constraint modes which associate physical displacements at the boundary $\mathbf{q}_{\mathtt{bd}}$ to physical displacements of elastic DOFs $\mathbf{q}_{\mathtt{I}}$.

$$\mathbf{\Psi}_{\mathtt{bd}} = -\tilde{\mathbf{K}}_{\mathtt{II}}^{-1}\tilde{\mathbf{K}}_{\mathtt{Ibd}} \tag{3.3}$$

The fixed interface modes are denoted $[\mathbf{\Psi}_{\mathtt{I}}]$, which is obtained with boundary DOFs fixed and with no force acting on the internal nodes

$$[\tilde{\mathbf{K}}_{\mathtt{II}} - \omega_0^2\tilde{\mathbf{M}}_{\mathtt{II}}]\mathbf{\Psi}_{\mathtt{I}} = 0 \tag{3.4}$$

while $[\mathbf{\Psi}_{\mathtt{C}}]$ represents a set of truncated modes in $[\mathbf{\Psi}_{\mathtt{I}}]$, the selection of the modes in $[\mathbf{\Psi}_{\mathtt{I}}]$ will be discussed via a convergence study in the numerical example later. Then the equilibrium equation of the reduced model is written as:

$$[\mathbf{K} - \omega^{\mathbf{2}}\mathbf{M}] \begin{pmatrix} \mathbf{q}_{\mathtt{bd}} \\ \mathbf{P}_{\mathtt{C}} \end{pmatrix} = \begin{pmatrix} \mathbf{f}_{\mathtt{bd}} \\ \mathbf{0} \end{pmatrix} \tag{3.5}$$

with

$$\mathbf{K} = \mathbf{B}^{\mathbf{T}}\tilde{\mathbf{K}}\mathbf{B} \quad , \quad \mathbf{M} = \mathbf{B}^{\mathbf{T}}\tilde{\mathbf{M}}\mathbf{B} \tag{3.6}$$

The MOR of the unit cell is illustrated in Fig. 3.1. The physical DOFs $\mathbf{q}_{\mathtt{I}}$ are replaced by $\mathbf{P}_{\mathtt{C}}$, the reduced modal DOFs of smaller size.

### 3.2.2 Wave Finite Element method with model reduction on 2D periodic structures

According to periodic structures theory [Bloch, 1929], the boundary displacements and forces can be related using $\lambda_x$ and $\lambda_y$, as given in Eq. (1.24) and (1.25). So the DOFs of the

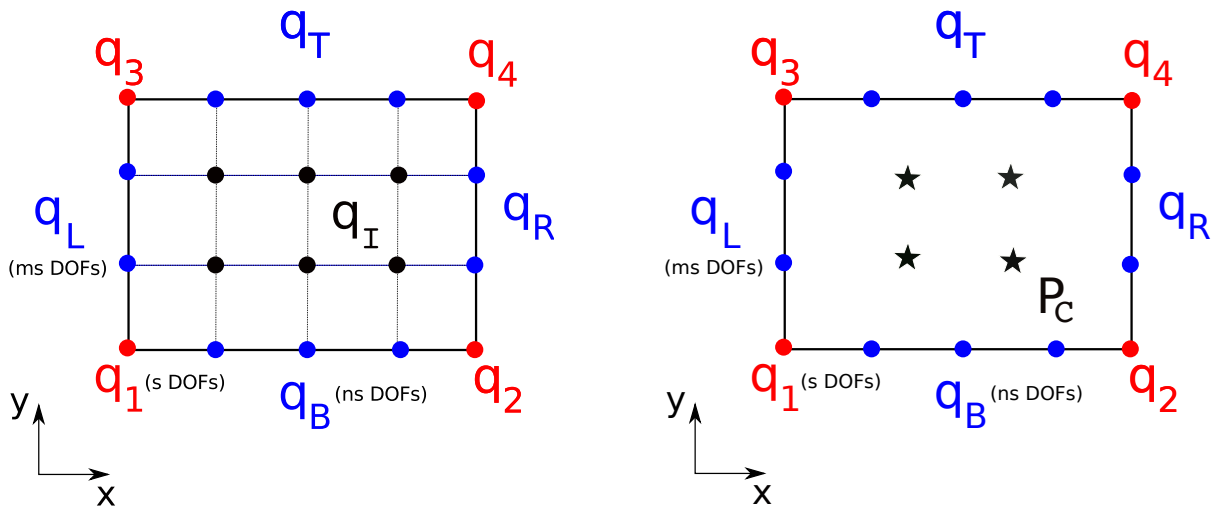


(a) Full model with physical internal DOFs $\mathbf{q}_{\mathtt{I}}$ (b) Reduced model with modal internal DOFs $\mathbf{P}_{\mathtt{C}}$

Figure 3.1: MOR on the unit cell of 2D periodic structure

reduced model $[\mathbf{q}_{\mathtt{bd}} \quad \mathbf{P}_{\mathtt{C}}]$ can be related to $[\mathbf{q}_{\mathtt{1}} \quad \mathbf{q}_{\mathtt{L}} \quad \mathbf{q}_{\mathtt{B}} \quad \mathbf{P}_{\mathtt{C}}]$ using $\mathbf{\Lambda_R}$

$$\begin{pmatrix} \mathbf{q}_{\mathtt{bd}} \\ \mathbf{P}_{\mathtt{C}} \end{pmatrix} = \mathbf{\Lambda_R}(\lambda_{\mathbf{x}}, \lambda_{\mathbf{y}}) \begin{pmatrix} \mathbf{q}_{\mathtt{1}} \\ \mathbf{q}_{\mathtt{L}} \\ \mathbf{q}_{\mathtt{B}} \\ \mathbf{P}_{\mathtt{C}} \end{pmatrix} \tag{3.7}$$

The sizes of $\mathbf{q}_{\mathtt{1}}$, $\mathbf{q}_{\mathtt{L}}$, $\mathbf{q}_{\mathtt{B}}$, $\mathbf{P}_{\mathtt{C}}$ are s, sm, sn and c respectively. The matrices $\mathbf{I}_{\mathtt{s}}$, $\mathbf{I}_{\mathtt{sm}}$, $\mathbf{I}_{\mathtt{sn}}$ and $\mathbf{I}_{\mathtt{C}}$ in $\mathbf{\Lambda_R}$ represents the identity matrix of size s, sm, sn and c.

$$\mathbf{\Lambda_R} = \begin{bmatrix} \mathbf{I}_{\mathtt{s}} & \mathbf{0} & \mathbf{0} & \mathbf{0} \\ \lambda_x \mathbf{I}_{\mathtt{s}} & \mathbf{0} & \mathbf{0} & \mathbf{0} \\ \lambda_y \mathbf{I}_{\mathtt{s}} & \mathbf{0} & \mathbf{0} & \mathbf{0} \\ \lambda_x \lambda_y \mathbf{I}_{\mathtt{s}} & \mathbf{0} & \mathbf{0} & \mathbf{0} \\ \mathbf{0} & \mathbf{I}_{\mathtt{sm}} & \mathbf{0} & \mathbf{0} \\ \mathbf{0} & \mathbf{0} & \mathbf{I}_{\mathtt{sn}} & \mathbf{0} \\ \mathbf{0} & \lambda_x \mathbf{I}_{\mathtt{sm}} & \mathbf{0} & \mathbf{0} \\ \mathbf{0} & \mathbf{0} & \lambda_y \mathbf{I}_{\mathtt{sn}} & \mathbf{0} \\ \mathbf{0} & \mathbf{0} & \mathbf{0} & \mathbf{I}_{\mathtt{C}} \end{bmatrix} \tag{3.8}$$

Similar to the nodal DOFs, we have

$$\mathbf{\Lambda_L}(\lambda_{\mathbf{x}}, \lambda_{\mathbf{y}}) \begin{pmatrix} \mathbf{f}_{\mathbf{bd}} \\ \mathbf{0} \end{pmatrix} = \mathbf{0} \tag{3.9}$$

while

$$\mathbf{\Lambda_L} = \begin{bmatrix} \mathbf{I_s} & \lambda_x^{-1}\mathbf{I_s} & \lambda_y^{-1}\mathbf{I_s} & \lambda_x^{-1}\lambda_y^{-1}\mathbf{I_s} & \mathbf{0} & \mathbf{0} & \mathbf{0} & \mathbf{0} & \mathbf{0} \\ \mathbf{0} & \mathbf{0} & \mathbf{0} & \mathbf{0} & \mathbf{I_{sm}} & \mathbf{0} & \lambda_x^{-1}\mathbf{I_{sm}} & \mathbf{0} & \mathbf{0} \\ \mathbf{0} & \mathbf{0} & \mathbf{0} & \mathbf{0} & \mathbf{0} & \mathbf{I_{sn}} & \mathbf{0} & \lambda_y^{-1}\mathbf{I_{sn}} & \mathbf{0} \\ \mathbf{0} & \mathbf{0} & \mathbf{0} & \mathbf{0} & \mathbf{0} & \mathbf{0} & \mathbf{0} & \mathbf{0} & \mathbf{I_C} \end{bmatrix} \tag{3.10}$$

Then eq. (3.5) can be rewritten as

$$\mathbf{\Lambda_L}(\lambda_\mathbf{x}, \lambda_\mathbf{y}) * (\mathbf{K} - \omega^\mathbf{2}\mathbf{M}) * \mathbf{\Lambda_R}(\lambda_\mathbf{x}, \lambda_\mathbf{y}) \begin{pmatrix} \mathbf{q_1} \\ \mathbf{q_L} \\ \mathbf{q_B} \\ \mathbf{P_C} \end{pmatrix} = \mathbf{0} \tag{3.11}$$

Eq. (3.11) includes three parameters $(\omega, \lambda_x, \lambda_y)$. The equation can take various forms, depending on the type of solution being sought. The first formulation fixes frequency $\omega$ and one between $(\lambda_x, \lambda_y)$, for example $\lambda_y$. It corresponds to the direct form of CWFEM2D. This may represent the situation where a known wave is incident on a straight boundary, so that $\lambda_y$ is given and all possibly solutions for $\lambda_x$ are sought which correspond to evanescent or propagation waves. Or another situation is to study the wave propagation in a closed cylindrical shell, where the wavenumber around the circumference can only take certain discrete values [Mace & Manconi, 2008]. The second formulation fixes $(\lambda_x, \lambda_y)$, and the value of $\omega$ are sought. It corresponds to the inverse form of CWFEM2D. This can be used to study the wave propagation in undamped structure or lightly damped with the assumption that the dispersion curves of the propagating waves are not significantly modified by the addition of damping [Cotoni *et al.*, 2008]. Both formulations lead to the same solutions when all the values of $(\omega, \lambda_x, \lambda_y)$ are covered.

Here we study the propagative wave in an undamped structure, so the second formulation is adapted and developed. Eq. (3.11) becomes a standard and linear eigenvalue problem of $\omega^2$ as follows

$$[\mathbf{K}'(\lambda_\mathbf{x}, \lambda_\mathbf{y}) - \omega^\mathbf{2}\mathbf{M}'(\lambda_\mathbf{x}, \lambda_\mathbf{y})] \begin{pmatrix} \mathbf{q_1} \\ \mathbf{q_L} \\ \mathbf{q_B} \\ \mathbf{P_C} \end{pmatrix} = \mathbf{0} \tag{3.12}$$

with

$$\mathbf{K}' = \mathbf{\Lambda_L}\mathbf{K}\mathbf{\Lambda_R}, \quad \mathbf{M}' = \mathbf{\Lambda_L}\mathbf{M}\mathbf{\Lambda_R} \tag{3.13}$$

It should be noted that when no damping is included, for the pure propagative wave, we have $|\lambda_x| = 1$ and $|\lambda_y| = 1$, and the matrix $\mathbf{\Lambda_L}$ is the conjugate transpose of the matrix $\mathbf{\Lambda_R}$. In addition, the stiffness and mass matrices $\mathbf{K}$ and $\mathbf{M}$ are symmetric positive definite matrices, thus the matrix $\mathbf{K}'$ and $\mathbf{M}'$ in Eq. (3.12) are positive definite Hermitian matrices. Therefore,

the eigenvalue problem leads to the solutions $(\omega^2, \phi')$, with $\omega^2$ real and positive and vectors $\phi'$ orthogonal. The eigen vector $\phi'$ calculated in Eq. (3.12) include only $[\mathbf{q}_1 \quad \mathbf{q}_\mathtt{L} \quad \mathbf{q}_\mathtt{B} \quad \mathbf{P}_\mathtt{C}]$

$$\phi' = \begin{pmatrix} \phi_1 \\ \phi_\mathtt{L} \\ \phi_\mathtt{B} \\ \phi_\mathtt{C} \end{pmatrix} \tag{3.14}$$

The eigen vector for $[\mathbf{q}_{\mathtt{bd}}^\mathtt{T} \quad \mathbf{P}_\mathtt{C}^\mathtt{T}]^\mathtt{T}$ is obtained by multiplying $\mathbf{\Lambda_R}$

$$\begin{pmatrix} \phi_{\mathtt{bd}} \\ \phi_\mathtt{C} \end{pmatrix} = \mathbf{\Lambda_R}\phi' \tag{3.15}$$

The eigen vector associated to the physical DOFs $[\mathbf{q}_{\mathtt{bd}}^\mathtt{T} \quad \mathbf{q}_\mathtt{I}^\mathtt{T}]^\mathtt{T}$ can be expressed using matrix $\mathbf{B}$ in 3.2.1.

$$\begin{pmatrix} \phi_{\mathtt{bd}} \\ \phi_\mathtt{I} \end{pmatrix} = \mathbf{B} \begin{pmatrix} \phi_{\mathtt{bd}} \\ \phi_\mathtt{C} \end{pmatrix} \tag{3.16}$$

So the associated wave shape for the unit cell is as follows

$$\phi = \begin{pmatrix} \phi_{\mathtt{bd}} \\ \phi_\mathtt{I} \end{pmatrix} = \mathbf{B}\mathbf{\Lambda_L}\phi' = \begin{bmatrix} \mathbf{I_n} & \mathbf{0} \\ \mathbf{\Psi}_{\mathtt{bd}} & \mathbf{\Psi}_\mathtt{C} \end{bmatrix} \mathbf{\Lambda_L}\phi' \tag{3.17}$$

The wave shape $\phi$ is represented using the constraint modes $\mathbf{\Psi}_{\mathtt{bd}}$ and reduced basis of fixed boundary modes $\mathbf{\Psi}_\mathtt{C}$ of the unit cell.

### 3.2.3 The result representations – Slowness surfaces and band structure

For 2D periodic structures, the behaviour is usually described using propagation constants $\mu_x$ and $\mu_y$ [Mead *et al.*, 1988; Ruzzene *et al.*, 2003]. They are related to the wavenumbers $k_x$ and $k_y$ in following manner:

$$\lambda_x = e^{\mu_x}, \lambda_y = e^{\mu_y}, \mu_x = -ik_xL_x, \mu_y = -ik_yL_y \tag{3.18}$$

where $L_x$ and $L_y$ representing the size of the unit cells in the $x$- and $y$- directions respectively.

The eigen solutions of $\omega$ in Eq.(3.12) can be expressed in different coordinate systems. The surfaces formed by $\omega = f(\mu_x, \mu_y)$ are usually named "phase constant surfaces" [Mead *et al.*, 1988; Ruzzene *et al.*, 2003] or "propagation surfaces" [Mead & Parthan, 1979], for $\omega = f'(k_x, k_y)$ are named "slowness surfaces" or "frequency surfaces" [Darinskii *et al.*, 2008]. The results in this work are presented in coordinate system $(k_x, k_y)$ and the name "slowness surfaces" is adopted since $k = \omega/c$, with $c$ the phase velocity of the wave.

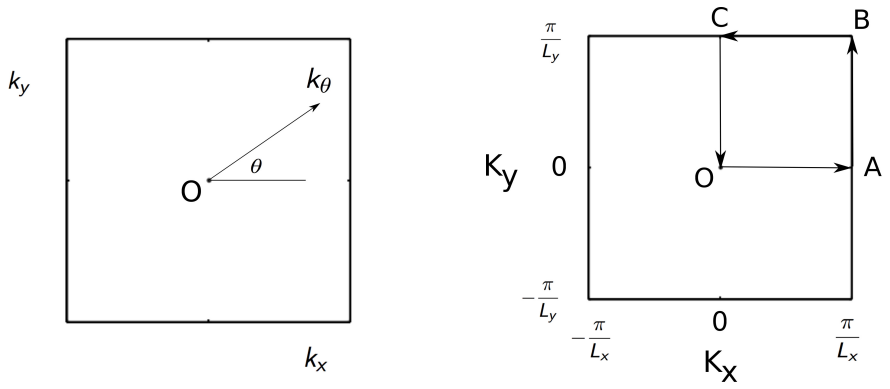


(a) Plane wave in $\theta$ direction with wavenumber $k_\theta$

(b) First Brillouin zone

Figure 3.2: $k$-space, IBZ (OABC), the contour of IBZ (O-A-B-C-O)

#### 3.2.3.1 Slowness surfaces

When no damping is included and only the purely propagative waves are studied, wavenumbers $(k_x, k_y)$ are real value and vary in the first Brillouin zone $[(-\pi/L_x, \pi/L_x), (-\pi/L_y, \pi/L_y)]$ [Brillouin, 1953]. The wavenumbers in the first Brillouin zone are discretised into $(k_x^{\mathtt{i}}, k_y^{\mathtt{j}})$, with $k_x^{\mathtt{i}}$ being the $\mathtt{i}$-th term, $k_y^{\mathtt{j}}$ being the $\mathtt{j}$-th term. The corresponding frequencies are sorted in the ascending order $\omega^{(\mathtt{i},\mathtt{j})}_{(1,2,\ldots\mathtt{k},\ldots\mathtt{n})}$. The $\mathtt{k}$-th slowness surface is formed by $\omega_{\mathtt{k}}^{(\mathtt{i},\mathtt{j})}$. When $x$ and $y$ are symmetric axes of the structure, the slowness surfaces are also symmetric with respect to the $k_x = 0$ and $k_y = 0$ axes. The symmetric property can be exploited to limit the variation of the wavenumbers to the IBZ ($k_x$ and $k_y$ positive).

The stop bands, modal density, energy flow direction and velocity may all be derived from the slowness surfaces. The absolute stop bands (if any) is a frequency band at which there is no slowness surface presents. The Poynting vector (i.e., the energy flow vector) at any point $(k_x, k_y)$ is the same as the gradient of slowness surface [Langley, 1994]. In the iso-frequency contour of the slowness surface ($k$-space), Poynting vector is normal to the contour curves. This property can be used to determine the direction of wave propagation and particularly in the investigation of directions where waves do not propagate. The phenomenon is known as wave beaming effect [Kohrs & Petersson, 2009; Langley & Bardell, 1997; Ruzzene *et al.*, 2003].

#### 3.2.3.2 Band structure

The 3D plot of the slowness surfaces is difficult to follow and to compare. A convenient and compact 2D representation of the slowness surface is the "band structure", which is obtained by varying the wavenumbers along the contour of the IBZ (O-A-B-C-O), as shown in Fig. 3.2(b). The wave number $k_\theta$ in the direction of propagation $\theta$ is related with $(k_x, k_y)$ using $k_x = k_\theta \cos\theta$

| | $k_x$ | $k_y$ | $k_\theta$ | Angle $\theta$ |
|---|---|---|---|---|
| O–A | $0 - \pi/L_x$ | 0 | $0 - \pi/L_x$ | $0^\circ$ |
| A–B | $\pi/L_x$ | $0 - \pi/L_y$ | $\pi/L_x - k_m$ | $0^\circ - \theta_m$ |
| B–C | $\pi/L_x - 0$ | $\pi/L_y$ | $k_m - \pi/L_y$ | $\theta_m - 90^\circ$ |
| C–O | 0 | $\pi/L_y - 0$ | $\pi/L_y - 0$ | $90^\circ$ |

Table 3.1: The wave vectors on the band structure (contour of IBZ)

and $k_y = k_\theta \sin\theta$, as illustrated in Fig. 3.2(a). The range of the wave vectors on the contour is listed in Tab. 3.1, with $\tan\theta_m = L_y/L_x$, $k_m^2 = (\pi/L_x)^2 + (\pi/L_y)^2$. It can be seen that all the propagation directions $\theta$ are covered by the contour, while $\theta$ in $90^\circ$ - $360^\circ$ can be deduced from the symmetry of the slowness surfaces. The band structures can be used to calculate the frequency ranges of stop bands and to analyse whether different slowness surfaces come into contact with each other, also to study the veering and locking phenomena and so on [Mace & Manconi, 2012; Perkins & Mote, 1986].

## 3.3 Application example - Beam grid

In this section, the proposed CWFEM2D is applied to a periodic beam grid. The obtained result is compared with the one issued from other methods, such as classical WFEM on full model, the reference and also the result obtained by the 2D spatial Discrete Fourier Transformation (DFT2D) of a stationary displacement field. The selection of the modes is discussed and the criterion to assure the convergence of the band structure is provided. The wave beaming effects phenomenon is studied in this section from slowness surface as well as from the harmonic forced displacement field. The wave-mode duality is observed and discussed at the bounding frequencies of stop bands.

### 3.3.1 Description of the model

A beam grid is a simple form of 2D periodic structure that can be tested experimentally. Langley and Bardell [Langley & Bardell, 1997] have carried out the experimental test on a beam grid constructed from strips of aluminium with bolted joints. The same structure is used here in order to compare the results of proposed method with their results. The periodic grid structure is constructed from an orthogonal array of aluminium strips as shown in Fig. 3.3. The strips are of rectangular cross-section with 19.06 mm $\times$ 1.59mm. The distance between the strips in the $x$-direction is of 115.38 mm, and in the $y$-direction is of 71.43 mm. At the crossing points, the joints are considered as a mass point of $6 \times 10^{-3}$ kg.

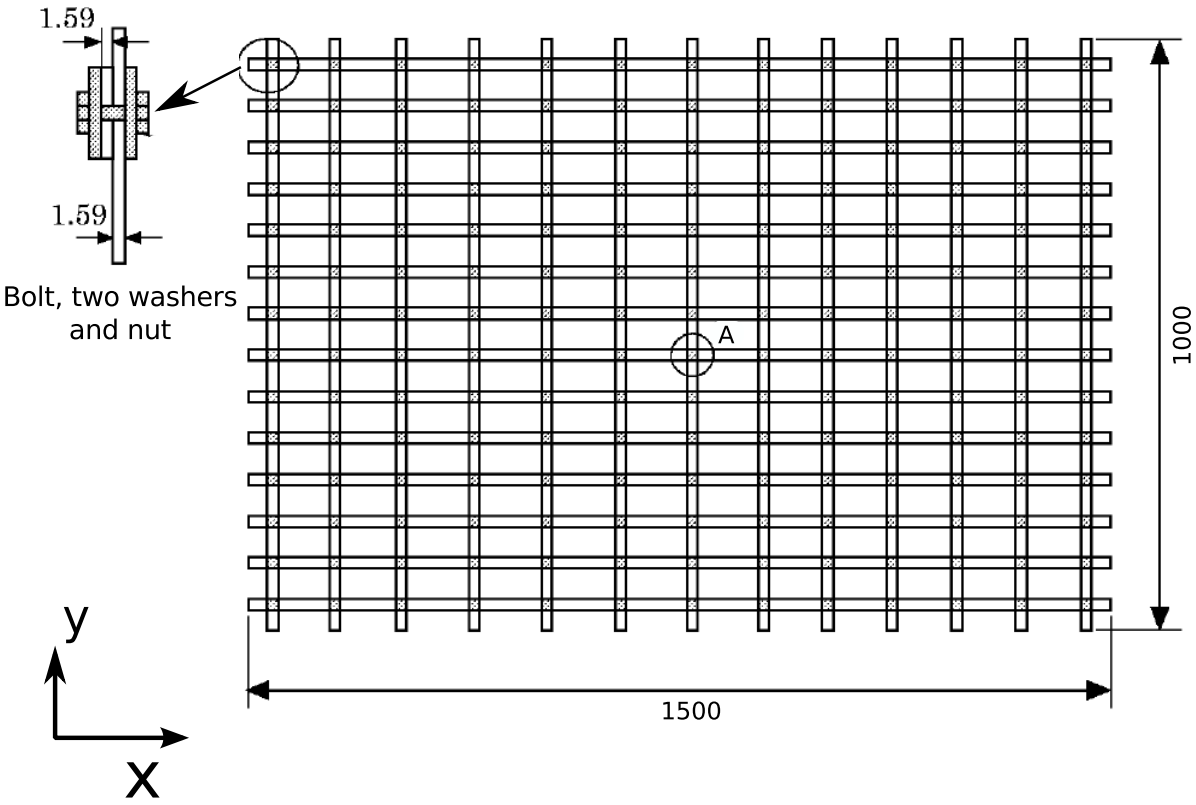


Figure 3.3: A schematic of the experimental structure in reference [Langley & Bardell, 1997]. The excitation is at position A. All dimensions are in mm.

The unit cell of the beam grid used in CWFEM2D is shown in Fig. 3.4. It should be noted that the choice of unit cell is not unique, but it is always wise to choose a unit cell with minimal number of boundary coordinates to decrease the computational size [Mead, 1975b]. The unit cell in Fig. 3.4 consists of $[\mathbf{q_1}, \mathbf{q_2}, \mathbf{q_3}, \mathbf{q_I}]$, therefore some of the terms in the formulations are not included. In the unit cell, the beam is modelled using element Beam188 in ANSYS. Beam188 is a three dimensional two-node Timoshenko element, with 6 DOFs per node. Since the cross-section of the beam is rectangular, the in-plane displacement and the out-of-plane displacement are decoupled. The present analysis is restricted to the out-of-plane bending of the beam components so the DOFs related to in-plane movement are fixed to zero, subsequently only ROT$X$, ROT$Y$ and U$Z$ are considered as DOFs. The joints are taken account as mass point. 1/2 mass is added at $\mathbf{q_1}$ and 1/4 mass is added to $\mathbf{q_2}$ and $\mathbf{q_3}$. So the whole beam grid with $(2 \times 1/4 + 1/2) = 1$ mass at the joint can be obtained by repeating this unit cell. The studied frequency range is between 0 - 1.5 kHz. To assure that each wavelength contains 10 elements, the two beams are both meshed with 30 elements.

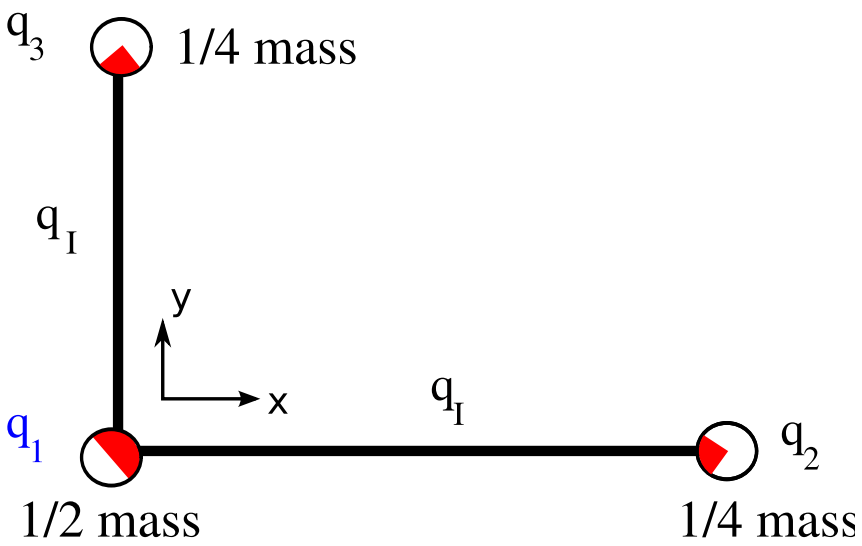


Figure 3.4: Unit cell of the beam grid

### 3.3.2 The selection of the modes and the convergence study

The selection of the internal modes $\Psi_{\mathtt{C}}$ among $\Psi_{\mathtt{I}}$ will be discussed here. The study is limited on the first four slowness surfaces, with $f_{max} = 2078$ Hz. The 2D plot of slowness surfaces - band structure is employed to compare the results from different selections. The four curves in band structure, from lower frequency to higher frequency are illustrated in blue, green, red and cyan color. They correspond respectively to 1st, 2nd, 3rd, 4th slowness surface.

The first internal mode with fixed boundary is around 630 Hz. The band structure with no internal mode taken is compared with the band structure for full model in Fig. 3.5. It can be seen that the reduced model is able to predict precisely only the 1st slowness surface (up to 370 Hz). For the 1st slowness surfaces, the model is fully represented by the constraint modes of the boundary $\Psi_{\mathtt{bd}}$. Boundary DOFs are considered as master DOFs and internal DOFs are considered as slave DOFs. It verifies the mesh of the unit cell in homogeneous waveguide when applying WFEM. For most of the homogeneous waveguide, a short representative section without internal nodes is taken as the unit cell. The frequency of the first internal mode of the section may be much higher compared to the frequency range of interest, which is limited into the 1st slowness surface. Accordingly, no internal mode needs to be taken, the model is fully represented by the boundary nodes. In this case, the internal node is not needed in the mesh of unit cell in homogeneous waveguides.

The band structure of the reduced model with the first 9 internal modes is compared with the one of the full model, as shown in Fig. 3.6. The reduced model includes all the fixed boundary mode $\Psi_{\mathtt{I}}$ with natural frequencies lower than $3 * f_{max}$. The error of the reduced model compared to the full model is estimated to be less than 0.15%, as shown in Fig. 3.7. It can be seen that the error increases with slowness surfaces, for the blue curve, it corresponds to the error on 1st

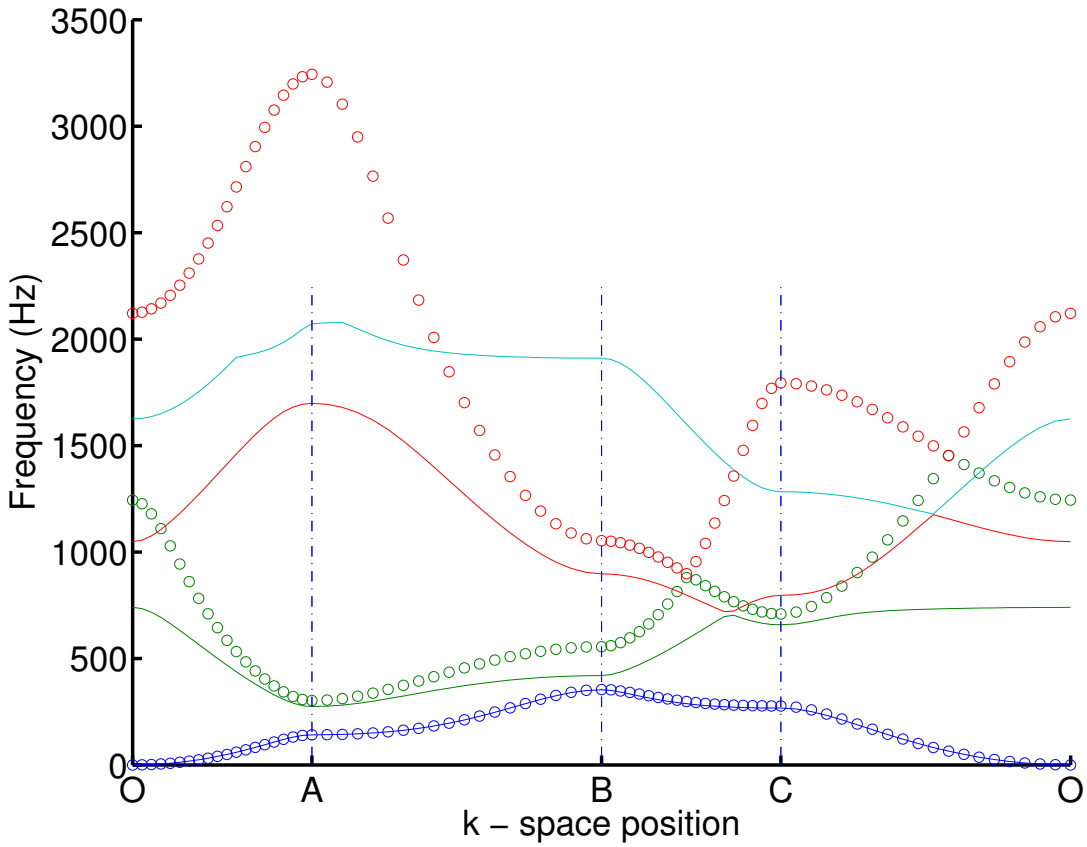


Figure 3.5: Band structure with WFEM2D on full model (−), CWFEM2D on reduced model with no internal mode (○)

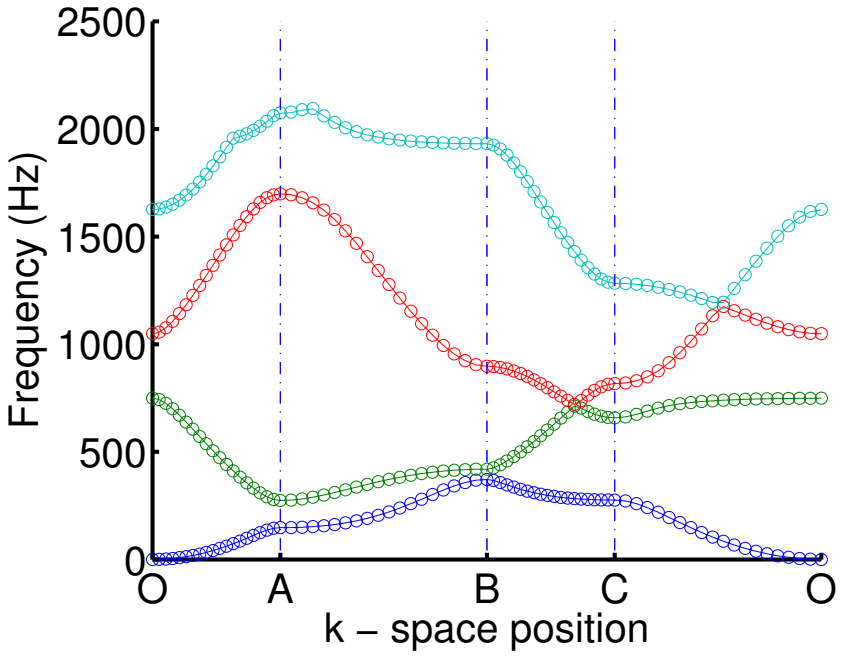


Figure 3.6: Band structure with WFE2DM on full model (−), CWFEM2D on reduced model with the first 9 internal modes (○)

slowness. The green, red and cyan curves correspond respectively the error on 2nd, 3rd and 4th slowness. It can be concluded that the reduced model converges to the full model when the internal modes with fixed boundary under $3 * f_{max}$ are retained.

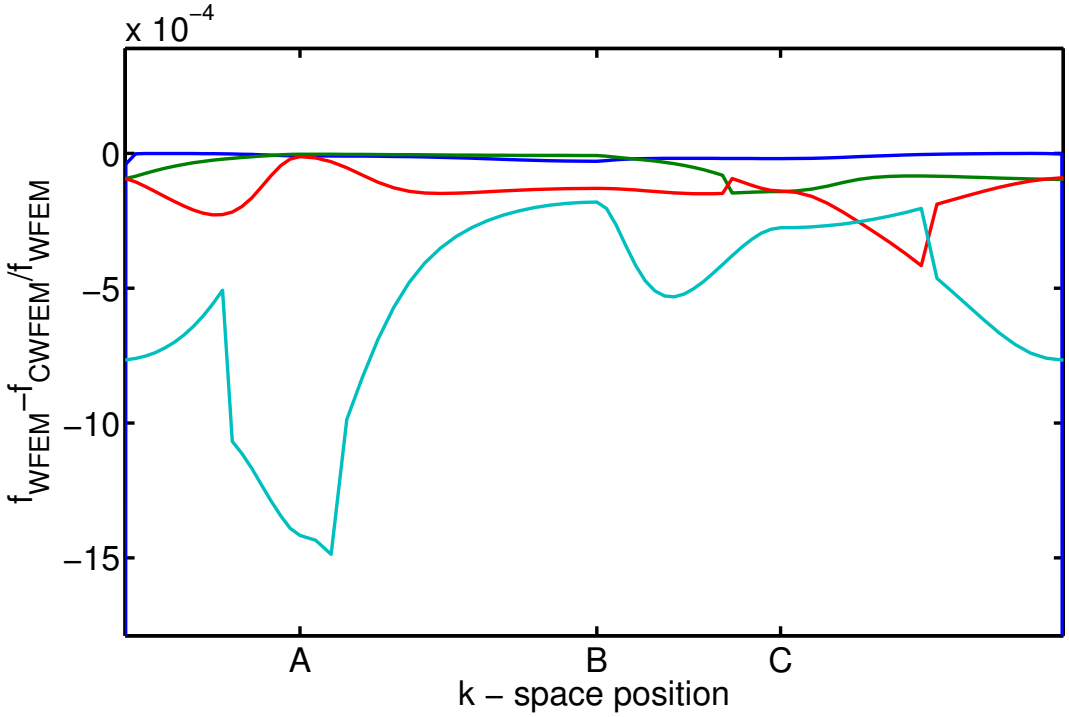


Figure 3.7: Error between the full model and reduced model with$3 * f_{max}$

| | Computation time | Number of DOFs |
|---|---|---|
| WFEM2D on full model | Linear eigen problem: 6.3 s | 183 |
| CWFEM2D on reduced model | Modal analysis: 0.02 s<br>Linear eigen problem: 0.04 s | 16 |
| Gain | 99% | 91% |

Table 3.2: Computation time to calculate the band structure

Lots of propagation characteristics can be observed from the band structure in Fig. 3.6. It can be seen that the 2nd curves comes into contact with the 3rd one in zone BC and the 3rd curves comes into contact with the 4th one in zone CO. This means that their corresponding slowness surfaces come into contact at this zone. The partial stop bands for $x-$ or $y-$ directions can be seen, while no absolute stop band is found.

The comparisons of the computation time of the full model with the reduced model are shown in Table 3.2. The gain of the proposed CWFEM2D on reduced model is more than 90% in both the number of DOFs and computation time. For more complicated 2D periodic waveguides such as stiffened plates which is studied in chapter 5, the reduction allow completing the study from days to less than half an hour.

### 3.3.3 The slowness surfaces and wave beaming effects

As shown by band structure in Fig. 3.6, with an appropriate selection of modal basis, CWFEM2D can predict precisely the propagation characteristics in the beam grid such as the slowness surfaces.

#### 3.3.3.1 The slowness surfaces

There are four slowness surfaces in the frequency range studied. It can be seen from Fig. 3.8 that the 3rd surface comes into contact with the 2nd surface and the 4th one, which is also shown in the band structure in Fig. 3.6. The gradient of the surfaces corresponds to the energy flow vector field, which is given in Fig.3.10(b)-3.12(b) in the following subsection.

#### 3.3.3.2 The $k$-space and wave beaming effect

The $k$-space will be calculated here to study the wave beaming effects of the structure at fixed frequency.

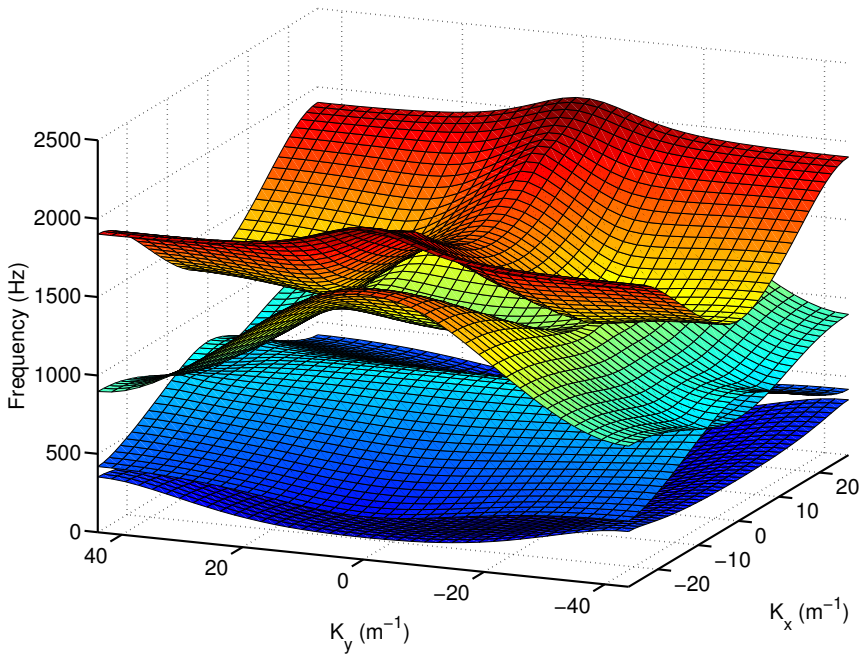


Figure 3.8: First four slowness surfaces

**The validation of CWFEM2D by the reference** $k$-space at 100 Hz, 600 Hz, 800 Hz, 1 kHz, 1.2 kHz, 1.4 kHz are given in the reference [Langley & Bardell, 1997], which are compared with the results calculated by the proposed CWFEM2D in Fig. 3.9. It can be seen that the results obtained on the reduced model conform to the results in the reference.

**DFT2D of a harmonic stationary displacement field** The stationary response of a finite periodic structure under an harmonic loading is obtained by the sum of excited waves from the loading point and reflected waves at the boundaries. The stationary response is related to the propagative travelling waves. So the DFT2D of the harmonic stationary field of a finite structure can give information about travelling waves in an infinite structure. The following steps should be carried out (1) A beam grid with 100 unit cells in the $x$-direction and 100 unit cells in the $y$-direction is modelled using FEM. (2) A harmonic excitation is placed at the center of the clamped grid. The out-of-plane stationary displacement field is normalized by the force and then extracted for post-processing. (3) The spatial DFT2D is applied to the real part of extracted displacement field, which leads to wavenumbers $k_x$ and $k_y$. So the $k$-space at the excitation frequency can be deduced.

In Fig. 3.10-3.12, the $k$-space obtained by the DFT2D are compared with the ones obtained by the CWFEM2D (illustrated by the green points), and differences between the two methods are very small. So it can be concluded that results obtained from a harmonic response of a finite structure with enough cells can be used to predict the propagation characteristics in an infinite structure. The harmonic displacement field will also be measured experimentally to deduce

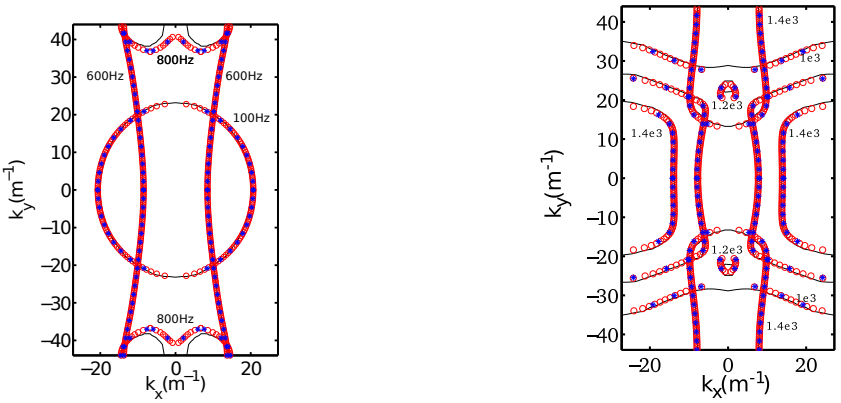


(a) 100Hz, 600Hz, 800Hz (b) 1kHz,1.2kHz,1.4kHz

Figure 3.9: $k$-space: Langley (–), WFEM2D on completed model ($*$), CWFEM2D on reduced model ($\circ$)

$k$-space in chapter 4.

At low frequency, e.g., 100 Hz, the beam grid behaves like an orthotropic homogeneous plate with equivalent parameters. The direction of the energy flow is shown in Fig. 3.10(c), which is normal to the $k$-space contour. It can also be seen from the displacement field in Fig. 3.10(b), the vibrational energy spreads in all directions.

However, at higher frequency such as 600 Hz and 1000 Hz, as shown in Fig. 3.11 and Fig. 3.12, the normal directions of the section are limited to specific angles. At 600 Hz, the wave is privileged in $x$ direction and forbidden in $y$ direction, which indicates a partial stop band for $y$ direction. However, at 1000 Hz, the wave is privileged in $y$ direction and forbidden in $x$ direction. The wave beaming effect phenomenon is observed. This phenomenon is confirmed by the experimental study of Langley & Bardell [1997]. Their test beam grid consisted of 13 strips in $x$ direction and 14 strips in $y$ direction, as shown in Fig. 3.3. One side of beam grid was treated with a damping sheet to produce a non-reverberant structure. The loss factor was averaged to be around 0.1. They observed also that the response of the system under harmonic excitation of 600 Hz showed strong beaming in $x$ direction, while strong beaming in $y$ direction was observed for harmonic excitation of 1000 Hz.

The wave beaming phenomena corresponds to partial stop bands for the forbidden direction. It can also be seen from the band structure in Fig. 3.6 that no wave at 600 Hz can be found between zone CO (wave to $y$ direction), and no wave at 1000Hz can be found between zone OA (wave to $x$ direction).

The directivity of the propagation can also be observed on the displacement field under the harmonic excitation at corresponding frequency, with energy concentrating to a limited angle, as show in 3.11(c) and 3.12(c).

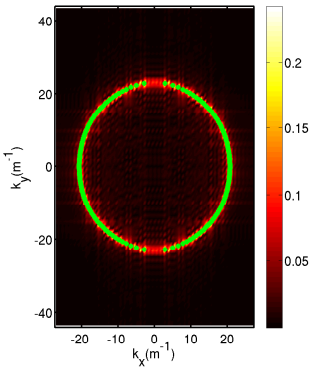


(a) $k$-space

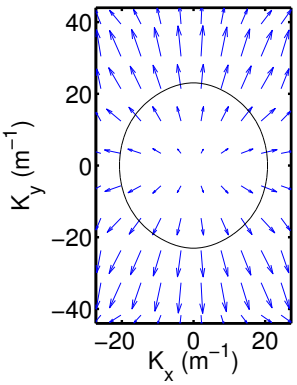


(b) Energy flow vector field (1st slowness surface)

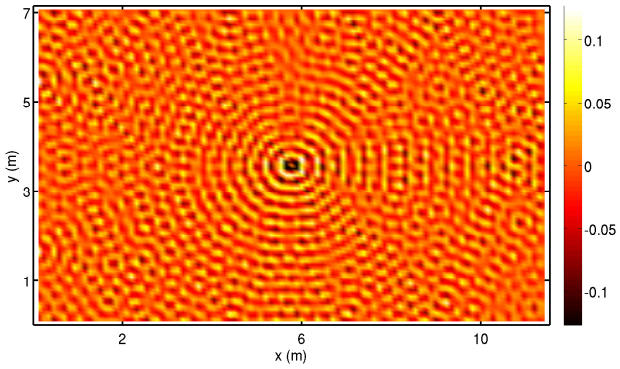


(c) Harmonic displacement field of 100 $\times$ 100 unit cells

Figure 3.10: Propagation without directivity at 100 Hz

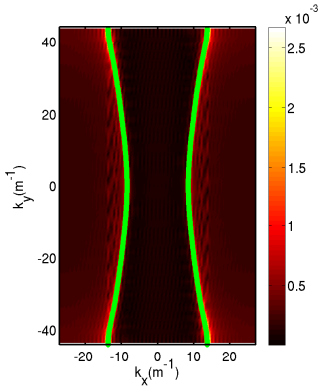


(a) $k$-space

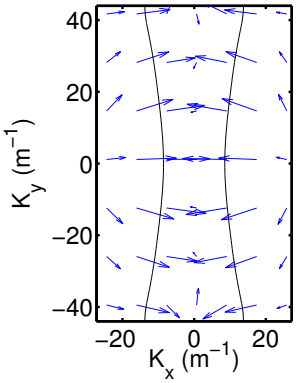


(b) Energy flow vector field (2nd slowness surface)

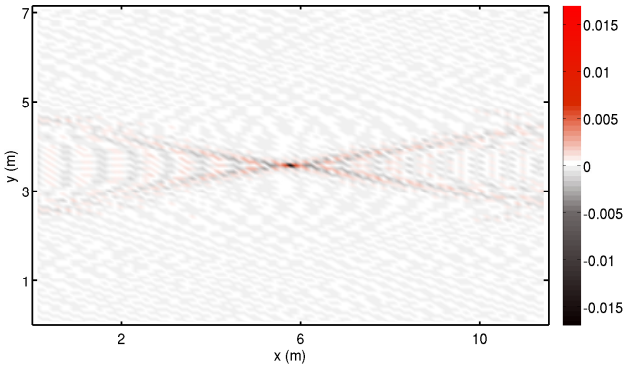


(c) Harmonic displacement field of 100 $\times$ 100 unit cells

Figure 3.11: Propagation with directivity to the $x$-direction at 600 Hz

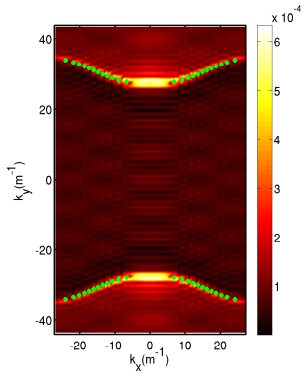


(a) $k$-space

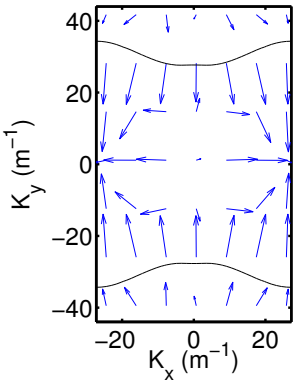


(b) Energy flow vector field (3rd slowness surface)

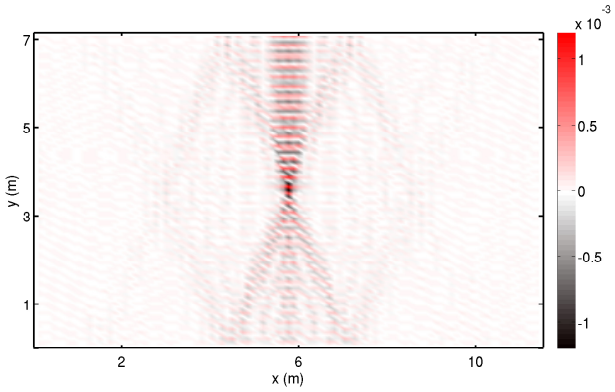


(c) Harmonic displacement field of 100 $\times$ 100 unit cells

Figure 3.12: Propagation with directivity to the $y$-direction at 1000 Hz

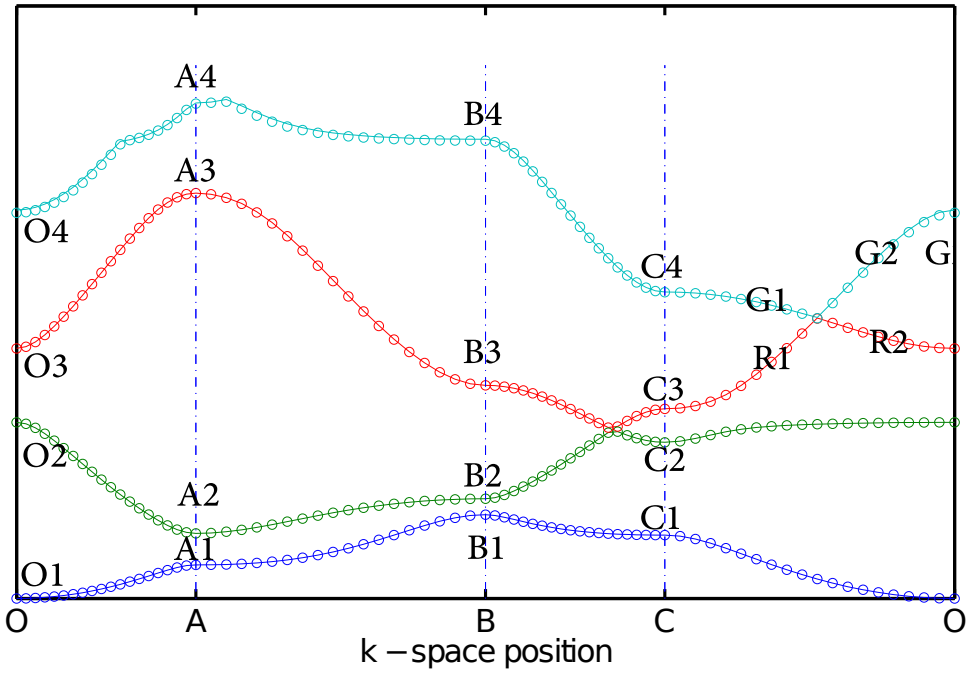


Figure 3.13: The points at where $\phi$ is studied on the band structure

### 3.3.4 The wave shape $\phi$

The wave description of the propagation contains $(k_x, k_y, \omega, \phi)$. Until now only $\omega = f(k_x, k_y)$ are studied. The wave shape $\phi$ calculated by CWFEM can be used to understand how the wave propagate in the structure and identify the types (longitudinal, shearing, flexural) of the waves propagating in the structures. The notation of the points where wave shapes are studied is given in Fig. 3.13. The wave shapes are given on a rectangular domain, which is easily extended from the unit cell.

The wave shape at intersecting points "R1", "R2", "G1", "G2" are given in Fig. 3.14. It can be seen that the wave shape at "R1" is similar to the one at "G2", and the wave shape at "G1" is similar to the one at "R2". If the waves are tracked by the correlation between complex mode shape using the Modal Assurance Criterion (MAC) [Ewins, 1984], the waves between OC should be tracked as shown in Fig. 3.15. It indicates that in one slowness surface, we may have two different kinds of wave shapes. So attention need to be drawn when it comes to the interpretation of the wave types along the slowness surfaces. Or it may be more suitable to classify the slowness surfaces by the wave shapes rather than frequency values.

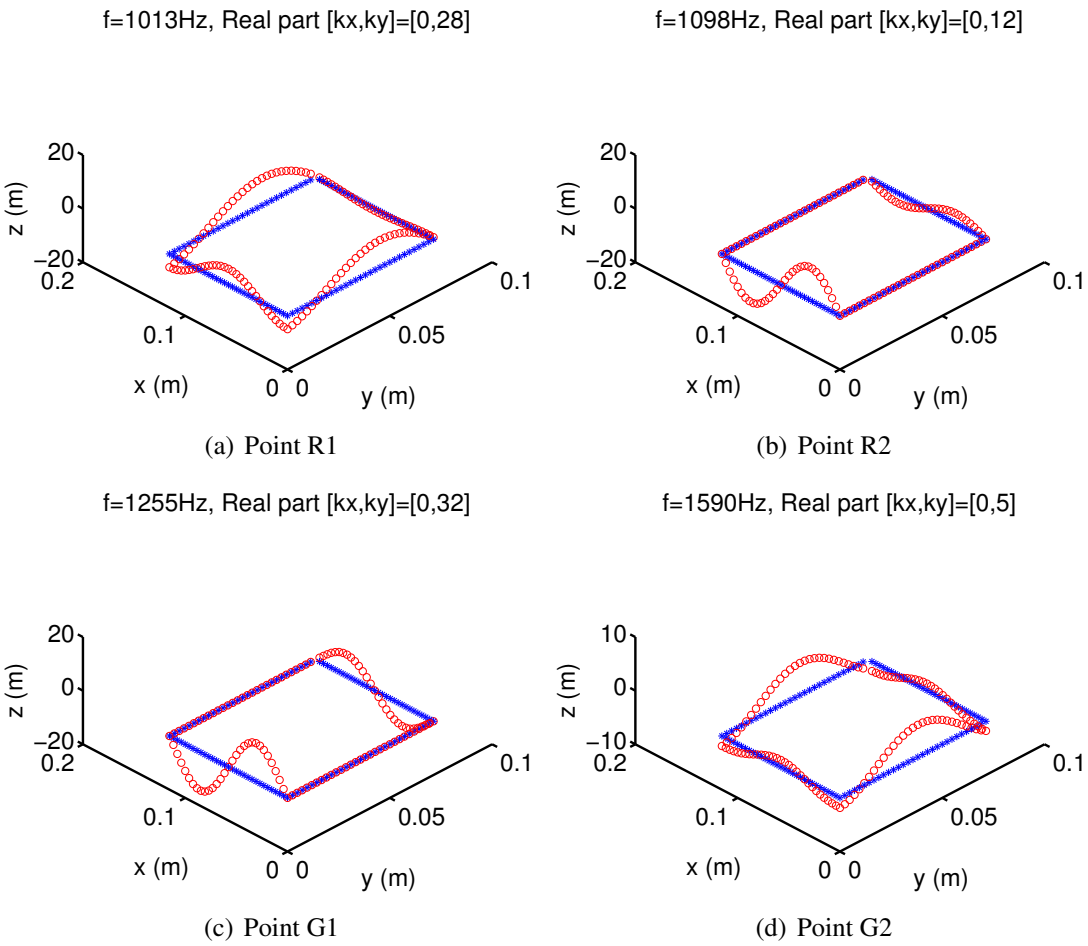


(a) Point R1 (b) Point R2

(c) Point G1 (d) Point G2

Figure 3.14: Propagative wave shape (CO), deformated (o), undeformed (∗)

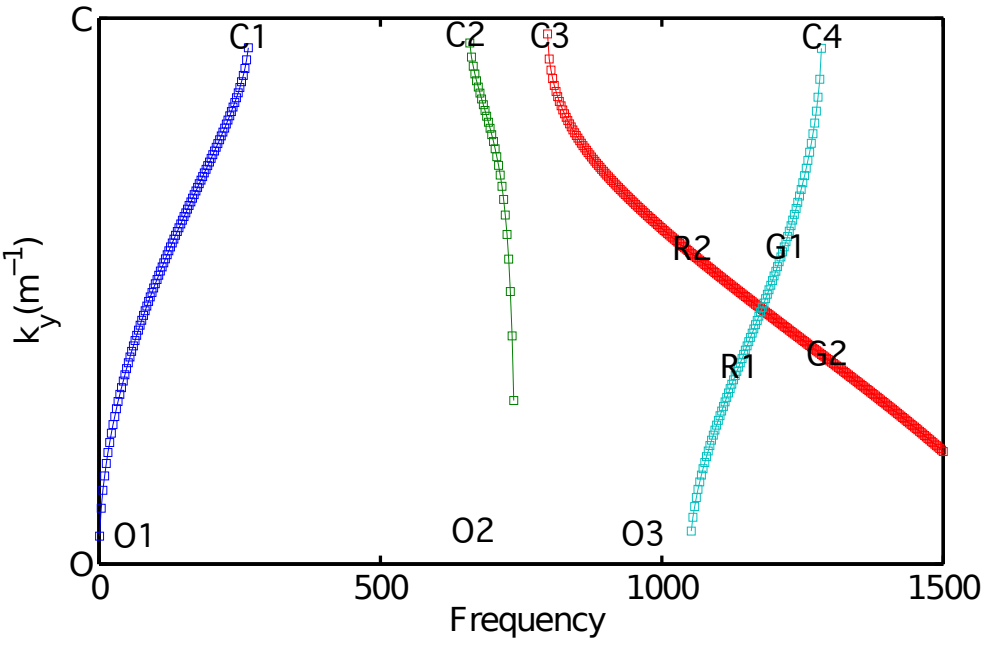


Figure 3.15: The waves between OC tracked using the MAC

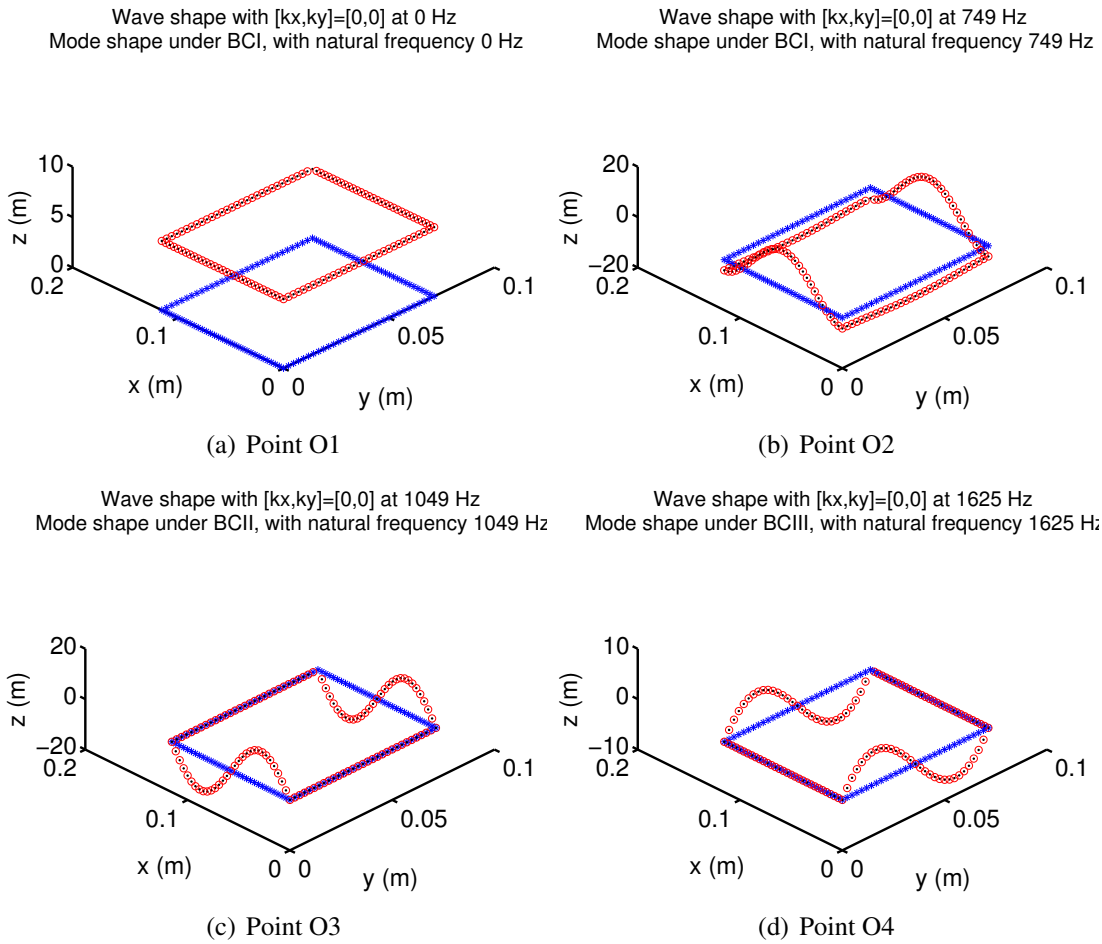


(a) Point O1 (b) Point O2

(c) Point O3 (d) Point O4

Figure 3.16: Wave shape at "O" (o), Cell mode shape (·), Undeformed unit cell (∗)

## 3.3.5 Wave-mode duality observation at bounding frequencies

In this subsection, the waves shapes and waves frequencies at bounding points "O", "A", "B", "C" are studied. Four types of boundary conditions of a symmetric unit cell are found, under which the cell modes correspond to the stationary waves at bounding points.

### 3.3.5.1 The wave shapes at bounding points of stop band

Firstly, the wave shapes at bounding points of stop band are given. The frequencies as well as the wave shapes are given at the bounding points "O", "A", "B", "C" in Fig. 3.16, Fig. 3.17, Fig. 3.18 and Fig. 3.19, respectively.

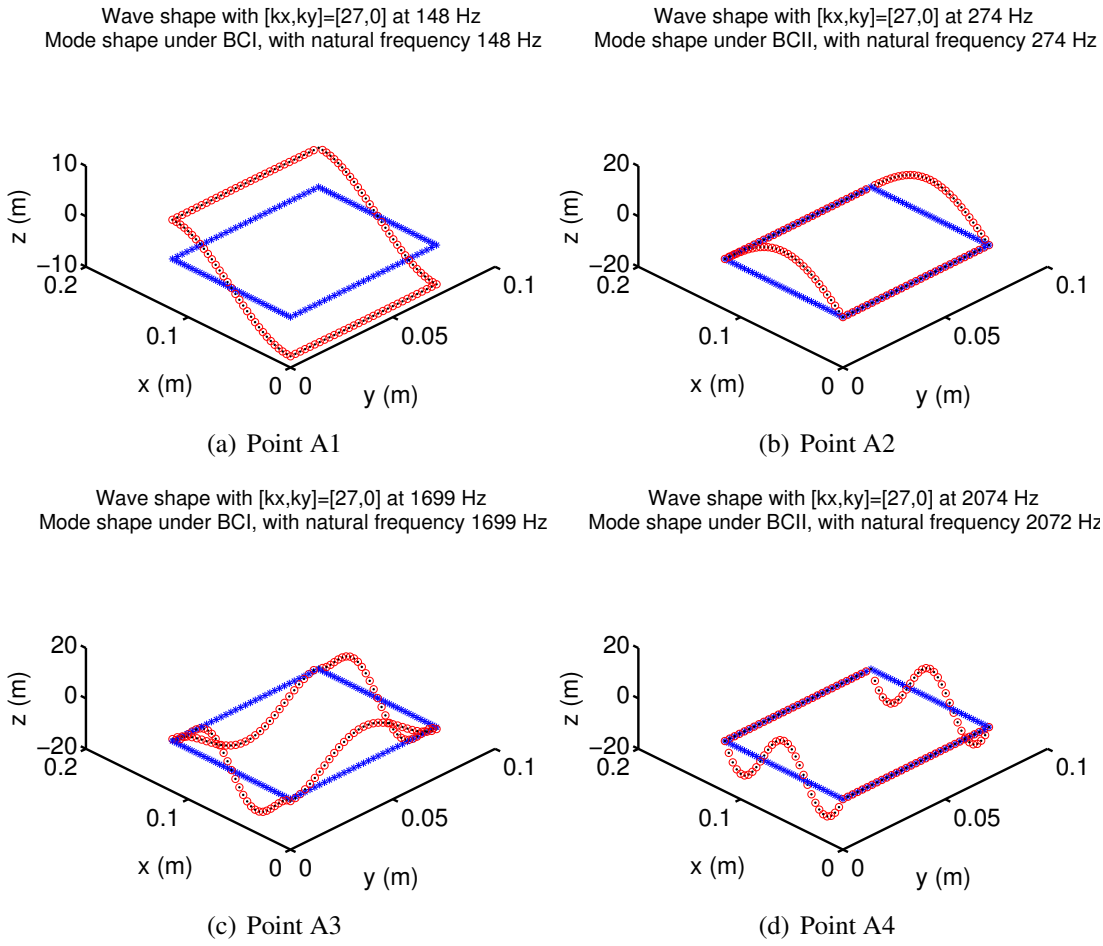


(a) Point A1 (b) Point A2

(c) Point A3 (d) Point A4

Figure 3.17: Wave shape at "A" (o), Cell mode shape ($\cdot$), Undeformed unit cell ($*$)

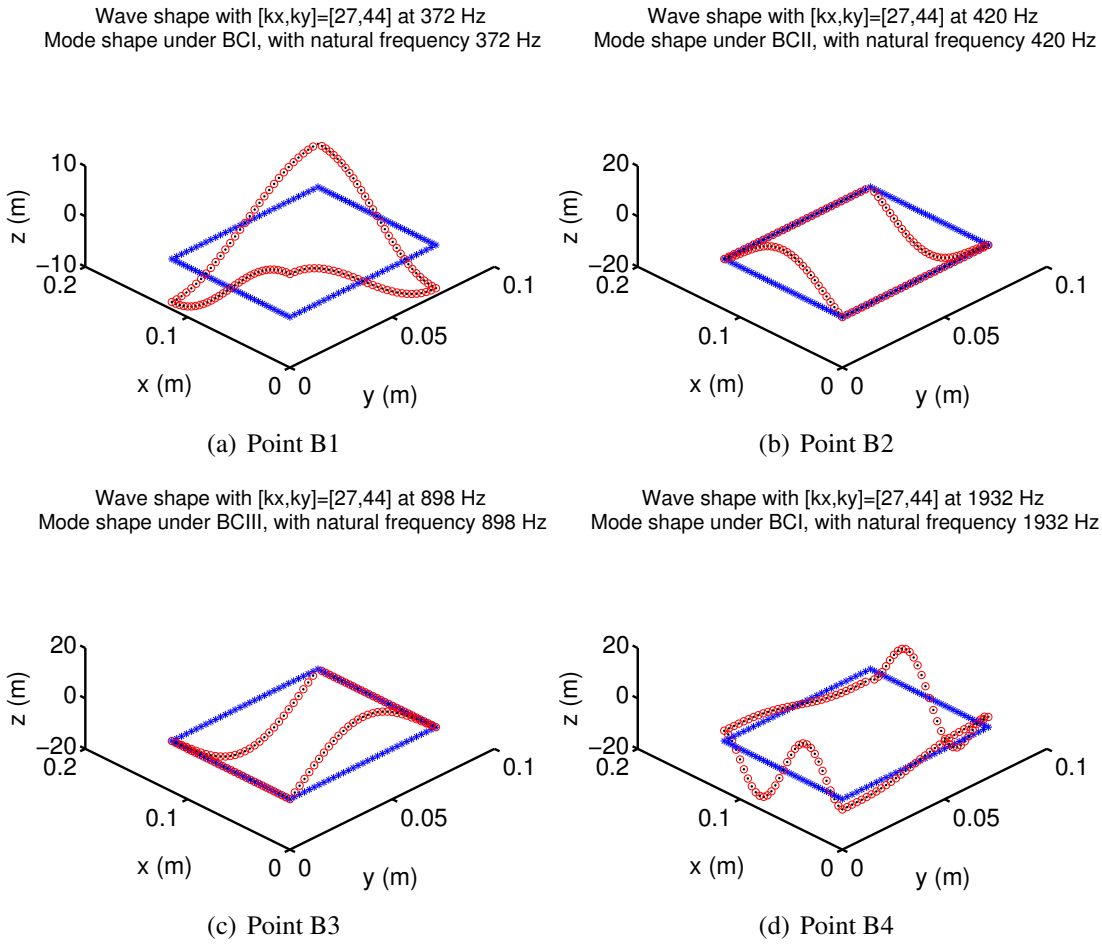


(a) Point B1 (b) Point B2

(c) Point B3 (d) Point B4

Figure 3.18: Wave shape at "B" (o), Cell mode shape ($\cdot$), Undeformed unit cell ($*$)

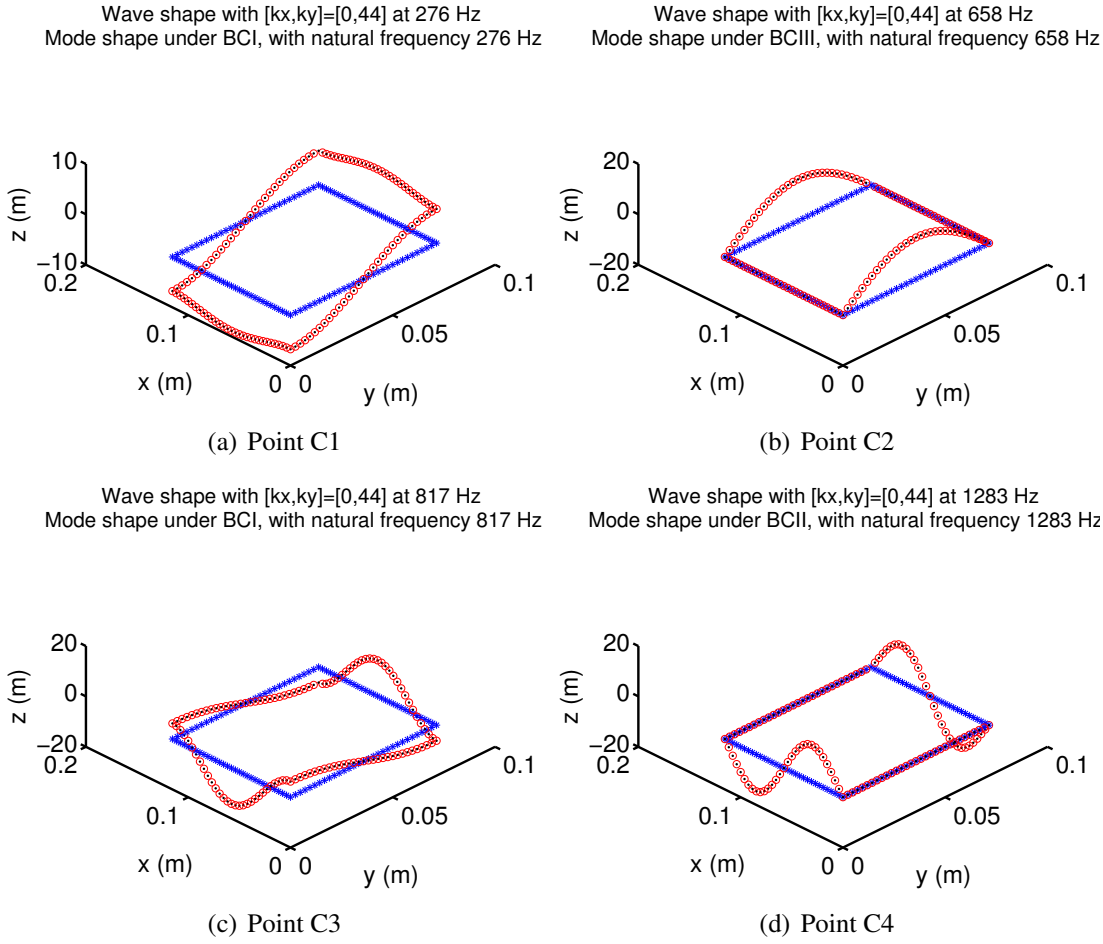


(a) Point C1 (b) Point C2

(c) Point C3 (d) Point C4

Figure 3.19: Wave shape at "C" (o), Cell mode shape (·), Undeformed unit cell (∗)

#### 3.3.5.2 The mode of the symmetric unit cell

The symmetric unit cell on which the cell modes are computed is given in Fig. 3.20. Since only the out-of-plane movement is taken account into, the displacement DOFs $\mathbf{q}$ contain only ROT$X$, ROT$Y$ and U$Z$. As mentioned in 1.5.4, there are two types of coupling DOFs between

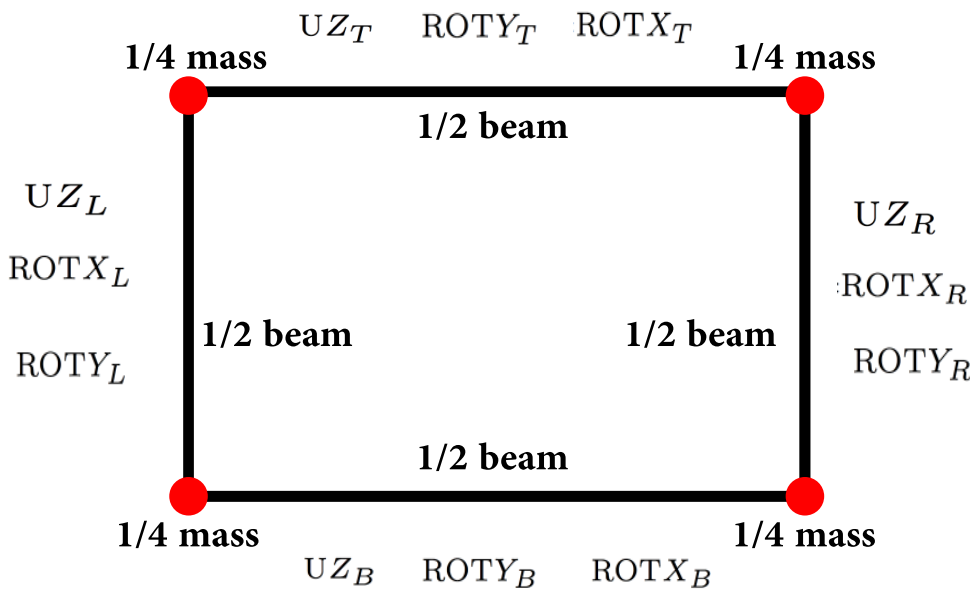


Figure 3.20: The symmetric unit cell of the beam grid on which the natural frequencies are computed

symmetric adjacent unit cells. Suppose a plane wave propagating in the $x$-direction, the structure can be considered as a 1D waveguide, the coupling coordinates contain only $\mathbf{q_L}$ and $\mathbf{q_R}$. According to the definition of type I and type II in 1.5.4, U$Z$ and ROT$X$ belong to the type I DOFs, ROT$Y$ belongs to the type II DOFs. For a plane wave propagating in the $y$-direction, the coupling DOFs contain $\mathbf{q_B}$ and $\mathbf{q_T}$, U$Z$ and ROT$Y$ belong to the type I DOFs, while ROT$X$ belongs to the type II DOFs.

With $\lambda_x = 1$, it means that the coupling DOFs $\mathbf{q}_\text{L}$ and $\mathbf{q}_\text{R}$ should have the same displacement. For symmetric mode in the $x$-direction, the type II DOFs at left and right side should be the oppose sign, so they should both equal to zero. For anti-symmetric mode in the $x$-direction, the type I DOFs should be zero. Similarly, the boundary conditions for all the cases with $\lambda_x = \pm 1$ and $\lambda_y = \pm 1$, symmetric and anti-symmetric modes can be deduced, which are given in Table 3.3. It can be seen that there are only four types of boundary conditions (BCI, BCII, BCIII, BCIV).

The cell modes under 2500 Hz at these types of boundary conditions are calculated and corresponding frequencies are given in Tab. 3.4. All the natural frequencies and mode shapes can be found among the bounding points “O”, “A”, “B”, “C” of the first six slowness surfaces. The natural frequencies in Tab. 3.4 are plotted in the band structure of the first six slowness

| | $\lambda_x = 1$ | | $\lambda_x = -1$ | |
|---|---|---|---|---|
| | Sym mode | Anti-sym mode | Sym mode | Anti-sym mode |
| $\lambda_y = 1$ Sym mode | (BC I) ROT$Y_L$=ROT$Y_R$=0 ROT$X_B$=ROT$X_T$=0 | (BC II) U$Z_L$=U$Z_R$=0 ROT$X_L$=ROT$X_R$=0 ROT$X_B$=ROT$X_T$=0 | (BC II) U$Z_L$=U$Z_R$=0 ROT$X_L$=ROT$X_R$=0 ROT$X_B$=ROT$X_T$=0 | (BC I) ROT$Y_L$=ROT$Y_R$=0 ROT$X_B$=ROT$X_T$=0 |
| $\lambda_y = 1$ Anti-sym mode | (BC III) ROT$Y_L$=ROT$Y_R$=0 U$Z_B$=U$Z_T$=0 ROT$Y_B$=ROT$Y_T$=0 | (BC IV) U$Z_L$=U$Z_R$=0 ROT$X_L$=ROT$X_R$=0 U$Z_B$=U$Z_T$=0 ROT$Y_B$=ROT$Y_T$=0 | (BC IV) U$Z_L$=U$Z_R$=0 ROT$X_L$=ROT$X_R$=0 U$Z_B$=U$Z_T$=0 ROT$Y_B$=ROT$Y_T$=0 | (BC III) ROT$Y_L$=ROT$Y_R$=0 U$Z_B$=U$Z_T$=0 ROT$Y_B$=ROT$Y_T$=0 |
| $\lambda_y = -1$ Sym mode | (BC III) ROT$Y_L$=ROT$Y_R$=0 U$Z_B$=U$Z_T$=0 ROT$Y_B$=ROT$Y_T$=0 | (BC IV) U$Z_L$=U$Z_R$=0 ROT$X_L$=ROT$X_R$=0 U$Z_B$=U$Z_T$=0 ROT$Y_B$=ROT$Y_T$=0 | (BC IV) U$Z_L$=U$Z_R$=0 ROT$X_L$=ROT$X_R$=0 U$Z_B$=U$Z_T$=0 ROT$Y_B$=ROT$Y_T$=0 | (BC III) ROT$Y_L$=ROT$Y_R$=0 U$Z_B$=U$Z_T$=0 ROT$Y_B$=ROT$Y_T$=0 |
| $\lambda_y = -1$ Anti-sym mode | (BC I) ROT$Y_L$=ROT$Y_R$=0 ROT$X_B$=ROT$X_T$=0 | (BC II) U$Z_L$=U$Z_R$=0 ROT$X_L$=ROT$X_R$=0 ROT$X_B$=ROT$X_T$=0 | (BC II) U$Z_L$=U$Z_R$=0 ROT$X_L$=ROT$X_R$=0 ROT$X_B$=ROT$X_T$=0 | (BC I) ROT$Y_L$=ROT$Y_R$=0 ROT$X_B$=ROT$X_T$=0 |

Table 3.3: Boundary conditions (BC) of symmetric unit cell

surfaces in Fig. 3.21.

| | ROT$Y_L$=ROT$Y_R$=0 | U$Z_L$=U$Z_R$=0 ROT$X_L$=ROT$X_R$=0 |
|---|---|---|
| ROT$X_B$=ROT$X_T$=0 | ( BC I ) 0Hz (O1) 148Hz (A1) 274Hz (C1) 372Hz (B1) 749Hz (O2) 817Hz (C3) 1699Hz (A3) 1930Hz (O5) 1932Hz (B4) 2165Hz (A5) | ( BC II) 274Hz (A2) 420Hz (B2) 1049Hz (O3) 1283Hz (C4) 2072Hz (A4) |
| U$Z_B$=U$Z_T$=0 ROT$Y_B$=ROT$Y_T$=0 | (BC III) 658Hz (C2) 898Hz (B3) 1625Hz (O4) 2049Hz (C5) | (BC IV) 2199Hz (A6) |

Table 3.4: Natural frequencies under 4 boundary conditions and corresponding points in band structures

The cell modes shapes under these boundary conditions are also plotted in Fig. 3.16 - 3.19. It can be seen that all the bounding points in the first four slowness surfaces (“O1-O4”,“A1-A4”, “B1-B4”, “C1-C4”) correspond to cell modes shown in Tab. 3.4, not only they have the same the frequencies, the wave shapes correspond also to the mode shapes.

As a conclusion, the cells modes at these boundary conditions are equivalent to the waves at bounding frequencies. The equivalence found by Mead [1975a,b] for 1D periodic structures is

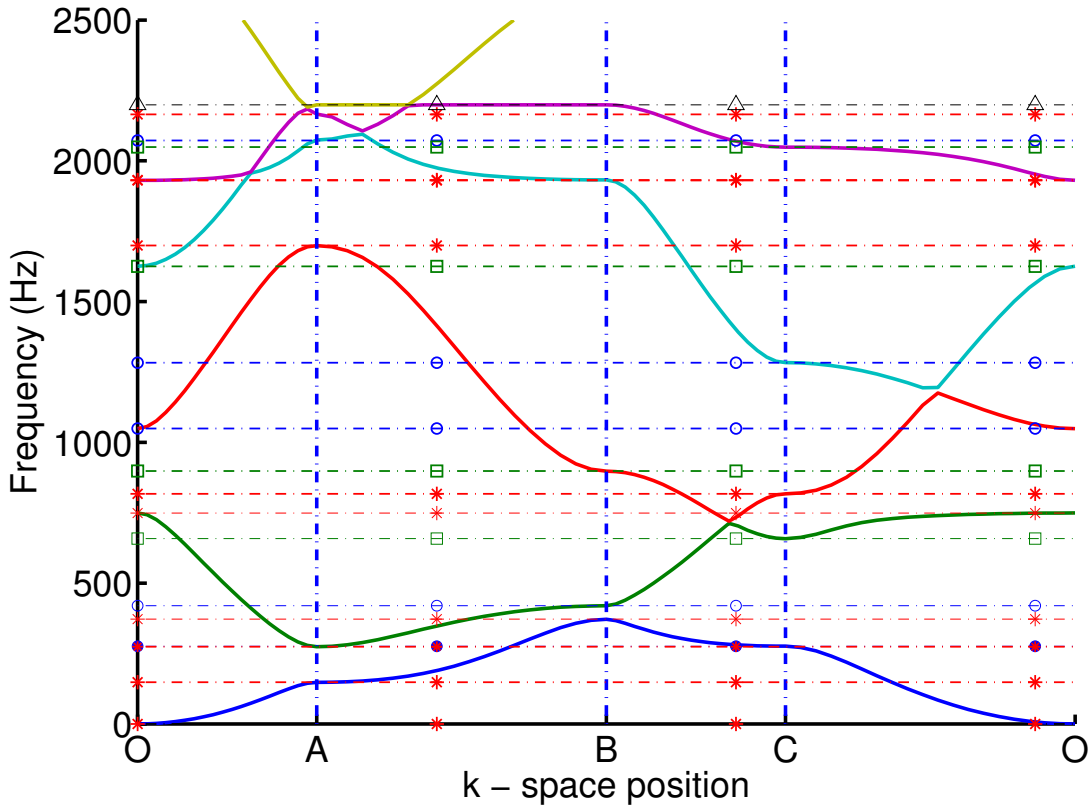


Figure 3.21: Band structure with natural frequencies of symmetric unit cell. BCI ($\cdot - *$), BCII ($\cdot - \circ$), BCIII ($\cdot - \square$), BCIV ($\cdot - \triangle$)

extended to 2D beam grid, as mentioned in section 1.5.4. According to wave-mode duality, cell modes correspond to stationary wave, so it is concluded that the waves at bounding frequencies of stop bands are stationary.

## 3.4 Conclusions

This chapter has extended the CWFEM to 2D periodic structures. The effectiveness of the proposed method was illustrated on a beam grid. Main conclusions of this work can be drawn as follows:

- The formulation of CWFEM2D was provided, which can be used to study the wave propagation in 2D periodic structures. The validation of the proposed method was realized through others methods: the results in the reference [Langley & Bardell, 1997], WFEM on full model, and DFT2D of the forced harmonic displacement field.

- The proposed CWFEM combines the advantages of CMS and WFEM. The method fully exploits the periodic propriety of the structure. It allows studying the influences of local

dynamic on global behaviour of structure with less computational cost. In the given numerical example, a gain of 99% in computation time was obtained.

- To assure the convergence of CWFEM, the truncated modes $\mathbf{\Psi_C}$ should include all the fixed boundary modes $\mathbf{\Psi_I}$ with natural frequency lower than three times of maximum frequency investigated. At low frequency, the static condensation of the internal DOFs can be applied, with boundary DOFs as master DOFs and internal DOFs as slave DOFs.

- CWFEM is able to predict the high frequency behaviour of the beam grid, where the directivity of the propagation appears.

- The iso-frequency contour of slowness surfaces obtained from a harmonic response of a finite structure can be used to predict the propagation characteristics in an infinite structure.

- The waves at bounding frequency of stop bands are stationary, they correspond to the cell modes under certain boundary conditions.

# Chapter 4

# Numerical and experimental investigation on wave propagation features in perforated plates

## 4.1 Introduction

Perforated plates are widely used in various engineering domain, from the micro-perforated panel used for noise control to the perforated structures used in heat exchangers of nuclear power plants. This chapter is dedicated to apply the proposed CWFEM to study perforated plates. The first objective of this chapter is to propose wave-based homogenization methods based on the dispersion relation identified by the CWFEM. The second objective is to validate CWFEM by the experimental result, by comparing the $k$-space obtained issued from the two approaches. The chapter can be considered as the application of CWFEM at low frequency to determine the equivalent model. However, the high frequency behaviour such as wave beaming effect phenomenon is also predicted by CWFEM and verified by experimental approach.

## 4.2 Determination of equivalent parameters at low frequency

For some special engineering applications, more than a million holes are contained in perforated plate (e.g., a shadow mask in a monitor). So it might be difficult to use the FEM to study these structures since it is time-consuming. The simplest way is to replace the perforated plate with an equivalent solid plate (homogenized plate) considering the weakening effect of the holes.

Several mode-based homogenization method are developed for the perforated plates, among which the method proposed by Jhung & JO [2006] is reviewed in 1.3.4.3 where its disadvantages are also discussed. To conquer these disadvantages, the wave-based approach to determine the equivalent parameters in perforated plate is proposed here.

### 4.2.1 Equivalent isotropic model

In a thin isotropic plate with Young's Modulus $E^*$ , density $\rho^*$, Poisson ratio $\nu^*$ and thickness $t^*$, there are three kinds of plane waves propagating inside: longitudinal wave with wavenumber $k_l$, shear wave with wavenumber $k_s$ and flexural wave with wavenumber $k_f$. The analytical forms for their dispersion relations are given in Eq. (4.1a) - Eq. (4.1c).

$$k_l = \omega / \sqrt{\frac{E^*}{(1-\nu^{*2})\rho^*}} \tag{4.1a}$$

$$k_s = \omega / \sqrt{\frac{E^*}{2(1+\nu^*)\rho^*}} \tag{4.1b}$$

$$k_f^2 = \omega / \sqrt{\frac{E^* t^{*2}}{12(1-\nu^{*2})\rho^*}} \tag{4.1c}$$

$$\rho^* t^* = (1-\tau)\rho t \tag{4.1d}$$

If a homogenized isotropic model of a perforated plate exists at low frequency, it means that the waves propagate in the same way to all directions, the wavenumber $k$ should be the same for all the directions. In that case, the $k$-space should form a circle. The waves propagating in all directions can be represented by the wave propagating in the $x$-direction. Once the dispersion relation to the $x$-direction is predicted by the CWFEM, it can be used to determine the equivalent parameters of its homogenized plate. An additional equation can be given in Eq. (4.1d) which supposes the mass per unit surface of the homogenized model is the same as the full model. $\tau$ is the ratio of the hole surface compared to total surface. So the four equivalent parameters $E^*, \rho^*, \nu^*, t^*$ can be determined using the four equations in Eq. (4.1). Although solutions found are frequency-dependant, they vary little in the low frequency range, as shown in the numerical examples afterwards. However, one may find big variations of the equivalent parameters around 0 Hz. The variation are mainly caused by numerical errors since the wavenumbers $k_l$ and $k_s$ could be very small around 0 Hz. So the equivalent values found around 0 Hz should be omitted.

The proposed wave-based method consists of the 4 following steps (1) Use CWFEM to derive the $k$-space for the flexural, longitudinal and shear waves, find the limit frequency for which the $k$-space is still a circle (2) Below the frequency limit, compute the dispersion relation of the wave propagating in the $x$-direction, identify different wave types according to their deformation shapes and find the values of $k_l, k_s, k_f$ (3) Solve Eq. (4.1) to find the equivalent

parameters. Eliminate the values with big variation around 0 Hz and compute the average value in the frequency range as the final equivalent parameters.

### 4.2.2 Equivalent orthotropic model for in-plane waves and isotropic model for out-of-plane waves

The weakening effects of the holes on the plate may be different for the in-plane waves and out-of-plane waves. Different models may be considered for the descriptions of two types of waves. An isotropic in-plane behaviour and an orthotropic out-of-plane behaviour may be identified (for model 3 in Tab. 4.1). Here the related formulations are given. The generalized-stress/generalized-strain relationship of a thin plate is governed by the following equation:

$$\begin{pmatrix} \mathbf{N} \\ \mathbf{M} \end{pmatrix} = \begin{bmatrix} \mathbf{A} & \mathbf{B} \\ \mathbf{B}^{\mathrm{T}} & \mathbf{D} \end{bmatrix} \begin{pmatrix} \boldsymbol{\varepsilon} \\ \boldsymbol{\chi} \end{pmatrix} \tag{4.2}$$

where $\boldsymbol{\chi}$ represents the curvature for the bending of the plate and $\boldsymbol{\varepsilon}$ represents the membrane strain for the in-plane motion. The matrices $\mathbf{A}, \mathbf{B}, \mathbf{D}$ are to be determined for the equivalent model. In thin perforated plates, the in-plane waves and out-of-plane waves are uncoupled, hence we have $\mathbf{B} = \mathbf{0}$. The matrices $\mathbf{D}$ and $\mathbf{A}$ are to be determined for the out-of-plane movement and in-plane movement respectively.

#### 4.2.2.1 Isotropic model for out-of-plane waves

The curvature for the bending of the plate $\boldsymbol{\chi}$ can be written as:

$$\boldsymbol{\chi} = \begin{pmatrix} -\dfrac{\partial^2 w}{\partial x^2} \\ -\dfrac{\partial^2 w}{\partial y^2} \\ -2\dfrac{\partial^2 w}{\partial x \partial y} \end{pmatrix} \tag{4.3}$$

$\mathbf{M}$ represents bending stress resultant per unit length

$$\mathbf{M} = \begin{pmatrix} M_x \\ M_y \\ M_{xy} \end{pmatrix} = \int_{-\frac{t}{2}}^{\frac{t}{2}} z \begin{pmatrix} \sigma_{xx} \\ \sigma_{yy} \\ \sigma_{xy} \end{pmatrix} dz = \mathbf{D}\boldsymbol{\chi} \tag{4.4}$$

For isotropic material, we have [Géradin & Rixen, 1992]

$$\mathbf{D} = \frac{Et^3}{12(1-\nu^2)} \begin{bmatrix} 1 & \nu & 0 \\ \nu & 1 & 0 \\ 0 & 0 & \frac{1-\nu}{2} \end{bmatrix} \tag{4.5}$$

The value in $\mathbf{D}$ can be determined once the wavenumber of the flexural wave is known, using the relation in Eq. (4.1c) and Eq. (4.1d).

$$\mathbf{D} = \frac{\omega^2 \rho^* t^*}{k_f^4} \begin{bmatrix} 1 & \nu & 0 \\ \nu & 1 & 0 \\ 0 & 0 & \frac{1-\nu}{2} \end{bmatrix} \tag{4.6}$$

The mass per unit surfaces remains the same as before with $\rho^* t^* = (1-\tau)\rho t$.

#### 4.2.2.2 Orthotropic model for in-plane waves

For the in-plane wave, the following relation can be established, with $\mathbf{N}$ the membrane stress resultant per unit length and $\boldsymbol{\varepsilon}$ the membrane strain

$$\mathbf{A}\boldsymbol{\varepsilon} = \mathbf{A} \begin{pmatrix} \varepsilon_{xx} \\ \varepsilon_{yy} \\ 2\varepsilon_{xy} \end{pmatrix} = \mathbf{N} = \begin{pmatrix} N_{xx} \\ N_{yy} \\ N_{xy} \end{pmatrix} = t \begin{pmatrix} \sigma_{xx} \\ \sigma_{yy} \\ \sigma_{xy} \end{pmatrix} \tag{4.7}$$

the strain-stress relations for an orthotropic material under plane-stress is as follows:

$$\begin{pmatrix} \sigma_{xx} \\ \sigma_{yy} \\ \sigma_{xy} \end{pmatrix} = \begin{bmatrix} \frac{E_x^*}{1-\nu_{xy}^*\nu_{yx}^*} & \frac{\nu_{yx}E_x^*}{1-\nu_{xy}^*\nu_{yx}^*} & 0 \\ \frac{\nu_{yx}^*E_x^*}{1-\nu_{xy}^*\nu_{yx}^*} & \frac{E_y^*}{1-\nu_{xy}^*\nu_{yx}^*} & 0 \\ 0 & 0 & G_{xy}^* \end{bmatrix} \begin{pmatrix} \varepsilon_{xx} \\ \varepsilon_{yy} \\ 2\varepsilon_{xy} \end{pmatrix} = \begin{bmatrix} C_{11} & C_{12} & 0 \\ C_{12} & C_{22} & 0 \\ 0 & 0 & C_{66} \end{bmatrix} \begin{pmatrix} \varepsilon_{xx} \\ \varepsilon_{yy} \\ 2\varepsilon_{xy} \end{pmatrix} \tag{4.8}$$

Suppose the same thickness is conserved, to find the value of the matrix $\mathbf{A}$, we need to determine the terms $C_{11}, C_{12}, C_{22}$ and $C_{66}$.

$$\mathbf{A} = t \begin{bmatrix} C_{11} & C_{12} & 0 \\ C_{12} & C_{22} & 0 \\ 0 & 0 & C_{66} \end{bmatrix} \tag{4.9}$$

Suppose $E_x^*$, $E_y^*$, $\nu_{xy}^*$, $\nu_{yx}^*$, $G_{xy}^*$, $\rho^*$ are the parameters of the orthotropic material, where $E_x^*/\nu_{xy}^* = E_y^*/\nu_{yx}^*$. For the plane wave propagating in angle $\theta$ with the $x$-direction, the wave vector can be expressed as a function of $\theta$ :

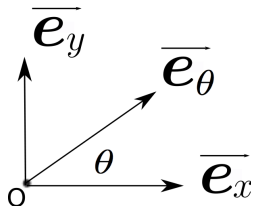


Figure 4.1: Wave vector in an orthotropic basis: notation

$$k_\theta \mathbf{e}_\theta = k_x \mathbf{e_x} + k_y \mathbf{e_y} = k_\theta(\cos\theta \mathbf{e_x} + \sin\theta \mathbf{e_y}) = k_\theta(a\mathbf{e_x} + b\mathbf{e_y}) \tag{4.10}$$

with $a = \cos\theta, b = \sin\theta$. The phase velocities for in-plane waves propagating in the orthotropic structure are given as follows [Royer & Dieulesaint, 2000]

$$c_{l,s}^2 = \frac{a^2 C_{11} + b^2 C_{22} + C_{66} \pm \sqrt{\Delta_m}}{2\rho^*} \tag{4.11}$$

with

$$\Delta_m = [(C_{11} - C_{66})a^2 + (C_{66} - C_{22})b^2]^2 + 4a^2b^2(C_{12} + C_{66})^2 \tag{4.12}$$

The upper sign for longitudinal wave ($c_l$), and lower sign for shear wave ($c_s$). Especially, we have

$$c_l(\theta = 0) = \sqrt{\frac{C_{11}}{\rho^*}}, \quad c_s(\theta = 0) = \sqrt{\frac{C_{66}}{\rho^*}}, \quad c_l(\theta = \frac{\pi}{2}) = \sqrt{\frac{C_{22}}{\rho^*}} \tag{4.13}$$

For a perforated plate, once the $k$-space at a fixed frequency is determined by CWFEM, the phase velocity of the waves can be easily deduced since $c_{l,s} = 2\pi f / k_{l,s}$. Then its homogenized plate with an orthotropic material can be found. If the mass per unit surface and the thickness are the same as the perforated plate, the equivalent density can be obtained as $\rho^* = (1 - \tau)\rho$. The velocities for wave propagating in $x$ and $y$ direction, as given in Eq. (4.13), can be used to compute $C_{11}$, $C_{22}$ and $C_{66}$. Then the value of $C_{12}$ can be determined by the wave propagating in another direction, knowing $k_x$ and $k_y$, the angle $\theta$ can be found since $\tan\theta = k_y/k_x$. Once the values $C_{11}, C_{12}, C_{22}, C_{66}$ are known, the components in matrix $\mathbf{A}$ can be determined using the relations in Eq. (4.9).

## 4.3 Experimental set-up and data post-processing

Experimental identification of wave propagation characteristics has proved to be a complicated task for two dimensional structures. The methods most often used to measure the propagating flexural wavenumbers within a structure [Chronopoulos *et al.*, 2013]. Here we use the experimental approach to identify the $k$-space of the flexural waves. It involves mainly two steps: First step is the measurement of the out-of-plane displacement field by laser scanner. Second step is the post-processing of the measurement data by DFT to deduce the $k$-space.

### 4.3.1 Experimental measurement of harmonic displacement field

The experimental setup is as shown in Fig. 4.2. The main measurement equipment is Polytec PSV-400 Scanning Vibrometer. Excitation signal is input into the electromagnetic vibration shaker, which transmits vibrations into the center of the perforated plate. A laser scanning head based on the Doppler effect is used to measure velocity of the plate, and it is transferred to the data manage system to study the vibration characteristic of the plate, the experimental signal flow is given in Fig. 4.3. The plate is hung with an elastic string to simulate free boundary conditions. No particular damping treatment of the plate is carried on.

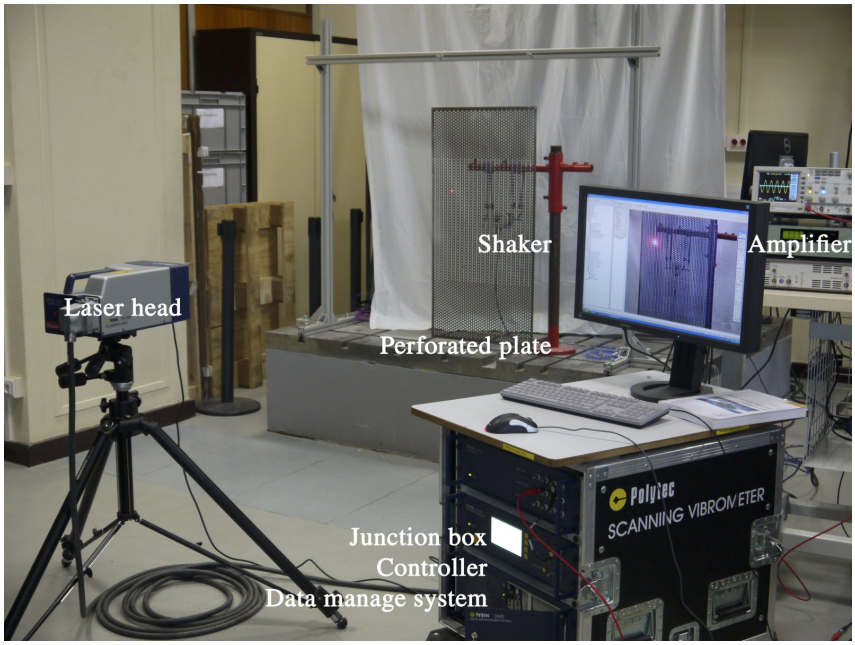


Figure 4.2: The experimental setup

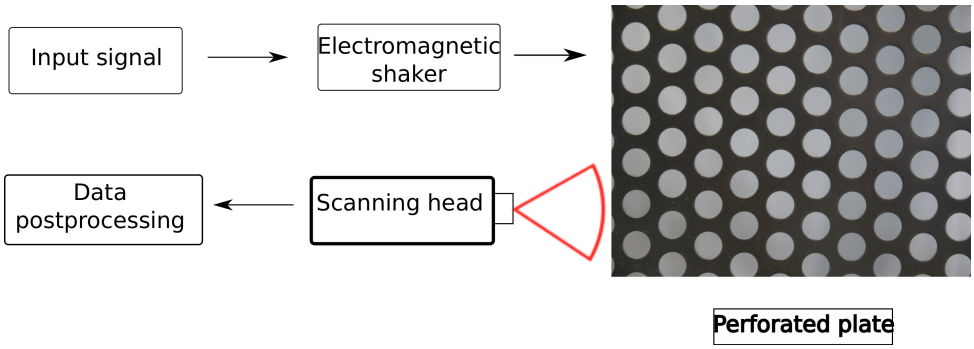


Figure 4.3: Schematic of the experimental signal flow

An impedance head with piezoelectric accelerometer and force gauge is mounted at the excitation point of the shaker. The coherence between the average amplitude of the scanning points and the force is examined to estimate the causality between the input and output.

For model 2 in Table.4.1, up to 3 kHz, a pseudo random signal of large band is used to excite

the plate, then the data manage system uses the Fast Fourier transformation (FFT) to calculate the frequency response function in all the excitation frequency range. However, the coherence input/output decreased in higher frequency (between 3 kHz - 3.5 kHz), as shown in Fig. D.1. To improve the coherence at higher frequency, the vibration energy is concentrated around an interested frequency. A pseudo random excitation centred at the frequency of interest with a width range of 20 Hz is used, good coherence is obtained in this case, as shown in Fig. D.2. During the whole experimental study, a FFT average of 10 measurements are performed at each scanned point, an overlap of 75% is used so as to minimize scanning time.

The spatial sampling of the scanning points equals to the length of the unit cell, the points at the corners of each unit cell are scanned. Once the forced response at all scanned points are obtained, the post-processing (DFT2D) allows deducing the $k$-space of the corresponding frequency, as illustrated in Fig. 4.4.

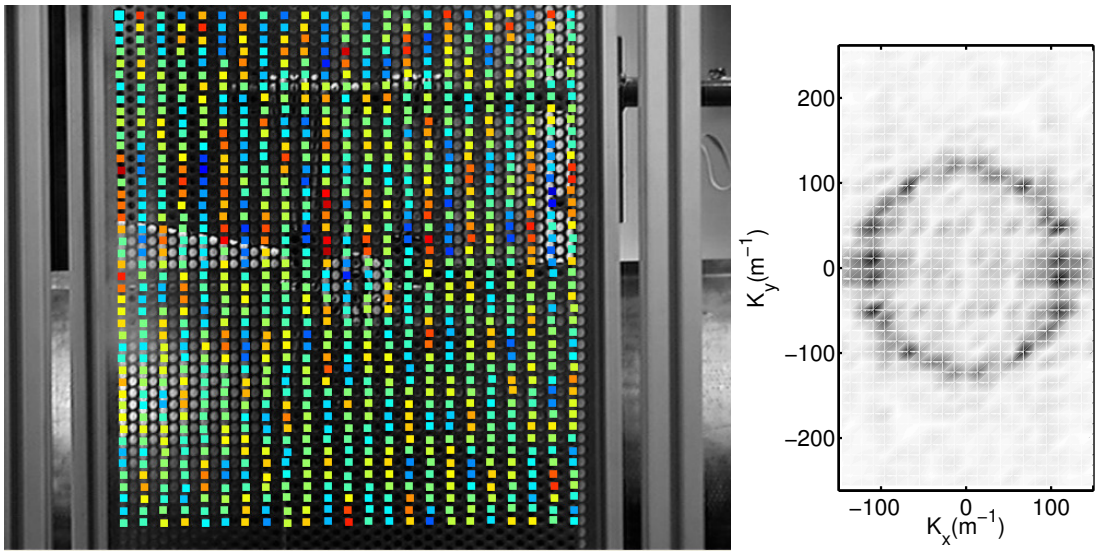


(a) Measured displacement field (b) $k$-space

Figure 4.4: Post-processing (DFT2D) of displacement field to obtain corresponding $k$-space

### 4.3.2 DFT2D - from displacement field to $k$-space

Once the displacement field is measured, the $k$-space can be deduced from DFT2D. In fact, there are several methods to post-process the experimental data, such as least squares methods [McDaniel & Shepard, 2000], discrete Fourier Transform (DFT) [Bolton *et al.*, 1998] and Prony series [Grosh & Williams, 1993]. The DFT presents two major advantages. First, it is bijective, having IDFT as its inverse transform, which allows easy filtration in the $k$-space. Second, it is very rapid. Through Fast Fourier Transform (FFT) like algorithm, very fast data processing can be achieved. However, for most of the case, the method has mainly three

drawbacks: Aliasing, leakage and $k$-space discrimination. For a spatial sampling of $L_x$ in the $x$-direction, and $L_y$ in the $y$-direction, aliasing refers to the error due to field discretization. DFT is $2\pi/L_x$ and $2\pi/L_y$ - periodic, which leads to erroneous value outside the domain $[-\pi/L_x, \pi/L_x]$ and $[-\pi/L_y, \pi/L_y]$. However, if $L_x$ and $L_y$ correspond to the smallest periods in the $x-$ and $y-$ direction of the 2D periodic structure, the wavenumbers lie always inside the domain $[-\pi/L_x, \pi/L_x]$ and $[-\pi/L_y, \pi/L_y]$. And $k$-space discrimination implies that the wavenumber is given only known over k-space grid, which may lead to poor resolution. For our experimental samples, there are more than 1000 unit cells in both plates, so $k$-space discrimination is no longer our concern. So DFT is employed to post-process the experimental data which assumes that:

1. **(H1)** The displacement field $\hat{w}(x, y)$ is given over a uniform spatial grid $\Big(x_i = i\Delta x, y_j = j\Delta y\Big)_{\substack{0\leq j\leq N_2-1\\ 0\leq i\leq N_1-1}}$. $\Delta x$ and $\Delta y$ are the space increments along $x$ and $y$ axis respectively, $N_1$ and $N_2$ are the number of measured data along $x$ and $y$ axis respectively.

2. **(H2)** Outside this grid the field is assumed to be $2D-$periodic ($\backslash$ symbol defines the euclidian ratio residue), namely :

$$\forall i, j \in \mathbb{N}^2\ , \quad \hat{w}(i\Delta x, j\Delta y) = \hat{w}\Big((i\backslash N_1)\Delta x, (j\backslash N_2)\Delta y\Big) \tag{4.14}$$

It can be readily shown that the family of exponential functions with discrete wavenumbers:

$$\Big(k_{xp} = p\Delta k_x, k_{yq} = q\Delta k_y\Big)_{\substack{0\leq q\leq N_2-1\\ 0\leq p\leq N_1-1}}$$

with $\Delta k_x = \frac{2\pi}{N_1\Delta x}$ and $\Delta k_y = \frac{2\pi}{N_2\Delta y}$ form a basis for complex functions space, so that the field $\hat{w}$ can be written in a single format :

$$\hat{w}(x_i, y_j) = \sum_{p=0}^{N_1-1}\sum_{q=0}^{N_2-1} \widehat{\hat{w}}(k_{xp}, k_{yq})\, \mathrm{e}^{\imath(k_{xp}x_i + k_{yq}y_j)} \tag{4.15}$$

The Discrete Fourier Transform $\hat{w} \longrightarrow \widehat{\hat{w}}$ is thus the following :

$$\widehat{\hat{w}}(k_{xp}, k_{yq}) = \frac{1}{N_1N_2}\sum_{i=0}^{N_1-1}\sum_{j=0}^{N_2-1} \hat{w}(x_i, y_j)\mathrm{e}^{-\imath(k_{xp}x_i + k_{yq}y_j)} \tag{4.16}$$

## 4.4 Numerical and experimental investigations on the perforated plates

In this section, the wave propagation features in different models of perforated plates have been studied. The dimensions of the perforated plates are given in Tab. 4.1. The pitches $L_x$ and $L_y$ correspond to the period length in the $x$ and $y$ directions. $\tau$ is the ratio of the hole surface compared to total surface. The thickness of the models is 1 mm except the model 1, which is of 3.6 mm. The thickness of plates is small compared to the pitch, so the theory of thin plate can be employed, the shell element is used in CWFEM and FEM. All the models are made by steel, with Young's Modulus $E$ = 210 GPa, Poisson ratio $\nu$ = 0.3, density $\rho$ = 7800 kg/m$^3$.

| Model | Hole shape | Penetration | Hole diameter | Pitch $L_x$ | Pitch $L_y$ | Hole surface ratio $\tau$ |
|---|---|---|---|---|---|---|
| 1 | Circulaire | Square | 30 | 72 | 72 | 14% |
| 2$*$ | Circulaire | Triangular | 8 | $12 \times \sqrt{3}$ | 12 | 40% |
| 3$*$ | Square | Square | 20 | 25 | 25 | 64% |
| 4 | Square | Square | 15 | 25 | 25 | 36% |
| 5 | Square | Square | 10 | 25 | 25 | 16% |
| 6 | Square | Square | 5 | 25 | 25 | 4% |

Table 4.1: Different models of perforated plate. $*$ refers to the experimental models (dimensions in mm)

In this section, CWFEM is applied to predict the wave propagation feature in all the five models. Experimental validations of the CWFEM are carried out on the model 2 and 3. Based on the dispersion relation, the homogenized plate of model 1, 2, 3 at low frequency are found and compared with the full models. The high frequency behaviour such as the wave-beaming effect is also observed and discussed in model 5.

### 4.4.1 Perforated plate with circular holes

The plate model 1 and 2 contain both circular holes, the definitions of their dimensions are shown in Fig. 4.5. In square penetration $L_x = L_y$, and in triangular penetration, $L_x = \sqrt{3}L_y$.

#### 4.4.1.1 Square penetration pattern

Model 1 is a perforated plate with circular holes in square penetration pattern, as shown in Fig. 4.5(a).

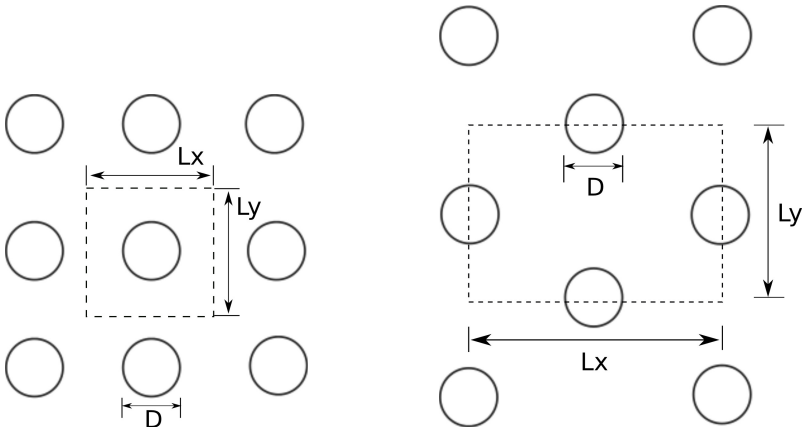


(a) Square penetration (b) Triangle penetration

Figure 4.5: Schema for perforated plates with circular holes and their unit cells used in CWFEM (- -)

**Homogenized model at low frequency** For the given model, it is verified that until 1500 Hz, both the flexural wave in Fig. 4.6(a) and the longitudinal wave (smaller wavenumber in Fig. 4.6(b)) propagate equally in all directions. The shear wave in Fig. 4.6(b) propagates in almost the same way in all directions. The method proposed to determine an equivalent isotropic model in 4.2.1 will be employed here. The frequency limit for the validation of the homogenized

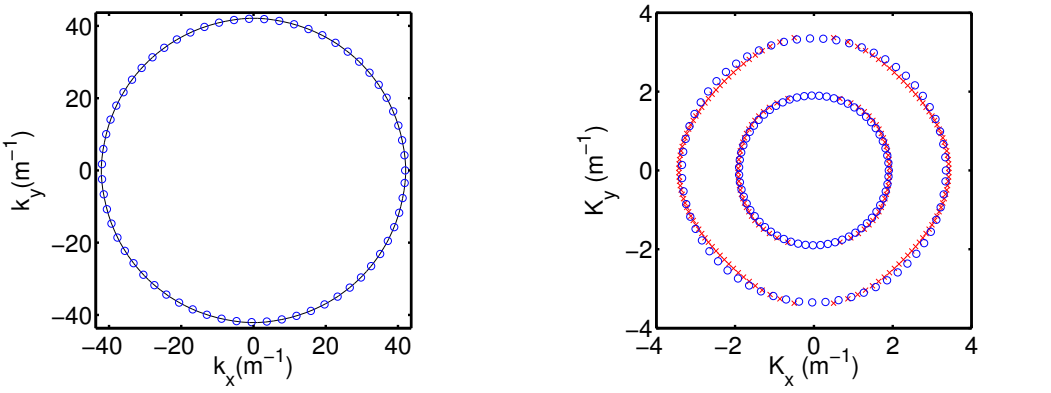


(a) $k$-space for flexural wave (b) $k$-space for longitudinal and shear waves

Figure 4.6: $k$-space at 1500 Hz (-/x) The curve fitting of a circle (o)

model is thus 1500 Hz. At this frequency, the wavelength for the flexural waves is around 0.15 m, which is almost twice of the period length. That differs from our previous knowledge that the homogenized model is valid only when the wavelength is much longer than the period length. The dispersion relation of the waves propagating in the $x$-direction is given in Fig. 4.7.

The three curves in Fig. 4.7 corresponds to three kinds of wave propagating in the $x$-direction. Their wave shapes are given on the boundary of the unit cell in Fig. 4.8. The smallest wavenumber corresponds to wave shape in Fig. 4.8(a), which is the longitudinal wave. The sec-

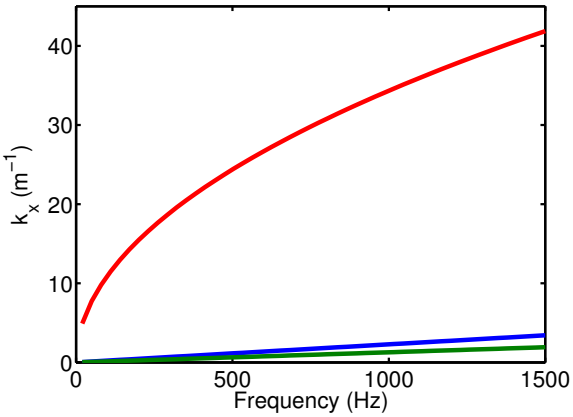


Figure 4.7: The dispersion relation in the $x$-direction

ond wavenumber corresponds to the shear wave shape in Fig. 4.8(b). The biggest wavenumber corresponds to flexural waves in Fig. 4.8(c). Once the wavenumbers $k_l$, $k_s$ and $k_f$ are determined, they can be used to determine the equivalent parameters.

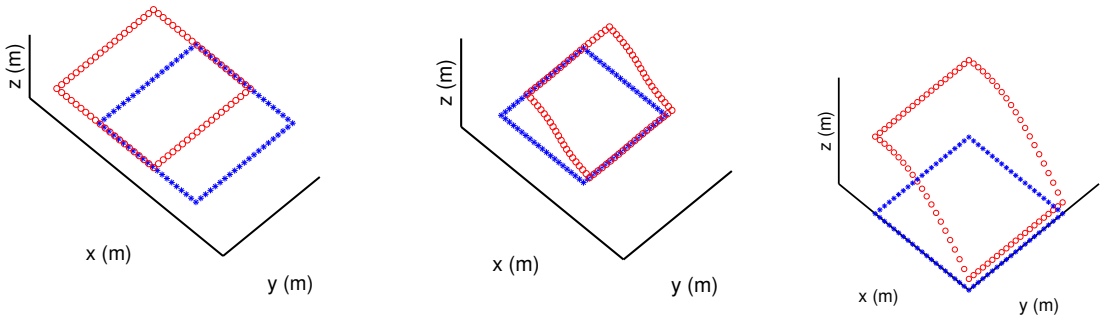


(a) Longitudinal wave shape (b) Shear wave shape (c) Flexural wave shape

Figure 4.8: Three kinds of wave shape (o) Undeformed unit cell ($*$)

It can be seen in Fig. 4.9 that the equivalent parameters remain stable in the frequency range. The average of these values is taken as the equivalent parameters, which leads to $E^* = 134$ GPa, $t^* = 3.8$ mm, $\nu^* = 0.37$, $\rho^* = 6458$ kg/m$^3$. The dispersion relation of the full model is compared to the one of the homogenized model in Fig. 4.10. The error is below 1% between the two results.

The validation of the homogenized model is also given on a finite plate through a modal analysis. The finite plate contains 6 cells in the $x$-direction and 6 cells in the $y$-direction. The model is clamped at the four sides. Natural frequencies of the homogenized model are compared to those of full model. Good correlation can be found between the two sets of natural

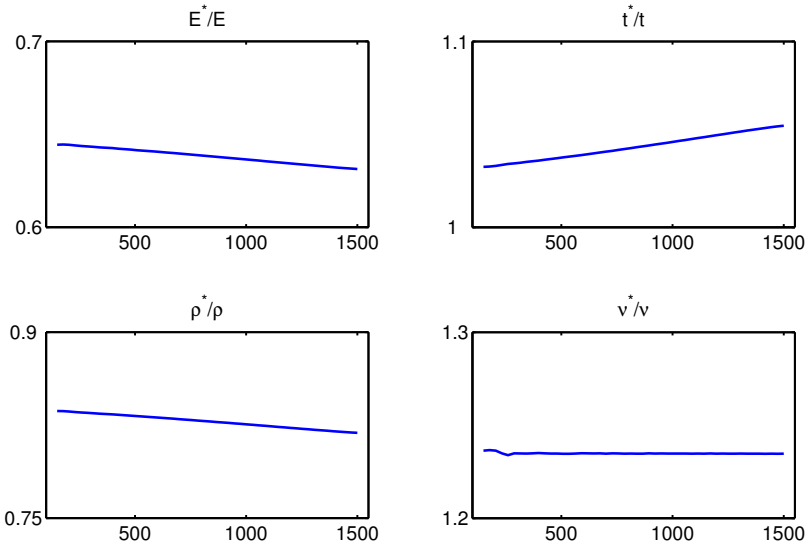


Figure 4.9: The equivalent parameters of the Model 1

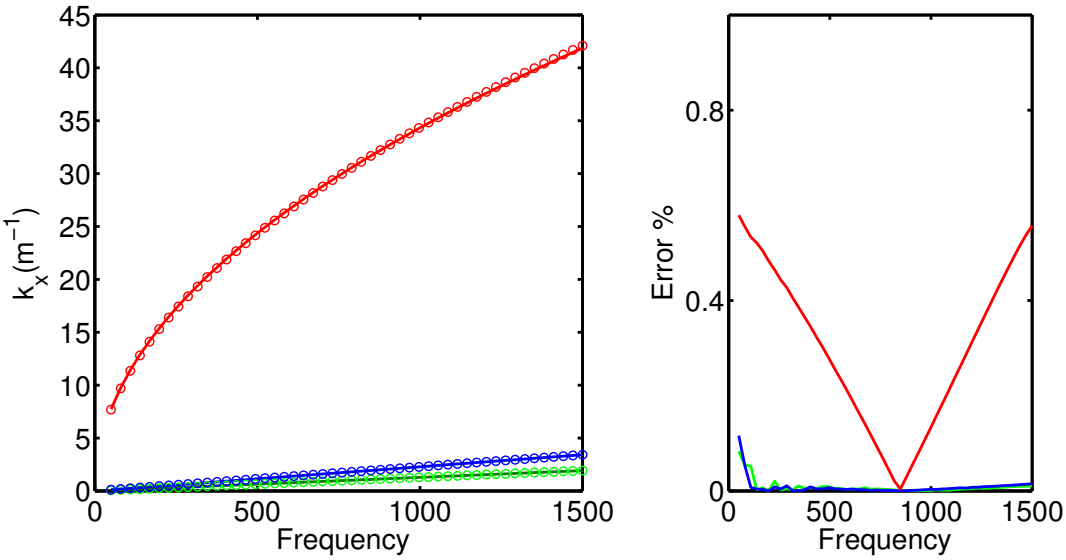


Figure 4.10: The dispersion relation of the full model (-) and the homogenized model (o). The error of the homogenized model compared to the full one

frequencies under 1500 Hz.

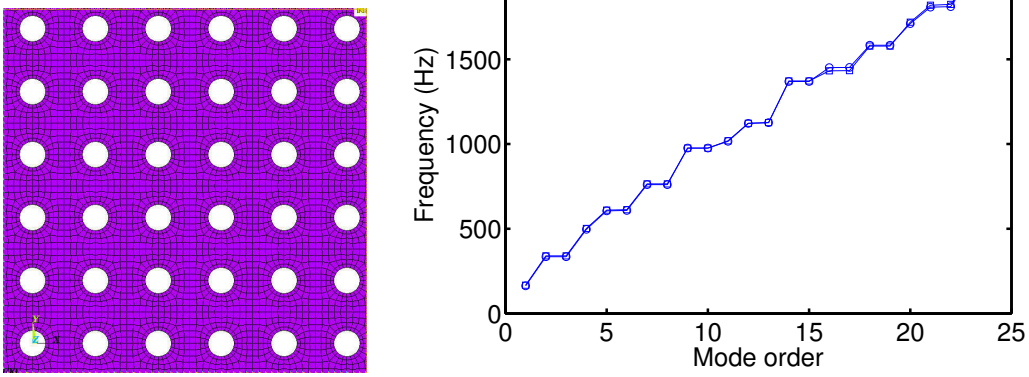


(a) Full model with 36 cells by FEM

(b) The natural frequencies of the full model (o) and homogenized model (□)

Figure 4.11: Validation of the homogenized model via modal analysis

#### 4.4.1.2 Triangular penetration pattern

The model 2 with circular holes and triangular penetration pattern is studied here. An experimental investigation is carried out on this model. A plate with 23 periods in the $x$-direction and 81 periods in the $y$-direction is excited by the shaker at the center. Due to the limited angle of the laser head, a grid formed by 23 points in the $x$-direction and 44 points in the $y$-direction around the center of the plate are scanned.

**Homogenized model at low frequency** The measured plate is excited firstly by a pseudo random signal center on 3000 Hz. Then DFT2D is performed to deduce $k$-space from the scanned displacement field. The results by the experimental investigation and by the CWFEM is given in Fig.4.12. It can be seen that two results correlate faire well with each other.

It is shown by Fig. 4.13 that until 4700 Hz, the waves propagate the same way in all directions. The $k$-space of the three types of waves remains circle at this frequency. So a homogenized isotropic model can be found which is valid until this frequency. Same as the previous model, the homogenized model is valid until the wavelength equals almost twice of the pitch in the $x$-direction $L_x$.

Since the plate behaves isotropic until 4700 Hz, the waves propagating in all directions can be represented by those propagating in one direction. The dispersion relation in the $x$-direction is given in Fig. 4.14. It can be seen that three types of waves propagate in the perforated plate. From the smallest wavenumber to the biggest wavenumber, longitudinal wave, shear wave and

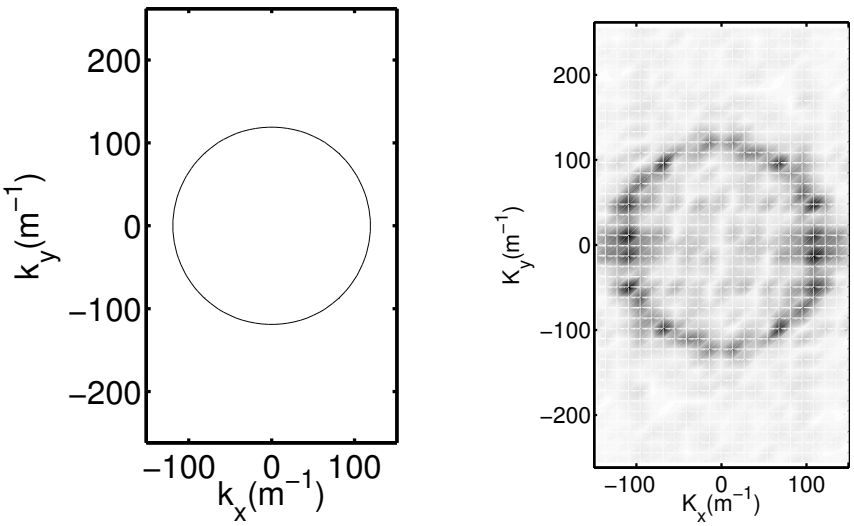


(a) CWFEM simulation (b) Experimental result

Figure 4.12: Comparasion of $k$-space by the simulation and experiment (flexural waves at 3000 Hz)

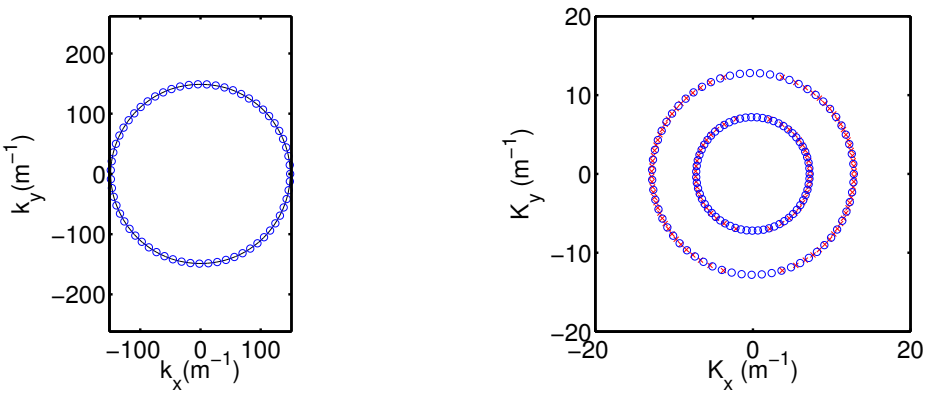


(a) $k$-space for flexural wave (b) $k$-space for longitudinal and shear waves

Figure 4.13: $k$-space at 4700 Hz (-/x) The curve fitting of a circle (o)

flexural wave are identified successively. Their wave shapes are given on the contour of the unit cell are shown in Fig. 4.15. The unit cell used in CWFEM is illustrated in Fig. 4.5(b), it contains half hole at each side, so as the wave shape.

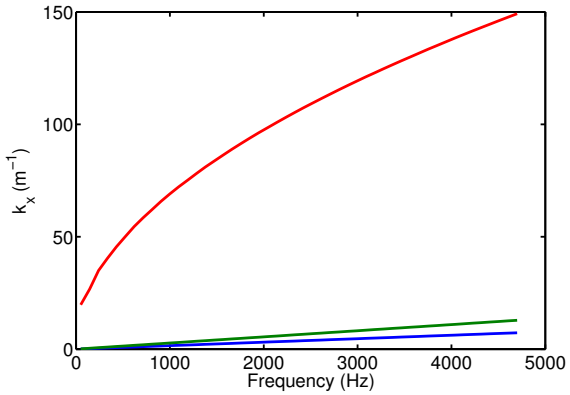


Figure 4.14: The dispersion relation in the $x$-direction

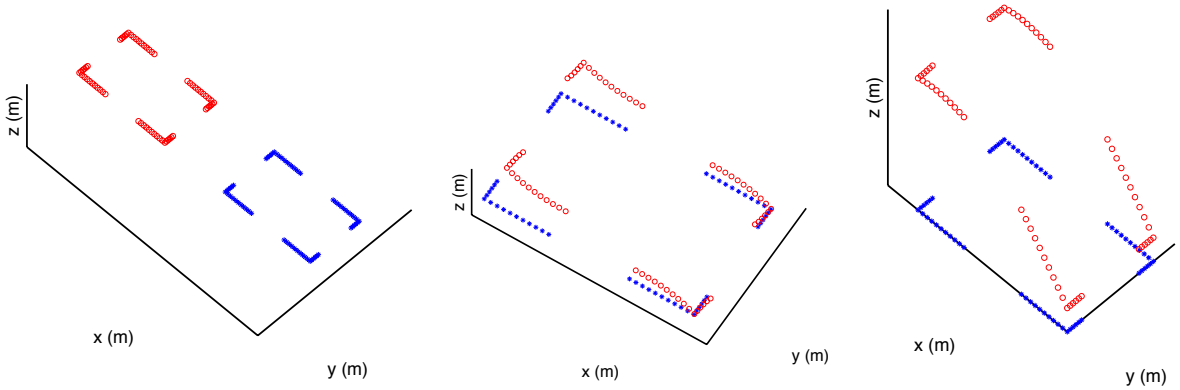


(a) Longitudinal wave shape (b) Shear wave shape (c) Flexural wave shape

Figure 4.15: Three kinds of wave shape (o) Undeformed unit cell ($*$)

The equivalent parameters for this frequency range are given in Fig. 4.16. They remain stable in the frequency range, the average of the values is taken as the equivalent one, which leads to to $E^* = 59$ GPa, $t^* = 1.1$ mm, $\nu^* = 0.36$, $\rho^* = 4124$ kg/m$^3$.

The dispersion relation of the homogenized model is computed by CWFEM, the result matches quite well with the one on full model. A difference of less than 0.3% in the frequency range is identified until 4700 Hz, as shown in Fig. 4.17.

The validation of the homogenized model is also carried on via modal analysis of finite plate. The plate is clamped at four sides, containing 6 unit cells in the $x$-direction and 7 in the $y$-direction. The natural frequencies under 4700 Hz of the two models are given in Fig. 4.18(b). The $x$ axis corresponds to the mode orders in $x$, the $n$th mode indicates that there is $n$ extrema in the $x$-direction. The mode orders in $y$ are illustrated by different curves. The curve with

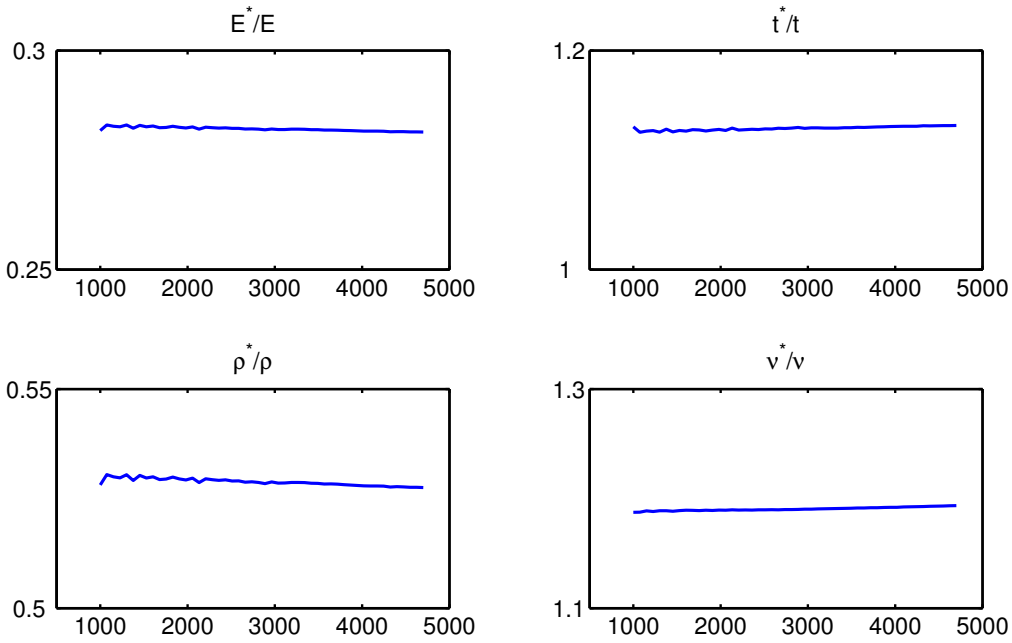


Figure 4.16: The equivalent parameters of the Model 2

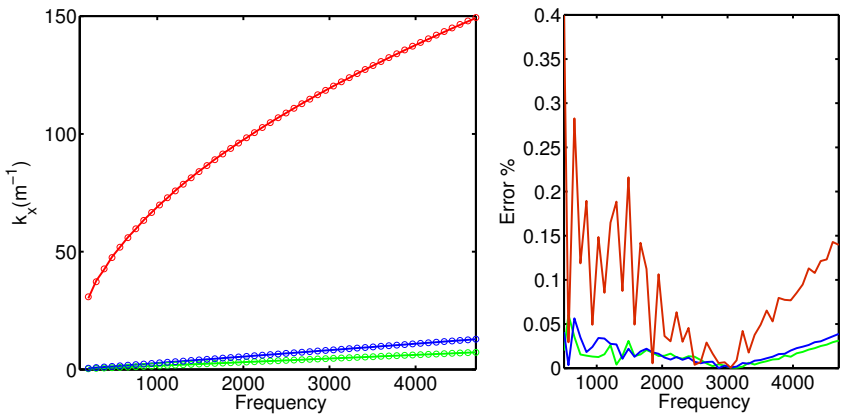


Figure 4.17: The dispersion relation of the full model (-) and the homogenized model (o). The error of the homogenized model compared to the full one

smallest frequency presents the 1st order in the $y$-direction, then the 2nd curve corresponds to 2nd order and so on. Good correlation between the natural frequencies of the full model and homogenized model has been observed. Biggest discrepancy of 5% is found at mode (2,3), with 2 extrema in the $x$-direction and 3 extrema in the $y$-direction. The natural frequency of this mode is at 4185 Hz for the full model, compared to 4034 Hz for the homogenized model.

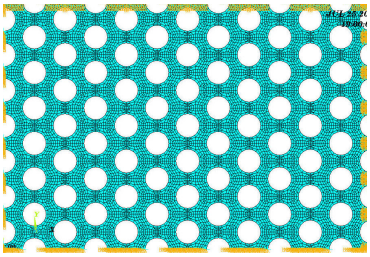

(a) Full model with 42 cells by FEM

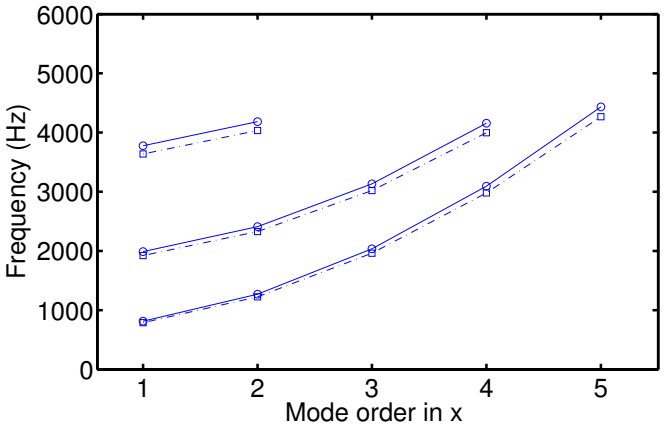


(b) The natural frequencies of the full model (o) and homogenized model (□)

Figure 4.18: Validation of the homogenized model via modal analysis

**High frequency range** At higher frequency, the plate behaves no longer isotropic. It can be told by the $k$-space in Fig. 4.19. Our experiment corroborates the simulation result by CWFEM at 8000 Hz. No privileged direction is observed at this frequency. The propagation directions cover almost all the angles.

### 4.4.2 Perforated plate with square holes

The study on model 3 with square holes under square penetration is conducted here. Experimental investigation is carried out on this model as well. The studied plate is of 1.2 m $\times$ 1 m , it contains 48 unit cells in the $x$-direction and 39 unit cells in the $y$-direction. The measured field of the laser forms a uniform spatial grid of 39 $\times$ 39 points in both directions.

The $k$-space at low frequency such as 2200 Hz is given in Fig. 4.20. It can be seen that flexural waves propagate in an isotropic way to all directions. However, the longitudinal and shear waves change with the propagating directions. The $k$-space for the two waves seems to form two ellipses which intersect with each other. However, as indicated in the zoom figure 4.20(c), it can be seen that they don't intersect. It is believed that the holes of big size play an important role here. In this model, the holes cover 64% of the whole area, compared to 14%

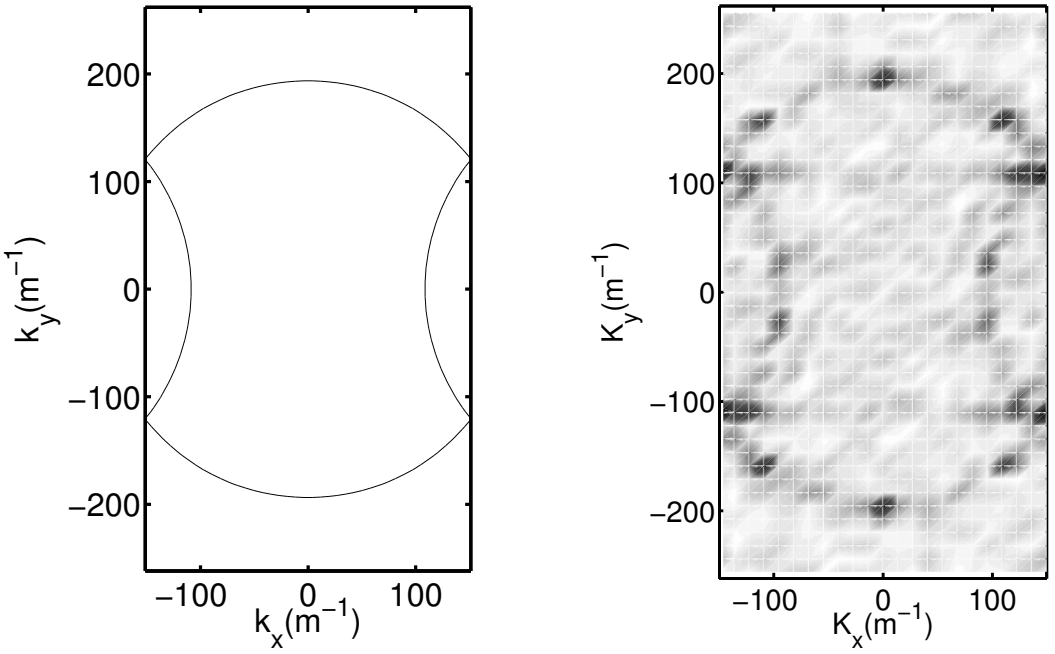


(a) CWFEM simulation (b) Experimental result

Figure 4.19: Comparasion of $k$-space by the simulation and experiment (flexural waves at 8000 Hz)

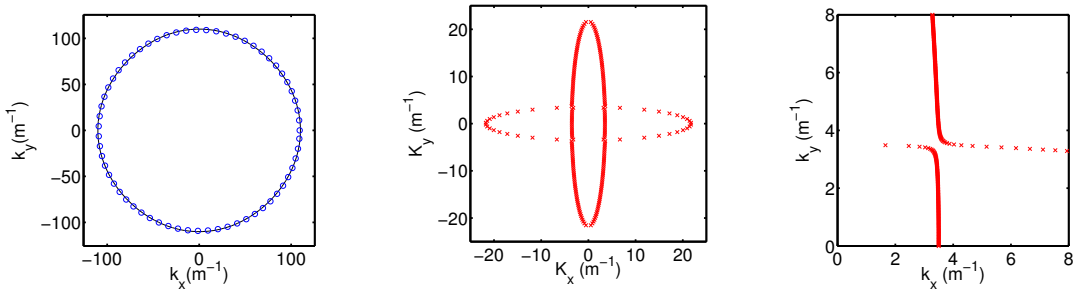


(a) For flexural wave (b) For longitudinal and shear waves (c) zoom of figure b

Figure 4.20: $k$-space at 2200 Hz (-/x) The curve fitting of a circle (o)

in model 1 and 40% in model 2. Three additional models, model 4, model 5 and model 6 are studied to validate this hypothesis. They have the same hole shape, with the same penetration pattern, only the hole size is changed. And the $k$-space of the longitudinal and shear waves for these models are given in Fig. 4.21(a), Fig. 4.21(b), Fig. 4.21(c) respectively. It can be seen that with the hole size decreases, the $k$-space of the waves become closer to a circle.

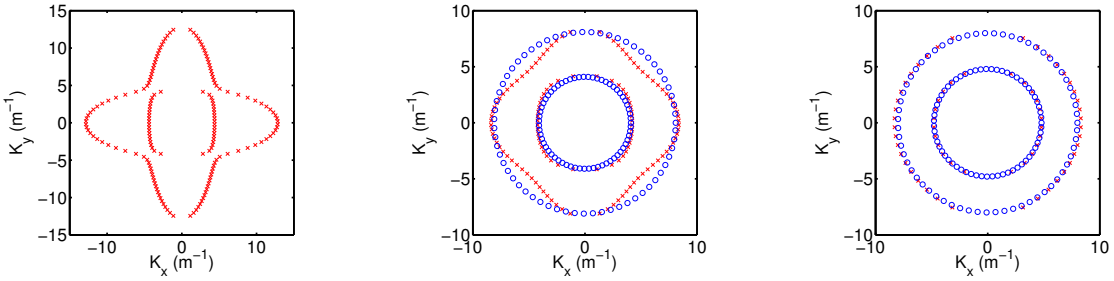


(a) Model 4 at 3000 Hz (b) Model 5 at 3200 Hz (c) Model 6 at 4000 Hz

Figure 4.21: $k$-space for longitudinal and shear waves at frequency where length of flexural wave equals to twice of the pitch. The curve fitting of a circle (o)

In addition, if we compare the model 2 with model 1 and model 4, where hole surface ratio $\tau$ equals respectively to 40%, 14% and 36%. It can be seen that the model 2 with each larger area of holes, behaves more isotropic than model 4 and model 1. So if one wants to design perforated plate which has isotropic propriety at low frequency, the circular holes with triangular penetration pattern is the best among three configurations.

#### 4.4.2.1 Equivalent homogenized model

For model 3, the method proposed in subsection 4.2.2 are employed which determines an isotropic model for out-of-plane waves and orthotropic model for in-plane waves. It can be seen from Fig. 4.20 that flexural waves behave isotropic until 2200 Hz. Based on Eq. (4.6) and (4.9), the matrices $\mathbf{D}$, $\mathbf{A}$ which determine respectively the out-of-plane and in-plane waves are as follows:

$$\mathbf{D} = 3.8 \begin{bmatrix} 1 & 0.3 & 0 \\ 0.3 & 1 & 0 \\ 0 & 0 & 0.35 \end{bmatrix}, \mathbf{A} = \begin{bmatrix} 4.38e7 & 3.4e6 & 0 \\ 3.4e6 & 4.38e7 & 0 \\ 0 & 0 & 1.1e6 \end{bmatrix} \tag{4.17}$$

The validity of the orthotropic model for in-plane movement is illustrated in Fig. 4.22. For the equivalent orthotropic model, $k$-space calculated based on the analytical formulation in Eq. (4.11) and by CWFEM concur well with the $k$-space by CWFEM on the full model of perforated plate.

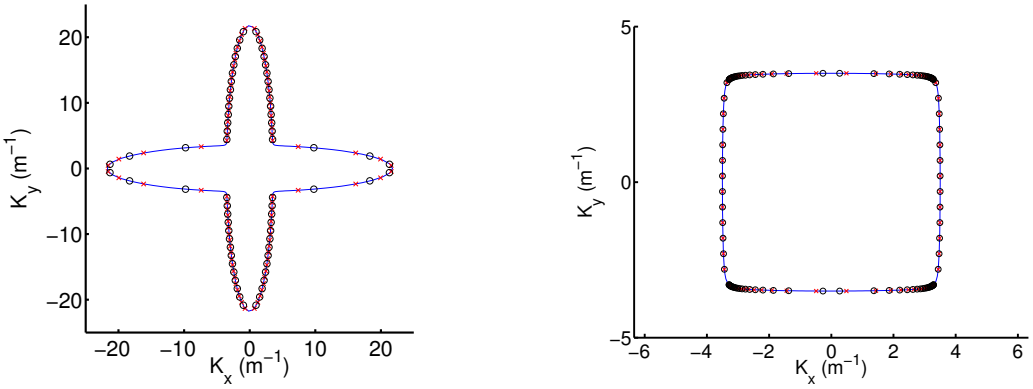


(a) Shear wave (b) Longitudinal wave

Figure 4.22: $k$-space for in-plane wave. Homogeneous plate with orthotropic materials: Analytical relation in Eq. (4.11) (-), CWFEM (o). Model 3 - Perforated plate with square holes by CWFEM (×)

#### 4.4.2.2 Validation by the experimental method

The $k$-space of the flexural wave in model 3 are deduced also by the DFT2D of the measured displacement field. The results are given at 1500 Hz, 2800 Hz and 5000 Hz in Fig. 4.23, Fig. 4.24 and Fig. 4.26. It can be seen that the experimental results are in good agreement with the simulation results by CWFEM.

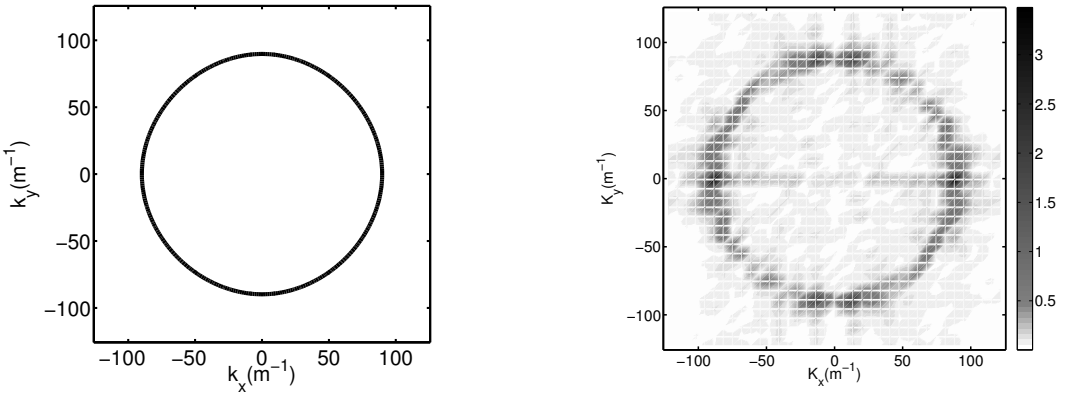


(a) CWFEM result (b) Experimental result

Figure 4.23: Comparasion of $k$-space by the simulation and experiment (flexural waves at 1500Hz)

It can be seen that at 1500 Hz, the flexural waves behaves isotropic in all directions.

At higher frequency such as 2800 Hz, the wave beaming effects phenomenon begins to appear, the propagation direction is privileged to the direction $y = \pm x$, and the propagation is limited to a certain angular range. However, the stationary displacement field doesn't possess

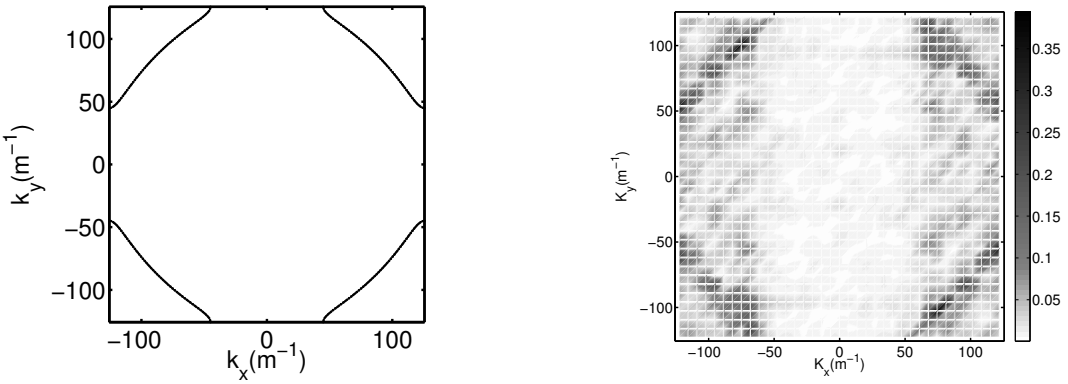


(a) CWFEM result (b) Experimental result

Figure 4.24: Comparasion of $k$-space by the simulation and experiment (flexural waves at 2800Hz)

evident privileged directions, as shown in Fig. 4.25. Since no particular damping treatment of the plate has been carried on, the reflected waves by the boundaries are added on the incident waves, forming the stationary displacement without showing the initial privileged propagation directions of the structure.

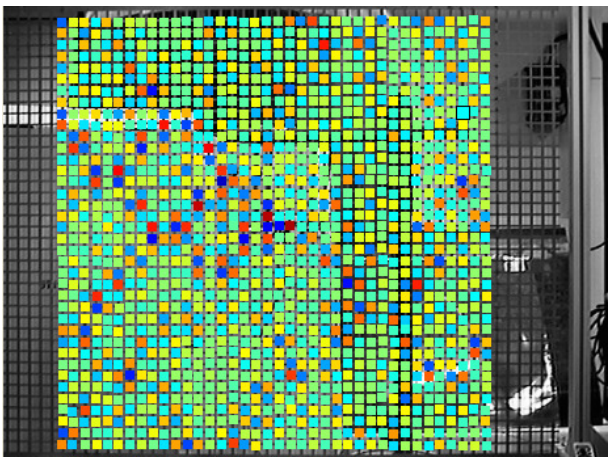

Figure 4.25: The measured displacement field at 2800 Hz

At 5000 Hz, the $k$-space identified experimentally shows also a big similarity with the one calculated by WEFM. No evident direction where the wave cannot propagate is observed. The presence of the noise in the experimental $k$-space may be due to the evanescent waves. Since the evanescent waves also contribute to the measured displacement field, while the numerical $k$-space includes only the propagating waves at this frequency.

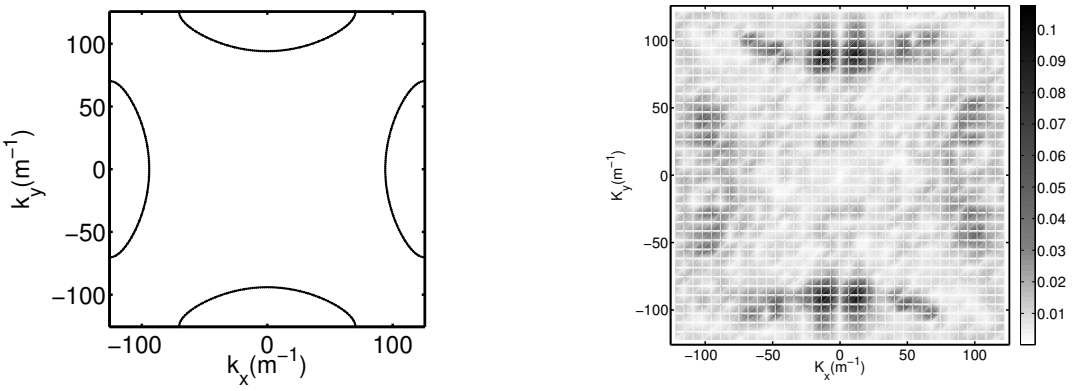


(a) CWFEM result (b) Experimental result

Figure 4.26: Comparasion of $k$-space by the simulation and experiment (flexural waves at 5000Hz)

## 4.5 Conclusions and perspectives

The wave propagating features in perforated plates in a broadband frequency range are studied both by CWFEM and experimental approach. The most important points can be summarized as follows:

- At low frequency, for the two perforated plates with circular holes under square and triangular penetration pattern, an isotropic behaviour was identified both for the in-plane and out-of-plane motion. Based on their dispersion relations predicted by CWFEM, a homogenization method was proposed to find the homogenized solid model. The method allows not only to find equivalent parameters such as Young's Modulus, mass density, Poisson ratio and thickness, but also to predict the frequency range where the homogenized model is valid. For the two models, the homogenized models were found almost until the wave length equals to twice of the period length. The method was also validated by the modal analysis, where natural frequencies of the homogenized model correlate with the ones of full model.

- For the perforated plate with square holes, an isotropic behaviour was identified for the out-of-plane wave while the in-plane waves behaved orthotropic. The homogenization method to find its equivalent model was proposed. The matrices in the generalized stress-strain relationship of the equivalent model were determined. Good agreement was observed between the $k$-space of the homogenized model and the full model.

- To obtain an isotropic behaviour for both the in-plane and out-of-plane waves, the perforated plate with circular holes under triangular penetration is the best among the three configurations treated in this chapter.

- Experimental investigation was carried out on two models. The displacement field was measured by a scanning laser. The $k$-space deduced by the DFT2D of the displacement field correlates well with one obtained by CWFEM. It is concluded that CWFEM is able to predict wave propagation characteristics at low frequency where homogenized model still exists and at high frequency where wave beaming effects phenomenon occurs.

Future investigations will address the application of homogenized method on other 2D periodic structures, such as thick perforated plate, laminated composite plates and honeycomb sandwich. The other criterion will be used to validate the homogenized model, such as the forced response of the structure.

# Chapter 5

# Wave propagation features in periodically orthogonally rib-stiffened plate

## 5.1 Introduction

Rib-stiffened panels are extensively used in automotive, aerospace and civil engineering. It ensures to some extent a compromise between their rigidity and their weight. In most of the studies, they are treated as periodic structures since the stiffeners are often distributed equispatially.

One classical approach is to represent the stiffened plate by an equivalent orthotropic plate of constant thickness having the same stiffness characteristics. The equivalent mass density can be defined by the conservation of mass and the equivalent stiffness values can be determined by the pure static considerations. The method can predict correctly wave propagation characteristics of unidirectionally stiffened plate at low frequency [Ichchou *et al.*, 2008]. However, for a orthogonally stiffened plates with stiffeners of different cross-section properties or unequally spaced, the orthotropic plate homogenization may no longer be applicable. Furthermore, equivalent model cannot be expected to yield good results for cases with large stiffener spacings [Chen & Xie, 2005]. Several analytical models have been developed to study both unidirectionally stiffened and orthogonally stiffened plates. Fahy & Lindqvist [1976] studied wave propagation in damped structures consisting of flat plates stiffened by one beam or two parallel beams. They supposed a pure flexural motion exists in the plates and pure flexural/torsional motion exist in the ribs. Dispersion curves were therefore deduced analytically and discussion of damping treatments for these structures was given. Lee & Kim [2002] modelled the stiffeners by a combination of lumped masses and translational and rotational springs to evaluate the sound transmission loss utilizing spatial harmonic technique developed by Mead & Pujara [1971]. Their model does not take into account the geometry of the stiffeners. Maury & Mattei

[2002] added the stiffeners onto the plate as a force, without taking the moment into account. Lin & Pan [2006] modelled the stiffeners of simply supported plates as forces and moments and evaluated the forced vibration of unidirectionally stiffened plates. A semi-analytical model is proposed by Mejdi & Atalla [2010], based on the modal expansion technique which account the moment and force coupling between ribs and plates. Analytical modelling of wave propagation in orthogonally rib-stiffened sandwhich structures is studied by Xin & Lu [2011] where the tensional, bending and torsional vibrations of rib-stiffeners are all considered.

In this chapter, the proposed numerical CWFEM is applied on the skin of the fuselage, which can be considered as a periodically orthogonally rib-stiffened plate. Attention is paid to study the mid and high frequency behaviour where the local modes of the unit cells play an important role in the dynamic behaviour. The chapter begins with the presentation of the model and some of the experimental results. Subsequently, the CWFEM is applied to calculate the wave propagation characteristic in stiffened plate, the results as well as the computation time have been compared with the WFEM. The modal density in mid- and high- frequency range is then deduced for a finite model with 100 unit cells. The concluding remarks are given at the end of this chapter.

## 5.2 Experimental study on the skin of the fuselage

Ichchou *et al.* [2011] have carried out an experimental study about the vibroacoustic control of fuselage. The same model of the skin is employed here. Some of the experimental results are given in this chapter to validate the numerical model.

### 5.2.1 Description of the experimental specimen

The measured fuselage skin is of 2 m length, and of 1.24 m width. The skin is stiffened with horizontal stringers in "Z" and vertical frames in "C". In the length, it contains 3 complete unit cells and half unit cell at each side. In the width, it contains 6 complete unit cells and half unit cell at each sides. The unit cell is given in Fig. 5.1, with the stringer at the bottom side and the frame at the left side. The length of the unit cell is $L_x = 0.51$ m, while the width is $L_y = 0.17$ m. The plate is of 1 mm thickness. The dimensions of the stringers and frames in Fig. 5.2 are $w_1$ = 6 cm, $w_2$ = 1.2 cm, $w_3$ = 2 cm, $w_4 = w_5$ = 1.45 cm. They both made of aluminium with thickness of 1 mm.

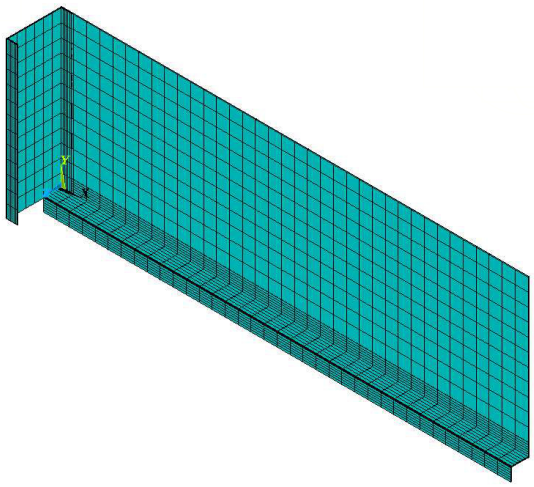

Figure 5.1: Unit cell of the stiffened plate

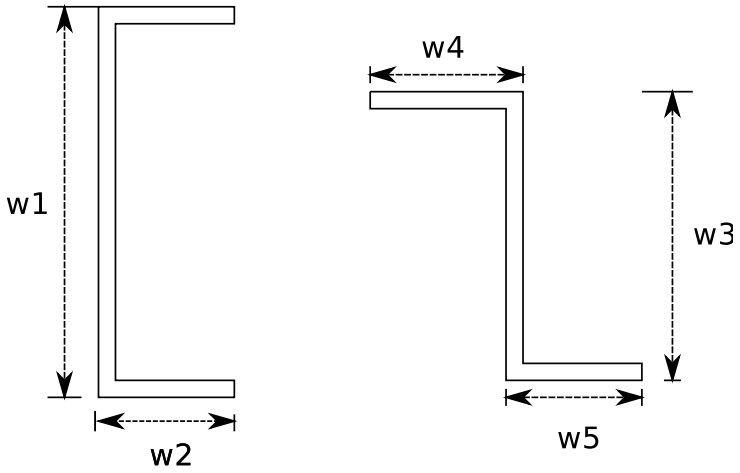


Figure 5.2: The dimension of the frame (Beam in "C") and the stringer (Beam in "Z")

### 5.2.2 Validation of the FE model by experimental results

The forced response until 1000 Hz of experimental specimen is scanned using laser vibrometer (Polytec PSV 400). The experimental setup is given in Fig. 5.3. The average response of a unit cell are displayed in Fig. 5.4.

The forced response of the stiffened plate exhibits a response band phenomenon. As shown in Fig. 5.4, below 100 Hz, global behaviour dominates. Local (1,1) mode dominates at 110 - 150 Hz, (2,1) at 170 - 220 Hz, (3,1) at 250 - 300 Hz, etc. Within each bandwidth, the number of local modes $(n, 1)$ of the same $n$ is determined by the number of gridded cells, i.e. around 7 for this case.

A finite stiffened panel with 4 complete unit cells in length and 7 complete unit cells in width has been modelled using FEM. A modal analysis is carried out on the FE model, as given

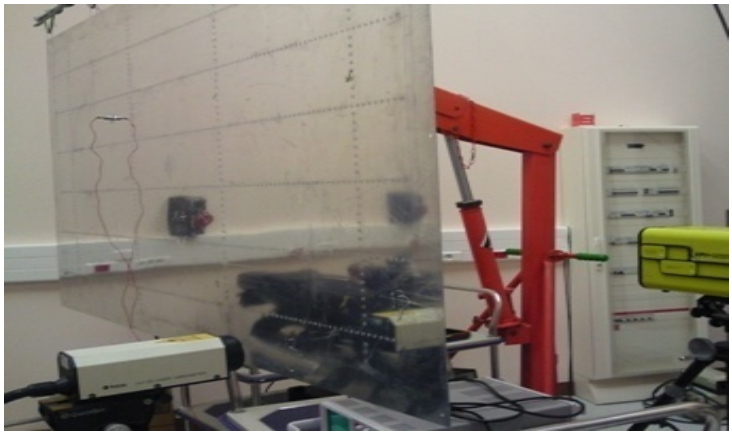

Figure 5.3: Experiment setup for scanning the local behaviour [Ichchou *et al.*, 2011]

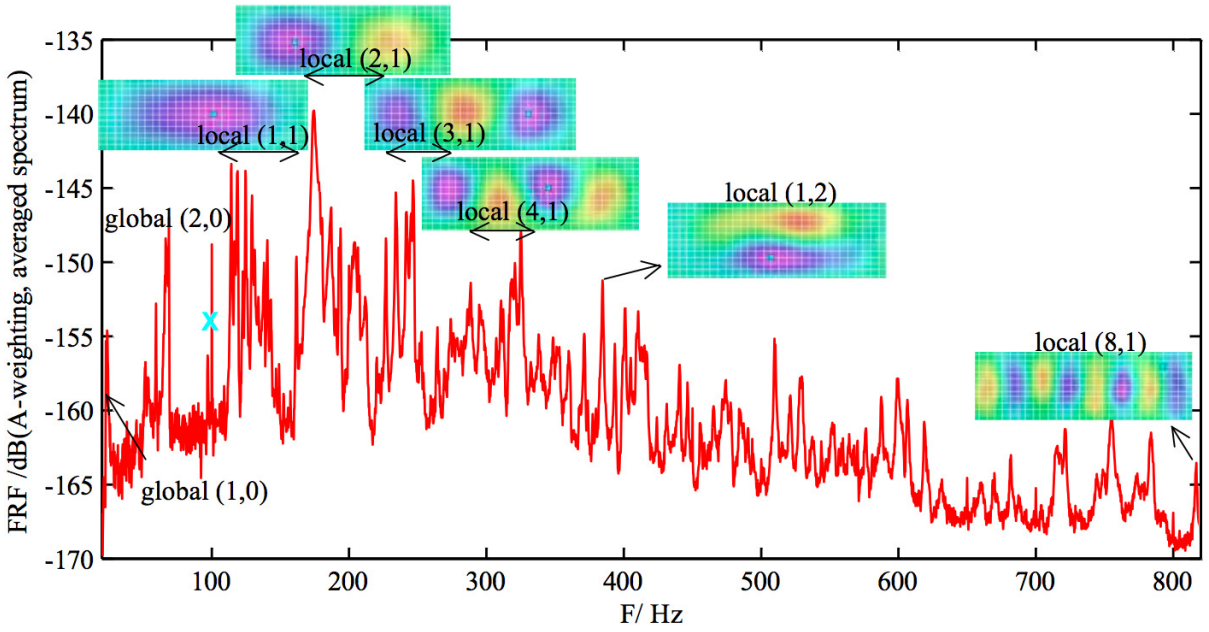


Figure 5.4: Frequency response function of the stiffened skin (averaged spectrum of one cell) [Ichchou *et al.*, 2011]

in Appendix C. It can be seen that the model is different from the experiment specimen at the boundaries. However, the local behaviour shouldn't be modified a lot. The element type shell 63 has been used for the plate, and beam 188 for the stringers and frames in ANSYS. To ensure the convergence of the mesh until 1000 Hz, the unit cell is divided into 36 elements in the $x$-direction and 12 elements in the $y$-direction. The modal analysis has been carried on the panel, with clamped boundary conditions at the four sides. The local mode (1,1) begins at 108 Hz (Fig. C.1) and dominates between 108 Hz - 165 Hz. The local mode (2,1) begins at 167 Hz (Fig. C.2) and dominates between 167 Hz - 218 Hz, the local mode (3,1) begins at 240 Hz. The frequency ranges of the local modes identified by FEM correlate well with the experimental measurement. Thus the unit cell of the model is validated.

## 5.3 Wave propagation characteristics in stiffened plate

Different from the precedent chapters, a beta damping of 0.5% is taken into consideration in the model. It is included by adding a structure damping matrix $\mathbf{K}' = \beta\mathbf{K}$, with $\beta = 0.5\%$. The dynamic stiffness matrix of the unit cell is now complex and becomes:

$$\mathbf{D} = \mathbf{K} + \mathrm{i}\mathbf{K}' - \omega^2\mathbf{M} = (1 + \beta\mathrm{i})\mathbf{K} - \omega^2\mathbf{M} \tag{5.1}$$

All the propagation characteristics given in this chapter are based on this damped model.

### 5.3.1 Wave propagating in the $x$-direction

The direct form of CWFEM is employed to calculate the dispersion relation for the waves propagating in the $x$-direction, as shown in Fig. 5.5. The imaginary part which corresponds to the damping is illustrated as well. It can be seen that CWFEM is able to predict also the damped waves with little decaying when propagating.

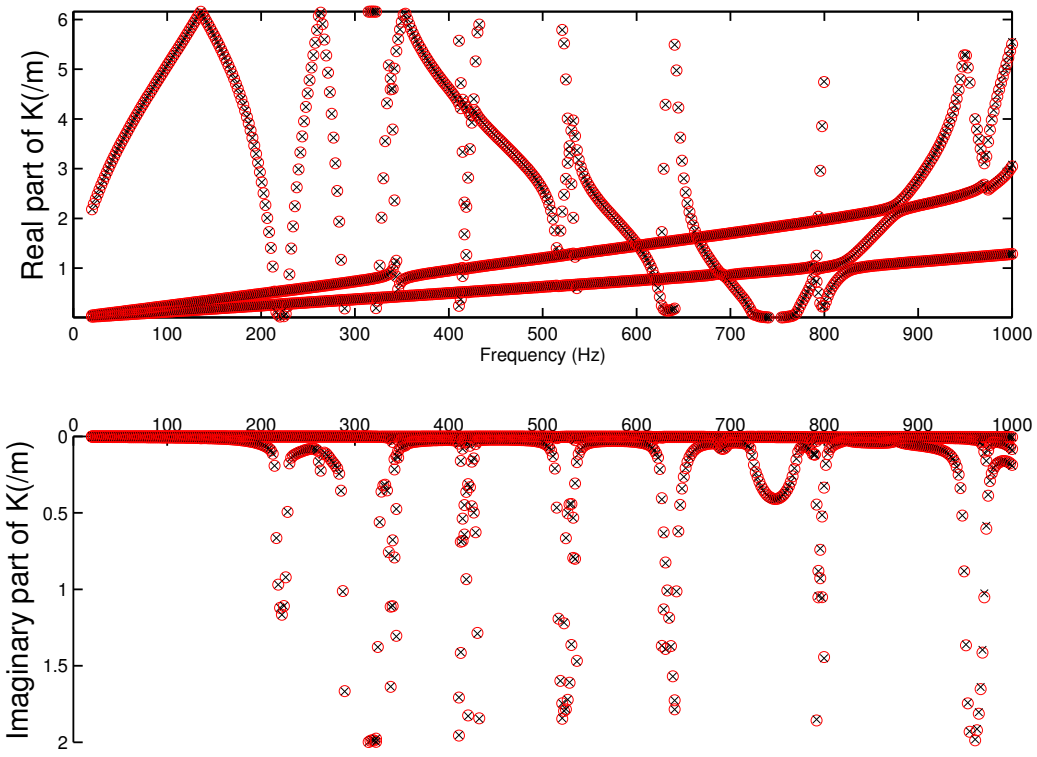


Figure 5.5: The dispersion relation for the waves propagating in the positive $x$-direction. CWFEM (o), WFEM ($\times$)

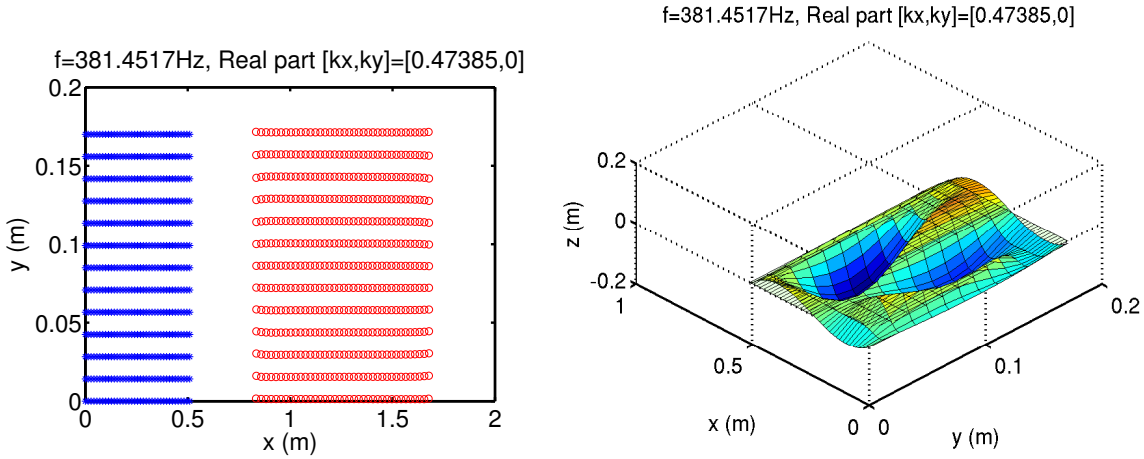


(a) In-plane deformation: undeformed (∗) deformed (o)

(b) Out-of-plane deformation

Figure 5.6: Wave shape of quasi-longitudinal wave propagating in the $x$-direction

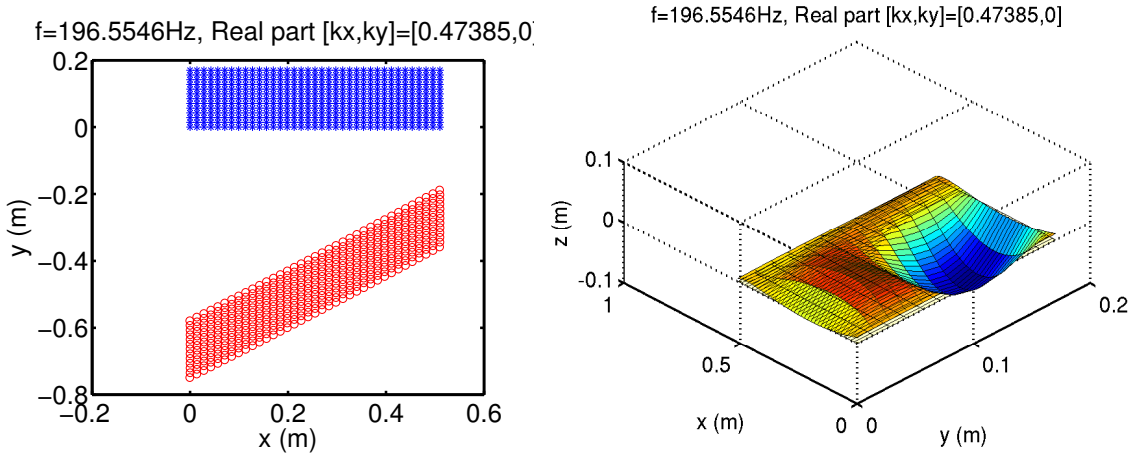


(a) In-plane deformation: undeformed (∗) deformed (o)

(b) Out-of-plane deformation

Figure 5.7: Wave shape of quasi-shear wave propagating in the $x$-direction

There are mainly three kinds of waves propagating in the stiffened panel. However, since the stiffeners and the frames are both eccentric, the in-plane and out-of-plane movements are coupled. The wave shape of quasi-longitudinal wave is shown in Fig. 5.6, with in-plane movement in Fig. 5.6(a) much bigger than out-of-plane movement in Fig. 5.6(b). Similar for the quasi-shear wave shape, as shown in Fig. 5.7. As for flexural wave shape in Fig. 5.8, the out-of-plane movement dominates with smaller in-plane deformation. It should be mentioned that all the wave shapes displayed in this chapter are normalized with respect to the mass matrix.

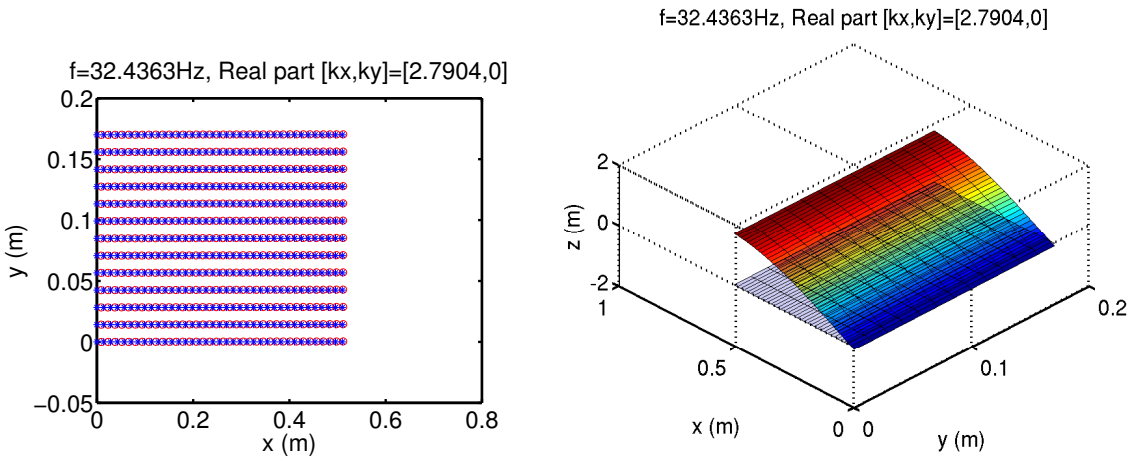


(a) In-plane deformation: undeformed (∗) deformed (o)

(b) Out-of-plane deformation

Figure 5.8: Wave shape of flexural wave propagating in the $x$-direction

### 5.3.2 Band structure

The inverse form of CWFM is applied to calculate the band structure of the propagation. Unlike the undamped beam grid in chapter 3, the solution of the eigen problem of Eq. (3.12) doesn't lead to real value of $\omega$. However, since the system is only slightly damped with ratio of 0.5%, the propagation characteristics are not modified significantly by the damping, the real part of $\omega$ is around 100 times of its imaginary part. So $\Re(\omega)$ is plotted in the band structure in Fig. 5.9. The result by CWFEM is validated by the WFEM result on full model. The "OA" part in the band structure corresponds to the dispersion relation of wave propagating in the $x$-direction, as given in Fig. 5.5. The different curves are related by the frequency values instead of wave shapes. Since the wavenumber of the in-plane wave is usually smaller compared to the flexural wave. The curves which are close to the frequency axis correspond to the in-plane wave, while the other part corresponds to the flexural waves. For flexural waves, there is a narrow stop band between 215 - 225 Hz, as shown in Fig. 5.10.

In CWFEM, all the 66 internal modes with fixed boundary under 3 kHz are taken into account. The result is proved convergent to the result by WFEM. Here the influence of internal modes on propagation is investigated. The band structure is computed with different sets of internal modes. Here the influence of the first two internal modes is shown, with the 1st internal mode at 201 Hz and the second mode at 224 Hz.

The first slowness surface is between 0 - 151 Hz, the second slowness surface (only the flexural waves) is between 136 - 215 Hz. As it can be seen in Fig. 5.11, the first slowness surface can not be entirely determined by the constraint modes of the boundary, contrary to the beam grid in chapter 3. For the waves propagating in the $x$-direction (OA1), the internal mode is not required, the global propagation is entirely determined by the constraint modes of

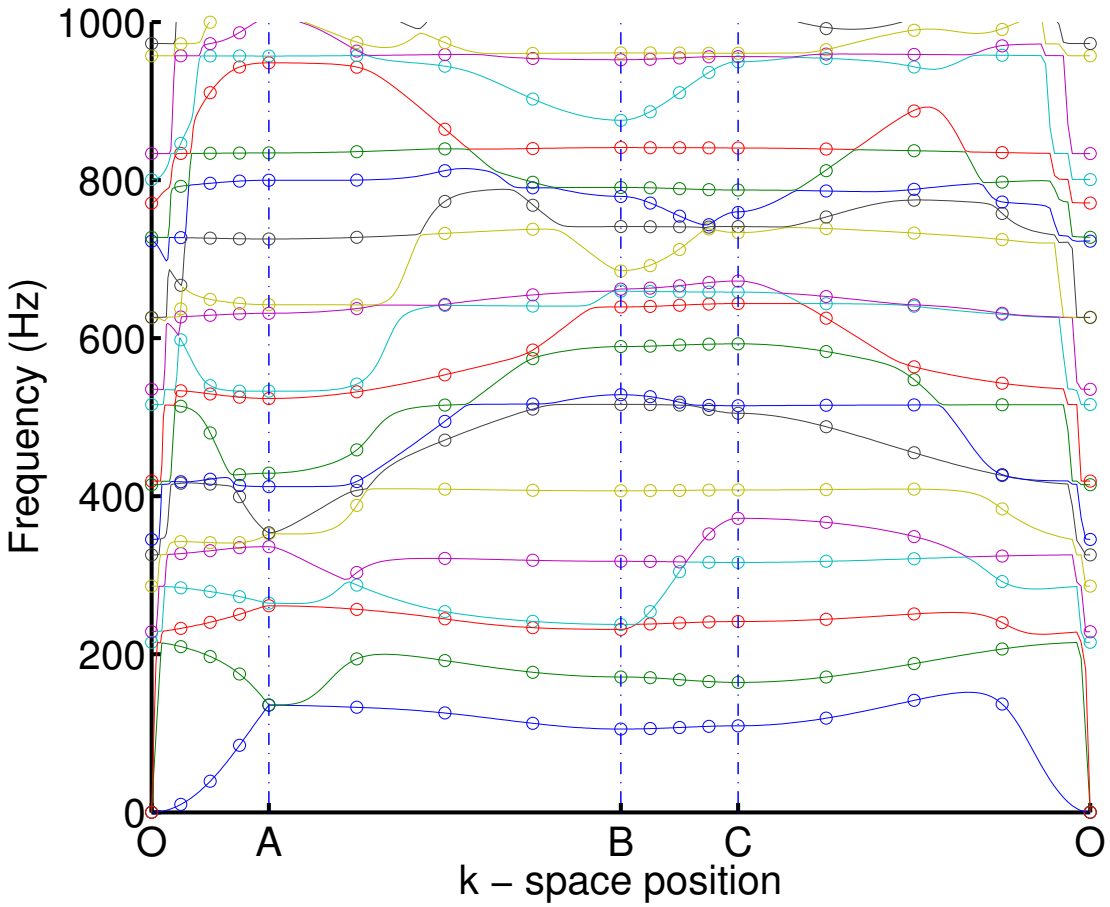


Figure 5.9: Band structure under 1 kHz by CWFEM (-) WFEM (o)

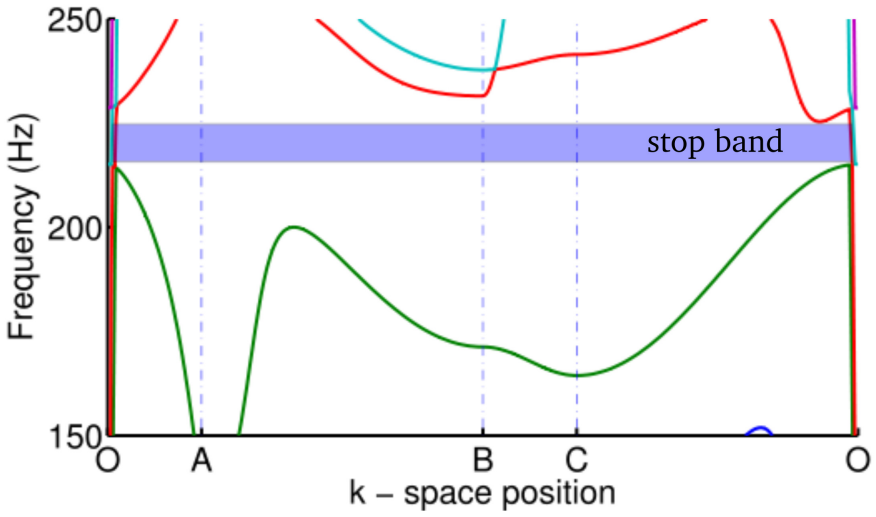


Figure 5.10: Stop band of flexural waves between 215 - 225 Hz

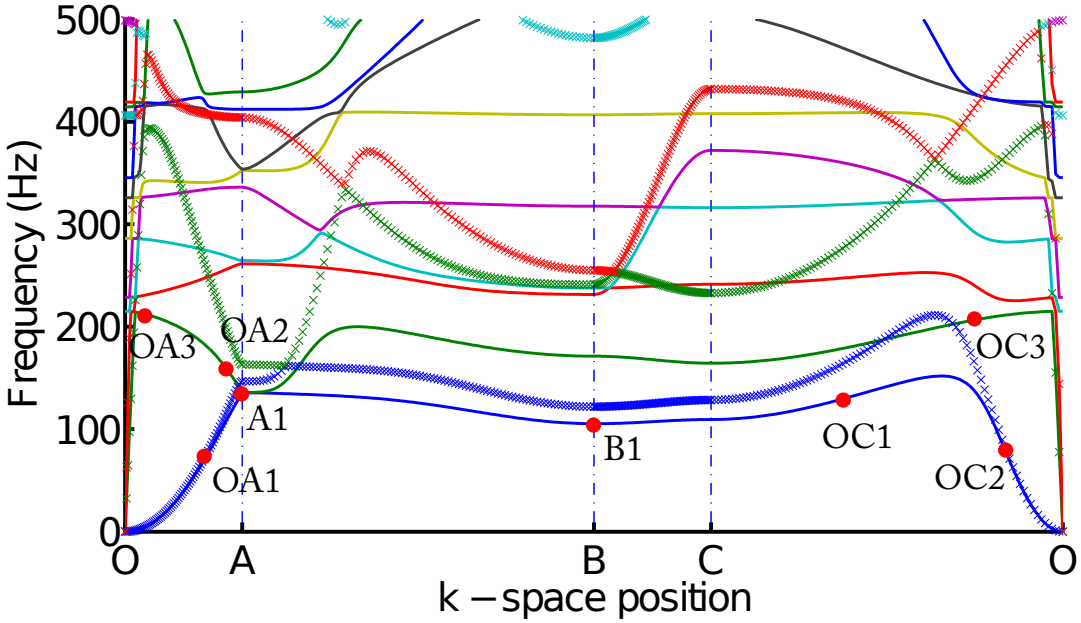


Figure 5.11: Band structure by CWFEM (-) with no internal mode (x)

the boundary. However, for waves propagating in other directions (B1, OC2), the first internal mode is needed, as shown in Fig. 5.12. If only the 2nd internal mode is taken without the 1st internal mode (Fig. 5.13), the points at 1st slowness surface (OA1, A1, B1, OC1, OC2) remain the same as if no internal mode is taken. It confirms the precedent conclusion that the 1st slowness surface is entirely determined by the 1st internal mode. For the second slowness surface, a good prediction at OC3 and OA3 is obtained. However, a better prediction at OA2 is obtained if only the 1st local mode is taken account into. So it can be concluded that the 1st internal mode play a more important role at OA2, while 2nd internal mode dominates at OA3. We need the first two internal modes to determine precisely the second slowness surface.

The contribution of the internal modes on global propagation can also be understood by observing the wave shapes. The wave shapes at the aforementioned points are given in Appendix B. To illustrate how the wave propagates through one unit cell to another, the wave shapes extended to 4 adjacent unit cells are plotted over a period $T$. For the propagation at frequency $\omega = 2\pi/T$, the wave shape can be written as $\phi \exp(i\omega t) = |\phi| \exp(i(\theta + \omega t))$. Therefore, $|\phi| \cos(\theta)$ corresponds to the wave shape at $t = 0$. And $|\phi| \cos(\theta + \pi/3)$ is found for the wave shape at $t = T/6$, a phase shift of $\pi/3$ is added when time advances $T/6$.

It have been concluded in chapter 3 that the points “O”, “A”, “B”, “C” on the band structure correspond to stationary waves. The conclusion is verified by the wave shapes at point “A1” and “B1” displayed in Fig. B.2 and Fig. B.3. For point “A1”, the nodes with zero displacement lie close to the left side and right side of the unit cell. And the anti-node with maximum displacement lie at the center of the unit cell. For point “B1”, the stationary nodes lie close to the boundary and the anti-node lies at the center of the unit cell.

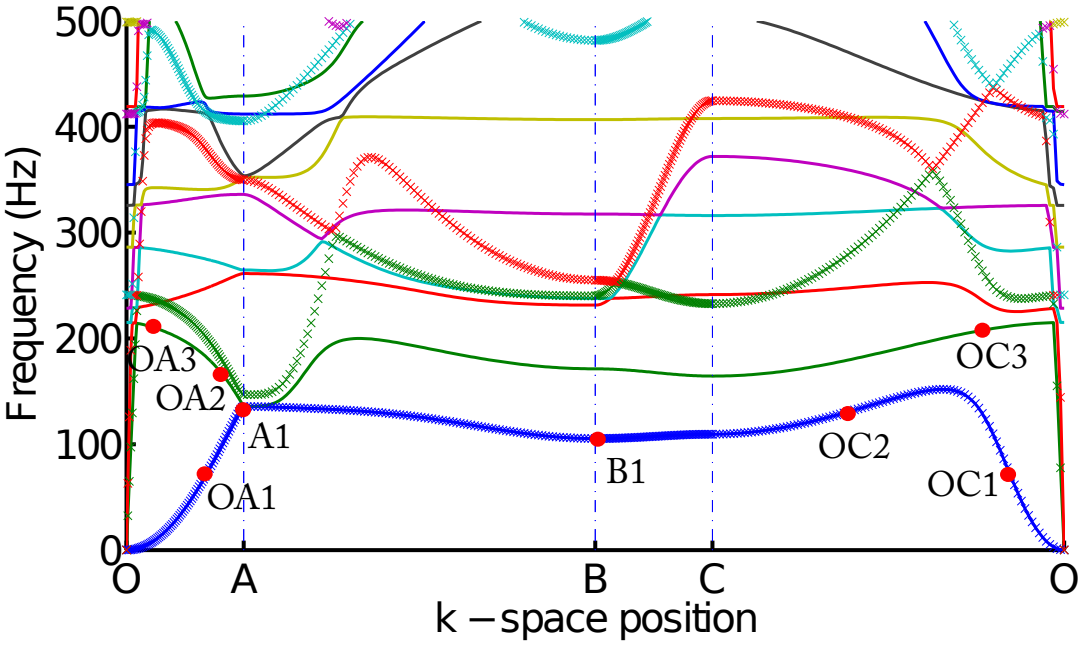


Figure 5.12: Band structure by CWFEM (-) with 1st internal mode (x)

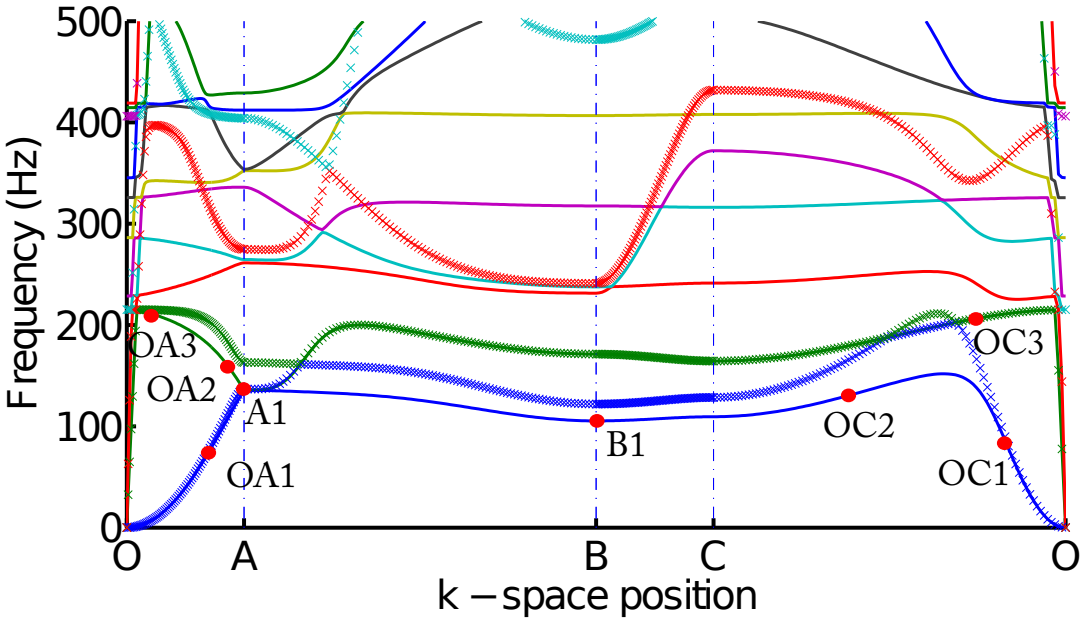


Figure 5.13: Band structure by CWFEM (-) with 2nd internal mode (x)

| | Computation time |
|---|---|
| WFEM2D | Linear eigen problem: 235 s $\times$ 1600 = 104 h |
| CWFEM2D | Modal analysis: 165 s<br>Linear eigen problem: 0.5 s$\times$ 1600 = 13 m<br>Total time = 16 m |

Table 5.1: Computation time to calculate the slowness surface by WFEM and CWFEM

At point "OA1", the 1st order of flexural wave towards the $x$-direction is identified, in Fig. B.4, we can identify the 1st order of flexural wave propagating in the $x$-direction. At point "OA2" in Fig. B.5, the higher order flexural waves appear. It can be remarked that in the unit cell, the wave propagates in the negative $x$-direction. In addition, the energy propagates also in the negative $x$-direction at this point, since the tangent of the band structure at this point should equal to the group velocity.

The first order of flexural wave propagating in the $y$-direction is identified at "OC1". The wave shapes are given in Fig. B.7. However, for "OC2", which belongs also to the first slowness surface, a higher order flexural wave appears. Similar as point "OA2", the wave seems to propagate in the negative $x$-direction in the unit cell at this point. In addition, the energy propagates in negative $x$-direction as well.

At higher frequency, the group velocity of many waves seems to approach zero. For example at "OC3", the tangent of the band structure at this point is close to zero. As for their wave shapes, as given in Fig. B.9, they seem like the local mode (2,1).

### 5.3.3 Slowness surfaces

With the CWFEM, the slowness surfaces of the stiffened plate can be obtained with relative ease compared to WFEM. The full model contains 2886 DOFs, with 2310 internal DOFs and 576 boundary DOFs. As for the reduced model, it contains only 66 internal modes with fixed boundary under 3000 Hz. In addition to the 576 boundary DOFs, the reduced model contains in total 642 DOFs. Thus the computation time to solve the eigen problem in Eq. (3.12) reduces from 235 seconds to 0.5 second for each iteration of $(k_x, k_y)$. To plot the slowness surfaces with good precision, 40 iterations of $k_x$ are taken in $[0, \pi/L_x]$ and 40 iterations of $k_y$ are taken in $[0, \pi/L_y]$. The slowness surfaces with $[-\pi/L_x, 0]$ or $[-\pi/L_y, 0]$ are obtained by doing the symmetry. The computation times by CWFEM and WFEM to calculate $40 \times 40 = 1600$ iterations are given in Tab. 5.1.

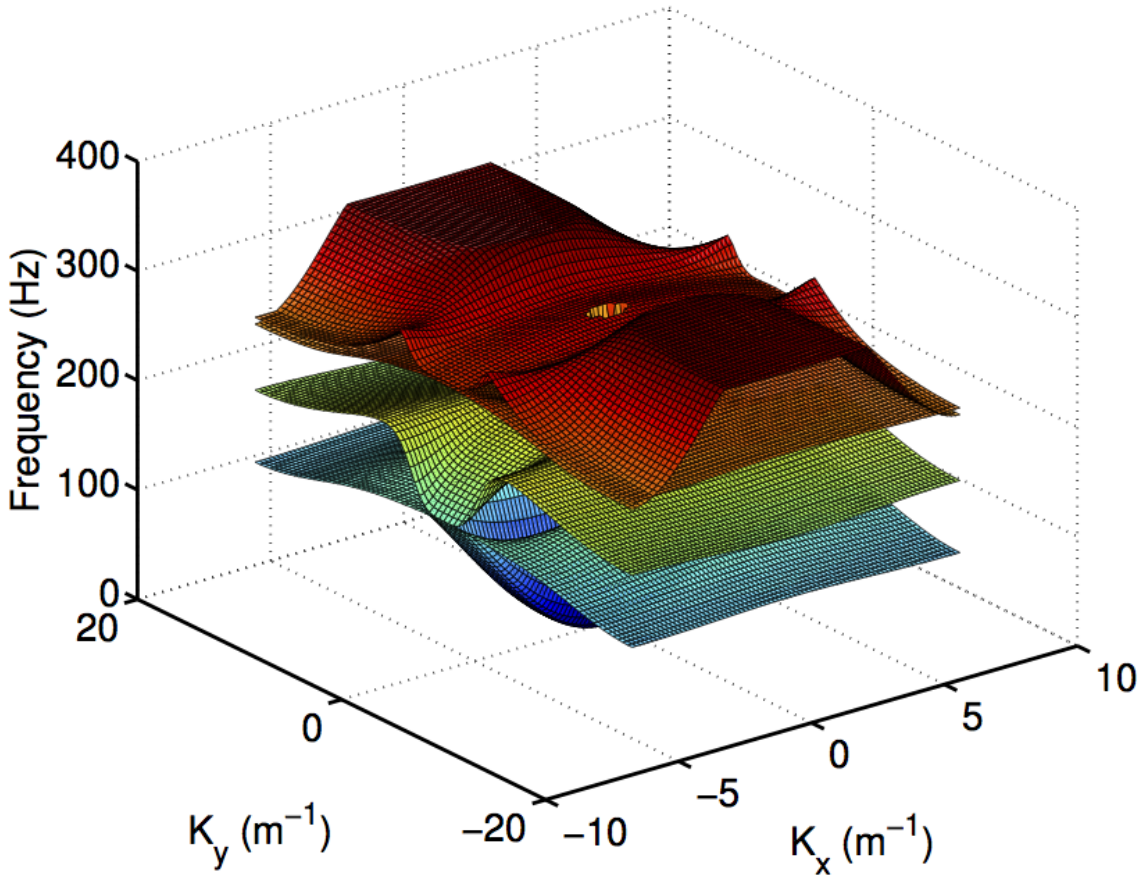


Figure 5.14: First four slowness surfaces

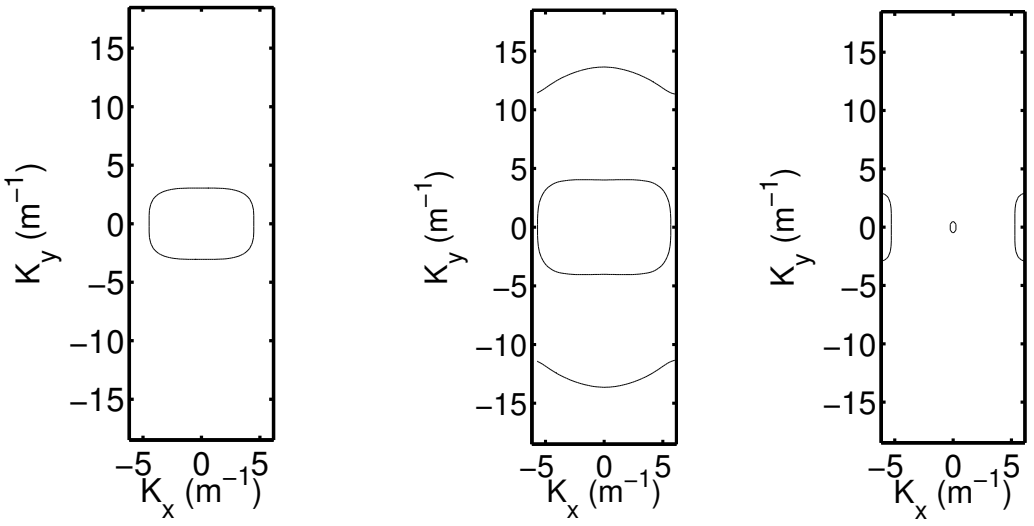


(a) Flexural wave at 80 Hz (b) Flexural wave at 120 Hz (c) Flexural wave and shear wave at 160 Hz

Figure 5.15: $k$-space identified by CWFEM

### 5.3.4 $k$-space computation

The $k$-space which corresponds to the iso-frequency contour of slowness surfaces is given at 80 Hz, 120 Hz and 160 Hz in Fig. 5.15. At 80 Hz, the global behaviour dominates, knowing that the 1st local mode begins at 108 Hz. It is already known that for the plate which is stiffened in one direction, a orthotropic model can be found with $k$-space in elliptic shape [Ichchou *et al.*, 2008]. Here a rounded rectangle is found at 80 in Fig. 5.15(a). It can be used to determine the equivalent model if it exists. At 160 Hz in Fig. 5.15(c), the wave beaming effect occurs, with flexural wave privileged in the $x$-direction. It corresponds to a partial stop band in the $y$-direction.

### 5.3.5 Modal density of finite stiffened plate

The modal density can be deduced from the slowness surfaces, using the formulation given in Eq. (1.68). The result obtained for a finite plate with both 10 unit cells in the $x$ and $y$ directions is given in Fig. 5.16. To validate the obtained result, the modal analysis of the FE model is carried on under different boundary conditions. As it can be seen in Fig. 5.16(a), a larger number of modes are identified under free boundary, while a smaller number of natural modes are found when the boundaries are clamped compared to the result obtained by CWFEM. A good correlation has been obtained between number of modes under simply supported boundary condition and CWFEM. More details about the relation of modes count and boundary conditions can be found in the reference [Xie *et al.*, 2004]. However, the boundary condition doesn't play

an important role for modal density at high frequency. Starting from around 200 Hz, a good correlation between the modal densities under different boundary conditions has been observed in Fig. 5.16(a). Remind that the local mode (2,1) dominates between 167 - 218 Hz. So it can be concluded that CWFEM can be used to determine the modal density for a finite structure with enough unit cells in mid- and high- frequency range.

## 5.4 Conclusion

In this chapter, CWFEM was applied to study the wave propagating characteristics in orthogonally rib-stiffened plate. Main conclusions can be listed as follows:

- CWFEM was validated by comparing the band structure obtained by WFEM. The method was proved to predict correct dispersion characteristics including structural damping.
- The wave shapes were studied at several points on the band structures. The waves at the bounding points “O, A, B, C” in band structure are stationary.
- Computation time was reduced significantly by CWFEM, allowing the calculation of slowness surfaces be accomplished from 4 days to only 16 minutes.
- CWFEM can predict modal density for a finite structure with enough unit cells in mid- and high- frequency range.

Further investigation will address the prediction of the forced response [Renno & Mace, 2014] or the transmission loss of the stiffened plates [Cotoni *et al.*, 2008].

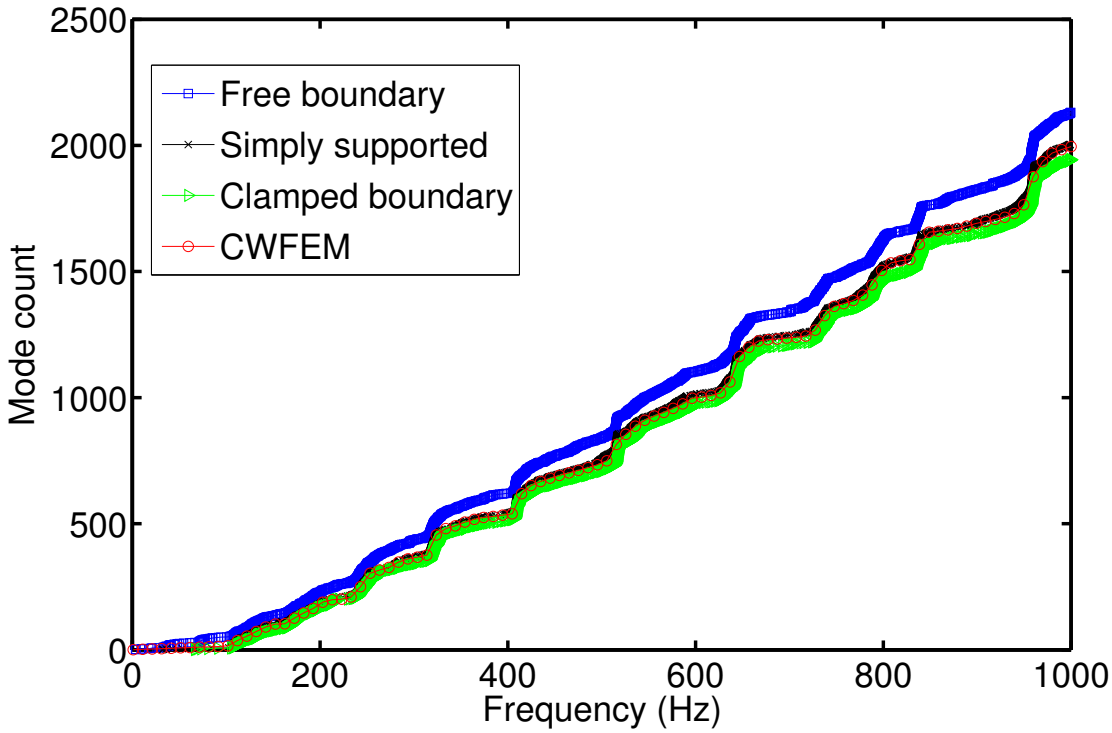


(a) Mode count

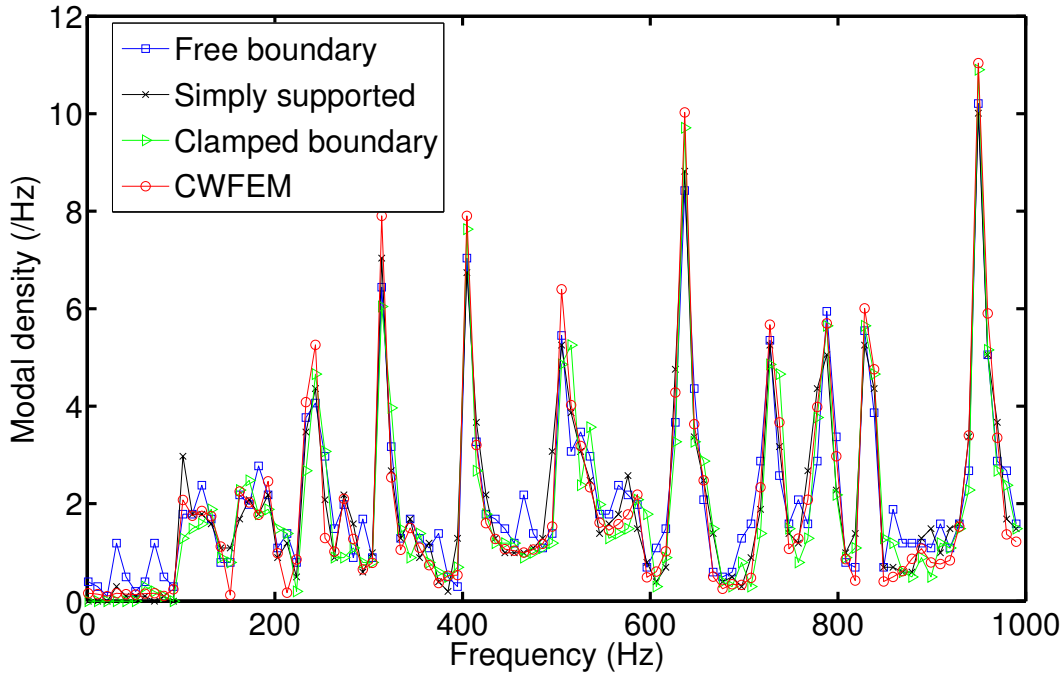


(b) Modal density

Figure 5.16: Modal density and mode count for stiffened plate with 100 unit cells

# Chapter 6

# Conclusions and Perspectives

## 6.1 Conclusions

The main findings and contributions of the conducted work are summarized below:

- The mode-based reduction technique was combined with the wave-based method to study the wave propagation in periodic structures. The modal description was employed to model the mesoscopic scale of the unit cell. The wave approach was then applied to study the global behaviours of the macroscopic structures. The wave-mode duality which assures the combination of the two approaches was discussed in chapter 1. The proposed method is referred as "CWFEM" for Condensed Wave Finite Element Method. Initially applied on 1D structures in chapter 2, it was subsequently extended to 2D structures in chapter 3. The validation of method was illustrated via several numerical examples. It was proved that the method is able to predict precisely wave propagation characteristics with significant reduction of computation time.

- To model the unit cell in CWFEM, the internal modes with natural frequency lower than three times of the maximum investigated frequency should be retained. In this case, CWFEM is able to predict correctly the propagating waves and some of the evanescent waves. There may be some discrepancies for the rapidly attenuating waves, however they have a negligible contribution to the forced response of the structure except at excitation point. Good correlation was found between the forced response by WFEM and CWFEM, as shown in chapter 2.

- The wave beaming effects in the beam grid was discussed in chapter 3. The phenomenon was observed both in the displacement field and the $k$-space. In this numerical example, it was verified that the waves at bounding frequencies of stop bands were stationary, they correspond to the cell modes under four special boundary conditions. The four boundary

conditions were identified and given as well.

- In chapter 4, CWFEM was applied to study wave propagation characteristics in perforated plates. Homogenization methods were proposed based on the obtained wave dispersion relation. Equivalent isotropic model was found for the perforated plates with circular holes with square and triangular penetration pattern. Good agreement was obtained between the natural modes of the homogenized model and full model. For perforated plate with square holes, an equivalent isotropic behaviour was obtained for out-of-plane waves and equivalent orthotropic model was found for in-plane waves. The $k$-space of the homogenized model concurs with the one of the full model.

- Experimental analyses were conducted on two models of perforated plate for the validation of CWFEM method. The out-of-plane displacement field under harmonic excitation is measured by a scanning laser, subsequently DFT2D is performed on the displacement field to deduce the $k$-space of the wave propagation. At low frequency, isotropic behaviour for out-of-plane waves was identified. At high frequency, wave beaming effects occur in one model. Good correlation was observed between the $k$-space predicted by CWFEM and the one measured by the experience.

- The wave propagation characteristics in a periodically stiffened panel were predicted by CWFEM in chapter 5. The influence of the first two internal modes on the global propagation in the structure was studied. Contrary to the beam grid where the 1st slowness surface was entirely determined by the constraint modes of the boundary, the 1st internal mode was needed to describe the wave propagation at 1st slowness surface in the stiffened plate. The slowness surfaces of the wave propagation were then used to compute modal density of a finite panel with 100 unit cells. The obtained results matched fairly well with the results by FEM. CWFEM allows the calculation of the slowness surfaces be done in 16 minutes instead of 4 days.

## 6.2 Perspectives

Periodic medium has attracted much attentions of the researchers and the field is experiencing continued growth in research activities. CWFEM is a general method which offers a range of applications over different kinds of periodic medium. The author attempts to foresee some probable perspective works as follows:

- Combine with the Statistical Energy Analysis (SEA) to predict vibroacoustic behaviours of stiffened plates, honeycomb sandwiches and composite panels [Chronopoulos *et al.*, 2014]. Analyse the influence of the unit cell with different geometries or materials on the

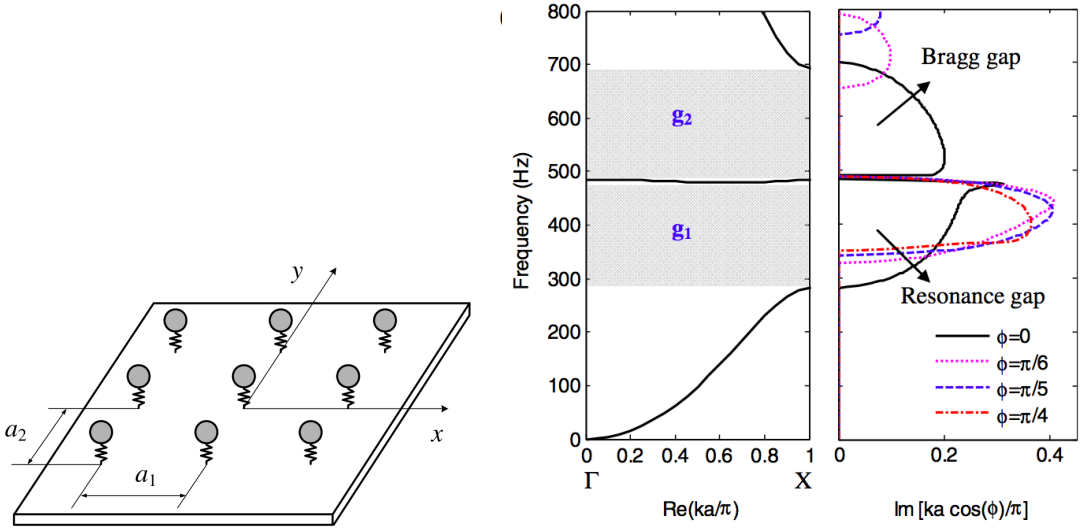


(a) Thin plate with a 2D periodic array of attached spring–mass resonators

(b) Band structure for the LR plate (TX for $x$ direction, $\phi$ represents the angle between the $x$-direction and propagation direction

Figure 6.1: Combination of Bragg gap and local resonance gap [Xiao *et al.*, 2012]

acoustic radiation and transmission loss. The SEA parameters, damping loss factor and engineering units response are all related to certain properties of the slowness surfaces, which can be derived directly by CWFEM.

- Design lightweight structures (such as honeycomb panels and multi-layed plates), with added internal local resonating elements to acquire excellent mechanical properties and stop bands at specified frequency range. The included local resonators can be various, from attached spring-mass resonators [Xiao *et al.*, 2012] to piezoelectric patches [Chen *et al.*, 2013; Spadoni *et al.*, 2009]. By tuning the local resonators, both the local resonance gap and Bragg gap can be significantly broadened [Xiao *et al.*, 2012]. Sometimes a super-wide pseudo-directional gap can be formed by a combination of the local resonance gap and the Bragg gap, as shown in Fig. 6.1(b). As for vibration control of plate with periodic arrays of shunted piezoelectric patches, the local resonance band gap is characterized by broadband behaviour and can be tuned through the selection of the shunting circuit resonance characteristics [Spadoni *et al.*, 2009]. CWFEM can be employed as a design tool for the selection of array configuration, spatial periodicity and shunting circuit of piezoelectric. Since the piezoelectric patches often involve more DOFs such as electric field and charge, the MOR in CWFEM becomes more advantageous when studying these structures.

- CWFEM can be applied to predict wave propagation characteristics in acoustic meta-materials or phononic crystals. These knowledges may be helpful for the design and application as vibration and acoustic shielding, acoustic absorption and acoustic/elastic

cloaking [Torrent & Sánchez-Dehesa, 2008].

- CWFEM will be extended to structures with cylindrical periodicity, to treat cylindrical and curved panels. Compared with flat panels, the mass and stiffness matrices in local coordinates must be rotated by the transform matrix to deduce the equation with global coordinates [Manconi & Mace, 2009].

- Apply the proposed homogenization method to find equivalent model for thick perforated plates, laminated composite plates and honeycomb sandwiches. High frequency homogenization tools which captures the interaction between different scales are also needed.

- For 2D periodic structures, the CWFEM formulation to compute wave propagation characteristics in a specified direction $\theta$ need to be investigated. Mace & Manconi [2008] proposed to fix $f$ and $\theta$ and solve wavenumber $k$, which leads to a polynomial or transcendental eigenvalue problem. To avoid selecting the real solutions from infinite number of solutions of a transcendental eigenvalue problem, Inquiete [2008] proposed an alternative way to study laminated composite plates. Instead of changing $\theta$ to study the wave propagating in different directions, he changed the orientation of the unit cell and studied always the wave propagating in the $x$-direction. In this way, he converted the problem from WFEM2D to WFEM1D. However, for periodic structures where unit cell is not arbitrary, the periodic pattern depends on the orientation direction of the unit cell. The 2D problem in the periodic structures can not be converted easily to 1D problem.

- Since the presence of damping is unavoidable in materials and structures, the damping effect in periodic structures will be investigated more in the further. Waves propagating in viscoelastic media can be characterised by complex frequency or complex wavenumbers according to whether time or spatial attenuation is involved [Manconi & Mace, 2010]. Thus the studies of damped structures may be carried out in two ways. The first one is to seek a wave dispersion solution for prescribed harmonic motion (real frequency, complex wavenumber) and the second one is concerned with obtaining a dispersion relation for free wave propagation (complex frequency). In the first category, Collet *et al.* [2011] proposed a formulation based on Floquet-Bloch decomposition whereby wave heading and frequency are used to scan the $k$-space and estimate the dispersion relations in structures with complex damping configuration. In the second category, a complex frequency is assumed which provides the usual frequency dispersion curves (affected by the presence of damping) and also curves associated with the temporal attenuation for each Bloch mode [Hussein *et al.*, 2014].

- Investigation are also needed to understand the sensitivity of the vibroacoustic behaviours the materials and manufacturing uncertainties. Since real structures are never perfectly periodic even in high precision applications such as aerospace. To treat this uncertainty

and relax the effects of periodicity, the vibroacoustic quantity of interest (mean square velocity, radiated power) can be band averaged [Legault *et al.*, 2011]. The localization effects caused by the small perturbations need to be considered since they can affect the response of periodic structures significantly [Hodges & Woodhouse, 1986].

# Appendix A

# The formulation of the matrices in Eq. (1.31)

The matrices $\mathbf{A}, \mathbf{B}, \mathbf{C}$ can be expressed by the partitioned matrices of $\mathbf{D}$, in the following formulations.

$$\mathbf{A}_{11} = \mathbf{D}_{12} + \mathbf{D}_{34} + \mathbf{D}_{32}\lambda_{\mathbf{y}}^{-1} + \mathbf{D}_{14}\lambda_{\mathbf{y}} \tag{A.1a}$$

$$\mathbf{A}_{1\mathtt{L}} = \mathbf{D}_{1\mathtt{R}} + \mathbf{D}_{3\mathtt{R}}\lambda_{\mathbf{y}}^{-1} \tag{A.1b}$$

$$\mathbf{A}_{1\mathtt{B}} = \mathbf{0} \tag{A.1c}$$

$$\mathbf{A}_{\mathtt{L}1} = \mathbf{D}_{\mathtt{L}2} + \mathbf{D}_{\mathtt{L}4}\lambda_{\mathbf{y}} \tag{A.1d}$$

$$\mathbf{A}_{\mathtt{LL}} = \mathbf{D}_{\mathtt{LR}} \tag{A.1e}$$

$$\mathbf{A}_{\mathtt{LB}} = \mathbf{0} \tag{A.1f}$$

$$\mathbf{A}_{\mathtt{B}1} = \mathbf{D}_{\mathtt{B}2} + \mathbf{D}_{\mathtt{T}4} + \mathbf{D}_{\mathtt{T}2}\lambda_{\mathbf{y}}^{-1} + \mathbf{D}_{\mathtt{B}4}\lambda_{\mathbf{y}} \tag{A.1g}$$

$$\mathbf{A}_{\mathtt{BL}} = \mathbf{D}_{\mathtt{BR}} + \mathbf{D}_{\mathtt{TR}}\lambda_{\mathbf{y}}^{-1} \tag{A.1h}$$

$$\mathbf{A}_{\mathtt{BB}} = \mathbf{0} \tag{A.1i}$$

And for the coefficients of the first order

$$\mathbf{B}_{11} = \mathbf{D}_{11} + \mathbf{D}_{22} + \mathbf{D}_{33} + \mathbf{D}_{44} + (\mathbf{D}_{31} + \mathbf{D}_{42})\lambda_{\mathbf{y}}^{-1} + (\mathbf{D}_{13} + \mathbf{D}_{24})\lambda_{\mathbf{y}} \tag{A.2a}$$

$$\mathbf{B}_{1\mathtt{L}} = \mathbf{D}_{1\mathtt{L}} + \mathbf{D}_{2\mathtt{R}} + (\mathbf{D}_{3\mathtt{L}} + \mathbf{D}_{4\mathtt{R}})\lambda_{\mathbf{y}}^{-1} \tag{A.2b}$$

$$\mathbf{B}_{1\mathtt{B}} = \mathbf{D}_{1\mathtt{B}} + \mathbf{D}_{3\mathtt{T}} + \mathbf{D}_{3\mathtt{B}}\lambda_{\mathbf{y}}^{-1} + \mathbf{D}_{1\mathtt{T}}\lambda_{\mathbf{y}} \tag{A.2c}$$

$$\mathbf{B}_{\mathtt{L}1} = \mathbf{D}_{\mathtt{L}1} + \mathbf{D}_{\mathtt{R}2} + \mathbf{D}_{\mathtt{L}3}\lambda_{\mathbf{y}} + \mathbf{D}_{\mathtt{R}4}\lambda_{\mathbf{y}} \tag{A.2d}$$

$$\mathbf{B}_{\mathtt{LL}} = \mathbf{D}_{\mathtt{LL}} + \mathbf{D}_{\mathtt{RR}} \tag{A.2e}$$

$$\mathbf{B}_{\mathtt{LB}} = \mathbf{D}_{\mathtt{LB}} + \mathbf{D}_{\mathtt{LT}}\lambda_{\mathbf{y}} \tag{A.2f}$$

$$\mathbf{B}_{\mathtt{B}1} = \mathbf{D}_{\mathtt{B}1} + \mathbf{D}_{\mathtt{T}3} + \mathbf{D}_{\mathtt{T}1}\lambda_{\mathbf{y}}^{-1} + \mathbf{D}_{\mathtt{B}3}\lambda_{\mathbf{y}} \tag{A.2g}$$

$$\mathbf{B}_{\mathtt{BL}} = \mathbf{D}_{\mathtt{BL}} + \mathbf{D}_{\mathtt{TL}}\lambda_{\mathbf{y}}^{-1} \tag{A.2h}$$

$$\mathbf{B}_{\mathtt{BB}} = \mathbf{D}_{\mathtt{BB}} + \mathbf{D}_{\mathtt{TT}} + \mathbf{D}_{\mathtt{TB}}\lambda_{\mathbf{y}}^{-1} + \mathbf{D}_{\mathtt{BT}}\lambda_{\mathbf{y}} \tag{A.2i}$$

The constant terms are

$$\mathbf{C}_{11} = \mathbf{D}_{21} + \mathbf{D}_{43} + \mathbf{D}_{41}\lambda_{\mathbf{y}}^{-1} + \mathbf{D}_{23}\lambda_{\mathbf{y}} \tag{A.3a}$$

$$\mathbf{C}_{1\mathtt{L}} = \mathbf{D}_{2\mathtt{L}} + \mathbf{D}_{4\mathtt{L}}\lambda_{\mathbf{y}}^{-1} \tag{A.3b}$$

$$\mathbf{C}_{1\mathtt{B}} = \mathbf{D}_{2\mathtt{B}} + \mathbf{D}_{4\mathtt{T}} + \mathbf{D}_{4\mathtt{B}}\lambda_{\mathbf{y}}^{-1} + \mathbf{D}_{2\mathtt{T}}\lambda_{\mathbf{y}} \tag{A.3c}$$

$$\mathbf{C}_{\mathtt{L}1} = \mathbf{D}_{\mathtt{R}1} + \mathbf{D}_{\mathtt{R}3}\lambda_{\mathbf{y}} \tag{A.3d}$$

$$\mathbf{C}_{\mathtt{LL}} = \mathbf{D}_{\mathtt{RL}} \tag{A.3e}$$

$$\mathbf{C}_{\mathtt{LB}} = \mathbf{D}_{\mathtt{RB}} + \mathbf{D}_{\mathtt{RT}}\lambda_{\mathbf{y}} \tag{A.3f}$$

$$\mathbf{C}_{\mathtt{B}1} = \mathbf{0} \tag{A.3g}$$

$$\mathbf{C}_{\mathtt{BL}} = \mathbf{0} \tag{A.3h}$$

$$\mathbf{C}_{\mathtt{BB}} = \mathbf{0} \tag{A.3i}$$

# Appendix B

# Wave shapes of stiffened plate during a period

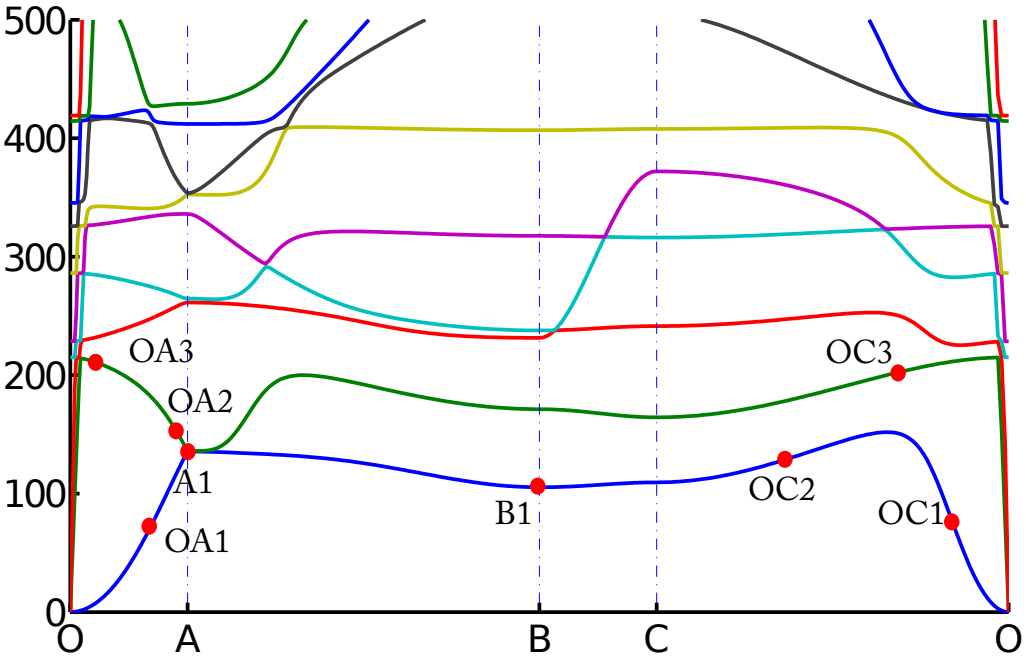


Figure B.1: The points in the band structure where wave shape is plotted

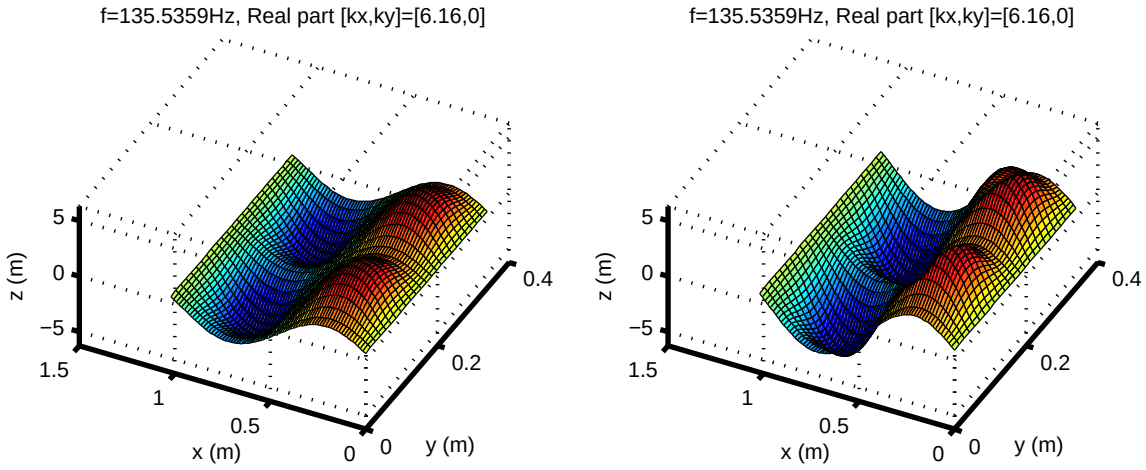


(a) At t=0




(b) At t=T/6

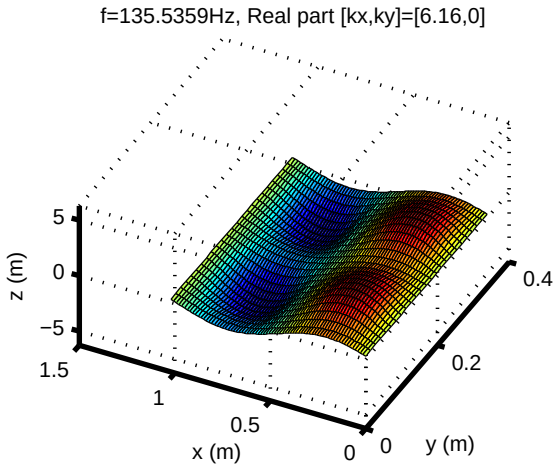


(c) At t=T/3

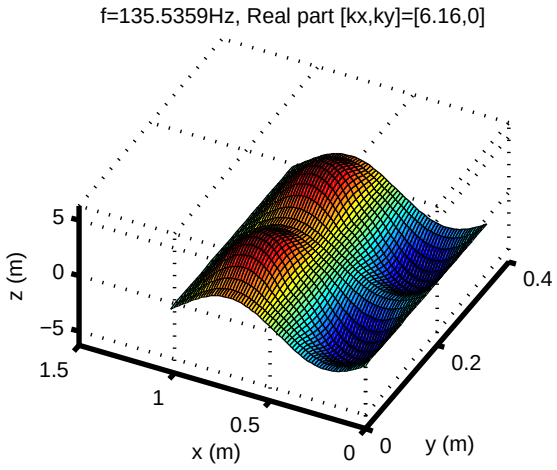


(d) At t=T/2

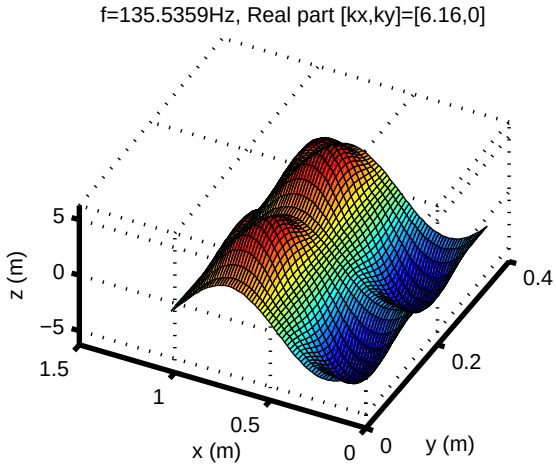


(e) At t=2T/3

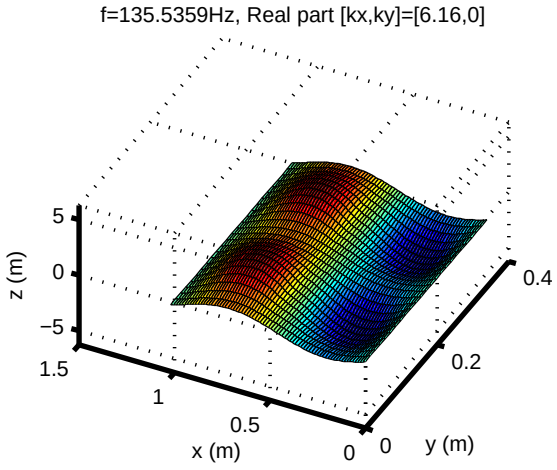


(f) At t=5T/6

Figure B.2: Wave shape at “A1” during a period

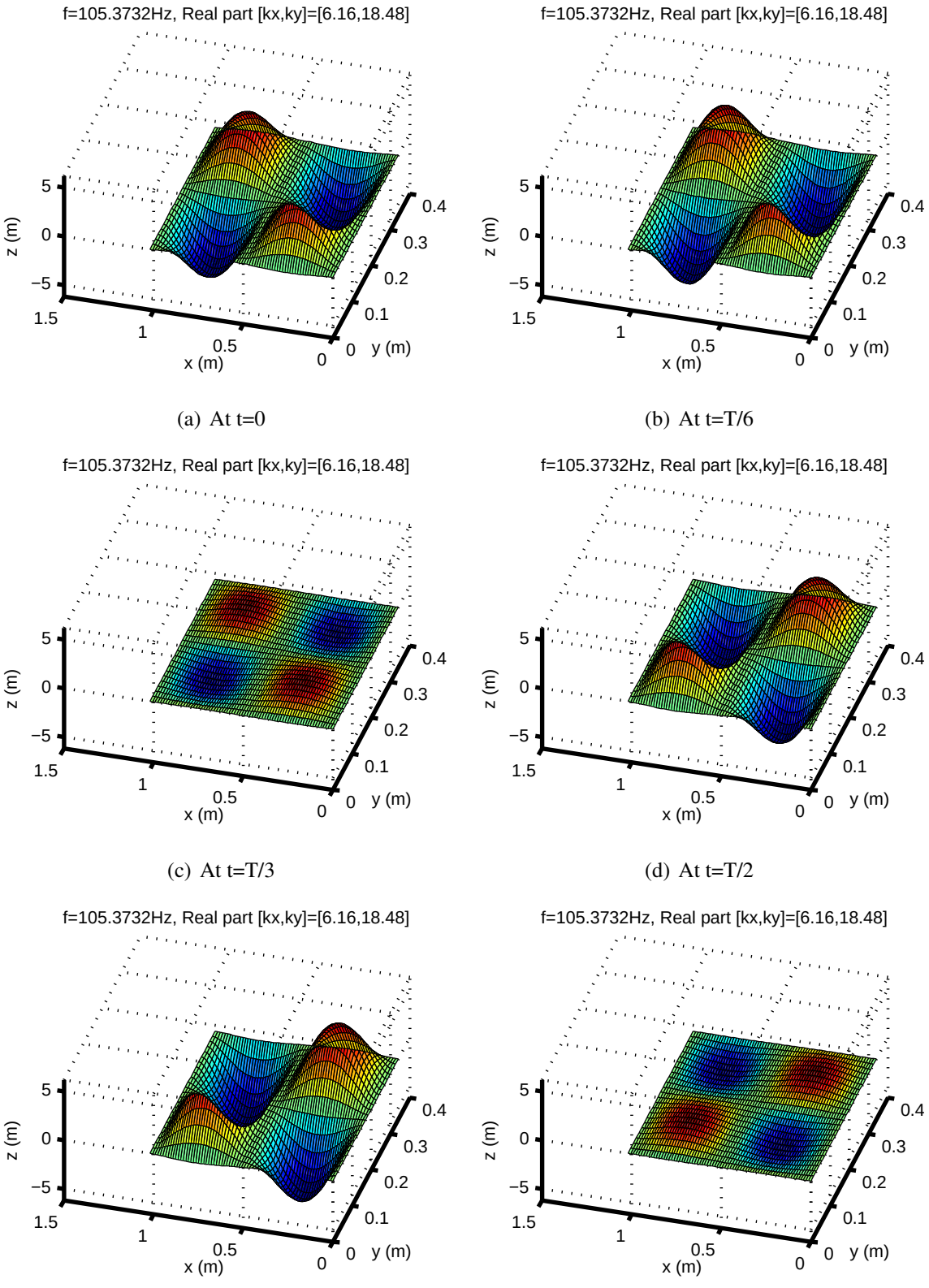


(a) At t=0

(b) At t=T/6

(c) At t=T/3

(d) At t=T/2

(e) At t=2T/3

(f) At t=5T/6

Figure B.3: Wave shape at “B1” during a period

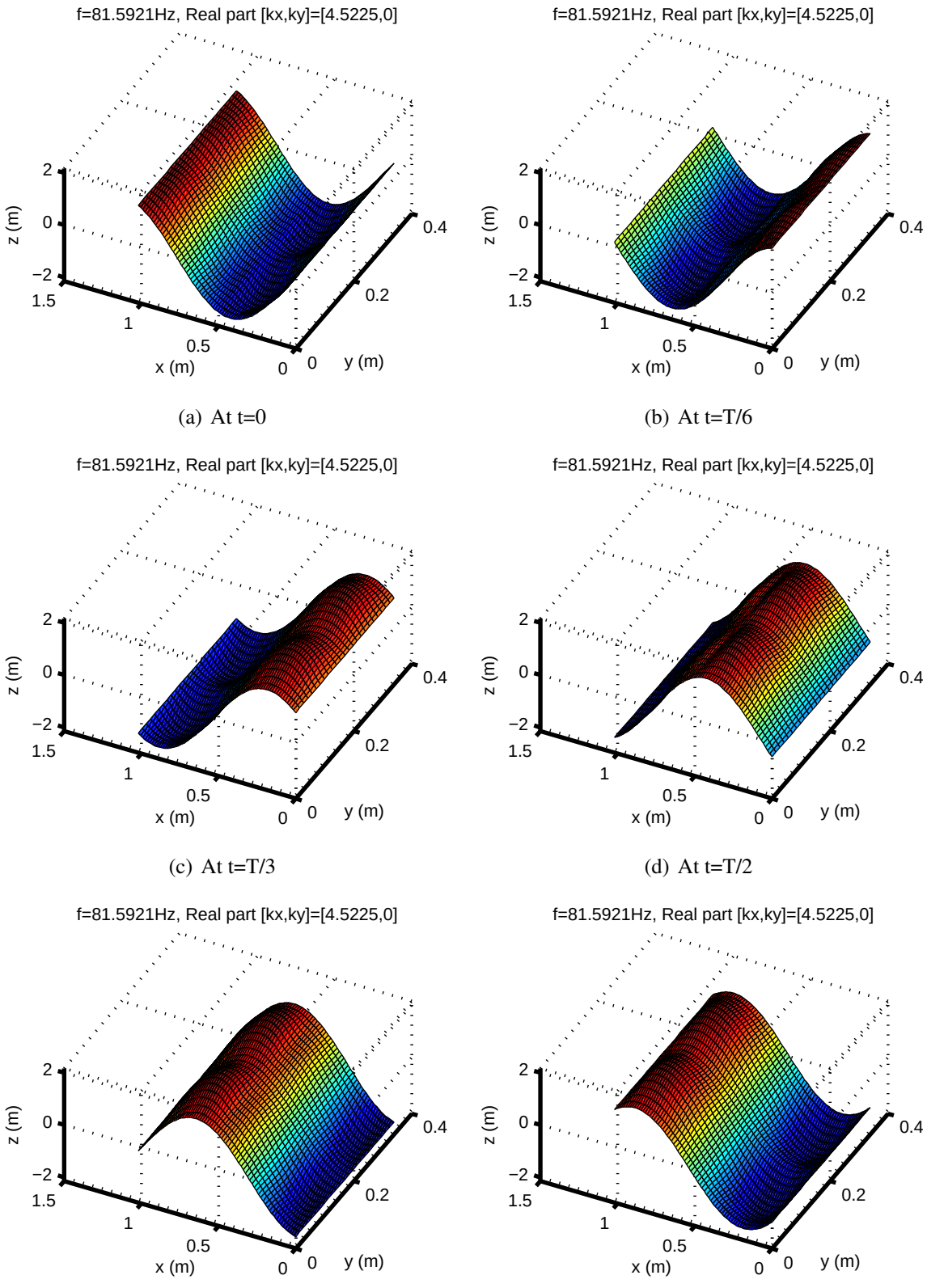


(a) At t=0

(b) At t=T/6

(c) At t=T/3

(d) At t=T/2

(e) At t=2T/3

(f) At t=5T/6

Figure B.4: Wave shape at “OA1” during a period

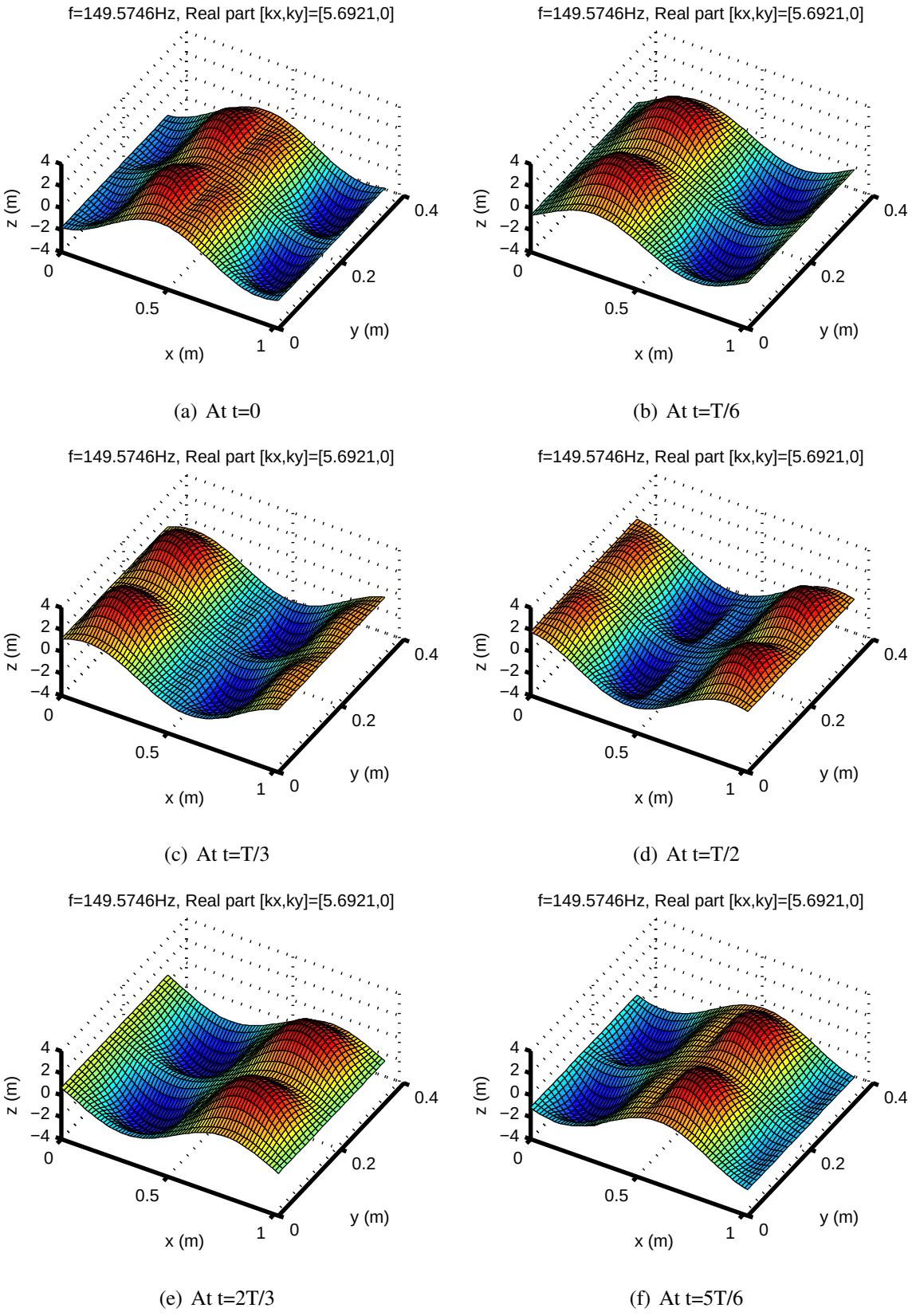


(a) At t=0

(b) At t=T/6

(c) At t=T/3

(d) At t=T/2

(e) At t=2T/3

(f) At t=5T/6

Figure B.5: Wave shape at “OA2” during a period

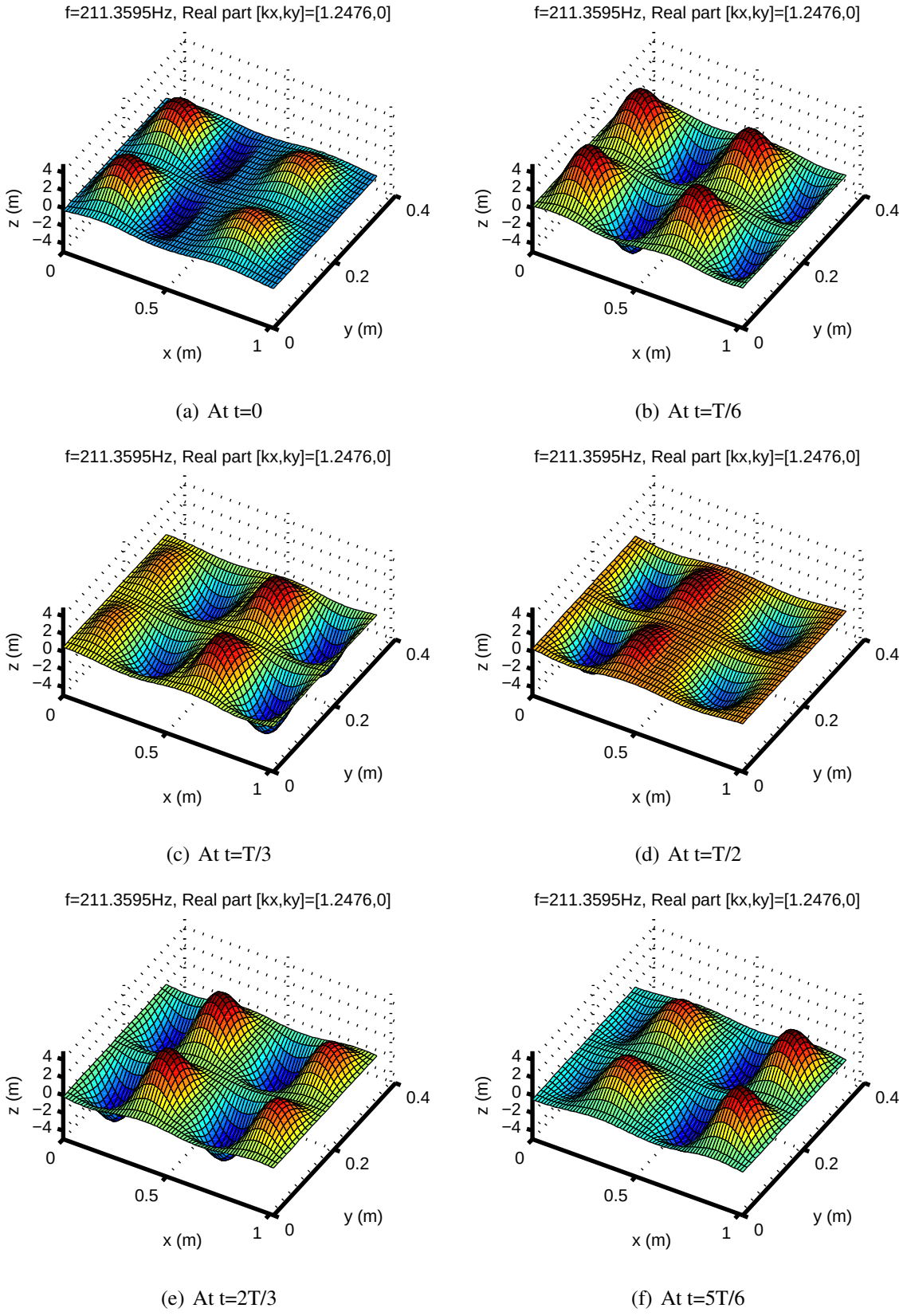


(a) At t=0

(b) At t=T/6

(c) At t=T/3

(d) At t=T/2

(e) At t=2T/3

(f) At t=5T/6

Figure B.6: Wave shape at “OA3” during a period

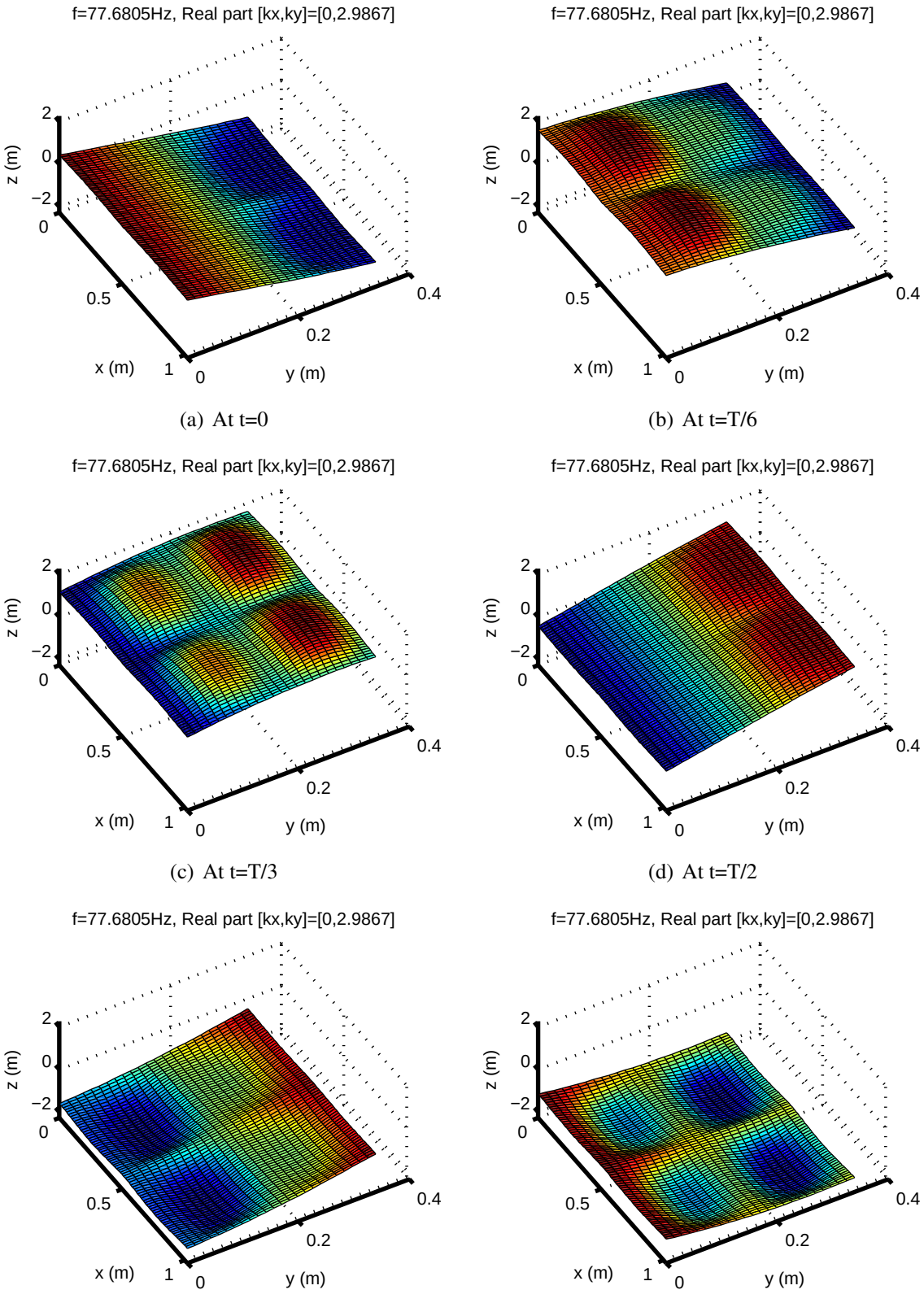


(a) At t=0

(b) At t=T/6

(c) At t=T/3

(d) At t=T/2

(e) At t=2T/3

(f) At t=5T/6

Figure B.7: Wave shape at “OC1” during a period

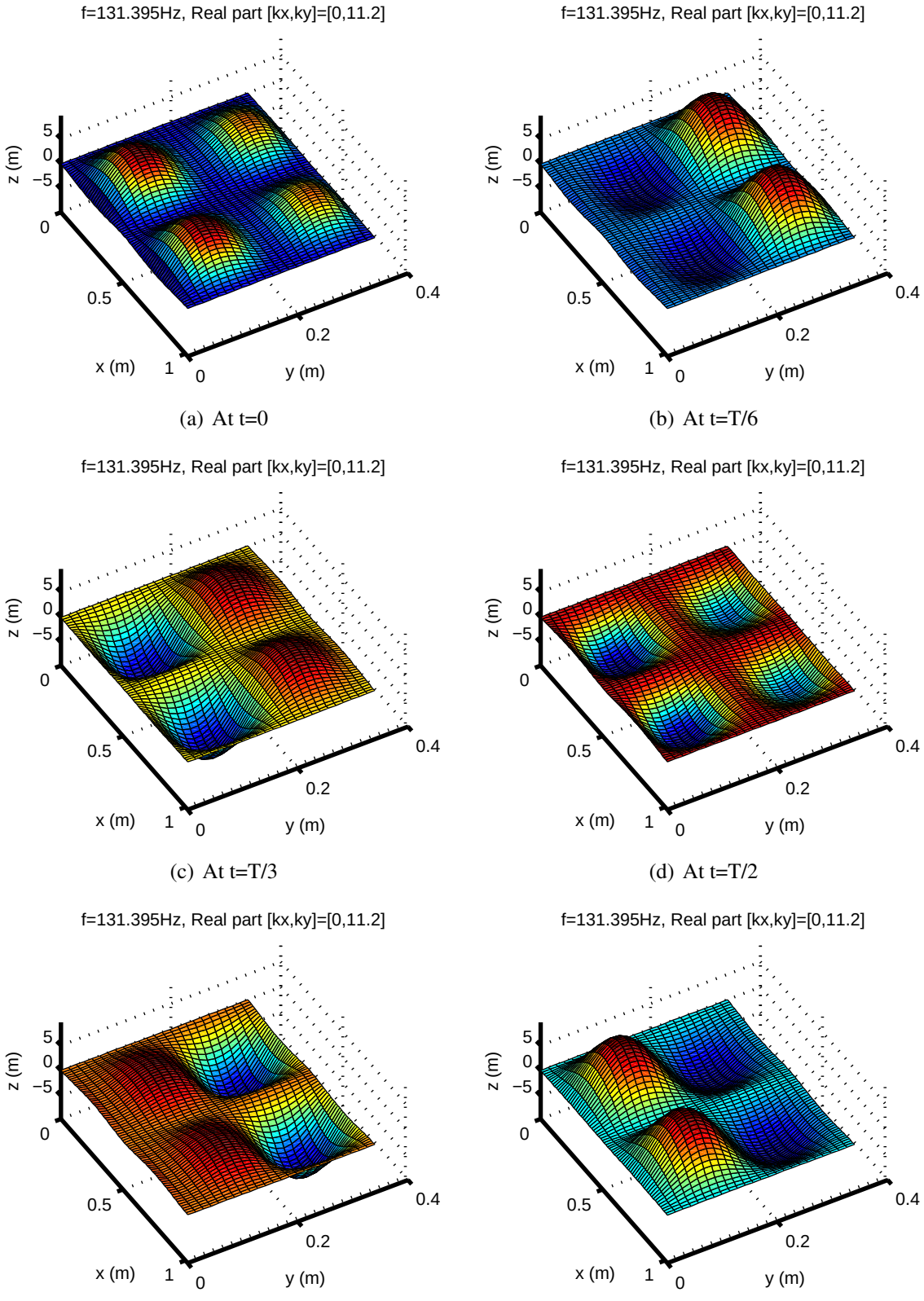


(a) At t=0

(b) At t=T/6

(c) At t=T/3

(d) At t=T/2

(e) At t=2T/3

(f) At t=5T/6

Figure B.8: Wave shape at “OC2” during a period

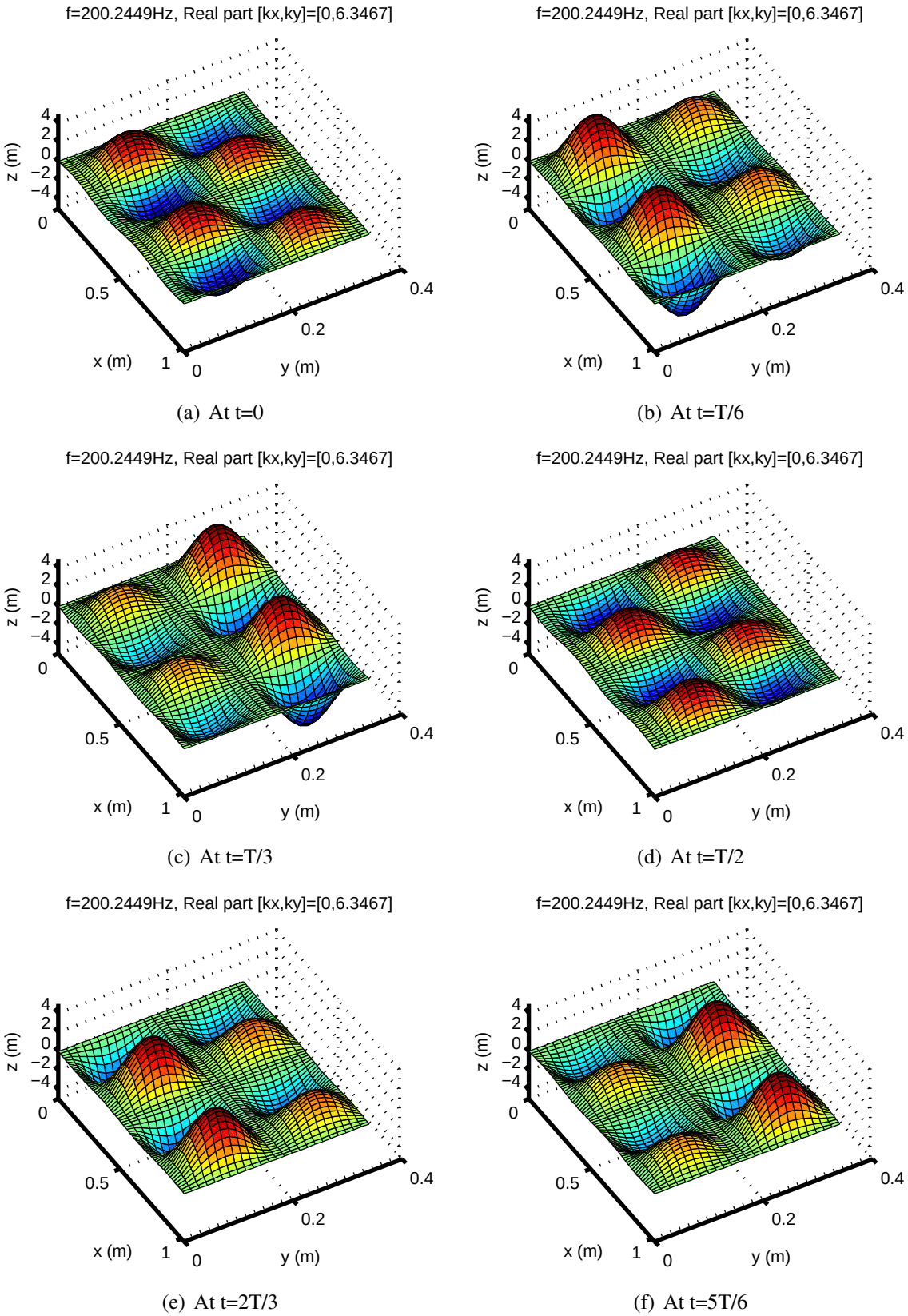


(a) At t=0

(b) At t=T/6

(c) At t=T/3

(d) At t=T/2

(e) At t=2T/3

(f) At t=5T/6

Figure B.9: Wave shape at “OC3” during a period

# Appendix C

# Modal analysis of the finite element model of the stiffened plate

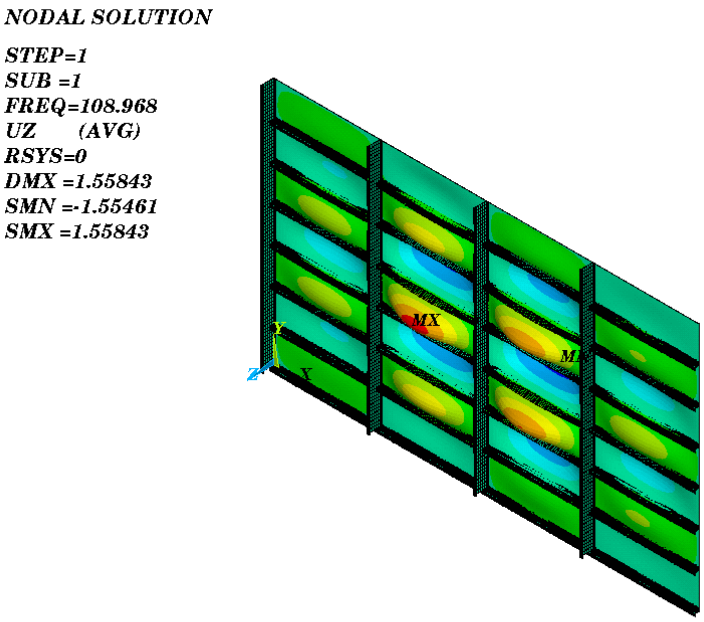


Figure C.1: First local mode (1,1) at 109 Hz

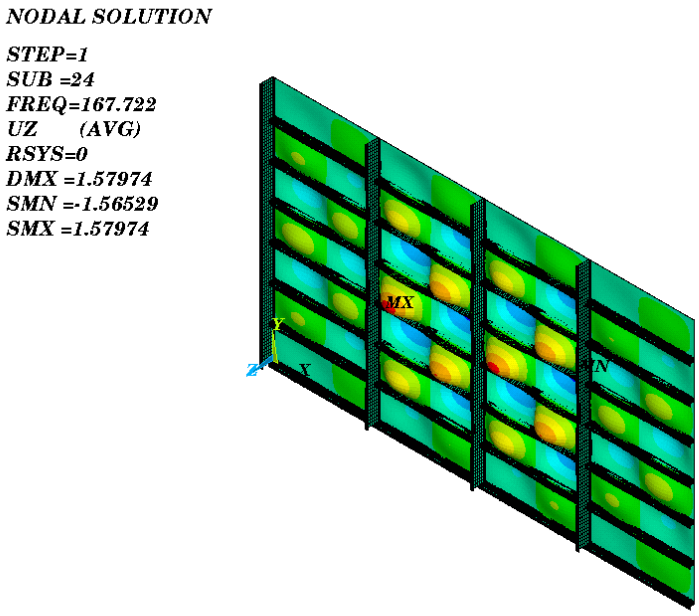


Figure C.2: First local mode (2,1) at 168 Hz

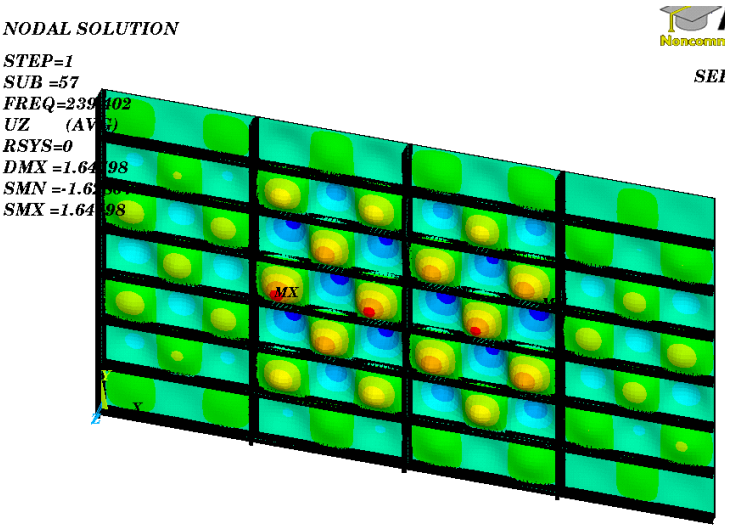


Figure C.3: First local mode (3,1) at 240 Hz

# Appendix D

# Some experimental measurements on perforated plate (model 2)

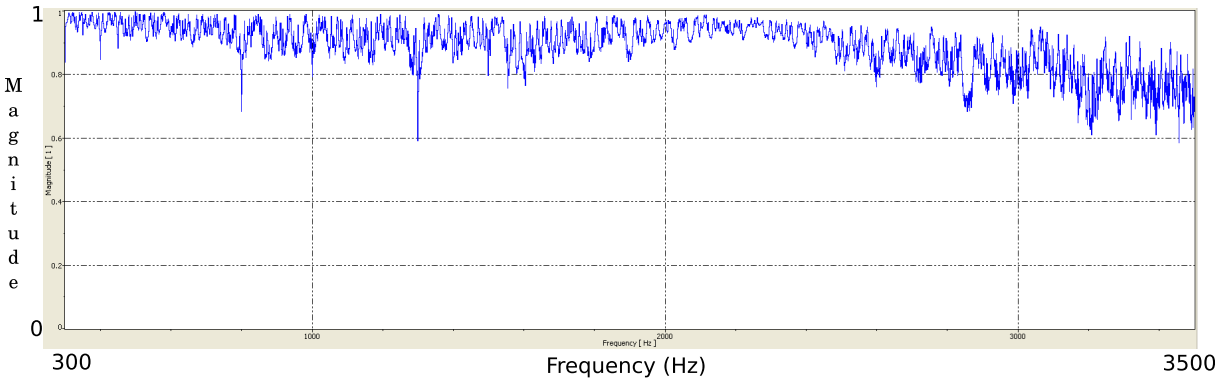


Figure D.1: Coherence between laser and force between 300 Hz-3500 Hz (force of excitation in the same frequency range)

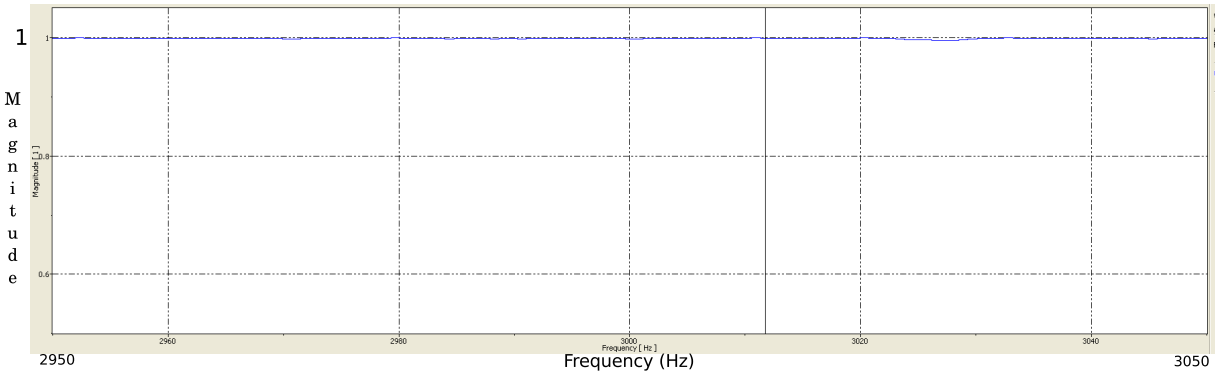


Figure D.2: Coherence between laser and force between 2950-3050 Hz (force of excitation in the same frequency range)

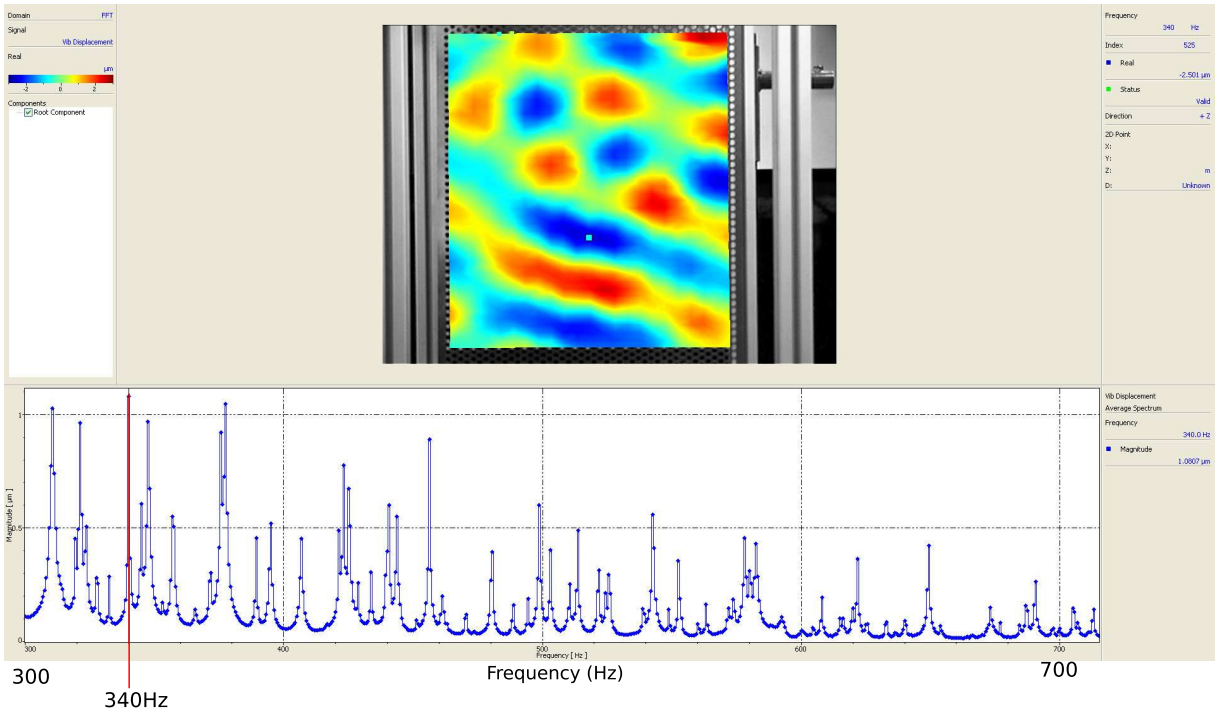


Figure D.3: Mode shape at 340 Hz (Top view) The average spectrum of the response to harmonic excitation (Bottom view)

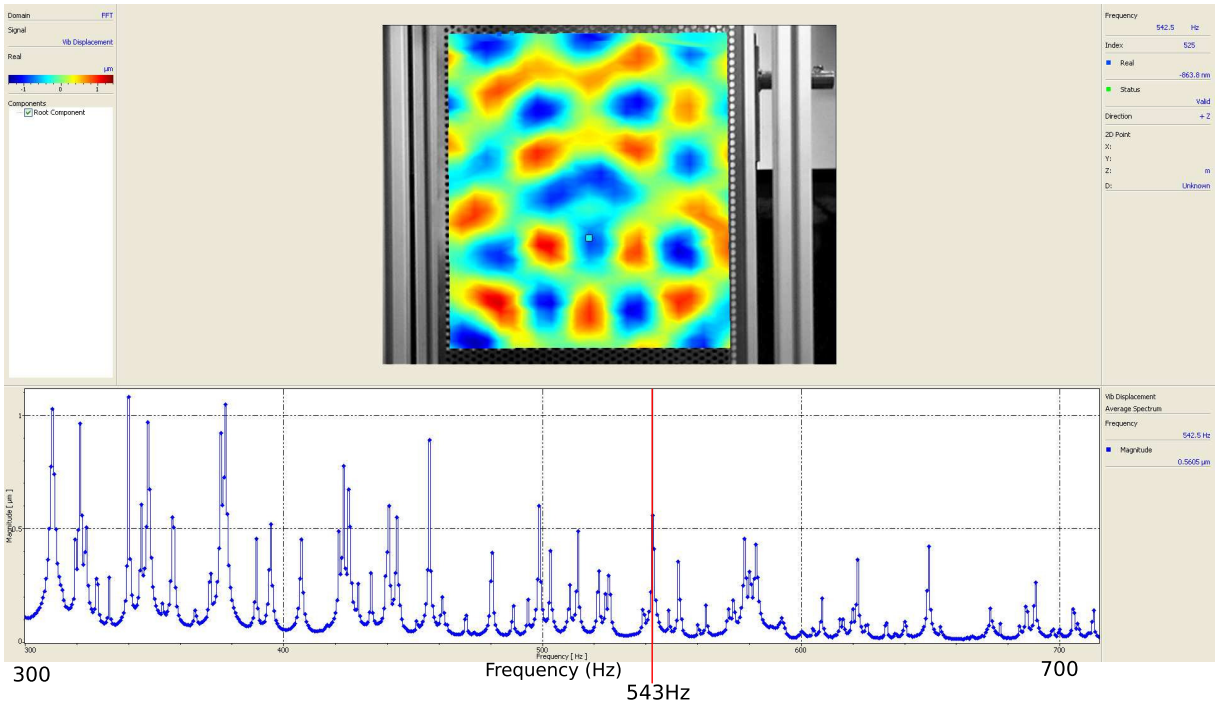


Figure D.4: Mode shape at 543 Hz (Top view) The average spectrum of the response to harmonic excitation (Bottom view)

# References


ACHAOUI, Y., KHELIF, A., BENCHABANE, S., ROBERT, L. & LAUDE, V. (2011). Experimental observation of locally-resonant and Bragg band gaps for surface guided waves in a phononic crystal of pillars. *Physical Review B*, **83**, 104201. 12

ANTOULAS, A.C. & SORENSEN, D.C. (2001). Approximation of large-scale dynamical systems: An overview. *International Journal of Applied Mathematics and Computer Science*, **11**, 1093–1121. 26

BLOCH, F. (1929). Über die Quantenmechanik der Elektronen in Kristallgittern. *Zeitschrift für Physik*, **52**, 555–600. 2, 10, 16, 60

BOLTON, J.S., KIM, Y.K. & SONG, H.J. (1998). The Wave Number Decomposition Approach to the Analysis of Tire Vibration. In *Proceedings of the Noise-Conference '98*. 93

BRADLEY, C.E. (1991). Acoustic Bloch wave propagation in a periodic waveguide. Tech. rep., The university of Texas at Austin, Texas. 43

BRILLOUIN, L. (1953). *Wave Propagation in Periodic Structures*. Dover Publication, New York, 2nd edn. 11, 35, 46, 64

CECCHI, A. & RIZZI, N.L. (2001). Heterogeneous elastic solids : a mixed homogenization-rigidication technique. *Internal journal of solids ans structures*, **38**, 29–36. 23

CHALLAGULLA, K.S., GEORGIADES, A.V. & KALAMKAROV, A.L. (2010). Asymptotic homogenization modeling of smart composite generally orthotropic grid-reinforced shells: Part I – theory. *European Journal of Mechanics - A/Solids*, **29**, 530–540. 23

CHEN, S., WANG, G., WEN, J. & WEN, X. (2013). Wave propagation and attenuation in plates with periodic arrays of shunted piezo-patches. *Journal of Sound and Vibration*, **332**, 1520–1532. 129

CHEN, Z. & XIE, W.C. (2005). Vibration localization in plates rib-stiffened in two orthogonal directions. *Journal of Sound and Vibration*, **280**, 235–262. 111

CHERN, R.L., CHANG, C.C., CHANG, C.C. & HWANG, R.R. (2003). Large full band gaps for photonic crystals in two dimensions computed by an inverse method with multigrid acceleration. *Physical review. E, Statistical, nonlinear, and soft matter physics*, **68**, 026704. 26

CHRONOPOULOS, D., TROCLET, B., BAREILLE, O. & ICHCHOU, M.N. (2013). Modeling the response of composite panels by a dynamic stiffness approach. *Composite Structures*, **96**, 111–120. 25, 91

CHRONOPOULOS, D., ICHCHOU, M., TROCLET, B. & BAREILLE, O. (2014). Computing the broadband vibroacoustic response of arbitrarily thick layered panels by a wave finite element approach. *APPLIED ACOUSTICS*, **77**, 89–98. 128

COLLET, M., OUISSE, M., RUZZENE, M. & ICHCHOU, M.N. (2011). Floquet Bloch decomposition for the computation of dispersion of two-dimensional periodic, damped mechanical systems. *International Journal of Solids and Structures*, **48**, 2837–2848. 130

COTONI, V., LANGLEY, R.S. & SHORTER, P.J. (2008). A statistical energy analysis subsystem formulation using finite element and periodic structure theory. *Journal of Sound and Vibration*, **318**, 1077–1108. 62, 124

CRAIG, R. & BAMPTON, M. (1968). Coupling of Substructures for Dynamic Analyses. *AIAA Journal*, **6**, 1313–1319. 26

CRASTER, R.V., KAPLUNOV, J., NOLDE, E. & GUENNEAU, S. (2012). Bloch dispersion and high frequency homogenization for separable doubly-periodic structures. *Wave Motion*, **49**, 333–346. 23

CREMER, L. & HECKL, M. (2005). *Structure-Borne Sound*. Springer, Berlin, Heidelberg, 3rd edn. 36

CREMER, L. & LEILICH, H.O. (1953). Zur Theorie der Biegeketten- leiter. *Arch. Elektr. Uebertrag*, **7**, 261–270. 8

DARINSKII, A.N., LE CLEZIO, E. & FEUILLARD, G. (2008). Acoustic wave degeneracies in two-dimensional phononic crystals. *Wave Motion*, **45**, 970–980. 63

DOBSON, D.C. (1999). An efficient method for band structure calculations in 2D photonic crystals. *Journal of Computational Physics*, **149**, 363–376. 26

DROZ, C., LAINÉ, J.P., ICHCHOU, M.N. & INQUIÉTÉ, G. (2014a). A reduced formulation for the free-wave propagation analysis in composite structures. *Composite Structures*, **113**, 134–144. 9, 29, 30, 159

DROZ, C., ZHOU, C.W., ICHCHOU, M.N. & LAINÉ, J.P. (2014b). Wave dispersion characteristics in orthogonally stiffened panels. In *Proceedings of the VISHNO 19th*, Aix-en-Provence, France. 4

DROZ, C., ZHOU, C.W., ICHCHOU, M.N. & LAINÉ, J.P. (2015). A hybrid wave-mode formulation for the vibro-acoustic analysis of 2d periodic structures. *submitted to Journal of sound and vibration*. 4

DUHAMEL, D., MACE, B.R. & BRENNAN, M.J. (2006). Finite element analysis of the vibrations of waveguides and periodic structures. *Journal of Sound and Vibration*, **294**, 205–220. 9, 18

ECONOMOU, E. & SIGALAS, M. (1993). Classical wave propagation in periodic structures: Cermet versus network topology. *Physical Review B*, **48**, 13434–13438. 10

EWINS, D.J. (1984). *Modal Testing: Theory and Practice*. Johy Wiley & Sons Inc, New York. 25, 76

FAHY, F. & LINDQVIST, E. (1976). Wave propagation in damped, stiffened structures characteristic of ship construction. *Journal of Sound and Vibration*, **45**, 115–138. 111

FLOQUET, G. (1883). Sur les équations différentielles linéaires à coefficients périodiques. *Annales scientifiques de l'École Normale Supérieure*, **12**, 47–88. 16

GÉRADIN, M. & RIXEN, D. (1992). *Théorie des vibrations: application á la dynamique des structures*. Masson, Paris. 90

GLADWELL, G.M.L. (1964). Branch mode analysis of vibrating systems. *Journal of Sound and Vibration*, **1**, 41–59. 26

GOFFAUX, C., SÁNCHEZ-DEHESA, J., YEYATI, A.L., LAMBIN, P., KHELIF, A., VASSEUR, J. & DJAFARI-ROUHANI, B. (2002). Evidence of fano-like interference phenomena in locally resonant materials. *Physical review letters*, **88**, 225502. 12

GROSH, K. & WILLIAMS, E.G. (1993). Complex wave-number decomposition of structural vibrations. *The Journal of the Acoustical Society of America*, **93**, 836. 93

HALKJAER, S., SIGMUND, O. & JENSEN, J.S. (2006). Maximizing band gaps in plate structures. *Structural and Multidisciplinary Optimization*, **32**, 263–275. 10

HECKL, M.A. (1964). Investigations on the Vibrations of Grillages and Other Simple Beam Structures. *The Journal of the Acoustical Society of America*, **36**, 1335. 8

HODGES, C.H. & WOODHOUSE, J. (1986). Theories of noise and vibration transmission in complex structures. *Reports on Progress in Physics*, **49**, 107–170. 131

HOUILLON, L., ICHCHOU, M.N. & JEZEQUEL, L. (2005). Wave motion in thin-walled structures. *Journal of Sound and Vibration*, **281**, 483–507. 16

HUANG, T.L., ICHCHOU, M.N., BAREILLE, O., COLLET, M. & OUISSE, M. (2013). Multimodal wave propagation in smart structures with shunted piezoelectric patches. *Computational Mechanics*, **52**, 721–739. 9

HUSSEIN, M.I. (2009). Reduced Bloch mode expansion for periodic media band structure calculations. *Proceedings of the Royal Society A*, **465**, 2825–2848. 29, 31

HUSSEIN, M.I., LEAMY, M.J. & RUZZENE, M. (2014). Dynamics of Phononic Materials and Structures: Historical Origins, Recent Progress, and Future Outlook. *Applied Mechanics Reviews*, **66**, 040802. 10, 11, 12, 130

ICHCHOU, M.N., BERTHAUT, J. & COLLET, M. (2008). Multi-mode wave propagation in ribbed plates: Part I, wavenumber-space characteristics. *International Journal of Solids and Structures*, **45**, 1179–1195. 111, 123

ICHCHOU, M.N., MENCIK, J.M. & ZHOU, W.J. (2009). Wave finite elements for low and mid-frequency description of coupled structures with damage. *Computer Methods in Applied Mechanics and Engineering*, **198**, 1311–1326. 9

ICHCHOU, M.N., BAREILLE, O. & ZHOU, W. (2011). Vibroacoustic control of fuselage panel. Tech. rep., Ecole Centrale de Lyon, Lyon. 112, 114, 161

INQUIETE, G. (2008). *Simulation numérique de la propagation des ondes dans les structures composites stratifiées*. Ph.D. thesis, Ecole Centrale de Lyon. 40, 130

JHUNG, M.J. & JO, J.C. (2006). Equivalent material properties of perforated plate with triangular or square penetration pattern for dynamic analysis. *Nuclear engineering and technology*, **38**, 689–696. 25, 88

KAFESAKI, M. & ECONOMOU, E. (1999). Multiple-scattering theory for three-dimensional periodic acoustic composites. *Physical Review B*, **60**, 11993–12001. 12

KALAMKAROV, A.L., HASSAN, E.M., GEORGIADES, A.V. & SAVI, M.A. (2009). Asymptotic homogenization model for 3D grid-reinforced composite structures with generally orthotropic reinforcements. *Composite Structures*, **89**, 186–196. 23, 24

KITTEL, C. (2004). *Introduction to Solid State Physics*. Wiley, 8th edition. 11, 43

KOHRS, T. & PETERSSON, A.T., BJÖRN (2009). Wave beaming and wave propagation in light weight plates with truss-like cores. *Journal of Sound and Vibration*, **321**, 137–165. 64

KUSHWAHA, M.S. & HALEVI, P. (1994). Band-gap engineering in periodic elastic composites. *Applied Physics Letters*, **64**, 1085. 10

KUSHWAHA, M.S., HALEVI, P., DOBRZYNSKI, L. & DJAFARI-ROUHANI, B. (1993). Acoustic band structure of periodic elastic composites. *Physical Review Letters*, **71**, 2022–2025. 1

LANGLEY, R. (1997). Some perspectives on wave-mode duality in SEA. In *IUTAM Symposium on Statistical Energy Analysis*, 1–12. 32

LANGLEY, R.S. (1994). On the modal density and energy flow characteristics of periodic structures. *Journal of Sound and Vibration*, **172**, 491–511. 35, 64

LANGLEY, R.S. & BARDELL, N.S. (1997). The response of two-dimensional periodic structures to harmonic point loading: a theoretical and experimental study of a beam grillage. *Journal of Sound and Vibration*, **207**, 521–535. 64, 65, 66, 71, 72, 84, 160

LEE, J.H. & KIM, J. (2002). Analysis of Sound Transmission Through Periodically Stiffened Panels By Space-Harmonic Expansion Method. *Journal of Sound and Vibration*, **251**, 349–366. 9, 111

LEGAULT, J. & ATALLA, N. (2009). Numerical and experimental investigation of the effect of structural links on the sound transmission of a lightweight double panel structure. *Journal of Sound and Vibration*, **324**, 712–732. 9

LEGAULT, J. & ATALLA, N. (2010). Sound transmission through a double panel structure periodically coupled with vibration insulators. *Journal of Sound and Vibration*, **329**, 3082–3100. 9

LEGAULT, J., MEJDI, A. & ATALLA, N. (2011). Vibro-acoustic response of orthogonally stiffened panels : The effects of finite dimensions. *Journal of Sound and Vibration*, **330**, 5928–5948. 131

LI, C., HUANG, D., GUO, J. & NIE, J. (2013). Engineering of band gap and cavity mode in phononic crystal strip waveguides. *Physics Letters A*, **377**, 2633–2637. 10

LIN, T.R. & PAN, J. (2006). A closed form solution for the dynamic response of finite ribbed plates. *The Journal of the Acoustical Society of America*, **119**, 917. 112

LIN, Y.K. & MCDANIEL, T.J. (1969). Dynamics of Beam-Type Periodic Structures. *Journal of Engineering for Industry*, **91**, 1133. 9, 49

LIU, Z. (2000). Locally Resonant Sonic Materials. *Science*, **289**, 1734–1736. 10

LIU, Z.Y., CHAN, C. & SHENG, P. (2002). Three-component elastic wave band-gap material. *Physical Review B*, **65**, 165116. 12

LYON, R.H. & DEJONG, R.G. (1995). *Theory and Application of Statistical Energy Analysis*, vol. 98. Butterworth-Heinemann, Boston, 2nd edn. 32

MACE, B.R. (1980a). Periodically stiffened fluid-loaded plates, I: Response to convected harmonic pressure and free wave propagation. *Journal of Sound and Vibration*, **73**, 473–486. 9

MACE, B.R. (1980b). Periodically stiffened fluid-loaded plates, II: Response to line and point forces. *Journal of Sound and Vibration*, **73**, 487–504. 9

MACE, B.R. (1980c). Sound radiation from a plate reinforced by two sets of parallel stiffeners. *Journal of Sound and Vibration*, **71**, 435–441. 9

MACE, B.R. & MANCONI, E. (2008). Modelling wave propagation in two-dimensional structures using finite element analysis. *Journal of Sound and Vibration*, **318**, 884–902. 39, 62, 130

MACE, B.R. & MANCONI, E. (2012). Wave motion and dispersion phenomena: veering, locking and strong coupling effects. *The Journal of the Acoustical Society of America*, **131**, 1015–28. 65

MACE, B.R., DUHAMEL, D. & BRENNAN, M.J. (2005). Finite element prediction of wave motion in structural waveguides. *The Journal of the Acoustical Society of America*. 18, 40

MANCONI, E. & MACE, B.R. (2009). Wave characterization of cylindrical and curved panels using a finite element method. *The Journal of the Acoustical Society of America*, 154–63. 130

MANCONI, E. & MACE, B.R. (2010). Estimation of the loss factor of viscoelastic laminated panels from finite element analysis. *Journal of Sound and Vibration*, **329**, 3928–3939. 130

MAURY, C. & MATTEI, P.O. (2002). Sound Transmission Through a Rib-Stiffened Plate: Comparisons of a Light-Fluid Approximation With Experimental Results. *Journal of Sound and Vibration*, 206–212. 111

MCDANIEL, J.G. & SHEPARD, W.S. (2000). Estimation of structural wave numbers from spatially sparse response measurements. *The Journal of the Acoustical Society of America*, **108**, 1674–82. 93

MEAD, D.J. (1973). A general theory of harmonic wave propagation in linear periodic systems with multiple coupling. *Journal of Sound and Vibration*, **27**, 235–260. 2

MEAD, D.J. (1975a). Wave propagation and natural modes in periodic systems : I.mono-coupled systems. *Journal of Sound and Vibration*, **40**, 1–18. 35, 43, 83

MEAD, D.J. (1975b). Wave propagation and natural modes in periodic systems: II. Multi-coupled systems, with and without damping. *Journal of Sound and Vibration*, **40**, 19–39. 17, 35, 66, 83

MEAD, D.J. (1990). Plates with regular stiffening in acoustic media: Vibration and radiation. *The Journal of the Acoustical Society of America*, **88**, 391. 9

MEAD, D.J. (1996). Wave propagation in continuous periodic structures: research contributions from southampton, 1964 to 1995. *Journal of Sound and Vibration*, **190**, 495–524. 9

MEAD, D.J. (2009). The forced vibration of one-dimensional multi-coupled periodic structures: An application to finite element analysis. *Journal of Sound and Vibration*, **319**, 282–304. 30

MEAD, D.J. & PARTHAN, S. (1979). Free wave propagation in two-dimensional periodic plates. *Journal of Sound and Vibration*, **64**, 325–348. 63

MEAD, D.J. & PUJARA, K.K. (1971). Space-harmonic analysis of periodically supported beams: response to convected random loading. *Journal of Sound and Vibration*, **14**, 525–541. 9, 111

MEAD, D.J. & WILBY, E.G. (1966). The random vibrations of a multi-supported heavily damped beam. *The shock and vibration bulletin*, **35**, 45–55. 9

MEAD, D.J., ZHU, D.C. & BARDELL, N.S. (1988). Free vibration of an orthogonally stiffened flat plate. *Journal of Sound and Vibration*, **127**, 19–48. 63

MEJDI, A. & ATALLA, N. (2010). Dynamic and acoustic response of bidirectionally stiffened plates with eccentric stiffeners subject to airborne and structure-borne excitations. *Journal of Sound and Vibration*, **329**, 4422–4439. 112

MENCIK, J.M. (2012). A model reduction strategy for computing the forced response of elastic waveguides using the wave finite element method. *Computer Methods in Applied Mechanics and Engineering*, **229-232**, 68–86. 29

MENCIK, J.M. & ICHCHOU, M.N. (2007). Wave finite elements in guided elastodynamics with internal fluid. *International Journal of Solids and Structures*, **44**, 2148–2167. 16, 41

MENCIK, J.M. & ICHCHOU, M.N. (2008). A substructuring technique for finite element wave propagation in multi-layered systems. *Computer Methods in Applied Mechanics and Engineering*, **197**, 505–523. 9

NEMAT-NASSER, S., IWAKUMA, T. & HEJAZI, M. (1982). On composites with periodic structure. *Mechanics of materials*, **1**, 239–267. 23

OLHOFF, N., NIU, B. & CHENG, G.D. (2012). Optimum design of band-gap beam structures. *International Journal of Solids and Structures*, **49**, 3158–3169. 43

ORRIS, R.M. & PETYT, M. (1974). A finite element study of harmonic wave propagation in periodic structures. *Journal of Sound and Vibration*, **33**, 223–236. 9

PERKINS, N.C. & MOTE, C.D. (1986). Comments on curve veering in eigenvalue problems. *Journal of Sound and Vibration*, **106**, 451–463. 65

RAYLEIGH, L. (1887). On the maintenance of vibrations by forces of double frequency, and on the propagation of waves through a medium endowed with a periodic structure. *Philosophical Magazine*, **XVII**, 145–159. 8

RENNO, J.M. & MACE, B.R. (2010). On the forced response of waveguides using the wave and finite element method. *Journal of Sound and Vibration*, **329**, 5474–5488. 41

RENNO, J.M. & MACE, B.R. (2014). Calculating the forced response of cylinders and cylindrical shells using the wave and finite element method. *Journal of Sound and Vibration*, **333**, 5340–5355. 124

ROYER, D. & DIEULESAINT, E. (2000). *Elastic Waves in Solids I - Free and Guided Propagation*. Springer, Berlin. 91

RUZZENE, M., SCARPA, F. & SORANNA, F. (2003). Wave beaming effects in two-dimensional cellular structures. *Smart Materials and Structures*, **12**, 363–372. 11, 63, 64

SIGALAS, M.M. & ECONOMOU, E.N. (1992). Elastic and acoustic wave band structure. *Journal of Sound and Vibration*, **158**, 377–382. 10

SPADONI, A., RUZZENE, M. & CUNEFARE, K. (2009). Vibration and Wave Propagation Control of Plates with Periodic Arrays of Shunted Piezoelectric Patches. *Journal of Intelligent Material Systems and Structures*, **20**, 979–990. 129

THORBY, D. (2008). *Structural Dynamics and Vibration in Practice*, vol. 54. Elsevier. 2, 3, 15, 28, 29, 159

TIAN, B.Y., TIE, B. & AUBRY, D. (2011). Elastic Wave Propagation in Periodic Cellular Structures. *Chinese Mechanical Engineering Society*, **76**, 217–233. 45

TORRENT, D. & SÁNCHEZ-DEHESA, J. (2008). Acoustic cloaking in two dimensions: a feasible approach. *New Journal of Physics*, **10**, 063015. 130

VASSEUR, J.O., DJAFARI-ROUHAI, B., DOBRZYNSKI, L., KUSHWAHA, M.S. & HALEVI, P. (1994). Complete acoustic band gaps in periodic fibre reinforced composite materials: the carbon/epoxy composite and some metallic systems. *Journal of Physics: Condensed matter*, **6**, 8759–8770. 10

WAKI, Y., MACE, B.R. & BRENNAN, M.J. (2009). Numerical issues concerning the wave and finite element method for free and forced vibrations of waveguides. *Journal of Sound and Vibration*, **327**, 92–108. 9, 18, 41, 43

WANG, G., LI, S., NGUYEN, H.N. & SITAR, N. (2007). Effective Elastic Stiffness for Periodic Masonry Structures via eigenstrain homogenization. *Journal of materials in civil engineering*, 269–277. 23

WANG, W.C. & LAI, K.H. (2003). Hybrid Determination of Equivalent Characteristics of Perforated Plates. *Society of Experimental Mechanics*, **43**, 163–172. 25

XIANG, H.J. & SHI, Z.F. (2009). Analysis of flexural vibration band gaps in periodic beams using differential quadrature method. *Computers & Structures*, **87**, 1559–1566. 43

XIAO, Y., WEN, J. & WEN, X. (2012). Flexural wave band gaps in locally resonant thin plates with periodically attached spring–mass resonators. *Journal of Physics D: Applied Physics*, **45**, 195401. 129, 162

XIAO, Y., WEN, J.H., YU, D. & WEN, X. (2013). Flexural wave propagation in beams with periodically attached vibration absorbers: Band-gap behavior and band formation mechanisms. *Journal of Sound and Vibration*, **332**, 867–893. 43

XIE, G., THOMPSON, D.J. & JONES, C.J.C. (2004). Mode count and modal density of structural systems: relationships with boundary conditions. *Journal of Sound and Vibration*, **274**, 621–651. 123

XIN, F.X. & LU, T.J. (2011). Analytical modeling of wave propagation in orthogonally rib-stiffened sandwich structures: Sound radiation. *Computers & Structures*, **89**, 507–516. 112

YU, D.L., LIU, Y.Z., QIU, J., WANG, G. & ZHAO, H.G. (2006). Complete flexural vibration band gaps in membrane-like lattice structures. *Physics Letters A*, **357**, 154–158. 10

YU, D.L., FANG, J.Y., CAI, L., HAN, X.Y. & WEN, J.H. (2009). Triply coupled vibrational band gap in a periodic and nonsymmetrical axially loaded thin-walled Bernoulli–Euler beam including the warping effect. *Physics Letters A*, **373**, 3464–3469. 43, 52, 54, 56

ZHANG, W., WANG, F., DAI, G. & SUN, S. (2007). Topology Optimal Design of Material Microstructures Using Strain Energy-based Method. *Chinese journal of aeronautics*, **20**, 320–326. 23

ZHONG, W.X. & WILLIAMS, F.W. (1995). On the direct solution of wave propagation for repetitive structures. *Journal of Sound and Vibration*, **181**, 485–501. 9, 17, 40, 41

ZHOU, C.W., LAINÉ, J.P., ICHCHOU, M.N. & ZINE, A.M. (2013a). Application de la réduction modale sur les guides d'ondes périodiques. In *Journées des Jeunes Chercheurs en vibrations, Acoustique et Bruit (3ème édition)*, Compiègne, France. 4

ZHOU, C.W., LAINÉ, J.P., ICHCHOU, M.N. & ZINE, A.M. (2013b). Application of wave finite element method on reduced models for the analysis of flexural waves in periodic beams. In *Proceedings of the MEDYNA 2013*, Marrakech, Morocco. 4

ZHOU, C.W., LAINÉ, J.P., ICHCHOU, M.N. & ZINE, A.M. (2014a). Free wave propagation in two-dimensional periodic beam grillage. In *Proceedings of the ICSV21*, Beijing, China. 4

ZHOU, C.W., LAINÉ, J.P., ICHCHOU, M.N. & ZINE, A.M. (2014b). The study of the wave propagation in periodic structures. In *7th Centrale-Beihang Workshop*, Beijing, China. 4

ZHOU, C.W., LAINÉ, J.P., ICHCHOU, M.N. & ZINE, A.M. (2014c). The study of two dimensional periodic structures using wave and modal coupled method. In *Journées des Jeunes Chercheurs en vibrations, Acoustique et Bruit (JJCAB) (4ème édition)*, Lyon, France. 4

ZHOU, C.W., LAINÉ, J.P., ICHCHOU, M.N. & ZINE, A.M. (2015a). Multi-scale modeling for two-dimensional periodic structures using a combined wave/mode based approach. *Computers and Structures*, in press. 4

ZHOU, C.W., LAINÉ, J.P., ICHCHOU, M.N. & ZINE, A.M. (2015b). Numerical and experimental investigation of wave propagation features in perforated plates. *submitted to Mechanical Systems and Signal Processing*. 4

ZHOU, C.W., LAINÉ, J.P., ICHCHOU, M.N. & ZINE, A.M. (2015c). Wave finite element method based on reduced model for one-dimensional periodic structures. *International Journal of Applied Mechanics*, in press. 4

ZHOU, W.J. & ICHCHOU, M.N. (2010). Wave propagation in mechanical waveguide with curved members using wave finite element solution. *Computer Methods in Applied Mechanics and Engineering*, **199**, 2099–2109. 16

# List of Figures

# List of Tables

# AUTORISATION DE SOUTENANCE

Vu les dispositions de l'arrêté du 7 août 2006,

Vu la demande des Directeurs de Thèse

Monsieur M. ICHCHOU et Monsieur A.M. ZINE

et les rapports de

Monsieur H. RIOU
Professeur - LMT Cachan - 61 av. président Wilson - 94235 Cachan cedex

Et de

Monsieur M. OUISSE
Professeur - FEMTO ST - Dép. Mécanique Appliquée - ENSMM - 24 chemin de l'Epitaphe
25000 Besançon

**Mademoiselle ZHOU Changwei**

est autorisée à soutenir une thèse pour l'obtention du grade de **DOCTEUR**

**Ecole doctorale MECANIQUE , ENERGETIQUE, GENIE CIVIL ET ACOUSTIQUE**

Fait à Ecully, le 27 novembre 2014

P/Le directeur de l'E.C.L.
La directrice des Etudes

ECOLE CENTRALE DE LYON
Service Scolarité
ECULLY

M-A. GALLAND